In incorporation improvement in InGaN based active region using InGaN pseudo substrate for monolithic white LED application

Armelle Even

To cite this version:

Armelle Even. In incorporation improvement in InGaN based active region using InGaN pseudo substrate for monolithic white LED application. Optics [physics.optics]. Université Grenoble Alpes, 2018. English. NNT : 2018GREAY008 . tel-01835620

HAL Id: tel-01835620
https://theses.hal.science/tel-01835620
Submitted on 11 Jul 2018

Communauté
UNIVERSITÉ Grenoble Alpes

THÈSE

Pour obtenir le grade de

DOCTEUR DE LA COMMUNAUTE UNIVERSITE GRENOBLE ALPES

Spécialité : **PHYSIQUE DES MATERIAUX**

Arrêté ministériel : 25 mai 2016

Présentée par

Armelle Even

Thèse dirigée par **Ivan-Christophe Robin**, et
encadrée par **Amélie Dussaigne**

préparée au sein du **Laboratoire d'Electronique et de Technologie de l'Information (LETI-CEA)**
dans **l'École Doctorale de Physique**

Amélioration de l'incorporation d'indium dans zone active à base d'InGaN grâce à la croissance sur pseudo-substrat InGaN pour l'application à la DEL blanche monolithique

In incorporation improvement in InGaN based active region using InGaN pseudo substrate for monolithic white LED application

Thèse soutenue publiquement le **27 février 2018**
devant le jury composé de :

Monsieur Nicolas Grandjean
Professeur, EPFL-LASPE, Rapporteur, Président
Monsieur Pierre Lefebvre
Directeur de recherche, CNRS-L2C, Rapporteur
Monsieur Henri Mariette
Directeur de recherche émérite, CNRS-NPSC, Examinateur
Monsieur Adrian Avramescu
Expert de haut niveau, OSRAM Opto Semiconductors GmbH, Examinateur
Monsieur David Sotta
Ingénieur-Chercheur, Soitec, Invité
Monsieur Ivan-Christophe Robin
Ingénieur-Chercheur, Aledia, Directeur de thèse
Madame Amélie Dussaigne
Ingénieur-Chercheur, CEA-Leti, Encadrante

Acknowledgements

Voici venu le temps des remerciements. Je tiens à exprimer ma reconnaissance envers toutes les personnes que j'ai croisées pendant ces trois années et qui ont rendu la réussite de cette thèse possible.

Cette thèse a été préparée au sein du laboratoire LMP au CEA-Leti. Je remercie Alain Millon pour m'avoir accueilli dans son laboratoire ainsi qu'Anne Roule qui a pris sa suite. Merci pour votre intérêt pour le sujet et d'avoir fait en sorte que cette thèse se déroule dans les meilleures conditions. Merci également à Bernard André pour l'accueil dans son service et pour les nombreux moyens mis à disposition.

En premier lieu, je remercie Amélie Dussaigne mon encadrante pour ses conseils avisés, son soutien sans faille et pour m'avoir appris à être plus autonome aussi. Ce fut un plaisir de travailler avec toi pendant ces trois années.
Merci à Ivan-Christophe Robin mon directeur de thèse pour ses suggestions et ses relectures du manuscrit. Merci pour m'avoir initié à la simulation, pour tes nombreuses idées et les échanges toujours très intéressants.

Je tiens à remercier tout particulièrement l'équipe de MOCVD du M23 dans laquelle je me suis sentie bien pendant ces trois années.
Je remercie Mathieu Lafossas pour m'avoir initié à la MOCVD et avoir partagé son expérience et ses connaissances sur l'équipement. Cette thèse n'aurait pas été possible sans un équipement en parfait état. Merci à Rémy Obrecht puis à Frédéric Barbier pour l'avoir assisté. Merci aussi pour les discussions sur les XRD et les couches "partiellement relaxées" et pour avoir partagé avec moi le suspens du lundi matin pour savoir si la RSM de 56 heures n'avait pas planté pendant le week-end ! Merci à vous trois pour vos coups de main quand j'en avais besoin.
Un grand merci à Pierre Ferret pour son initiation à la diffraction aux rayons X des nitrures. Merci également pour les nombreuses discussions passionnantes sur tout un tas de sujets (sur la thèse mais pas que) et pour m'avoir fait me poser les bonnes questions et prendre un peu de recul quand cela était nécessaire.

Je remercie également mes collègues doctorants Gautier Laval et Timotée Journot pour avoir été de très bonne compagnie pendant cette thèse. Merci à Gautier pour m'avoir bien accueilli dans l'équipe, pour avoir répondu à mes questions et pour avoir toujours veillé à ce que l'équipe ne m'oublie pas pour aller manger malgré mon exil au D6 ! Merci à Timotée pour les bavardages dans le bureau, je te souhaite courage pour la rédaction ! Merci aussi à Sofia Boughaleb et Benjamin Samuel qui ont fait leur stage dans l'équipe et continuent en thèse. Je vous souhaite plein de réussite dans votre thèse et bon courage aussi.

Je remercie la team du LMP D6 pour m'avoir accueilli dans leur couloir, Dominique Giotta, Jean-Louis Santailler et les autres. Merci pour votre bonne humeur constante tout au long de ces trois années. Une pensée particulière pour Aymeric Tuaz mon co-bureau, merci de m'avoir supporté et pour la compagnie quand toutes les lumières du couloir étaient depuis longtemps éteintes ! Merci à toutes les autres personnes du LMP, Bérangère Hyot, Carole Pernel et les autres. Un remerciement particulier à Roselyne Templier pour son initiation au MEB et sa bonne humeur.

Une pensée pour François Levy, merci pour avoir fait le lien entre l'équipe et Soitec. Merci également pour tes précieux conseils, relectures et pour ta compagnie en conférence (on se souviendra longtemps de l'ouragan et des 24 h coincés à l'hôtel à Orlando !).

Je remercie l'équipe qui a réalisé le processing de mes LEDs en salle blanche du D6, un merci particulier à Helge Haas pour avoir été toujours disponible pour répondre à mes questions sur la techno. Du côté d'Aledia, merci à Michael Delalande pour les nombreux coups de mains sur la PL du M23 et à Florian Dupont pour avoir accepté de prendre les vendredis comme jours de manips ce qui a bien arrangé toute l'équipe !

Je voudrais également remercier toutes les personnes avec qui j'ai collaboré à la PFNC. Merci à Adeline Grenier pour ses analyses de sonde atomique et pour sa disponibilité pour m'en expliquer les principaux ressorts. Un remerciement à David Cooper pour ses analyses d'holographie électronique et ses explications. Je tiens également à remercier Névine Rochat pour ses analyses de cathodoluminescence et pour m'avoir initié à cette technique de caractérisation. Merci aussi à Christophe Licitra pour la formation et l'aide sur le montage de micro-photoluminescence. Merci également à Eric Robin pour ses caractérisations EDX et à Denis Mariolle pour m'avoir formé à l'utilisation de l'AFM.

J'adresse mes remerciements à l'équipe de la ligne ID01 à l'ESRF. Merci à Tobias Schulli, à Carsten Richter pour ses analyses détaillées, à Marie-Ingrid Richard et à Yves-Matthieu Le Vaillant pour avoir fait le lien entre Soitec, l'ESRF et le CEA-Leti.

Merci à l'entreprise Soitec et aux personnes impliquées dans le projet InGaNOS pour avoir accepté de nous faire parvenir les substrats InGaNOS qui ont permis d'obtenir ces résul-

tats intéressants. Un remerciement particulier à David Sotta pour avoir accepté d'être membre invité dans ce jury de thèse.
Je remercie également les rapporteurs de ce manuscrit, Nicolas Grandjean et Pierre Lefebvre ainsi que Henri Mariette et Adrian Avramescu pour avoir accepté de faire partie de ce jury et pour l'interêt qu'ils ont porté à cette thèse.

Merci aux amis de Grenoble et d'ailleurs pour leur amitié tout au long de ces trois années. Je remercie mes parents pour m'avoir donné le goût aux sciences et pour leur soutien pendant la durée de cette thèse mais également tout au long de mes études supérieures. Merci aussi à mes soeurs, Morgane et Blandine.

Et enfin, merci à Benjamin pour son soutien infaillible malgré la distance.

Table des matières

List of acronyms

AFM	Atomic Force Microscopy
APT	Atome Probe Tomography
CIE	Comission Internationale de l'Eclairage
CL	Cathodoluminescence
CT	Color Temperature
CRI	Color Rendering Index
ECV	Electrochemical Capacitance Voltage
EDX	Energy Dispersive X-ray spectroscopy
EQE	External Quantum Efficiency
ESRF	European Synchrotron Radiation Facility
FWHM	Full Width at Half Maximum
HAADF	High Angle Annular Dark Field
HRXRD	High Resolution X-ray Diffraction
III-N	III Nitrides
IL	Interlayer
IQE	Internal Quantum Efficiency

LED	Light Emitting Diode
MBE	Molecular Beam Epitaxy
MOCVD	MetalOrganic Chemical Vapor Deposition
MOVPE	MetalOrganic Vapor Phase Epitaxy
MQW	Multiple Quantum Wells
NID	Not Intentionally Doped
PAMBE	Plasma Assisted Molecular Beam Epitaxy
PL	Photoluminescence
PLD	Pulsed Layer Deposition
QD	Quantum Dot
QB	Quantum Barrier
QCSE	Quantum Confined Stark Effect
QW	Quantum Well
RBS	Rutherford Back Scattering spectrometry
RC	Rocking Curve
RGB	Red Green Blue
RMS	Root Mean Square
RSM	Reciprocal Space Mapping
SAG	Selective Area Growth
SIMS	Secondary Ion Mass Spectroscopy
SL	SuperLattice
SEM	Scanning Electron Microscope
STEM	Scanning Transmission Electron Microscope
TCAD	Technology Computer Aided Design

TD	Threading Dislocation
TEM	Transmission Electron Microscope
TMIn	Tri Methyl Indium
UCSB	University of California, Santa Barbara
UL	Underlying Layer
UV	Ultra Violet
XRD	X-ray Diffraction
WPE	Wall Plug Efficiency
YAG	Yttrium Aluminum Garnet

Introduction

The 2014 Physics Nobel Prize was awarded to Isamu Akasaki, Hiroshi Amano and Shuji Nakamura "*for the invention of efficient blue light-emitting diodes (LEDs) which has enabled bright and energy-saving white light sources*" based on the InGaN/GaN material system. Since the 1970's, this material system had been extensively studied but because of the low material quality and the resistivity of the p-type layers, the research was abandoned. Yet, in 1989, Amano *et al.* [1] succeeded in activating the magnesium dopant in GaN yielding the first p-n junction. Nakamura *et al.* then fabricated the first blue LED, by inserting InGaN/GaN Quantum Wells (QWs) in the active region in 1994 [2].
Then, with the addition of YAG (Yttrium Aluminum Garnet) phosphors, white light emission was achieved [3]. In comparison to other sources of white light (incandescent light bulb, fluorescent lamp...), white LEDs present several advantages like their long lifetime and their good luminous efficacy. As a consequence, LED lighting market share is growing and the LED lighting penetration was 22 % in 2017 and is expected to reach up to 63 % in 2022 [4]. Nonetheless, phosphor-based LEDs present some problems related to the phosphor lifetime and stability of emission wavelength with operating temperature (incompatible with a good quality lighting) as well as losses associated with the phosphor-down conversion. Alternatively to this converted approach, the white monolithic LED was introduced in 2001 [5] with an active region composed of blue and yellow emitting QWs. Yet, the efficiency of such LEDs is limited by the low efficiency of the yellow or red emitting QWs .

LEDs are also widely used for the display, backlighting and liquid crystal application. However, if LEDs consistuting the blue pixels are manufactured with AlInGaN material system, the material consistuting the LEDs of the red colored pixels is different, the AlInGaP material system is employed. For the green (or yellow) pixels, there is no material system which provides efficient LED emission but they are usually AlInGaN based. This problem is reffered to as the "green gap". The integration of the RGB (Red Green Blue) pixels grown with different material systems is also troublesome for micro-displays and the ideal would be to grow the three RGB pixels with III-N.

But, if the III-N based compounds can theoretically cover the whole visible range, their efficiency decreases as the emission wavelength is increased. This phenomenon is partly attributed to the low miscibility of indium in GaN and to the strain between the InGaN QWs of the active region and the GaN on sapphire usually used as the substrate. In addition, the internal electric field which is increased as the QWs are widenned or when indium content is increased furthers hampers the LED efficiency. Furthermore, the strain is also responsible for the compositionnal pulling effect which prevents an easy indium incorporation and therefore limits the emission wavelength. Moreover, the efficiency droop for high carrier injections which is already problematical for blue light emission, is aggravated for long wavelength emission.

To tackle the green gap problem with the AlInGaN material system, in this thesis, we propose to grow an LED structure on a relaxed InGaN substrate. Thanks to this process, a higher indium incorporation rate should be observed [6] as well as a reduction of the internal electric field [7]. As InGaN bulk does not exist, the InGaN pseudo-substrates called InGaNOS are used for this study. They are manufactured by Soitec using their Smart Cut technology. On these substrates, a full InGaN structure can be grown. These structures may then be used to fabricate monochromatic LEDs in the green, yellow or even red range for the integration of RGB pixels or high quality lighting. Alternatively, an efficient white monolithic LED can be considered thanks to this growth process.

The first chapter details the specificities of the InGaN alloy. The properties of the InGaN material in its relaxed and strained states are described with a particular focus on the issues related to the growth of InGaN on GaN. Then, an exhaustive review of the characterization techniques to quantify the indium content in InGaN thick layer and InGaN QWs is presented to determine which techniques will be used to characterize the samples in this thesis.

The different types of white LEDs are described in chapter 2. The white monolithic LED suffers from the unbalanced carrier distribution between the different MQWs of the active region and the low efficiency of the green and red QWs. A simulation study that uses InGaN in the barriers is shown to control the distribution of the carriers. The issues related to the green gap are then reported together with the existing solutions to overcome it. This leads us to unveil our original solution for an efficient LED emitting at long wavelength based on a full InGaN structure on InGaN substrate.

In the third chapter, solutions are studied to reach long wavelengths on GaN on sapphire. First, attempts based on simple variations of the growth parameters show the intrinsic limitations. Structures using thick InGaN or InGaN/GaN superlattices are then studied with a preliminary study of the InGaN layers on GaN. Next, a study to reduce the surface segregation of indium in InGaN/GaN QWs is conducted.

In Chapter 4, the InGaN pseudo-substrates called InGaNOS and their fabrication process are introduced. Then, a detailed study of the InGaN regrown layers on InGaNOS substrates is presented with an example of a particular structure based on the use of GaN interlayers. Later, the homogeneity of the emission at the sub-micrometer scale is assessed thanks to experiments done at the European Synchrotron Radiation Facility (ESRF). Subsequently, in Chapter 5, the MQWs grown on InGaNOS substrates and GaN templates are characterized throuroughly. The internal quantum efficiencies measured for these structures are benchmarked to the existing literature. Lastly, the properties of the first LED grown on an InGaNOs substrate are described with a focus on the remaining challenges to achieve efficient emission at long wavelength.

References of the introduction

[1] H. Amano, M. Kito, K. Hiramatsu and I. Akasaki. *Jpn. J. Appl. Phy.* **28**, L2112 (1989).

[2] S. Nakamura, T. Mukai and M. Senoh. *Appl. Phy. Lett.* **64**, 1687 (1994).

[3] K. Bando, K. Sakano, Y. Noguchi and Y. Shimizu. *J.of Light & Visual Evt* **22**, 2 (1998).

[4] J. Wu. *Smart Lighting, Niche Lighting and Lighting in Emerging Countries are Top Three Driving Forces for Global LED Lighting Market Trend.* LED Inside (2017).

[5] B. Damilano, N. Grandjean, S. Vézian and J. Massies. *J. Cryst. Growth* **228**, 466 (2001).

[6] Y. Inatomi, Y. Kangawa, T. Ito, T. Suski, Y. Kumagai, K. Kakimoto and A. Koukitu. *Jpn. J. Appl. Phy.* **56**, 078003 (2017).

[7] S. H. Park, T. H. Chung, J. H. Baek and D. Ahn. *Jpn. J. Appl. Phy.* **54**, 2 (2015).

1

Growth of InGaN alloy

This first chapter introduces the concepts for the growth of InGaN-based LEDs. First, some of the properties of the AlInGaN material system will be presented. The nature of the InGaN alloy will be particularly detailed. Then, we will focus on the specific growth of InGaN on GaN and its difficulties. We will especially describe the issues related to strain. Finally, a review of the techniques to quantify indium content in InGaN thick layers and in InGaN quantum wells will be presented.

1.1 Properties of AlInGaN system

1.1.1 Structural properties

1.1.1.1 Crystallography

AlInGaN-based semiconductors are compounds formed by the association of atoms from the column III of the periodic table (aluminum, gallium and indium) and nitrogen atom from the column V. Two different crystalline structures can be found : a stable hexagonal form called wurtzite and a meta-stable cubic form of zinc-blende type. Cubic form material with good quality remains hard to manufacture because of its thermodynamical instability. Therefore, only wurtzite structures will be studied throughout this thesis.

Figure 1.1 represents the wurtzite unit cell of GaN. The gallium (Ga) and nitrogen (N) atom individually form a sublattice which is of hexagonal type. The Bravais hexagonal unit cell is a prism which has base edges of same length a and desoriented of 120°. The height of the prism is noted c.

In the three index hexagonal coordinate system (a_1, a_2, c) associated with this unit cell, Ga atoms are localized at $(0, 0, 0)$ and $(2/3, 1/3, 1/2)$ and N atoms at $(0, 0, u)$ and $(2/3, 1/3, u+1/2)$ with $u = 0.378$.

We therefore have two hexagonal sub-lattices, one formed by the Ga atoms and the other formed by the N atoms having an offset of 3/8 along c axis. The a and c lattice parameters of GaN, InN and AlN are given in table 1.1.

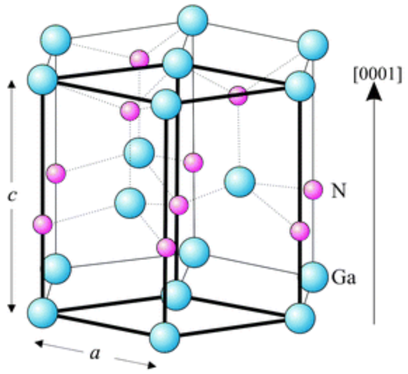

FIGURE 1.1 – Crystalline unit cell of wurtzite GaN [1].

III-N	a (Å)	c (Å)
GaN [2]	3.1878	5.185
AlN [3]	3.112	4.981
InN [4]	3.538	5.703

TABLE 1.1 – a and c lattice parameters of wurtzite structure for GaN, AlN and InN.

Usually for the hexagonal cell, the 4 Bravais-Miller indice notation (h, k, i, l) is used with $i = -(h + k)$ but the (h, k, l) notation is also used. Some of the planes, including c-planes $\{0001\}$ perpendicular to c axis and the m-planes $\{1\bar{1}00\}$ parallel to the c axis are represented in Figure 1.2.

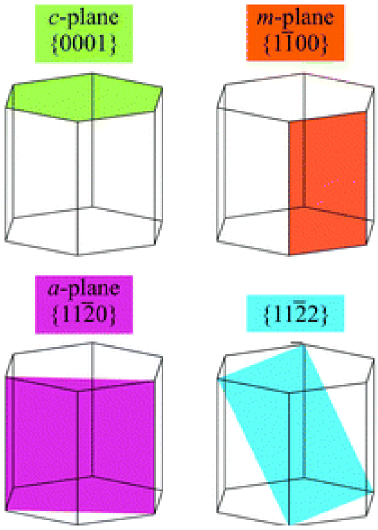

FIGURE 1.2 – Depiction of the plans of the wurtzite structure with their Bravais-Miller notation [1].

1.1.1.2 Polarity

The structure of the wurtzite cell is not centrosymmetric as the dangling bonds at the surface of the material in (0001) and (000$\bar{1}$) are not equivalent. As pictured in Fig.1.3, when the Ga atom has three bonds in the direction oppposite to the growth direction, the material is known as Ga-polar. Conversely, when the N atom has three bonds in the growth direction, the material is named N-polar. The (0001) face of the crystal is called Ga-face (noted as +c) and the (000$\bar{1}$) face is called N-face and noted as -c.

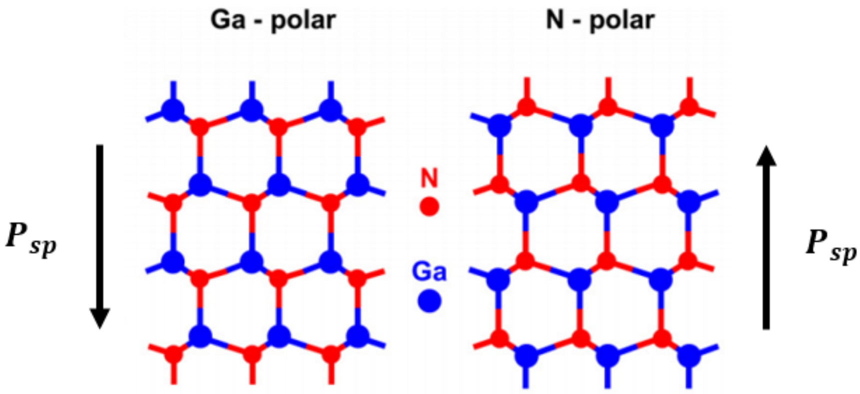

FIGURE 1.3 – Ga polarity and N polarity of wurtzite structure of GaN from [5].

1.1.2 Electronic and electric properties

1.1.2.1 Spontaneous polarization

In the wurtzite structure, the barycenters of negative and positive charges do not coincide. This spatial separation of electrons and holes creates a dipole and gives rise to spontaneous polarization. The spontaneous polarization vector is illustrated in Fig. 1.3. Table 1.2 summarizes the values of spontaneous polarization for AlN, GaN and InN compiled by Vurgaftman [6] *et al.*.

III-N	$P_{sp}(C.m^{-2}))$
GaN	-0.034
AlN	-0.090
InN	-0.042

TABLE 1.2 – Value of spontaneous polarization for GaN, AlN and InN from [6].

For the InGaN alloy, the spontaneous polarization can be expressed with the following formula [7] :

$$P_{sp}(InGaN) = x \times P_{sp}(InN) + (1 - x) \times P_{sp}(GaN) - b \times x \times (1 - x) \tag{1.1}$$

The recomended value for the bowing parameter b by Vurgaftman [6] *et al.* is $b = 0.037$ $C.m^{-2}$.

1.1.2.2 InGaN bandgap energy

The lattice parameter of III-nitrides ternary alloys can be expressed with the Vegard's law [8] from the values of the lattice parameters of the the binary compounds presented in 1.1. Vegard's law can only be applied in the case where we consider completely relaxed material.

$$a_{In_xGa_{1-x}N} = x \times a_{InN} + (1 - x) \times a_{GaN} \tag{1.2}$$

$$c_{In_xGa_{1-x}N} = x \times c_{InN} + (1 - x) \times c_{GaN} \tag{1.3}$$

For the expression of the bandgap energy a third term called the bowing parameter has to be added to the Vegard's law :

$$Eg_{In_xGa_{1-x}N} = x \times Eg_{InN} + (1 - x) \times Eg_{GaN} + b \times (1 - x) \times x \tag{1.4}$$

The values of the bandgap for the binary compounds are given in Table 1.3 from the review of Vurgaftman *et al.*[6]. The value given for the bowing parameter of InGaN can vary between 1.4 eV and 2.8 eV depending on the sources and on the In content and InGaN thickness, the value recomended by Vurgaftman *et al.* for small In contents [6] is 1.4 eV.

III-N	E_g (eV)
GaN	3.510
AlN	6.25
InN	0.78

TABLE 1.3 – Energy bandgaps for GaN, AlN and InN at 0 K in the wurtzite structure from [6].

1.2 InGaN alloy

1.2.1 Indium miscibility in GaN

Because of the difference in size between the Ga atom (covalent radius of 126 pm) and the In atom (covalent radius of 144 pm) and the small binding energy between In and N, the miscibility of In in GaN is very poor. Ho *et al.* [9] studied the thermodynamics of the bulk InGaN alloy. The phase diagram (Fig. 1.4) they established shows that at the temperatures necessary for InGaN growth (typically between 650$^\circ C$ and 800$^\circ C$), the alloy is unstable over a wide range of compositions (also shown in [10] and [11]).
Typically, when In content is greater than 25 %, phase separation may occur [12]. This has been evidenced in several experimental studies in layers grown by MBE [13] and MOVPE [14].

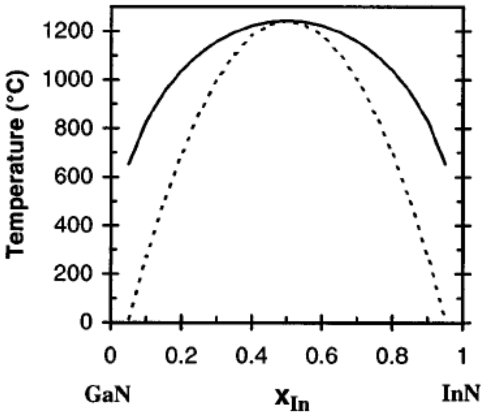

FIGURE 1.4 – Phase diagram for the $In_xGa_{1-x}N$ alloy. Binodal (solid) and spinodal (dashed) curves [9].

1.2.2 InGaN growth conditions- MOVPE and MBE

1.2.2.1 MetalOrganic Vapor Phase Epitaxy (MOVPE)

In this thesis, all samples were grown using MetalOrganic Vapor Phase Epitaxy (MOVPE) in an Aixtron Closed-Coupled Showerhead 6x2 inches reactor. In this technique, the growth is conducted in a reactor with cold walls. Only the substrate is heated and maintained at the desired growth temperature. The gas precursors used for the growth of GaN are trimethylgallium ($TMGa$) and ammonia (NH_3). For the growth of the InGaN alloy, triethylgallium ($TEGa$) is usually preferred to supply Ga atoms and trimethylindium ($TMIn$) to supply In atoms. The ammonia and the other species ($TMIn$, $TMGa$, $TEGa$) are introduced separately in the reactor in order to avoid any side reaction. The species are either carried by hydrogen (under the H_2 form), nitrogen (under the N_2 form) and they will meet at the substrate's surface. Subjected to heat, they will dissociate by pyrolysis. Atoms resulting from decomposition are then adsorbed on the substrate's surface and diffuse until their incorporation or desorption. The chemical residues are then evacuated using the carrier gases. For GaN, the equation of the decomposition is as follows :

$$Ga + NH_3 \leftrightarrows GaN + 3/2 \quad H_2 \tag{1.5}$$

Typically, GaN growth is conducted around 1000-1100 ˚C. However, growth of InGaN requires lower temperatures between 650 ˚C and 800 ˚C because In atoms desorb at higher temperatures. For InGaN growth, $TEGa$ is preferred to $TMGa$ to suppply Ga atoms as the breakdown of the molecules constituing the gas occurs at a lower temperature and carbon contamination is reduced. The growth temperature is a key parameter and will be used as a setting parameter to control the incorporation of indium in the layer. While GaN growth rate can be set at a rather high value (about 2.2 μm/h in our case), InGaN growth rate is compelled to be very low (about 0.1 μm/h in our case) because of the low NH_3 cracking efficiency at the InGaN growth temperatures. Indeed, NH_3 cracking efficiency decreases with the temperature [15].

To compensate this low cracking efficiency, the flux of NH_3 is set at a high value. The V/III ratio corresponds to the ratio of the flux of NH_3 over the flux of the others precursors ($TMGa$ or $TEGa$, $TMIn$).

In this thesis, GaN growth was conducted under H_2 atmosphere while for InGaN layers, N_2 was preffered.

1.2.2.2 Molecular Beam Epitaxy (MBE)

In case of MBE, lower growth temperatures are needed, usually around 550 ˚C. This low temperature could be a reason explaining the low structural quality of the InGaN/GaN quantums wells (QWs) grown by MBE due to the presence of high point defect density [16]. For a particular type of MBE, the plasma assisted MBE (PAMBE), 100 % of the nitrogen is active. With this technique, the whole range of indium compositions is attainable.

1.2.3 Nature of InGaN alloy

1.2.3.1 Indium inhomogeneities

Because of the difficulty to incorporate In in GaN, the InGaN alloy presents an inhomogeneous distribution. It has been evidenced in samples grown by MOVPE [17], [18], [19], [20],[21], [22] and by MBE [17], [20], [23] and for different growth directions [24], [25]. Fig. 1.5 displays the results of the Atom Probe Tomography (see annex C.4) characterization for two InGaN/GaN quantum wells (QWs) in one of our Multiple Quantum Well (MQW) structures emitting at 500 nm (sample E presented in chapter 5). The position of indium atoms in the QWs are given by the red dots. The mean In content is measured to be 17.5 %. The isocurves in In composition reveal strong inhomogeneities.

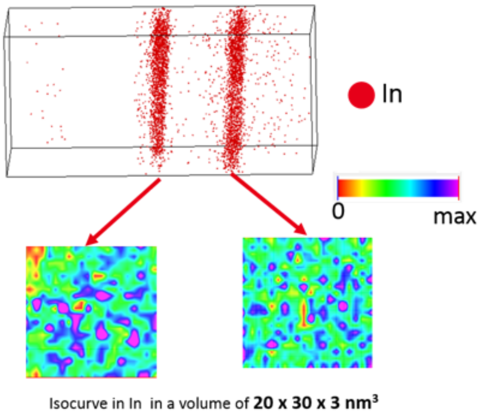

FIGURE 1.5 – 3D reconstruction of a volume of 20 × 30 × 3 nm^3 for an active region of an InGaN/GaN MQW sample and In isocurves for the two first QWs.

1.2.3.2 Carrier localization in InGaN

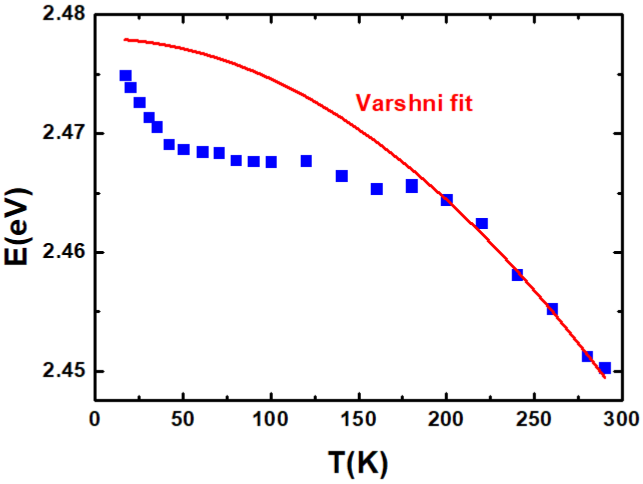

FIGURE 1.6 – PL energy vs Temperature for a green emitting $InGaN/GaN$ MQW structure.

Fig. 1.6 shows the evolution with temperature of the central emission energy of the PL spectrum of InGaN/GaN MQW emitting in the green range. This curve follows an "S-shape" and deviates from the Varshni equation [26] which normally governs the evolution of the bandgap energy with temperature. This behavior has been reported in InGaN/GaN MQWs [27], [28] and in InGaN thin films [29], [30], [31], [32]. The phenomenon evidences a temperature-dependant localization of carriers.

The S-shape of the curve may be explained using Fig. 1.7 from [33]. The situation at low temperature is as on Fig. 1.7 (a), all the carriers are distributed randomly on the different potential minima. When the temperature is increased, the thermal activation allows carriers to diffuse into the deepest potential wells (Fig. 1.7 (b)) which provokes a red-shift of the emission energy. Fig. 1.7 (c) then illustrates the phase of stabilization of emission energy or blue-shift, even the more localized carrier start to be mobile. Finally when the temperature is high enough, thermalization of carrier becomes more and more important (Fig. 1.7 (d)) and the carriers become fully delocalized and the emission energy follows Varshni's law.

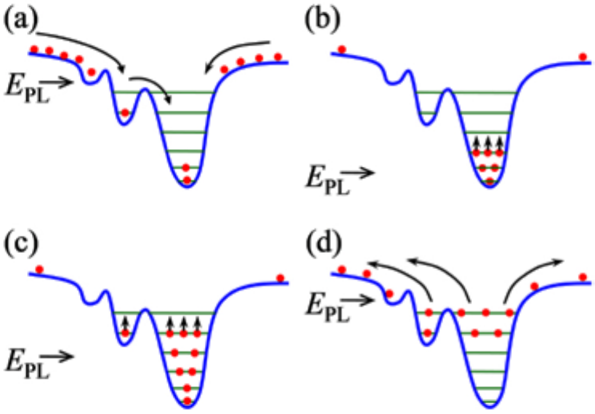

FIGURE 1.7 – Schematic diagrams indicating the possible mechanism of carrier transfer amongst the potential fluctuations in an MQW structure at different temperatures [33].

1.2.3.3 Indium clustering

Fig 1.8 displays the In distribution in an N-polar InGaN/GaN quantum well analyzed by Atom Probe Tomography (APT). In content presents a strong variation, with regions poor in indium and regions where the indium content reaches up to 30 %. This sample presents indium clustering.

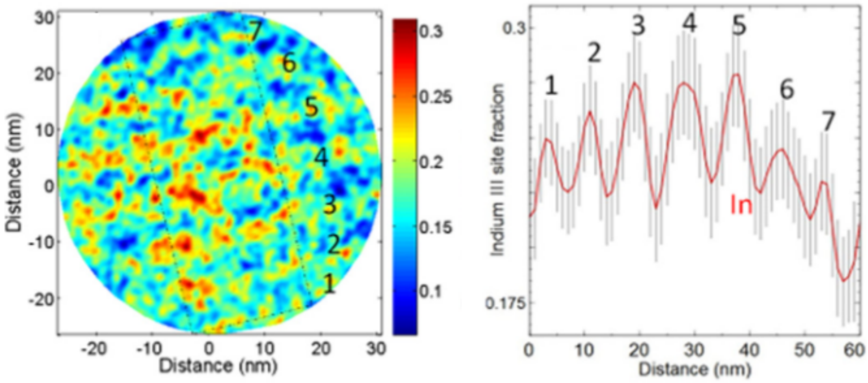

(a) (b)

FIGURE 1.8 – 2D distribution of In composition in an InGaN/GaN QW (a) Indium fraction profile from the sampling volume displayed on the left (b) (from [25]).

An indium cluster is a region where there is an abnormal high concentration of indium. The presence of indium clusters was reported in some of these references [17], [19], [20], [22]. Jinschek *et al.* [34] report In contents up to 40 % and cluster sizes of 1-3 nm. Most of these studies use TEM to characterize the samples and visualize the position of In atoms. Yet, beam damage effects have been demonstrated [35]. Therefore, indium clustering evidenced by TEM must be questionned and extreme care should be used when employing this technique. Even data acquired after a minimum time sets an upper limit for inhomogeneity. Humphreys *et al.* [36] demonstrated that the indium clustering observed on TEM images was the result of beam damage as their APT reconstruction showed that the indium composition was the one of a random alloy. Several other groups observed that their samples showed no sign of indium clusterization [37], [38]. Using TEM below the damage threshold, Baloch *et al.* also evidenced no clustering in their samples [39].

But clustering does exist in certain cases. Using APT, Tang *et al.* [40] found evidence of clustering in their QW grown on a-plane orientation while their samples grown on c-plane were cluster-free. In order to assess the presence of clusters, the distribution with the distance to nearest indium atom or the distribution with the In fraction is plotted (see Fig. 1.9). If the distribution follows the binomial distribution, we are in a presence of a random alloy like in the case of the sample on c-plane here. Otherwise, if the distribution deviates from the binomial distribution, there is evidence for indium clustering. Since the reconsideration of the indium clustering, it has been evidenced several times on c-plane [41] and other orientations [25], [40].

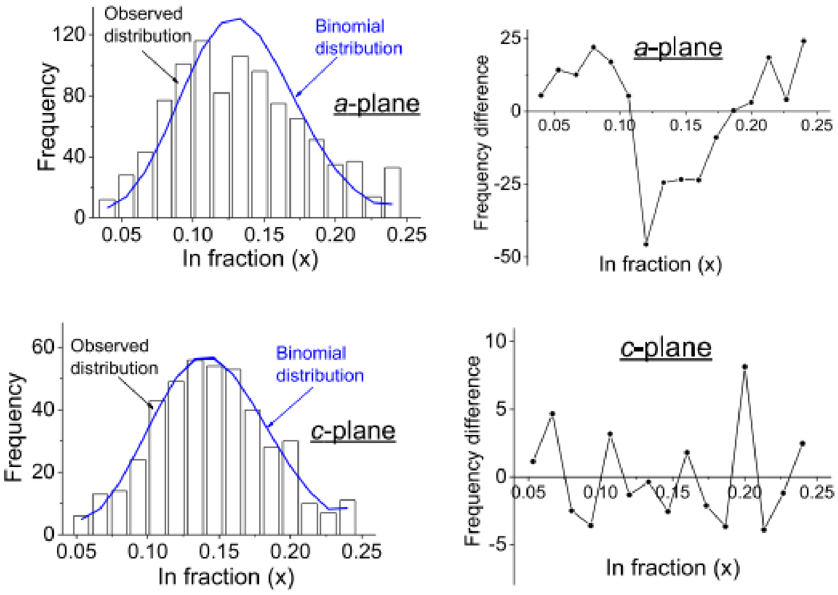

FIGURE 1.9 – Frequency distribution analysis of InGaN/GaN MQW samples grown on a-plane and c-plane from [40]. The c-plane sample on the bottom has a distibution which follows the binomial distribution characteristic of the random alloy while the a-plane sample deviates from that distribution which reveals the presence of indium clustering.

The presence of indium clusters probably depends on the growth conditions of the InGaN layers and the indium content. The reason for this indium clustering is not clear. Since indium clustering is observed in the vicinity of c-screw dislocations, Lei *et al.* suggested that there is an interaction between these dislocations and the In atoms [42].

1.2.3.4 Origin of carrier localization

There are several hypotheses for the origin of the carrier localization. Since many groups observed indium clustering sometimes to an extent where they could be considered as Quantum Dots (QDs), they believed carriers were localized at these clusters, a theory mentionned for example in [22], [43], [44], [45]. Since the reconsideration of the clustering question, it was shown that localization occured even in samples showing a random alloy distribution [36], [46], [38]. By comparing their model calculation to their experimental observations, Graham *et al.* proposed that well width fluctuations were responsible for this localization [46]. A difference of one monolayer is already enough to justify a localization energy of 58 meV in their case.

But, these QW width variations are not required to observe the localization of carriers. Indeed, theoretical studies of Bellaiche *et al.* for InGaN bulk predicted that localization of holes may happen even in layers showing random alloy distribution whereas in the case of InGaAs and AlGaAs, clusters of a few atoms are necessary [47]. Hangleiter *et al.* [48] proposed that carriers localize in the vicinity of V-pits (see 1.3.2.3) therefore preventing them to recombine at the dislocations. The theory was confirmed recently with a detailed cathodoluminescence (CL) study by Massabuau *et al.* [49]. They attributed this localization to the formation of In-N chains and atomic condensates in the vicinity of dislocations, an opinion shared by Chichibu *et al.*[50]. We will report in chapter 2 on the beneficial effects of this localization on QW efficiency.

1.3 Heteroepitaxy of InGaN on GaN

III-N substrates of wide diameter with a reasonable price are not widely available. Therefore, homoepitaxy (growth of a material on a substrate of same nature and composition) can rarely be considered. Heteroepitaxy (growth on a material of different nature) of III-N material is a great challenge. Here, we focus on the heteroepitaxy of InGaN on GaN as it is a process encountered during the growth of InGaN-based LEDs. The GaN that serves as a substrate is either bulk GaN known as free-standing (FS) GaN or GaN strained on sapphire substrate.

1.3.1 Lattice mismatch and biaxial strain

1.3.1.1 Lattice mismatch

When a material of in-plane lattice parameter a_L is grown on a substrate of in-plane lattice parameter a_S, the in-plane lattice parameter is imposed by the substrate layer. The lattice mismatch between the layer and the substrate is expressed as follows :

$$\Delta a/a = (a_L - a_S)/a_S \tag{1.6}$$

Two cases may be found. As illustrated in Fig 1.10, when $a_L < a_S$ the above layer is said to be under tensile strain. In the case when $a_L > a_S$, the layer is under compressive strain. This is the case of InGaN on GaN.

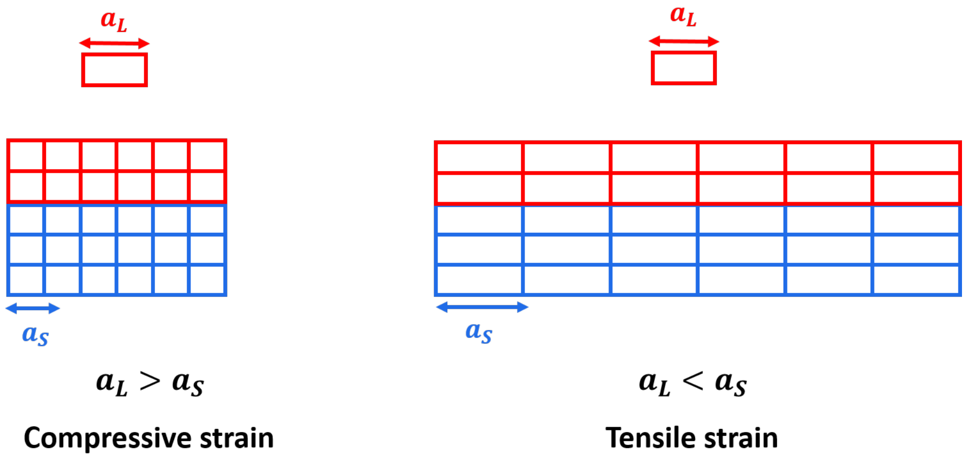

FIGURE 1.10 – Schematic representation of the strain of the grown layer (lattice parameter a_C) according to the substrate's lattice parameter.

The lattice mismatch between InN and GaN is equal to 11%, which foreshadows high lattice mismatch for the growth of InGaN on GaN even for small In contents.

There are cases when the layer is neither fully strained on the substrate nor fully relaxed as if it were bulk material. The relaxation percentage is defined as follows [51] :

$$R = \frac{a_L^{meas} - a_S}{a_L^{relax} - a_S} \tag{1.7}$$

with a_L^{meas}, the a lattice parameter of the layer as measured and a_L^{relax}, the a lattice parameter of the material constituing of the layer in the completely relaxed case.

1.3.1.2 Biaxial strain

As the total volume is maintained, the out-of-plane c parameter will vary as a function of the a lattice parameter. This phenomenon known as biaxial strain is isotropic in the plane and may be described by Hooke's law in the case of III-N submitted to small deformations.

$$\sigma = C.\varepsilon \tag{1.8}$$

σ is the the tensor of stress in the material related to ε, the tensor of strain by C, the tensor of elastic coefficients. In the case of the wurtzite structure, the tensort C corresponds to a 6×6 matrix with 5 independant coefficients.

$$\begin{pmatrix} \sigma_{xx} \\ \sigma_{yy} \\ \sigma_{zz} \\ \sigma_{xy} \\ \sigma_{yz} \\ \sigma_{zx} \end{pmatrix} = \begin{pmatrix} c_{11} & c_{12} & c_{13} & 0 & 0 & 0 \\ c_{12} & c_{11} & c_{13} & 0 & 0 & 0 \\ c_{13} & c_{13} & c_{33} & 0 & 0 & 0 \\ 0 & 0 & 0 & c_{44} & 0 & 0 \\ 0 & 0 & 0 & 0 & c_{11} & 0 \\ 0 & 0 & 0 & 0 & 0 & \frac{1}{2}(c_{11} - c_{12}) \end{pmatrix} \cdot \begin{pmatrix} \varepsilon_{xx} \\ \varepsilon_{yy} \\ \varepsilon_{zz} \\ \varepsilon_{xy} \\ \varepsilon_{yz} \\ \varepsilon_{zx} \end{pmatrix} \tag{1.9}$$

The relative deformation of the layer is defined from the variation between the value of the lattice parameter (a, c) and their value in the relaxed case (a_0, c_0). It will be negative in the case of compressive strain and positive in the case of tensile strain.

$$\varepsilon_{xx} = \varepsilon_{yy} = \frac{a - a_0}{a_0} \tag{1.10}$$

$$\varepsilon_{zz} = \frac{c - c_0}{c_0} \tag{1.11}$$

If no force is applied to the material, the direction [0001] is not under strain. Therefore, the only components of the strain which are not equal to zero are the ones along the growth plane. Hence :

$$\sigma_{zz} = 2c_{13}\,\varepsilon_{xx} + c_{33}\,\varepsilon_{zz} = 0 \tag{1.12}$$

The values of elastic constants c_{13} and c_{33} may be found in table 1.4. The values for ternary alloys are determined with a linear interpolation between the values for the binary compounds.

The dependance of deformation along the growth axis on the deformation parallel to the surface is expressed as follows

$$\varepsilon_{zz} = -\frac{2\,c_{13}}{c_{33}}\varepsilon_{xx} \tag{1.13}$$

III-N	$c_{13}(GPa)$	$c_{33}(GPa)$
GaN	100 [52],104 [53],106 [54],103 [55]	392 [52],376 [53],388 [54],405 [55]
AlN	127 [52],112 [53],108 [55]	382 [52],383 [53],373 [55]
InN	94 [52], 92 [55]	200 [52],224 [55]

Table 1.4 – Value of elastic coefficients for GaN, AlN and InN.

The factor $-\frac{2\,c_{13}}{c_{33}}$ is known as the biaxial Poisson coefficient. It can be expressed as a function of the isotropic Poisson coefficient ν.

$$\nu_c = -\frac{\varepsilon_{zz}}{\varepsilon_{xx}} = \frac{2\,c_{13}}{c_{33}} = -\frac{2\,\nu}{\nu - 1} \quad \text{with} \quad \nu = \frac{c_{13}}{c_{13} + c_{33}} \tag{1.14}$$

The value of the Poisson isotropic coefficient is given to be $\nu_{GaN} = 0.183$ [56] for MOVPE GaN and $\nu_{InN} = 0.272$ [55] for InN. The value for InGaN at a given composition x can be linearly interpolated between the values for the end members.

The variation of the in-plane stress is therefore related to the in-plane strain with M the elasticity modulus.

$$\sigma_{xx} = (c_{11} + c_{12} - \frac{2\,c_{13}^2}{c_{33}})\,\varepsilon_{xx} = M\,\varepsilon_{xx} \tag{1.15}$$

The elastic energy is related to the stress and to the strain of the material. For a thin layer, the energy per unit area is expressed as a function of the thickness of the material h :

$$\frac{E_{élastic}}{S} = \frac{1}{2}\,\sigma_{ij}\,\varepsilon_{ij}\,h = M\,h\,\varepsilon_{xx}^2 \tag{1.16}$$

In the case of pseudomorphic growth (when the layer is fully strained) the composition of the layer may be deduced from the measurement of c lattice parameter with the following formula from [51] :

$$x = \frac{1-\nu}{1+\nu} \times \frac{c_{meas}^{InGaN} - c_0^{GaN}}{c_0^{InN} - c_0^{GaN}} \tag{1.17}$$

The values of the c lattice parameters of the binary compounds may be found in table 1.1.

1.3.1.3 Critical thickness

When the layer has a lattice mismatch with the substrate, the plastic energy stored in the layer increases with the thickness of the grown layer. When the layer remains under

the critical thickness h_C, the growth is pseudormophic. Then, if a layer is grown above the critical thickness, metamorphic growth occurs and the layer relaxes through generation of dislocations (see paragraph 1.2.2 on defects).
In the case of InGaN on GaN, the in-plane strain is very large. For instance an $In_{0.1}Ga_{0.9}N$ layer grown on GaN has an in-plane strain of 1% [57].
Fig. 1.11 gathers data from experimental studies for the growth of InGaN on GaN as well as the theoretical predictions from two models described later (see (a) and (b)). From the experimental data, we expect that for an indium content under 20 %, layers up to 100 nm thickness may be obtained but as soon as the indium content is above 20-25 %, the critical thickness is limited to a few monolayers, which may be critical even for the growth of QW.

The following paragraphs review some theoretical models for the determination of critical thickness applied to growth of InGaN on GaN. For all the models, some of the parameters are dependant on the indium composition noted as x.

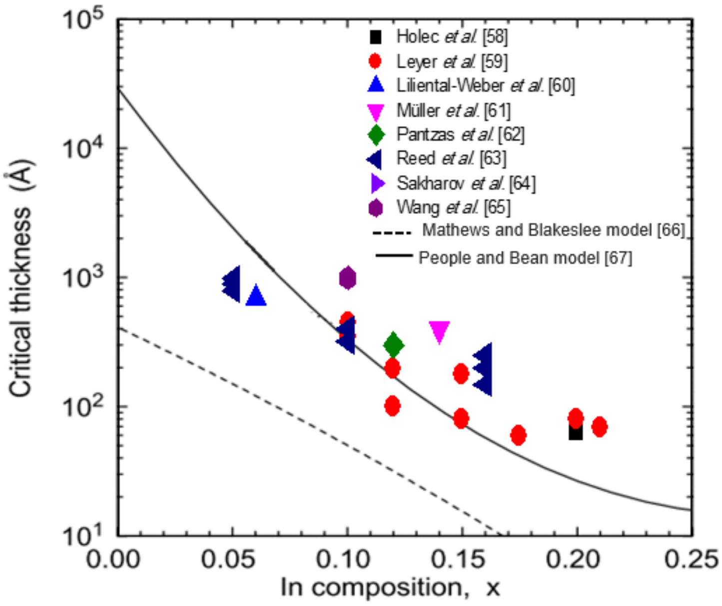

FIGURE 1.11 – Experimental critical thickness of InGaN on GaN dependence on the indium content [58], [59], [60], [61], [62], [63], [64], [65] and theoretical models [66],[67] adapted from [68].

a- Mathews and Blakeslee (Mechanical Equilibrium model) [66] In this theory, misfit is accommodated by generations of a rectangular array of non interacting edge dislocations.

$$h_C = \frac{b}{2\pi f} \times \frac{1-\nu(x)cos^2\alpha}{(1+\nu(x))cos\lambda} \times (ln\frac{h_C}{b}+1) \tag{1.18}$$

with α angle between the dislocation line and its Burger vector
with λ angle between the glide plane of the dislocation and the interface
with b norm of Burger's vector

b- People and Bean (Energy balance model) [67] In the energy balance model, the critical thickness h_C is reached when the areal strain energy density of the layer exceeds the self-energy necessary for the formation of an isolated screw dislocation at a distance h_C from the free surface.

$$h_C(x) = (\frac{1-\nu(x)}{1+\nu(x)}) \times (\frac{1}{16\pi\sqrt{2}}) \times (\frac{b^2}{a(x)}) \times (\frac{1}{f^2(x)}) \times ln(\frac{h_C(x)}{b}) \tag{1.19}$$

with $\nu(x)$ Poisson coefficient
with $a(x)$ in-plane lattice parameter with $f(x) = \Delta a/a$ lattice mismatch

c- Frank and Van der Merve [69] Van der Merwe was the first to calculate the critical thickness based on energy considerations. We reach the critical thickness when the interfacial energy between the layer and the substrate reaches the minimum energy necessary for the generation of dislocations.

$$h_C = \frac{Kb^2}{4\pi B\varepsilon_0 b_{||}^{edge}} \times ln\frac{h_C E_D}{b} \tag{1.20}$$

with $B = \dfrac{2\mu(1+\nu)}{1-\nu}$
with $b||^{edge}$ the magnitude of the edge component of the Burger's vector
with ε_0 native lattice mismatch
with E_D energy of the dislocation core
with $K = \dfrac{\mu}{1-\nu}$

d- Fischer [70] In 1994, Fischer *et al.* presented a new refined model taking into account the interaction between straight misfit dislocations.

$$x = \frac{bcos\lambda}{0.0836h_C} \times \frac{1-(\nu(x)/4)}{4\pi cos^2\lambda(1+\nu(x))} \times ln(h_C/b) \tag{1.21}$$

In Fig. 1.11, one can notice that the experimental critical thicknesses deviate from the theoretical predictions from the energy balance model [67] and mechanical equilibrium model [66] for the high indium contents. This discrepancy may be attributed to a series of factors. As the InGaN alloy has some peculiarities (indium inhomogeneities, high density of dislocations...), the theoretical models may not be adapted to this material . Experimentally, the critical thickness could depend on the growth conditions that are used. Nonetheless, we can see that for very high indium contents like the ones necessary for the growth of quantum wells for color LEDs, the critical thickness will in any case be limited to only a few nanometers.

1.3.1.4 2D-3D Transition

Several groups report a change in growth mode above a certain thickness [71],[72] in the growth of InGaN on GaN. The growth process may be described by the Fig. 1.12. During the first part, the growth is pseudormorphic, a 2D growth mode is observed and the In content is rather homogeneous. In a second phase, 3D growth starts and the InGaN islands can coherently relax near their top. Then, the tips on the top get more indium-rich while the trenches contain less indium.

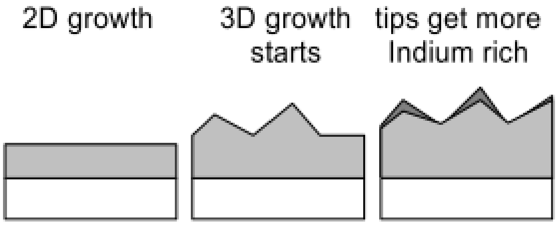

FIGURE 1.12 – Mechanism of InGaN growth on GaN and the 2D-3D transition as proposed by [72].

1.3.1.5 Dependance of bandgap on strain

The behavior of InGaN layers strained on GaN will differ from relaxed InGaN. Orsal *et al.* [73] determined the bandgaps of relaxed and strained InGaN layers dependence on In content from room temperature photoluminescence and cathodoluminescence measurements plotted in Fig.1.13. As disclosed above, the bandgap of InN and the bowing parameter of InGaN can be set to 0.78 eV and 1.4 eV, respectively in the relaxed case at 0 K [6] although many different values may be found in the litterature. Depending on the

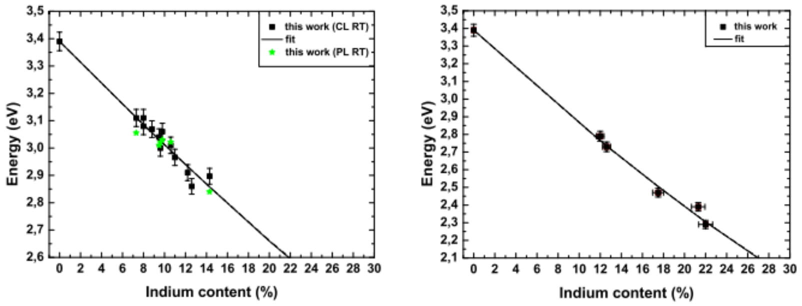

(a) (b)

FIGURE 1.13 – Low In content dependence of the bandgap emission energy in fully strained (a) and relaxed (b) InGaN layers from [73].

sources, at 300 K these values can vary between 0.64 and 0.77 eV. In the strained case, the theory predicts a theoretical increase of 0.1 eV [73] and therefore the InN bandgap is expected to vary between 0.74 and 0.87 eV. For these range of InN bandgaps, the fitting of the curves in Fig. 1.13 gives the bowing parameter dependency in the relaxed and strained case. The bowing parameter may be calculated as [73] :

$$b_{strained} = 1.154 \times E_g^{InN} + 0.396 \tag{1.22}$$

$$b_{relaxed} = 1.230 \times E_g^{InN} + 2.010 \tag{1.23}$$

1.3.2 Defects in InGaN

When the lattice mismatch between the layer and the substrate is substantial as in the case of InGaN on GaN, structural defects appear.

1.3.2.1 Point defects

There are several types of point defects :

- Extra atoms or self interstitials
- Impurities either at interstitial location or substituing for other atoms (oxygen and carbon mostly)
- Missing atoms or vacancies

Point defects appear in InGaN because of the low growth temperature. They will be more numerous in an MBE-grown layer which requires temperatures of about 550˚C compared to an MOVPE-grown layer with temperatures about 750 ˚C.

1.3.2.2 Dislocations

Dislocations may be defined by their unit vector parallel to their propagation direction and their Burgers vector which norm b represents the amplitude of the local deformation of the lattice. There are three types of threading dislocations represented on Fig. 1.14 :

- Screw dislocations also noted c. Their Burgers vector is parallel to unit vector and with the direction <0001>
- Edge dislocations noted c. Their Burgers vector is perpendicular to their unit vector and with the direction $<11\overline{2}0>$
- Mixed dislocations which have a screw and an edge component with a Burgers vector along a+c and equal to 1/3 $<11\overline{2}3>$.

Dislocations preferentially move along specific crystallographic planes. A dislocation glide occurs when the dislocation moves in the surface which contains both its unit vector and its Burgers vector. The glide of the dislocation helps to relax the strain in the crystal.

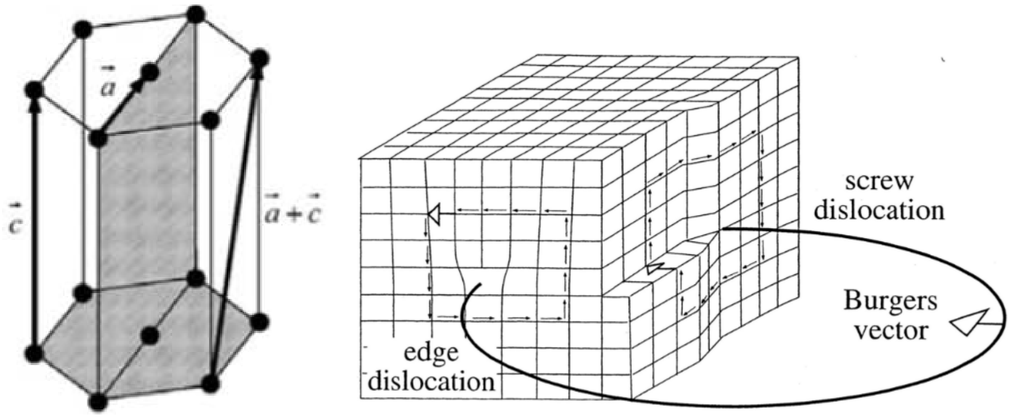

(a) (b)

FIGURE 1.14 – Direction of the Burgers vector of the wurtzite structure [74] (a) and the different types of dislocations [75] (b).

1.3.2.3 V-pits

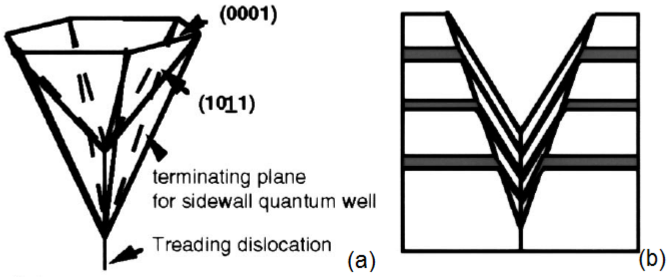

FIGURE 1.15 – Perspective view (a) and cross-section view (b) showing the six sides of the open hexagonal pyramid defined by the $\{10\bar{1}1\}$ planes [76].

Another very common defect called V-pit or IHP (for Inverted Hexagonal Pyramid) has been evidenced in InGaN-based structures. Fig 1.15 pictures a perspective and a cross section schematic view of a V-pit. At the V-pit apex, a threading dislocation is found. Shiojiri *et al.*[77] showed that the dislocation forms when the dislocation meets the InGaN QW and propagates to the free surface after the V-pit as can be seen on these TEM images in Fig. 1.16. The V-pit sidewalls are oriented as the $\{10\bar{1}1\}$ planes.

The formation mechanism has been tentatively explained by several groups. According to Northrup *et al.* [78], V-pits developp when dislocation cores open up during the growth of the InGaN MQW. It has been observed that a rise in the indium content is related to an enlargment and a multiplication of V-pits. V-pit growth is explained by a reduced incorporation of Ga on the $\{10\bar{1}1\}$ planes compared to the $\{0001\}$ surface. Indium atom is suspected to act as a differential surfactant causing this differenciation ([78], [76]). The high growth temperature of GaN (around 1050˚C) as compared to the one necessary for the growth of MQW (typically between 650˚C and 800˚C) explains the fact that these defects are very rarely seen in GaN. The surface diffusion lengths are then high enough to prevent any deviation from a planary growth.

For others [79],[80], [81], [82] the formation of V-pits in InGaN/GaN (0001) is favorable as it is suspected to be one of the principal mechanism for relaxation of strain. According to Song *et al.* [80] the gliding of dislocations is not possible in InGaN layers because of the low growth temperature. Therefore the strain relief may occur thanks to the V-defects.

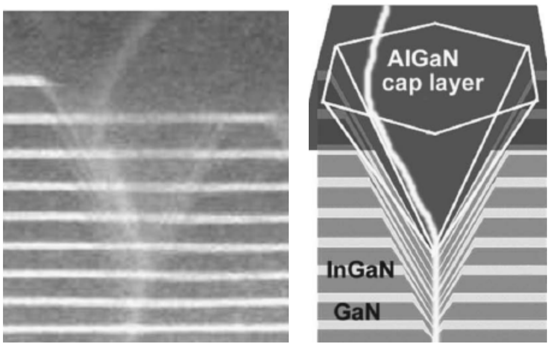

(a) (b)

FIGURE 1.16 – HAADF (High Angle Annular Dark Field)-STEM (Scanning Transmission Electron Microscopy) image of a capped $In_{0.2}Ga0.8N$(2.5 nm)/GaN (8 nm) MQW layer grown on a GaN :Si layer (a) Schematic diagram of the structure of the V defect, which nucleates at a threading dislocation in the first $In_{0.2}Ga0.8N$ QW (b) from [77].

1.3.3 Piezoelectric polarization and Quantum Confined Stark Effect

1.3.3.1 Piezoelectric polarization

Piezoelectricity is a phenomenon ocurring in some materials which, when subject to mechanical stress, acquire electrical polarization. A difference of potential appears as well as electric charges at the surface. As InGaN is grown on GaN, the lattice parameters (a, c) deviate from the nominal ones (a_0, c_0). Piezoelectric polarization is related to the relative deformation of the layer ε_{xx} and to the elastic (c_{13},c_{33}) and piezoelectric constants (e_{31},e_{33}) :

$$P_{PZ} = 2\varepsilon_{xx} \times (e_{31} - \frac{e_{33}c_{13}}{c_{33}}) \tag{1.24}$$

We give the values of the piezoelectric constants for AlN, GaN and InN in table 1.5. The elastic constant values may be found in table 1.4.

The magnitude of piezoelectric polarization in InGaN/GaN QW is very large. In this case, spontaneous polarization is negligible compared to piezoelectric polarization [84]. Piezoelectric polarization for InGaN may be expressed as a function of the values for GaN and InN [7]. Unlike spontaneous polarization, piezoelectric polarization follows Vegard's law without additional term :

$$P_{PZ}(In_xGa_{1-x}N, \varepsilon_{xx}) = xP_{PZ}(InN, \varepsilon_{xx}) + (1-x)P_{PZ}(GaN, \varepsilon_{xx}) \tag{1.25}$$

III-N	$e_{31}(C.m^{-2})$	$e_{33}(C.m^{-2})$
GaN	-0.49	0.73
AlN	-0.60	1.46
InN	-0.57	0.97

TABLE 1.5 – Value of piezoelectric coefficients for GaN, AlN and InN [83].

1.3.3.2 Internal electric field

For a single QW with quantum barriers (QB), we evaluate the effect of piezoelectric polarization on the internal electric field of the QW for a growth along the c-axis.
The charge surface density at the interface between the QW and the QB is defined as :

$$\sigma_{intQW/QB} = n(P_{QB} - P_{QW}) \tag{1.26}$$

P_{QB} and P_{QW} are the total polarization (piezoelectric and spontaneous) at each side of the interface. n is the vector normal to the (0001) surface.
The vector of the displacement field $D = \varepsilon F + P$ is conserved between the two materials. The electric field is noted F.

$$\varepsilon_{QW}\varepsilon_0 F_{QW} - \varepsilon_{QB}\varepsilon_0 F_{QB} = P_{QB} - P_{QW} \tag{1.27}$$

ε_0 is the dieletric constant of vacuum and ε_{QW} and ε_{QB} are the dielectric constants of the material of the QW and QB respectively.

We have a continuity of the band structures implying :

$$t_{QW}F_{QW} + t_{QB}F_{QB} = 0 \tag{1.28}$$

with t_{QW} and t_{QB} the thciknesses of the QW and the QB respectively. If we express the internal electric field in the quantum well as a function of polarization, we get the following equation :

$$F_{QW} = \frac{t_{QW}(P_{QB} - P_{QW})}{\varepsilon_{QW}\varepsilon_0 t_{QW} + \varepsilon_{QB}\varepsilon_0 t_{QB}} \tag{1.29}$$

Lefebvre *et al.* [85] have experimentally determined the electric field in InGaN/GaN MQW to be around 2.5 MV/cm for an indium content of 20%. For a similar content Bernardini *et al.* [86] theoretically calculated a value of 3.3 MV/cm. The differences may be explained by the fact that the interfaces of the quantum well are not ideal (as detailed in paragraph on indium segregation).

1.3.3.3 Quantum Confined Stark Effect (QCSE

The internal electric field has an influence on the transition energy in the quantum well. This effect is known as the Quantum Confined Stark Effect (QCSE). The fundamental transition energy in a QW (*i.e.* between conduction band and heavy hole band) is expressed as follows : :

$$E_{e-hh} = e_1 + hh_1 + E_g^{QW} - R_y - eF_{QW}t_{QW} \tag{1.30}$$

e_1 and hh_1 are the electron and hole energy levels in the well ; respectively. E_g^{QW} is the energy of the bandgap of the material constituing the well and R_y is the excitonic Rydberg energy (exciton binding energy). The term $-eF_{QW}t_{QW}$ accounts for the influence of the internal electric field. As a consequence, the transition energy is lowered compared to a square QW [87]. The red-shift in the emission wavelength gets bigger all the more as the internal electric field is increased or the QW wider.

Fig 1.17 (a) is a representation of the band structure for a $GaN/In_{0.2}Ga_{0.2}N$ QW with no internal polarization on the left and with taking it into account on the right. Under the influence of the electric field, the QW gets into a triangular shape. Besides the red-shift in the transition energy, a detrimental phenomenon appears : the reduction of the oscillator strength. As can be observed in Fig. 1.17 (b) the shape of the band structure results in spatial separation of the electron and hole wavefunctions, leading to a reduced overlap integral. The oscillator strength proportional to the square of the overlap integral. The consequence is a reduction of the radiative recombination rate as the radiative carrier lifetime is proportional to the inverse of the square of the oscillator strength [88]. This effect is stronger if the well is wider [89] or the electric field bigger. This trend is one of the reasons for the decrease of efficiency observed for long wavelength LEDs as will be detailed in chapter 2.

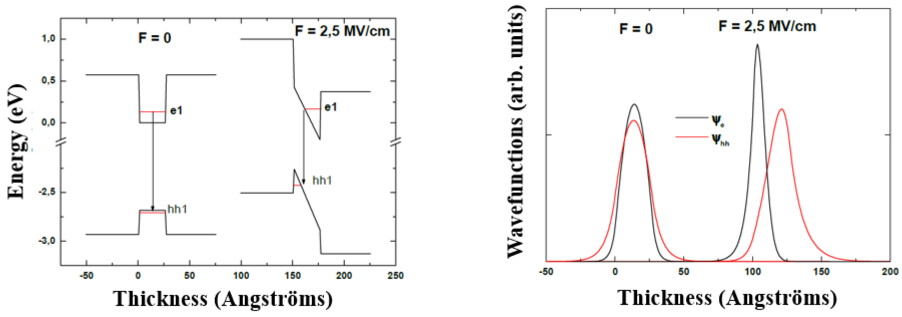

(a) (b)

FIGURE 1.17 – Theoretical band structure of a 3-nm wide $GaN/In_{0.2}Ga_{0.8}N$ QW without taking into account polarization (left) taking it into account with an electric field of 2.5 MV/cm (right) (a). Electron (black) and hole (red) wavefunctions in this QW with and without electric field (b) (from [90]).

The effect of the electric field decreases as carrier injection increases. Indeed, the accumulation of carriers in the QW screens the internal electric field. Therefore, a blue shift is observed for high carrier injections [91], [92].

1.3.4 Strain and In incorporation

1.3.4.1 Effect of strain on indium miscibility

We presented in 1.2.1, the phase diagram for bulk InGaN. Karpov [93] conducted further thermodynamic calculations in order to determine the phase diagram for InGaN strained on GaN. Fig. 1.18 features the two different phase diagrams, for the relaxed case on top and in the case of InGaN strained on GaN at the bottom. The strain shifts the diagram towards the high indium contents and stabilizes the InGaN layer. In this strained case, InGaN growth should be easy for indium contents up to 25 %. However, it is known that even for smaller indium contents like the ones needed for blue LEDs ($\simeq$ 15 %), InGaN growth requires special growth conditions as described in 1.2.2 (low growth rate, etc). These theoretical phase diagrams show a tendency of stabilization of the alloy with increasing compressive strain but may differ from the experimental reality.

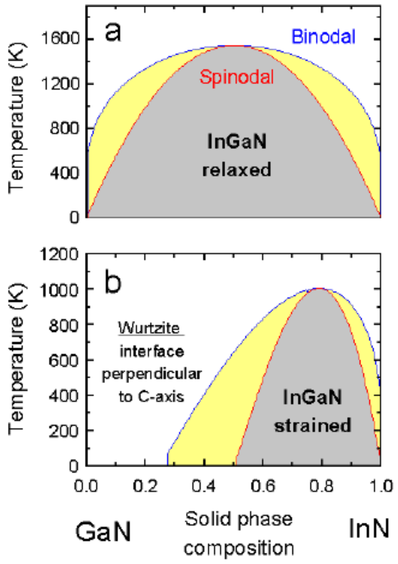

FIGURE 1.18 – Phase diagram of wurtzite InGaN in the case of relaxed layer (a) and in the case of InGaN layer strained on GaN for a growth along the c-axis (b) [93].

1.3.4.2 Compositional pulling effect

The InGaN alloy is almost never found in a relaxed state. As we saw before, the growth of InGaN on GaN puts the layer under strain. This strain will further hinder indium incorporation. This phenomenon known as the compositional pulling effect was theoretically predicted by Inatomi *et al.* [94] by thermodynamical analysis. Experimentally, it was evidenced by Pereira *et al.* [95]. Depth resolved strain and In content measurements along an InGaN layer grown on GaN revealed stronger In content in the more relaxed regions despite keeping the In flux constant. Hiramatsu *et al.* [96] observe the same effect while growing InGaN layers with different lattice mismatch in respect to the substrate. The phenomenon was also noted when growing large stacks of InGaN/GaN MQW [97]. The indium atom which is larger than the Ga atom is believed to be pushed out of the lattice to reduce the deformation energy as the layer is forced to adapt to a smaller lattice parameter relative to its nominal lattice parameter. The sketch of Fig. 1.19 illustrates that phenomenon.

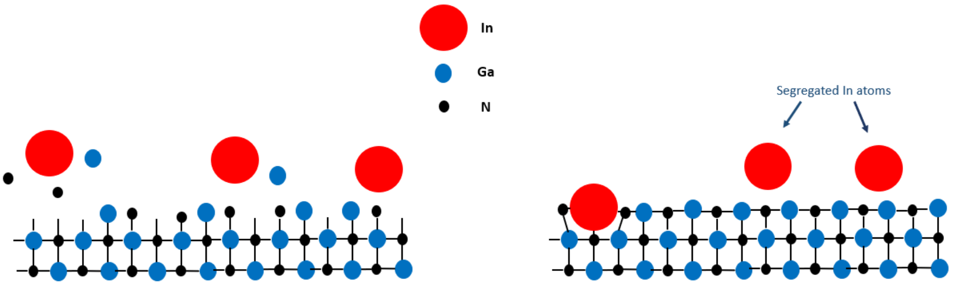

(a) (b)

FIGURE 1.19 – Sketch illustrating the compositional pulling effect. In (a) In, Ga and N atoms are arriving on a GaN layer surface. Because of the large size of the In atom as compared to the Ga atom, it is more favorable for the Ga atoms to incorporate into the lattice, leaving In atoms on the surface to be incorporated in the next atomic layer (b).

Since indium has a a tendency to desorb, InGaN layers are also unstable when subject to high temperatures. Typically a deterioration of the quality of the InGaN layer has been observed at temperatures starting from 900 ˚C. InGaN layers with a higher indium content are more likely to be deteriorated. The phenomenon was observed for InGaN layers [98] but also for MQW structures grown by MOVPE [99], [100] and MBE [16]. This could later be a problem for the realization of high indium content active regions for green LEDs as p-doped GaN layers are typically grown at temperatures above 900 ˚C.

1.3.4.3 In segregation

Because of the problems of pulling effect and miscibility mentionned above, InGaN/GaN MQWs do not have an ideal rectangular shape as evidenced for both MBE [101] and MOVPE [102]. Dussaigne *et al.* [101] simulated an InGaN/GaN quantum well profile shown in Fig. 1.20. The model which was used was developped by Muraki *et al.* [103].
In this model, we assume that a fraction R of the atoms of the layer segregates into the next layer. R is known as the segregation coefficient. The well width in monolayers is noted N and the nominal In composition is noted x_0. The composition is given for the

n^{th} monolayer as :

$$x_n = x_0(1 - R^n) for \quad 1 < n < N(well) \tag{1.31}$$

$$x_n = x_0(1 - R^n)R^{n-N} for \quad n > N(barrier) \tag{1.32}$$

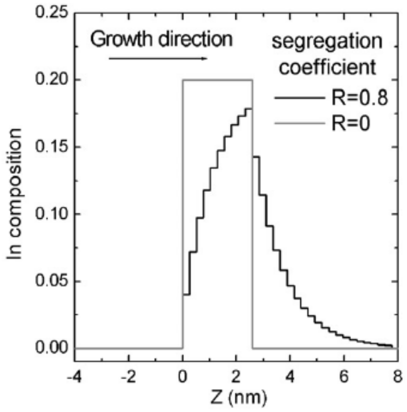

FIGURE 1.20 – In composition profile of a 10 ML $In_{0.2}Ga_{0.8}N$ QW with a surface segregation coefficient of R=0.8 (black line) and R=0 (gray line) [101].

The phenomenon of segregation has an influence on the emission energy and the characteristics of the quantum well. As the indium content is smaller than the nominal value, a blue-shift occurs. Furthermore, as indium spreads into the barrier, the well is wider than expected. This widening will lower the radiative recombination rate because of QCSE as explained above. Fig. 1.21 shows the impact of segregation on emission energy depending on the quantum well width.

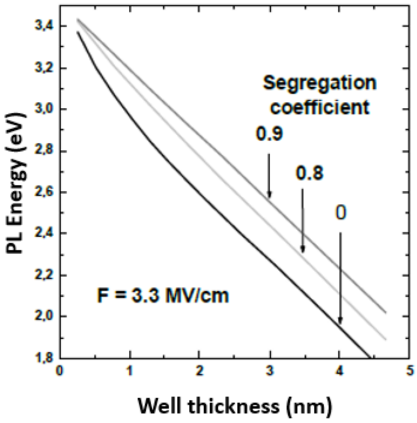

FIGURE 1.21 – PL energy vs QW width for $In_{0.2}Ga_{0.8}N$ QW from [90].

1.4 Quantification of indium in InGaN

Since we have access to several characterization techniques in CEA-Leti, a indium quantification study was led on two reference samples. The idea was to determine which technique is the best to analyze our samples thereafter.
We grew two reference samples. Sample 1 (Fig. 1.22 (a)) consists in an InGaN buffer layer grown on a GaN template. The expected thickness is 300 nm. During the whole growth, the TMIn flux was maintained at a constant value. Based on previous experiments we expect an indium content of approximately 5%.
Sample 2 (Fig. 1.22 (b)) consists in four InGaN/GaN MQWs grown on a GaN template. The temperature was gradually decreased from QW to QW in order to have four different indium compositions. The expected indium contents are 5%, 10%, 15% and 20% respectively from the bottom to the top of the structure.

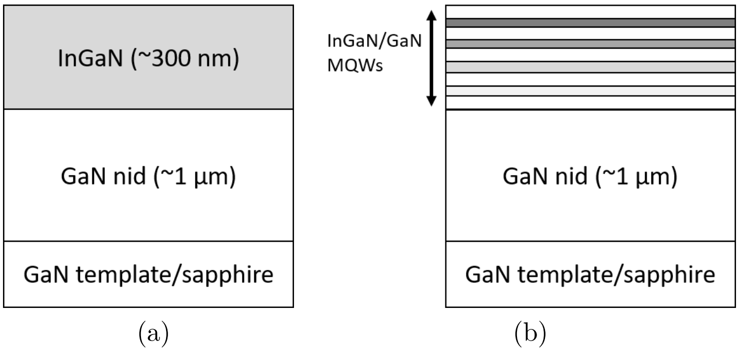

(a) (b)

FIGURE 1.22 – Structures of the reference sample 1 (a) reference sample 2 (b) (not to scale). nid stands for non intentionally doped.

Because of the nature of the InGaN alloy as described in 1.2.1, quantifying the indium content with accuracy is a complex problem. With all the following techniques, the In composition given below will be a mean composition of the analyzed volume.

1.4.1 Rutherford Back Scattering spectrometry (RBS)

The RBS technique is briefly described in annex C.7. It has been used previously to quantify In content in InGaN layers for instance by Pereira *et al.* [104].

Quantification in InGaN thick layer For our analyses, the chamber was maintained under a vacuum of $2 \times 10^{-6} Torr$. The ion flux was composed of ${}^{4}He^{+}$ particles at an energy of $2.3 MeV$. The analysis surface is of a few mm^2. The retro-diffused particles are analyzed with a detector at an angle of 160° from the initial direction. The detector yields the results as plotted in Fig. 1.23. On the absciss is plotted the energy of the particles detected after retro-diffusion. On the ordinate is the number of particles seen by the detector which represents the concentration of the element detected at a given depth.

The energy at which the particle is detected depends both on its nature (In which is heavier than Ga will be detected at a higher energy) and on its depth in the sample as the ion will have lost more energy after colliding with more atoms. The response is therefore a correlation between the different layers and the different elements consistuting the sample. For the analysis, a simulation has to be carried out to fit the experimental data. Using the values of 6.81 g/cm^3 and 6.15 g/cm^3 for the densities of InN and GaN, the thickness of the InGaN layer is estimated around 250 nm. For the simulation the N concentration is assumed to be 50% throughout the whole sample. For this technique the In composition is given as relative to all elements in the sample (In, Ga, N), the values have to be multiplied by 2 if one wants to compare with the In content as we usually define it, relatively to GaN.

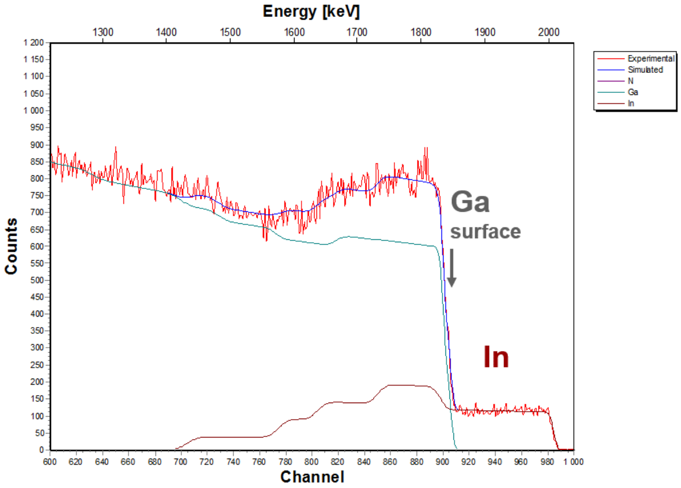

Figure 1.23 – Simulated and experimental RBS profiles of the number of particles vs their energy as detected for sample 1.

The results indicate a growing indium content from the bottom of the InGaN layer and then a decrease of the content. These results are not compliant with the process of relaxation of InGaN and our knowledge about the pulling effect (as detailed in paragraph 1.2.3.2) which would indicate a monotonous increase of the indium content along the whole InGaN layer as the In flux is maintained during the growth. Some other simulation made to comply with this assumption were not relevant as the N content had to be set different from 50% and to vary along the sample.

To conclude, RBS is a powerful technique but quite challenging in its interpretation. It can only be used in the case of thick layers as the depth resolution is above 10 nm.

1.4.2 Atomic Probe Tomography (APT)

This technique is described in annex C.3 and was previously used to measure the indium content in InGaN layers (see [105] for instance).

Quantification in InGaN thick layer Because of constraints related to the tip preparation, only the bottom of the InGaN layer (close to the GaN interface) was analyzed. Unlike what is usually observed for instance for the quantification of aluminum in AlGaN, the In concentration does not depend on the evaporation conditions This has been previously demonstrated at University of California, Santa Barbara (UCSB) [25] and with the set-up used for this analysis. Therefore we can be quantitative using APT. For sample 1, results are given by the plot in Fig. 1.24 . The In content is measured to be around 7 % in average but there is a lot of noise in the measurement.

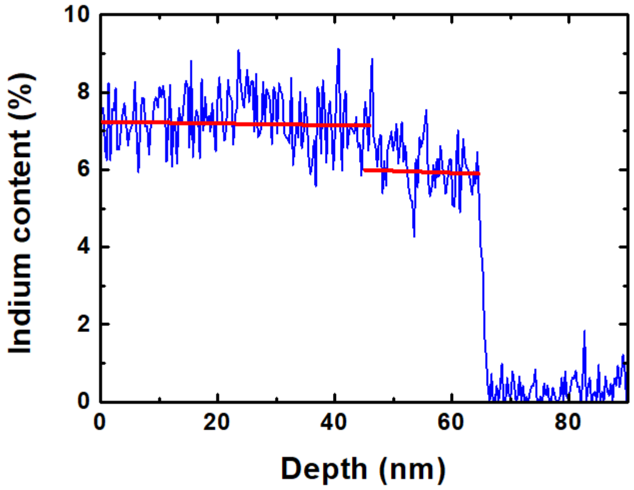

FIGURE 1.24 – Quantification of In in sample 1 using APT.

Quantification in InGaN/GaN MQW Fig 1.25 displays the In content for the MQWs of sample 2. The In content was determined to be 3.3 %, 9.4 %, 14.6 % and 19.5 % respectively.

Fig. 1.26 features the 3D reconstruction of sample 2. We can see the distribution of indium atoms in red here. The In concentration isocurves show the existence of some enriched zones with In content up to three times larger locally. These inhomogeneities are characteristic of InGaN layers as was previously reported in section 1.2.3.1.

APT is a powerful technique that allows determining the indium content both in InGaN thick layers and in InGaN MQW. Furthermore, thanks to the 3D reconstruction of the sample, the distribution of indium atoms can be visualized at the nanometer scale, allowing for assessment of the presence of indium clustering in the samples.

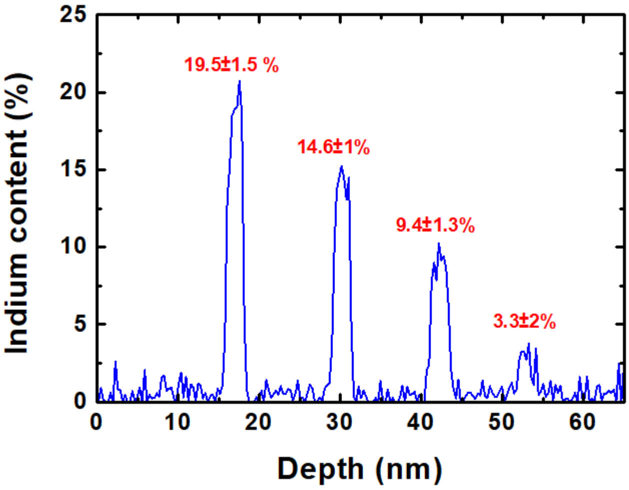

FIGURE 1.25 – Quantification of In composition in the MQWs of sample 2 using APT.

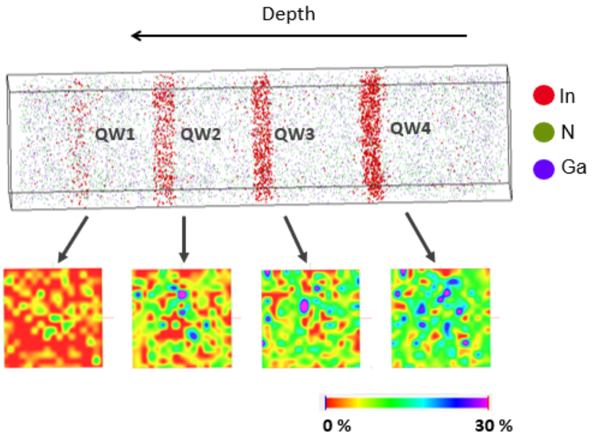

FIGURE 1.26 – 3D reconstruction of a volume of 15x15x1.5 nm^3 from sample 2 and In isocurves for the four MQW.

1.4.3 Energy-dispersive X-ray spectroscopy (EDX)

This method is briefly described in annex C.6. EDX was implemented in a TEM used in STEM-mode (Scanning Transmission Electron Microscope). Here, the standards used for the calibration of the microscope for Ga, In and N are GaN, InAs and Si_3N_4, respectively. The resolution is about 1 nm. The chemical indentification was conducted with the method of the zêta-factors (annex C.6). This method has previously been used to quantify In in InGaN, see for instance [25].

Quantification in InGaN thick layer The analyzed surface size is about 100 nm*100 nm. Fig. 1.27 plots the measured In content for sample 1. We see a slight increase of the In content from 4.7 % at the bottom to 5.6 % at the surface of the InGaN layer although there is a large uncertainty as there is a lot of noise.

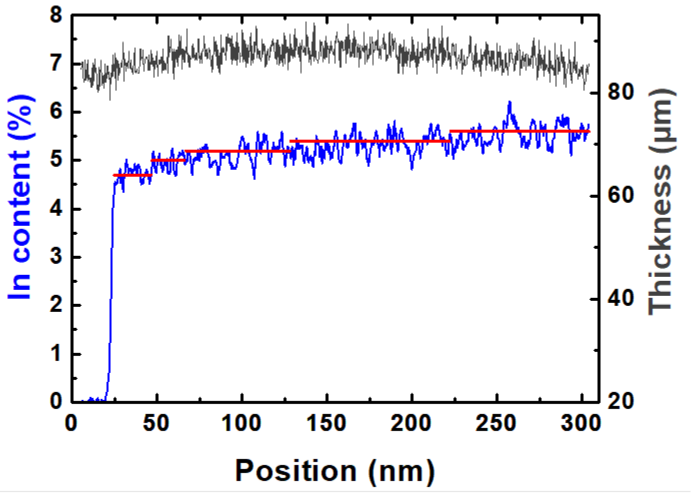

FIGURE 1.27 – In content in sample 1 as measured by EDX. A fitting to the experimental data is displayed in red. The thickness of the TEM specimen is also plotted in dark gray.

Quantification in InGaN/GaN MQW Sample 2 was analyzed using the same experimental and analysis conditions as sample 1. The In composition profile was fitted taking into account the beam resolution which is about 1 nm. Fig. 1.28 shows the experimental data and the fitted profile. The In composition from the bottom QW to the top QW is given to be 1.8, 6.4, 15.7 and 16.7 % respectively.

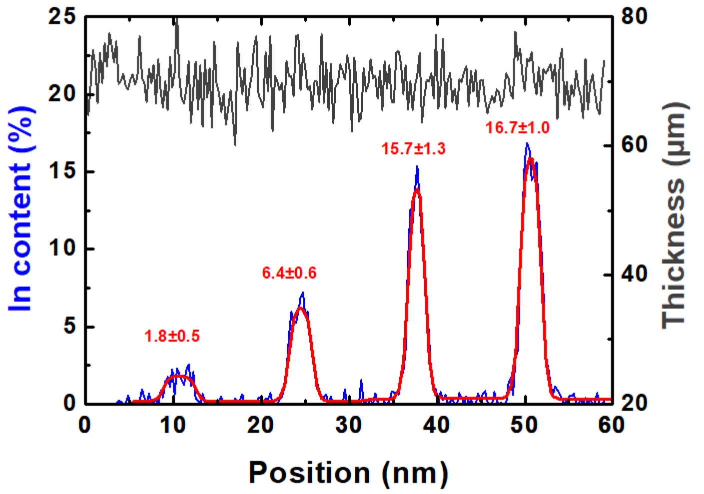

FIGURE 1.28 – In content in sample 2 as measured by EDX. A fitting of the experimental data which accounts for the beam resolution is shown in red. The thickness of the TEM specimen is also plotted in dark gray.

1.4.4 Secondary Ion Mass Spectrometry (SIMS)

SIMS characterization technique is briefly described in the annex C.6. Here, the analyzed surface was of a few hundred of microns square.

Quantification in InGaN thick layer The In profile measured for reference sample 1 is given in Fig. 1.29. The average measured In composition is 4.3% with a slight increase from the bottom to the surface of the sample. The standard which is used for the quantification of indium has a very low indium content (0.017%) which may affect the accuracy of the value.

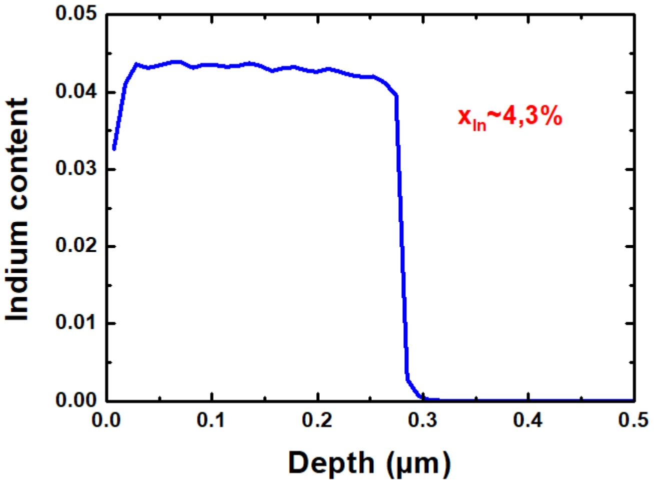

FIGURE 1.29 – In composition profile of sample 1 as measured by SIMS.

SIMS is an interesting technique to quantify indium in InGaN thick layers although the value may be underestimated because of the nature of the standard described above. The in-depth resolution of the SIMS (around 5-10 nm depending on the roughness of the surface) will not allow us to use it for the analysis of InGaN/GaN MQW.

1.4.5 Photoluminescence (PL)

The photoluminescence characterization technique is described in annex B.

Quantification in InGaN thick layer The PL spectrum was acquired at 15K, and the sample was excited by a 325 nm He-Cd laser. The size of the laser spot was about 200 μm^2. For sample 1, the PL spectrum is plotted in Fig. 1.30. The emission peak has a large FWHM, which is a characteristic of the PL emission from the InGaN alloy, a phenomenon explained by the presence of alloy inhomogeneities [18]. The main peak presents a shoulder which would imply two layers of InGaN with different In contents. One of the hypotheses is that one of the peaks can be attributed to the emission of the defects like proposed by Ponce *et al.* [57] and as observed by Tao *et al.* [106] with cathodoluminescence (especially around the V-pits). The fact that this other contribution content is not observed with the more local techniques might be due to the fact that the experimentalist chose a defect free zone to perform the measurement. The main peak at 388.7 nm and the second peak at

398.0 nm correspond to an In content of 6.8% and 8.5 % respectively as we assume that the InGaN layer is strained on GaN (this hypothesis is later verified thanks to XRD).

The In content of 6.8 % as deduced with PL is quite large compared to what was obtained with other techniques. This might be due to the phenomenon of carrier localization which implies that the most part of the emission comes from the In-rich regions.

Quantification in InGaN/GaN MQW Photoluminescence can also be used to quantify indium content in InGaN MQW although an assumption on the electric field has to be made according to equation 1.30. The value of 3.3 MV/cm from [86] for an In content of 20% was taken as a reference and the values of the electric field were calculated proportionally to their In content. The experimental conditions were the same as the ones used for the analysis of sample 1. For the calculation the segregation is assumed to be zero, therefore we underestimate the In content. From our calculations, the peak emitting at 368.6 nm, 401.7 nm, 457.1 nm and 518.3 nm correspond to In contents of 2%, 5.9%, 14.1%, 19.6% respectively. If we take into account the segregation at the first interface with a segregation coefficient of R=0.4, we get slightly higher values of 2%, 6.1%, 14.4% and 20.1 %.

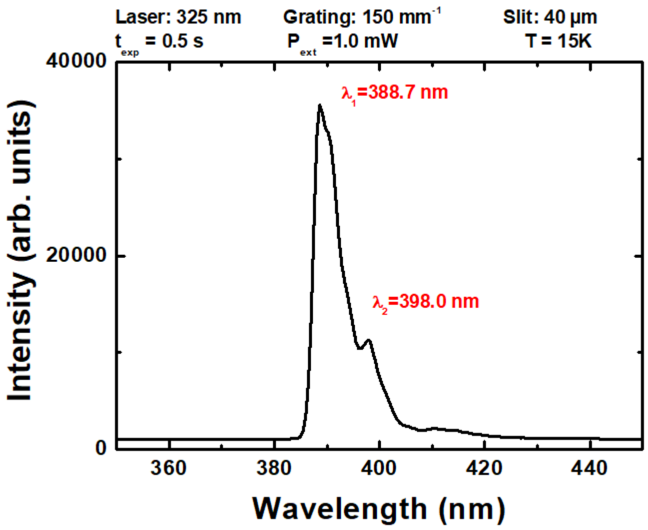

FIGURE 1.30 – PL spectrum of sample 1 acquired at 15K with a 325 nm He-Cd laser.

PL is a technique that can be applied to quantify indium in InGaN thick layers. However, the strain state has to be known. In the case of InGaN/GaN MQW, in addition to the knowledge of the strain state and the QW width, an hypothesis has to be made on the internal electric field and the segregation coefficient which complicates the implementation of this method in samples that are not well known. Moreover, using optical absorption would be more appropriate to avoid the approximation related to the Stokes shift. Furthermore, if the MQW contain indium-rich clusters, carrier localization may induce an overestimation of the indium content. In the following chapters, PL will mainly

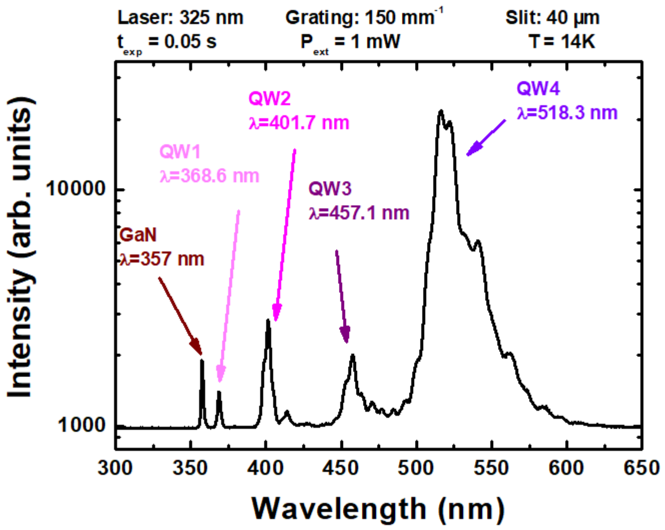

FIGURE 1.31 – PL spectrum of sample 2 acquired at 15K with a 325 nm He-Cd laser.

be used to see a tendency and compare the samples between one another and not for obtaining an accurate value of the indium content.

1.4.6 Cathodoluminescence (CL)

In order to understand the presence of the two peaks in the PL spectra of sample 1, a cathodoluminescence study was undergone. This technique is described in annex C.2. Contrary to PL, CL does not suffer from optical limitations of the lenses and hence can be used to obtain accurate mappings of desired areas with step as small as 5 nm even if one should be careful with the interpretation as carriers may diffuse.

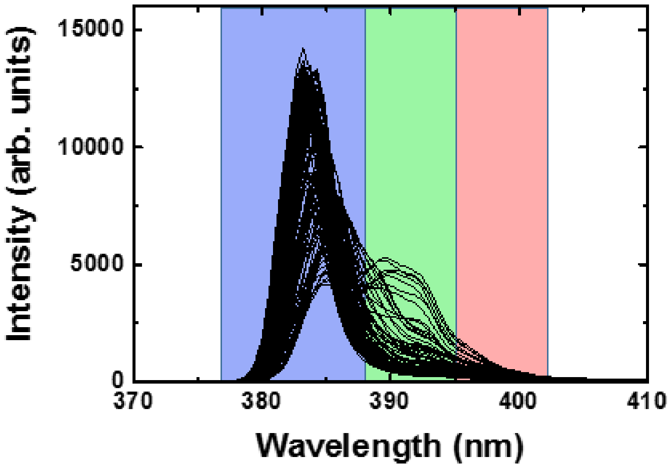

FIGURE 1.32 – CL spectra captured on different parts of sample 1. The emission was fitted in the blue, green and red regions of the spectra.

Here the sample was scanned with an electron energy of 3 keV. Fig. 1.32 plots the spectra obtained on the scanned area. Using different center wavelengths, the blue, green and red

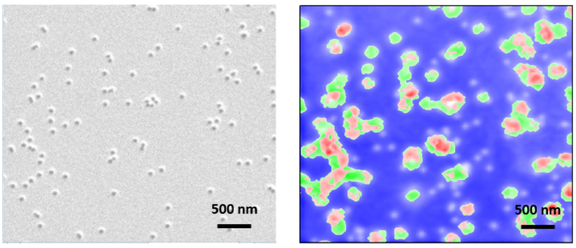

(a) (b)

FIGURE 1.33 – SEM image (a) and associated CL mapping (b) of sample 1. Colors coded according to Fig. 1.32.

parts of the spectrum were fitted. Fig. 1.33 maps the peak intensities related to these peaks (right) with the corresponding SEM image (left) .It appears that the luminescence of the main peak at 383 nm (in blue) is much less intense in the areas of the V-pits as observed before in the litterature (with PL [107]).
A second luminescence peak centered around 398 nm emerges from the vicinity of the V-defects. This peak corresponds to the $\{10\bar{1}1\}$ sidewalls. The enhanced indium incorporation on this orientation is probably the origin of this emission that we also see in PL (see section 2.2.3.1 for more details about incorporation of indium on semi-polar orientations).
The third emission pictured in red is primarily located at the center of the V-pit. Its origin may be related to the accumulation of indium on the TD at the origin of the formation of the V-pit.

1.4.7 High Resolution X-Ray Diffraction (HRXRD)

This method and the experimental set-up are described in annex A.

Quantification in InGaN thick layer The In content estimation requires a knowledge of the relaxation state of the grown InGaN layer on GaN. A reciprocal space mapping (RSM) is therefore realized on an asymetrical reflexion. For reference sample 1, the RSM on the (1 0 5) reflexion is presented on Fig. 1.34.
The signal on the top originates from the GaN layer and the signal at the bottom from the InGaN layer (larger c lattice parameter). As described in [51], the broadening of the reciprocal lattice points in InGaN along the vertical direction is characteristic of a small layer thickness. The broadening in the horizontal direction indicates either the presence of lateral strain or composition fluctuations. Based on the observations with the other characterization methods, composition inhomogeneities indeed play a role. Here we can clearly observe that despite the horizontal broadening the reciprocal lattice points of the InGaN and GaN layer are aligned in the vertical direction. This is clear evidence that the InGaN layer is fully strained on the GaN layer (the a lattice parameter of the InGaN layer is equal to the one of the GaN layer).

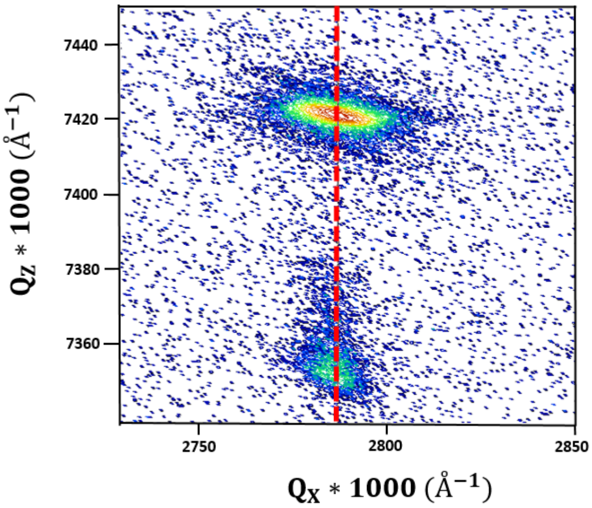

FIGURE 1.34 – Reciprocal space mapping of sample 1 on the (1 0 5) reflection.

The $2\theta - \omega$ scan of the (0 0 2) reflexion is plotted in Fig. 1.35. The presence of two InGaN peaks is a characteristic of a structure in which relaxation has occured. Nonetheless, given the previous conclusion on RSM and the observation of the surface with Atomic Force Miscropy (AFM) (which still reveals a large value of roughness of 7nm), we conclude that the relaxation has not occured.

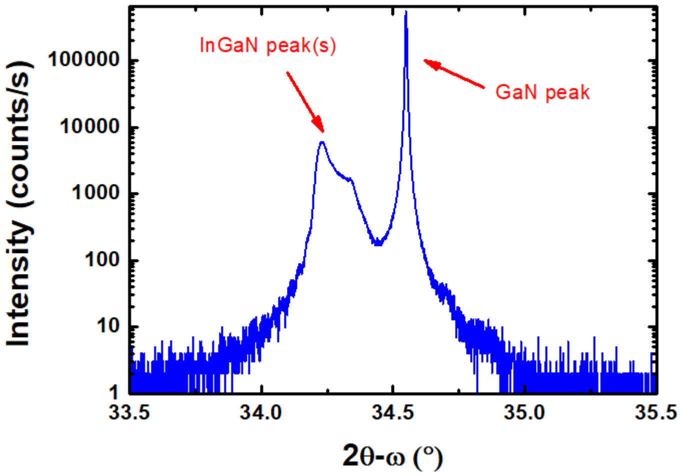

FIGURE 1.35 – $2\theta - \omega$ scan of sample 1 on the (0 0 2) reflection.

The determination of the indium composition from the $2\theta - \omega$ scan using the equation 1.16 gives In contents of 6.6% and 4.5% for the two different peaks with the strongest contribution coming from the peak at 6.6 %. We have not yet found a plausible explanation for the presence of the second peak. Indeed, the CL observation does not match the XRD results. If the second XRD peak was attributed to the V-pits sidewalls, it should correspond to a higher indium content (smaller angle) and not a smaller one (higher angle).

Quantification in InGaN quantum wells For sample 2, X-ray characterization has not been used as the interpretation would be difficult because of the correlation of all the satellite peaks relative to the different indium contents in the MQW existing here. Nevertheless, this technique is widely used for In composition determination in MQW [51] as the experimental data may easily be fitted if the quantum wells have abrupt interfaces, same composition and good structural quality.

1.4.8 Conclusion

This In quantification study revealed that an accurate determination of the indium content requires the implementation of advanced/expensive methods and the interpretation of the results can be delicate. Tables 1.6 and 1.7 summmarize the results obtained with the different techniques for sample 1 and sample 2 respectively.

Quantification technique	x_{In} (%)
APT	7.0 ± 1.5
EDX	5.2 ± 0.5
SIMS	4.3
PL	6.8
XRD	6.6

Table 1.6 – Summary of the indium quantification study for sample 1.

Among the methods implemented here, the more suitable for the analysis of InGaN thick layers are EDX as well as APT, XRD and PL. The use of Raman spectroscopy has not been investigated here but this method may be suitable for an estimation of the In content in the layers.

Quantification technique	x_{In} (%) QW1	x_{In} (%) QW2	x_{In} (%) QW3	x_{In} (%) QW4
APT	3.3 ± 2	9.4 ± 1.3	14.6 ± 1.0	19.5 ± 1.5
EDX	1.8 ± 0.5	6.4 ± 0.6	15.7 ± 1.3	16.7 ± 1.0
PL	2.0	5.9	14.1	19.6

Table 1.7 – Summary of the indium quantification study for sample 2.

For the quantification in InGaN/GaN MQW, EDX and APT appear as the more accurate methods. XRD may also be used if the quantum wells are all the same and present abrupt well/barrier interfaces. The only method available to scan at the nanometer scale is APT. It will be used to assess the distribution of indium atoms in the quantum wells.

Conclusion

In this chapter we described the properties of III-Nitrides with a focus on the InGaN alloy. The specifities of the heteroepitaxy of InGaN on GaN were reviewed. The lattice mismatch between the high indium content QW necessary for long wavelength emission and the GaN template is responsible for several detrimental phenomena. Among them are the presence of numerous defects, the large piezoelectric field, segregation and the compositional pulling effect. The next chapter will review how this affects the implementation of white and long-wavelength LEDs.

Finally, we listed and tested all of the characterization techniques available at CEA-Leti to quantify the indium content in InGaN thick layers and in InGaN MQW. In the following chapters, we will particularly use XRD and SIMS for the determination of indium content in InGaN thick layers while XRD, EDX and APT will be employed in the case of InGaN MQW.

References of chapter 1

[1] T. Zhu and R. A. Oliver. *Phys. Chem. Chem. Phys.* **14**, 9558 (2012).

[2] C. M. Balkas and R. F. Davis. *J. Am. Ceram. Soc.* **79**, 2309 (1996).

[3] W. Paszkowicz, S. Podsiadło and R. Minikayev. *J. Alloy Compd.* **382**, 100 (2004).

[4] W. Paszkowicz. *Powder Diffr.* **14**, 258 (1999).

[5] S. Keller, H. Li, M. Laurent, Y. Hu, N. Pfaff, J. Lu, D. F. Brown, N. a. Fichtenbaum, J. S. Speck, S. P. Denbaars and U. K. Mishra. *Semicond. Sci. Tech.* **29**, 113001 (2014).

[6] I. Vurgaftman and J. R. Meyer. *J. Appl. Phys.* **94**, 3675 (2003).

[7] V. Fiorentini, F. Bernardini and O. Ambacher. *Appl. Phy. Express* **80**, 1204 (2002).

[8] H. W. King and Y. L. Vegard. *J. Mater. Sci.* **1**, 79 (1921).

[9] I. Ho and G. Stringfellow. *Appl. Phy. Lett.* **69**, 2701 (1996).

[10] T. Saito, Y. Arakawa and T. In. *Phys. Rev. B* **60**, 1701 (1999).

[11] J. Adhikari and D. A. Kofke. *J. Appl. Phys.* **95**, 6129 (2004).

[12] A. Koukitu and H. Seki. *J. Cryst. Growth* **189-190**, 13 (1998).

[13] D. Doppalapudi, S. N. Basu and T. D. Moustakas. *J. Appl. Phys.* **512**, 1389 (1998).

[14] N. A. El-Masry, E. L. Piner, S. X. Liu and S. M. Bedair. *Appl. Phy. Lett.* **72**, 40 (1998).

[15] M. Mesrine, N. Grandjean and J. Massies. *Appl. Phy. Lett.* **72**, 350 (1998).

[16] N. A. K. Kaufmann, A. Dussaigne, D. Martin, P. Valvin, T. Guillet, B. Gil, F. Ivaldi, S. Kret and N. Grandjean. *Semicond. Sci. Tech.* **27**, 105023 (2012).

[17] V. Potin, E. Hahn, A. Rosenauer, D. Gerthsen, B. Kuhn, F. Scholz, A. Dussaigne, B. Damilano and N. Grandjean. *J. Cryst. Growth* **262**, 145 (2004).

[18] M. Takeguchi, M. R. McCartney and D. J. Smith. *Appl. Phy. Lett.* **84**, 2103 (2004).

[19] Y.-S. Lin, K.-J. Ma, C. Hsu, S.-W. Feng, Y.-C. Cheng, C.-C. Liao, C. C. Yang, C.-C. Chou, C.-M. Lee and J.-I. Chyi. *Appl. Phy. Express* **77**, 2988 (2000).

[20] D. Gerthsen, E. Hahn, B. Neubauer, V. Potin, A. Rosenauer and M. Schowalter. *Phys. Status Solidi C* **0**, 1668 (2003).

[21] D. Behr, J. Wagner, A. Ramakrishnan, H. Obloh and K. H. Bachem. *Appl. Phy. Lett.* **73**, 241 (1998).

[22] H. K. Cho, J. Y. Lee, N. Sharma, C. J. Humphreys, G. M. Yang, C. S. Kim, J. H. Song and P. W. Yu. *Appl. Phy. Lett.* **79**, 2594 (2001).

[23] N. Wieser, O. Ambacher, H. P. Felsl, L. Gorgens and M. Stutzmann. *Appl. Phy. Lett.* **74**, 3981 (1999).

[24] J. T. Griffiths, F. Oehler, F. Tang, S. Zhang, W. Y. Fu, T. Zhu, S. D. Findlay, C. Zheng, J. Etheridge, T. L. Martin, P. A. J. Bagot, M. P. Moody, D. Sutherland, P. Dawson, M. J. Kappers, C. J. Humphreys and R. A. Oliver. *J. Appl. Phys.* **119**, 0 (2016).

[25] B. Bonef, M. Catalano, C. Lund, S. P. Denbaars, S. Nakamura, U. K. Mishra, M. J. Kim and S. Keller. *Appl. Phy. Lett.* **110**, 143101 (2017).

[26] Y. Varshni. *Physica* **34**, 149 (1967).

[27] Y. H. Cho, G. H. Gainer, A. J. Fischer, J. J. Song, S. Keller, U. K. Mishra and S. P. DenBaars. *Appl. Phy. Lett.* **73**, 1370 (1998).

[28] S. Chichibu, T. Azuhata, T. Sota and S. Nakamura. *MRS Proc.* **449**, 653 (1996).

[29] H. P. D. Schenk, M. Leroux and P. de Mierry. *J. Appl. Phys.* **88**, 1525 (2000).

[30] S. Chichibu, T. Azuhata, T. Sota and S. Nakamura. *Appl. Phy. Lett.* **2822**, 19 (1997).

[31] G. B. Stringfellow. *J. Cryst. Growth* **312**, 735 (2010).

[32] T. Y. Wu, C. C. Chang, K. K. Tiong, Y. C. Lee, S. Y. Hu, L. Y. Lin, T. Y. Lin and Z. C. Feng. *Opt. Mater.* **35**, 1829 (2013).

[33] H. Wang, Z. Ji, S. Qu, G. Wang, Y. Jiang, B. Liu, X. Xu and H. Mino. *Opt. Express* **20**, 3932 (2012).

[34] J. R. Jinschek, R. Erni, N. F. Gardner, A. Y. Kim and C. Kisielowski. *Solid State Commun.* **137**, 230 (2006).

[35] T. M. Smeeton, C. J. Humphreys, J. S. Barnard and M. J. Kappers. *J. Mater. Sci.* **41**, 2729 (2006).

[36] C. J. Humphreys. *Philos. Mag.* **87**, 1971 (2007).

[37] S. Kret, P. Dłuzewski, A. Szczepańska, M. Zak, R. Czernecki, M. Kryśko, M. Leszczyński and G. Maciejewski. *Nanotechnology* **18**, 465707 (2007).

[38] M. J. Galtrey, R. A. Oliver, M. J. Kappers, C. J. Humphreys, P. H. Clifton, D. Larson, D. W. Saxey and A. Cerezo. *J. Appl. Phys.* **104**, 013524 (2008).

[39] K. H. Baloch, A. C. Johnston-Peck, K. Kisslinger, E. A. Stach and S. Gradečak. *Appl. Phy. Lett.* **102**, 191910 (2013).

[40] F. Tang, T. Zhu, F. Oehler, W. Y. Fu, J. T. Griffiths, F. C. P. Massabuau, M. J. Kappers, T. L. Martin, P. A. J. Bagot, M. P. Moody and R. A. Oliver. *Appl. Phy. Lett.* **106**, 072104 (2015).

[41] G. H. Gu, D. H. Jang, K. B. Nam and C. G. Park. *Microsc. mincroanal.* **19**, 99 (2013).

[42] H. Lei, J. Chen and P. Ruterana. *Appl. Phy. Lett.* **96**, 161901 (2010).

[43] A. Reznitsky, A. Klochikhin, S. Permogorov, L. Tenishev, W. Lundin, A. Usikov, M. Schmidt and C. Klingshirn. *Phys. Status Solidi C* **283**, 280 (2002).

[44] K. O'Donnell, R. Martin and P. Middleton. *Phys. Rev. B* **82**, 237 (1999).

[45] Y. Narukawa, Y. Kawakami, M. Funato, S. Fujita, S. Fujita and S. Nakamura. *Appl. Phy. Lett.* **70**, 981 (1997).

[46] D. M. Graham, A. Soltani-Vala, P. Dawson, M. J. Godfrey, T. M. Smeeton, J. S. Barnard, M. J. Kappers, C. J. Humphreys and E. J. Thrush. *J. Appl. Phys.* **97**, 103508 (2005).

[47] L. Bellaiche, T. Mattila, L.-W. Wang, S.-H. Wei and A. Zunger. *Appl. Phy. Lett.* **74**, 1842 (1999).

[48] A. Hangleiter, F. Hitzel, C. Netzel, D. Fuhrmann, U. Rossow, G. Ade and P. Hinze. *Phys. Rev. Let.* **95**, 1 (2005).

[49] F. C. P. Massabuau, P. Chen, M. K. Horton, S. L. Rhode, C. X. Ren, T. J. O'Hanlon, A. Kovacs, M. J. Kappers, C. J. Humphreys, R. E. Dunin-Borkowski and R. A. Oliver. *J. Appl. Phys.* **121**, 013104 (2017).

[50] S. F. Chichibu, A. Uedono, T. Onuma, B. a. Haskell, A. Chakraborty, T. Koyama, P. T. Fini, S. Keller, S. P. Denbaars, J. S. Speck, U. K. Mishra, S. Nakamura, S. Yamaguchi, S. Kamiyama, H. Amano, I. Akasaki, J. Han and T. Sota. *Nat. Mater.* **5**, 810 (2006).

[51] M. a. Moram and M. E. Vickers. *Rep. Prog. Phys.* **72**, 036502 (2009).

[52] K. Kim, W. Lambrecht and B. Segall. *Phys. Rev. B* **56**, 7018 (1997).

[53] K. Shimada, T. Sota and K. Suzuki. *J. Appl. Phys.* **84**, 4951 (1998).

[54] A. Polian, M. Grimsditch and I. Grzegory. *J. Appl. Phys.* **79**, 3343 (1996).

[55] A. F. Wright. *J. Appl. Phys.* **82**, 2833 (1997).

[56] M. A. Moram, Z. H. Barber and C. J. Humphreys. *J. Appl. Phys.* **102**, 023505 (2007).

[57] F. A. Ponce, S. Srinivasan, A. Bell, L. Geng, R. Liu, M. Stevens, J. Cai, H. Omiya, H. Marui and S. Tanaka. *Phys. Status Solidi B* **240**, 273 (2003).

[58] D. Holec, Y. Zhang, D. V. S. Rao, M. J. Kappers, C. McAleese and C. J. Humphreys. *J. Appl. Phys.* **104** (2008).

[59] M. Leyer, J. Stellmach, C. Meissner, M. Pristovsek and M. Kneissl. *J. Cryst. Growth* **310**, 4913 (2008).

[60] Z. Liliental-Weber, K. M. Yu, M. Hawkridge, S. Bedair, A. E. Berman, A. Emara, D. R. Khanal, J. Wu, J. Domagala and J. Bak-Misiuk. *Phys. Status Solidi C* **6**, 2626 (2009).

[61] M. Muller, G. D. W. Smith, B. Gault and C. R. M. Grovenor. *Acta Mater.* **60**, 4277 (2012).

[62] K. Pantzas, G. Patriarche, G. Orsal, S. Gautier, T. Moudakir, M. Abid, V. Gorge, Z. Djebbour, P. L. Voss and A. Ougazzaden. *Phys. Status Solidi A* **209**, 25 (2012).

[63] M. J. Reed, N. a. El-Masry, C. a. Parker, J. C. Roberts and S. M. Bedair. *Appl. Phy. Lett.* **77**, 4121 (2000).

[64] A. V. Sakharov, W. V. Lundin, E. E. Zavarin, M. A. Sinitsyn, A. E. Nikolaev, S. O. Usov, V. S. Sizov, G. A. Mikhailovsky, N. A. Cherkashin, M. Hytch, F. Hue, E. V. Yakovlev, A. V. Lobanova and A. F. Tsatsulnikov. *Semiconductors* **43**, 841 (2009).

[65] H. Wang, D. S. Jiang, U. Jahn, J. J. Zhu, D. G. Zhao, Z. S. Liu, S. M. Zhang, Y. X. Qiu and H. Yang. *Phys. B* **405**, 4668 (2010).

[66] J. W. Matthews, S. Mader and T. B. Light. *J. Appl. Phys.* **41**, 3800 (1970).

[67] R. People and J. C. Bean. *Appl. Phy. Lett.* **47**, 322 (1985).

[68] S. E. Park, O. B. Byungsung and C. R. Lee. *J. Cryst. Growth* **249**, 455 (2003).

[69] F. C. Frank and J. H. van der Merwe. *Proc. Royal Soc. London. Series A. Math. Physi. Sci.* **198**, 205 LP (1949).

[70] A. Fischer, H. Kiihne and H. Richter. *Phys. Rev. Let.* **73**, 2712 (1994).

[71] S. Pereira. *Thin Solid Films* **515**, 164 (2006).

[72] M. Pristovsek, J. Stellmach, M. Leyer and M. Kneissl. *Phys. Status Solidi C* **6**, 565 (2009).

[73] G. Orsal, Y. El Gmili, N. Fressengeas, J. Streque, R. Djerboub, T. Moudakir, S. Sundaram, A. Ougazzaden and J. Salvestrini. *Opt. Mater. Express* **4**, 1030 (2014).

[74] C. Passchier and R. A. Trouw. *Microtectonics.* Springer (2005).

[75] P.-M. Coulon. *Croissance et Caractérisation de Nanofils/Microfils de GaN.* Ph.D. thesis, Université de Nice-Sophia Antipolis (2014).

[76] X. H. Wu, C. R. Elsass, A. Abare, M. MacK, S. Keller, P. M. Petroff, S. P. Denbaars, J. S. Speck and S. J. Rosner. *Appl. Phy. Lett.* **72**, 692 (1998).

[77] M. Shiojiri, C. C. Chuo, J. T. Hsu, J. R. Yang and H. Saijo. *J. Appl. Phys.* **99**, 073505 (2006).

[78] J. Northrup and J. Neugebauer. *Phys. Rev. B* **60**, R8473 (1999).

[79] A. V. Lobanova, A. L. Kolesnikova, A. E. Romanov, S. Y. Karpov, M. E. Rudinsky and E. V. Yakovlev. *Appl. Phy. Lett.* **103**, 152106 (2013).

[80] T. L. Song. *J. Appl. Phys.* **98**, 84901 (2005).

[81] S. Srinivasan, L. Geng, R. Liu, F. A. Ponce, Y. Narukawa and S. Tanaka. *Appl. Phy. Lett.* **83**, 5187 (2003).

[82] C. Bazioti, E. Papadomanolaki, T. Kehagias, T. Walther, J. Smalc-Koziorowska, E. Pavlidou, P. Komninou, T. Karakostas, E. Iliopoulos and G. P. Dimitrakopulos. *J. Appl. Phys.* **118**, 155301 (2015).

[83] F. Bernardini, V. Fiorentini and D. Vanderbilt. *Phys. Rev. B* **56**, 4 (1997).

[84] F. Bernardini and V. Fiorentini. *Appl. Surf. Sci.* **166**, 23 (2000).

[85] P. Lefebvre, A. Morel, M. Gallart, T. Taliercio, J. Allègre, B. Gil, H. Mathieu, B. Damilano, N. Grandjean and J. Massies. *Appl. Phy. Lett.* **78**, 1252 (2001).

[86] F. Bernardini and V. Fiorentini. *Phys. Status Solidi B* **216**, 391 (1999).

[87] T. Takeuchi, S. Sota, M. Katsuragawa, M. Komori, H. Takeuchi, H. Amano and I. Akasaki. *Jpn. J. Appl. Phy.* **36**, L382 (1997).

[88] S. F. Chichibu, a. C. Abare, M. S. Minsky, S. Keller, S. B. Fleischer, J. E. Bowers, E. Hu, U. K. Mishra, L. a. Coldren, S. P. Denbaars and T. Sota. *Appl. Phy. Lett.* **73**, 2006 (1998).

[89] N. Grandjean, B. Damilano, S. Dalmasso, M. Leroux, M. Laügt and J. Massies. *Phys. Status Solidi A* **176**, 219 (1999).

[90] A. Dussaigne. *Diodes électroluminescentes blanches monolithiques.* Ph.D. thesis, Université de Nice-Sophia Antipolis (2005).

[91] Y. S. Kim, A. Kaneta, M. Funato, Y. Kawakami, T. Kyono, M. Ueno and T. Nakamura. *Appl. Phy. Express* **4**, 052103 (2011).

[92] Z. H. Zhang, W. Liu, Z. Ju, S. Tiam Tan, Y. Ji, Z. Kyaw, X. Zhang, L. Wang, X. Wei Sun and H. Volkan Demir. *Appl. Phy. Lett.* **104**, 1 (2014).

[93] S. Y. Karpov. *MRS Internet J. Nitride Semicond. Res.* **3**, 16 (1999).

[94] Y. Inatomi, Y. Kangawa, T. Ito, T. Suski, Y. Kumagai, K. Kakimoto and A. Koukitu. *Jpn. J. Appl. Phy.* **56**, 078003 (2017).

[95] S. Pereira, M. R. Correia, E. Pereira, K. P. O'Donnell, C. Trager-Cowan, F. Sweeney and E. Alves. *Phys. Rev. B* **64**, 205311 (2001).

[96] K. Hiramatsu, Y. Kawaguchi, M. Shimizu, N. Sawaki, T. Zheleva, R. F. Davis, H. Tsuda, W. Taki, N. Kuwano and K. Oki. *MRS Internet J. Nitride Semicond. Res.* **2**, 1 (1997).

[97] G. Schmidt, M. Müller, P. Veit, F. Bertram, J. Christen, M. Glauser, J. F. Carlin, G. Cosendey, R. Butté and N. Grandjean. *Appl. Phy. Lett.* **105**, 032101 (2014).

[98] G. T. Thaler, D. D. Koleske, S. R. Lee, K. H. a. Bogart and M. H. Crawford. *J. Cryst. Growth* **312**, 1817 (2010).

[99] M. S. Oh, M. K. Kwon, I. K. Park, S. H. Baek, S. J. Park, S. H. Lee and J. J. Jung. *J. Cryst. Growth* **289**, 107 (2006).

[100] W. Lee, J. Limb, J.-H. Ryou, D. Yoo, T. Chung and R. D. Dupuis. *J. Elect. Mater.* **35**, 587 (2006).

[101] A. Dussaigne, B. Damilano, N. Grandjean and J. Massies. *J. Cryst. Growth* **251**, 471 (2003).

[102] Z. Deng, Y. Jiang, W. Wang, L. Cheng, W. Li, W. Lu, H. Jia, W. Liu, J. Zhou and H. Chen. *Sci. Rep.* **4**, 6734 (2014).

[103] K. Muraki, S. Fukatsu and Y. Shiraki. *Appl. Phy. Lett.* **61**, 4 (1992).

[104] S. Pereira, M. R. Correia, E. Pereira, C. Trager-Cowan, F. Sweeney, K. P. O'Donnell, E. Alves, N. Franco and A. D. Sequeira. *Appl. Phy. Lett.* **81**, 1207 (2002).

[105] T. Mehrtens, M. Schowalter, D. Tytko, P. Choi, D. Raabe, L. Hoffmann, H. Jönen, U. Rossow, A. Hangleiter and A. Rosenauer. *Appl. Phy. Lett.* **102**, 132112 (2013).

[106] T. Tao, T. Zhi, B. Liu, Y. Li, Z. Zhuang, Z. Xie, D. Chen, P. Chen, R. Zhang and Y. Zheng. *Phys. Status Solidi A* **211**, 2823 (2014).

[107] T. Shin, X.-S. Li, D.-S. Ko, J.-Y. Won, S.-H. Kim, J. Kim, J. Kim, Y. Tak, J.-Y. Kim, G.-S. Park and E. Lee. *Chem. Phys.* **436-437**, 51 (2014).

2

White and color LEDs

2.1 White LEDs

2.1.1 Colorimetry

The perception of colors by the human eye is ruled by two different types of sensors in our retina, the rods and the cones. The rods measure the luminance while the cones are responsible for color. There are three types of cones, which are sensitive to blue, green and red wavelengths. The response of the eye was characterized on a sample of the population. An average of the perception of colors was established by the CIE (Commission Internationale de l'Eclairage). The three color matching functions of the cones x^*, y^*, z^* are plotted as a function of wavelength in Fig. 2.1.

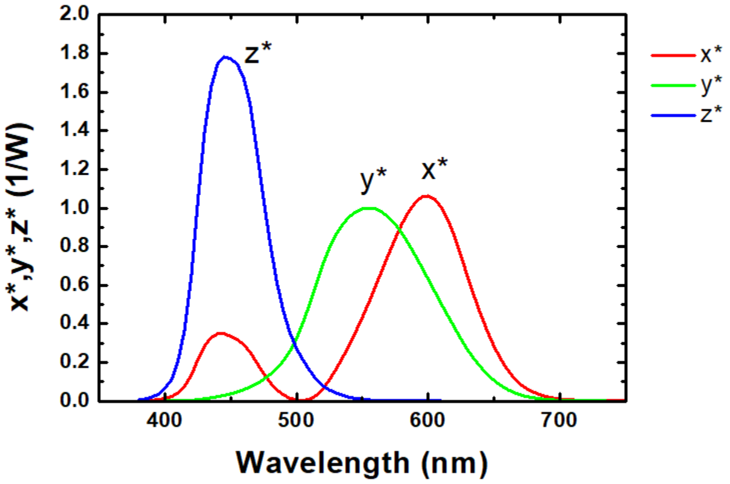

FIGURE 2.1 – CIE 1931 color matching functions. These functions correspond to the curves of sensitivity of the cones on the retina.

A color is defined by X, Y, Z, the relative stimulus of the cones calculated as follows :

$$X = \int_{\lambda} x^*(\lambda) P(\lambda) d\lambda \tag{2.1}$$

$$Y = \int_{\lambda} y^{*}(\lambda)P(\lambda)d\lambda \tag{2.2}$$

$$Z = \int_{\lambda} z^{*}(\lambda)P(\lambda)d\lambda \tag{2.3}$$

with $P(\lambda)$ the luminous power spectra, the emitted power by unit wavelength.
The chromaticity coordinates are then defined as :

$$x = \frac{X}{X+Y+Z} \tag{2.4}$$

$$y = \frac{Y}{X+Y+Z} \tag{2.5}$$

$$z = \frac{Z}{X+Y+Z} \tag{2.6}$$

The chromaticity diagram (Fig. 2.2) is a chart made to define the colors visible to the human eye. Each point of the diagram represents a color which is defined by x and y chromaticity coordinates. The monochromatic colors are pictured on the edges of the diagram whereas white light is found at the center (chromacity coordinates of (0.33, 0.33)).

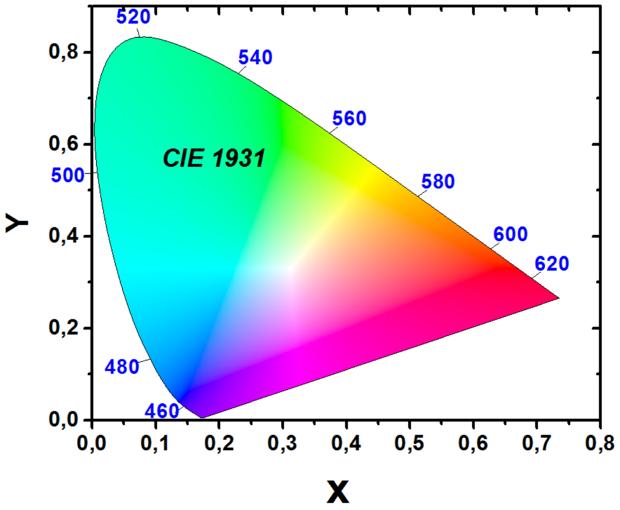

FIGURE 2.2 – Chromaticity diagram CIE 1931. On the edges of the diagram, are the monochromatic colors and at the center is the white light.

Color temperature (CT) The color temperature of a light source is defined as the temperature at which an ideal black-body radiator would need to be heated at in order to radiate light at a color comparable to the source color. The CT is particularly useful to compare white light sources as different nuances of cold white and warm white may be found. For instance, the color temperature of a candle is around 1800 K while tungsten halogen has a color temperature of 3200 K.

Color rendering index (CRI) The color rendering index is a number between 0 and 100 which accounts for the aptitude of a light source to restitute the colors of an object compared to the ability of a reference source of same color temperature. Even if the light has perfect white chromaticity, the color rendering can be very poor. The light of the day has a CRI of 100 by its definition. The determination of the CRI is made with a specific set of 14 test color samples [1].

Luminous efficacy The luminous efficacy (in Lumens/Watt) is the capacity for a light source to produce luminous flux from an electric Watt (W). The luminous efficacy may be considered for the light source alone or for the whole device (light source with power supply). If a source has a high luminous efficacy it means it is cost-effective as one needs little power to produce a large amount of light.

2.1.2 Different types of white lights

2.1.2.1 Non LEDs sources of white light

Fig. 2.3 (from [2]) summarizes the luminous efficacy of the main types of white light sources. The current and projection of the cost of kilolumen in US dollars is plotted in Fig. 2.4.

The incandescent light bulb produces electric light using a wire filament which glows when subjected to very high temperatures. The filament,originally made of carbon was then replaced with tungsten. Since most of the energy is converted into heat, the efficiency is very poor. The luminous efficacy of a typical incandescent lamp is about 16 lm/W and the CRI is 100.

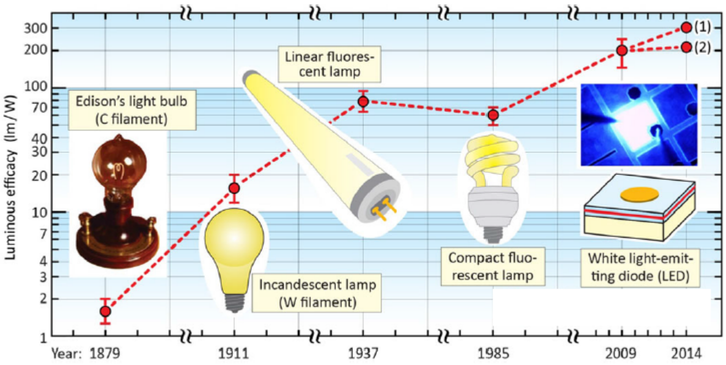

FIGURE 2.3 – Temporal development of the luminous efficacy of different types of lamps from [2].

In fluorescent lamps, an electric current excites mercury vapor which produces UV light which is then converted into visible light by the phosphors deposited on the walls of the

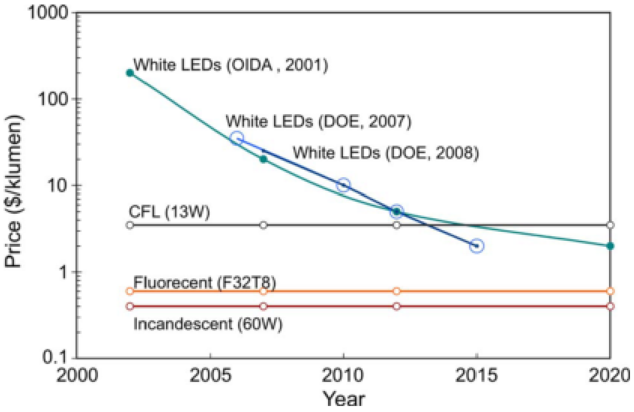

FIGURE 2.4 – White light sources cost projections in lm/W. The turquoise and dark blue curves represent the cost projection for white LEDs by the US Departement of Energy in 2001 and 2007/2008 [3].

tube. Fluorescent lamps are more expensive than incandescent light bulbs but has much better luminous efficacy of about 60 lm/W with a CRI close to 100. However, they contain mercury, potentially harmful for humans and the environment.
The light-emitting diode (LED) is an opto-electronic device which emits light when an electric current runs through it. Even if some white LEDs reach very high CRI many LEDs have CRI under 90. The price of the lumen remains important compared to other sources even if there is a strong decreasing tendency with time (see Fig.2.4)

Despite their cost and their perfectible CRI, LEDs are now replacing light incandescent bulbs and fluorescent lamps. According to the US departement of Energy LED lighting is expected to represent 48 % of lumen-hour sale of the general illumination market by 2020 and 84 % by 2030 in the USA [4].

Indeed, LEDs present many advantages compared to the other sources of white light mentionned before [2] :

- Available in a wide range of color temperatures (2700K-6000K)
- No mercury is contained in the lamps (in contrast to fluorescent lamps)
- Long lifetime operation about 25 000 hours (at 70 % lumen maintenance) to compare to 1 000 and 12 000 hours for light incandescent bulbs and fluorescent lamps respectively
- Very good luminous efficacy (comparison shown in Fig. 2.3)

According to the US Departement of Energy report of 2014 [4], if the current trends in terms of price and performance continue, the lighting energy consumption should be reduced by 40% compared to a scenario with no further market penetration of LEDs.

2.1.2.2 White LEDs

There are several ways to produce white light using LEDs. Since the breakthrough initiated by the first efficient blue LEDs in 1995 [5], phosphor converted LEDs are the most common type of white LEDs.

Blue LED pumping a yellow phosphor In this type of LED , the light from a blue LED is partially absorbed by the phosphor while the remaining part is transmitted. As several types of phosphors were tested, (YAG :Ce) Cerium-doped yttrium-aluminum garnet phosphor appeared as the best candidates to generate white light with good chromaticity coordinates. Fig. 2.5 features the emission spectrum of one of the first phosphor based white LED by Bando *et al.* [6].

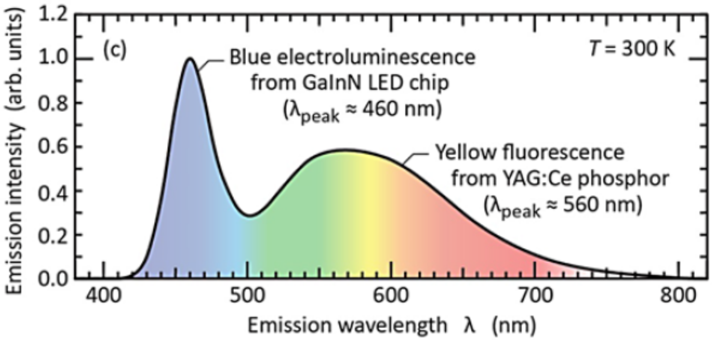

FIGURE 2.5 – Emission spectrum of a phosphor-based white LED from [2] adapted from [6].

The luminous efficacy of this type of LEDs can be very high with a record of 249 lm/W reached by Narukawa *et al.* in 2010 [7].
Blue/phosphor-based white LEDs present several disavantages. Their efficiency is limited by in-built efficiency losses due to the conversion of blue light (Stokes shift). The best Wall Plug Efficiencies (WPE) of these LEDs reach about 60% [8], [7]. Furthermore, the dichromatic nature of the source limits the CRI to values around 75-80 [1]. The phosphor package system does not age as well as the LED, mainly because of its poor resistance to high temperatures [9] leading to changing shades of white. When carrying ageing tests, Meneghini *et al.* [10] observed a shift of the chromaticity coordinates towards bluish light attributed to a degradation of the phosphor conversion efficiency.

UV LED and phosphor It is also possible to combine an UV LED with three phosphors emitting blue, green and red light. This process uses a similar approach as conventional fluorescent lamps. Because it is a trichromatic source, much better CRI can be obtained using this solution. A CRI of 97 has been demonstrated by Radkov *et al.* [11]. Moreover, the emission is not dependant on the UV emission wavelength as the visible emission comes only from the phosphors [1].

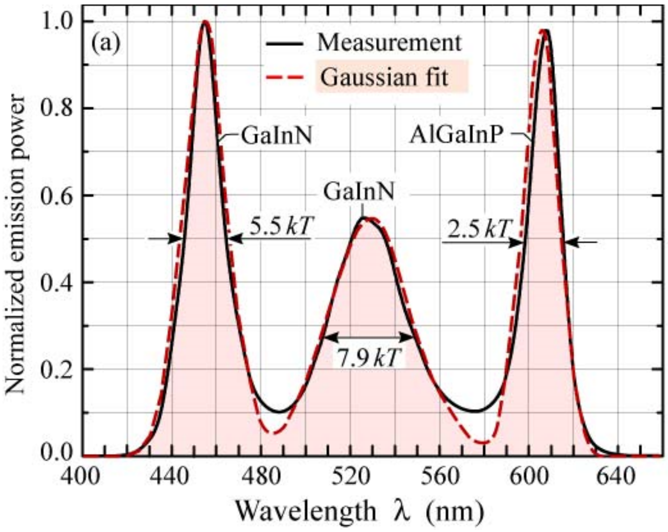

FIGURE 2.6 – Emission spectrum of tri-chromatic white LED constructed by combining spectra from three separate orange (InGaAlP), green and blue LEDs (InGaN) (from [14].

Despite the better CRI, UV phosphor-based LEDs suffer from the same problems as blue phosphor based LEDs. In this case, the effect of the Stokes shift is even greater as full conversion is used as opposed to partial conversion for blue/phosphor based white LEDs and as the difference of wavelength between the source and the converter is bigger. The efficiency of such devices is also still limited by the efficiency of UV LEDs themselves even if recent progress was made on this topic [12].

Combination of RGB LEDs A simple approach for generating white light is to combine blue, green and red LEDs as was imagined early by Stinson [13]. Fig. 2.6 presents the emission spectrum of a white LEDs combining three LEDs emitting at 455, 525 and 605 nm and reaching a CRI of 86 [14]. The blue and green LEDs are InGaN-based while the orange LED is using AlInGaP. A luminous efficiency of 318 lm/W has been achieved.

Because of the narrow emission linewidths of LEDs (as compared to emission of the phosphors), the CRI is very sensitive to a change in the emission wavelength of the LEDs. Furthermore, yellow/red AlInGaP based-LEDs behave differently with temperature [15]. This effect may be counterbalanced by adjusting the power ratios of the LEDs [14]. Taylor *et al.* [8] showed that a key parameter to improve the CRI is the green LED. The ideal green LED for this purpose would have a broad emission centered at 547 nm. As detailed on the paragraph on the green gap, such sources are still not efficient enough. Furthermore, the three power drivers necessary to control the three LEDs have an additional cost.

White Organic LEDs (WOLEDs) OLEDs use of either small molecules or polymers as active layers. Many materials have been tested but efficient devices with good quality of white still have not been manufactured. One can cite the attempt by Reineke *et al.* [16] who achieved a good efficiency of 90 lm/W using a multilayer device. The CRI was 80 with chromaticity coordinates of (0.44 ; 0.46). The group of Xu *et al.* [17] achieved a fine tuning of the chromaticity coordinates (0.33 ; 0.33) using a polymer codoped with two phosphorescent dyes. The efficiency was rather small (5.5 lm/W). OLEDs have the advantage to propose an option of flexible displays and are already widely used for several applications. Nonetheless they have typical lifetimes around 5000 hours under operation, far less than their inorganic counterparts [18]. The scaling to large devices is also one of the challenges this technology faces [19].

2.1.3 White monolithic LEDs : Principles and raising issues

2.1.3.1 Principle

White light can also be obtained by combining several QWs emitting at different wavelengths. Fig. 2.7 schematically illustrates the principle of white monolithic emission. In this case the active zone consists in five QWs of same width, the emission wavelength is adjusted with the indium content. Compared to the phosphor approach, white monolithic LEDs do not require an additional processing step after the growth. Furthermore, they avoid the problems related to the aging of the phosphor that are causing color unstability.

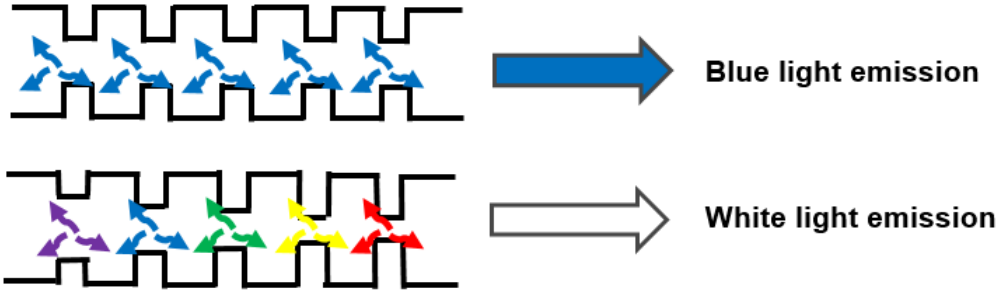

FIGURE 2.7 – Schematic representation of the principle of white monolithic emission.

Damilano *et al.* demonstrated in 2001 the first white monolithic LED [20] grown by MBE. The active region is composed of blue and yellow-emitting QWs. The indium content remained constant (0.15-0.2) and the emission wavelength was controlled by tuning the well widths. A good set of chromaticity coordinates was obtained (0.29, 0.31).

2.1.3.2 Issues

There are several problems that still prevent the implementation of efficient white monolithic LEDs. Indeed, the luminous efficacy is limited by the poor quality of the emission in the yellow/red range. It is even more difficult to reach a good efficacy when the wells are thickenned to reach longer wavelengths because the hole and electron wavefunctions are further separated (see paragraph on QCSE in chapter 1).

Secondly, in an architecture with different QWs emitting at different wavelengths in the active region, the emission must be properly balanced between the QWs to ensure a white emission of good quality. Carrier distribution has been studied in standard InGaN/GaN QWs. By using dual wavelength devices and by comparing PL and EL spectra, it was shown that emission is always stronger on the quantum well on the p-side [21], [22]. This characteristic is explained by the low mobility of holes (as compared to the mobility of electrons), in the structure, which get trapped in the well closer to the p-type and have difficulty of diffusing in the wells closer to the n-side.

In white monolithic LEDs, the dependence of EL with injection current was studied by Dalmasso *et al* [23] and Dussaigne *et al* [24]. Fig. 2.8 (a) shows the dependency of the EL spectra with increasing injection current for the white monolithic LED presented in [24]. The corresponding color chromaticity coordinates are plotted on Fig. 2.8 (b). One can clearly see an instability of the chromaticity coordinates and hence of the quality of white light with the injection current. The CRI of this structure reaches 70. Compared to the first structure by Damilano *et al.* the last QW was thickenned, allowing it to emit in the red range.

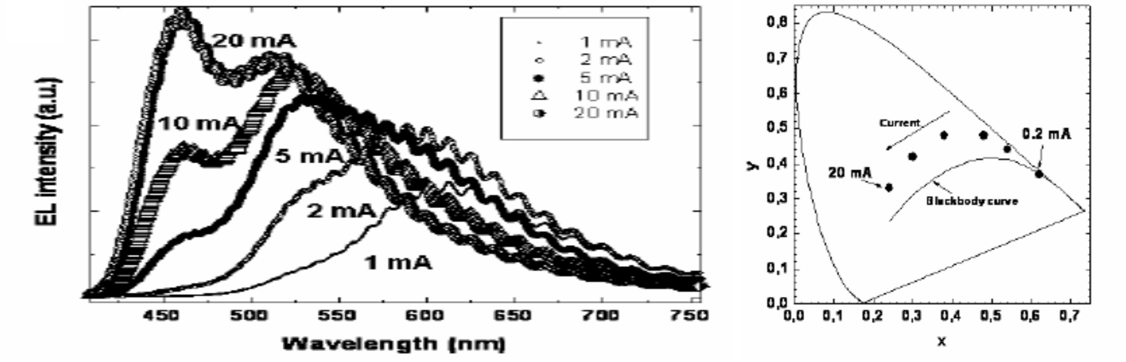

(a) (b)

FIGURE 2.8 – EL spectra of white monolithic LEDs (a) and corresponding chromaticity coordinates (b) for different forward currents from [24].

Because of the problems related to the transport of carriers, the position of the different QWs in the structure is crucial. Either the QWs emitting at the longer wavelengths are positionned on the p-side or on the n-side. The more intuitive solution is to place them on the p-side because these QWs could lower the material quality of the subsequent layers (since they are either thick or with a high indium content) by increasing the strain at the beginning of the growth of the active region. Nonetheless, one could advocate that in that case these long wavelength emitting QWs reabsorb a part of the light emitted by the smaller wavelength emission therefore decreasing the efficiency.

In 2002 Nichia released the results of its white monolithic LED grown by MOVPE [25]. They tested the effect of the position of the QWs in the stucture on the electroluminescence spectra. When using blue and yellow QWs the best were obtained by placing the yellow QW on the p-side, they demonstrated a CRI of 43 and an efficiency of 11 lm/W. With the use of red, green and blue QWs they improved the CRI to 80 but at the cost of reducing the efficiency to 7.9 lm/W, in this case the red QW was placed on the n-side.

Original architectures of white monolithic LEDs were proposed to avoid dealing with the problems of transport in the active region. Park *et al.* [26] fabricated laterally distributed blue and green QWs using Selective Area Growth (SAG). They propose to use the same process to fabricate white LEDs. In this case, Electroluminescence (EL) intensity ratio showed very little variation with current thanks to the parallel injection. Lim *et al.* [27] fabricate double concentric hexagonal pyramids. The incorporation of indium in the MQWs is different on the polar and semi-polar different facets $\{10\bar{1}1\}$ $\{11\bar{2}2\}$ $\{11\bar{2}0\}$ and $\{0001\}$ of the architecture (more details on the incorporation of indium on semi-polar planes in 2.2.2). The combination of the emission from the different facets yields white light emission with a CRI of 75 and rather stable chromaticity coordinates ((0.361, 0.390) at 20 mA). The same principle was used by Song *et al.* in 2017 [28] using multi-facet GaN templates. Thanks to three different contributions, a good set of chromaticity coordinates of (0.306, 0.333) is obtained. These solutions all involve steps of complicated processing (pre-growth for the substrate or after).

Instead of having different QWs in the active region all injected electrically, a part of the emission can be optically triggered. The advantages of this approach is that lower carrier densities are observed compared to electrical injection, minimizing Auger recombination and carrier screening effects [29]. Using this idea, Damilano *et al.* demonstrate a white light-emitting source in which blue InGaN/GaN LED optically pumps yellow InGaN/GaN QWs. A very good CRI of 89.1 with chromaticity coordinates of (0.26,0.25) was obtained thanks to a broad yellow emission [30]. Lu *et al.* [31] also achieve good chromaticity coordinates by using a similar principle and using an InGaN underlayer. Similarly, Yang *et al.* [32] demonstrated a CRI of 62 with a structure in which yellow-emitting QDs are grown under InGaN/GaN QWs. A good set of chromaticity coordinates (0.335, 0.420) was also reached by Soh *et al.* [33]. In this case, blue/green QWs pump InGaN/GaN QWs emitting in the red range thanks to an introduction of indium rich InGaN nanostructures during the growth. A similar process was used by Kowsz *et al.* [29] on semipolar direction $\{20\bar{2}1\}$. An electrically injected blue QW is pumping green and red QW. Here, the doping profile was designed to enhance the electrical field and red-shift the emission. A CRI of 70 and chromaticity coordinates of (0.33, 0.35) were obtained. Two LEDs may also be grown on top of each other as demonstrated by Chen *et al.* [34] when a blue LED was grown on top of a green LED on the same substrate. Chromaticity coordinates of (0.2, 0.3) and luminous efficiency of 0.8 lm/W were achieved.

An inovative solution was proposed by Sheu *et al.* [35]. Here, blue emission from InGaN/GaN QWs is combined with yellow emission which is achieved by doping with Si and Zn in the InGaN QW. The doping gives rise to donor and deep acceptor levels emitting in the yellow range.The control of the chromaticity coordinates is made by the tuning of the In content and the doping levels. However, Si and Zn doping deteriorate the QW leading to a poor emission efficiency. Another solution was proposed by Huang *et al.* [36]. They generate red-emission with Ag nanorod arrays embedded in the p-GaN region which creates Ga-vacancies after thermal bonding. The Donor-Acceptor pair red transition related to Ga-vacancies combined with the blue emission of the InGaN/GaN QW gives rise to white light emission but at high current injection only. In 2015, Ben Sedrine *et al.* achieve white light emission by the combination of an InGaN/GaN QW and the yellow band associated with defects[37]. Using an annealing treatment at 1000 ° C, they demonstrate rather stable chromacity coordinates with laser excitation power. The appearance of In-rich yellow-emitting QDs in blue QWs attributed to phase separation grown by Wang *et al.* showed a stable white light when varying the injection current from 20 mA to 60 mA [38].

To achieve a better balance of the carriers in a blue LED structure, Kuo *et al.* demonstrated that adding indium in the barriers was a good solution [39], [40]. Furthermore, this solution also improves the efficiency of the QWs by reducing the QCSE. We propose to implement this solution in a white monolithic diode.

2.1.4 White monolithic LEDs : Simulation on carrier distribution with indium in the barriers

A simulation study was led in order to evaluate the impact of the introduction of indium in the barriers for the carrier distribution and the emission of a white monolithic LED. The TCAD simulation tool SILVACO Atlas was used. The band structure and wave function analysis are based on self-consistent 3-band k.p formalism for wurtzite structure. We took into account strain calculation, carrier screening, spontaneous and piezoelectric polarization. For all simulations, the layers are strained on GaN.

As a reference, we consider a typical LED structure with a 500 nm-thick n-GaN layer (donor concentration $= 1 \times 10^{19} \quad cm^{-3}$). The active region consists in three undoped 2.5 nm-width QWs sandwiched between four 6 nm-wide undoped GaN barrier layers. The nominal quantum wells compositions vary from 15% to 40% from the p-side to the n-side. The p-type region consists of a 200 nm Mg-doped GaN layer (acceptor concentration $= 2 \times 10^{19} \quad cm^{-3}$). The operating temperature is assumed to be 300K. Nonradiative carrier lifetimes for the wells were chosen accordingly to the indium content to account for the creation of nonradiative recombination centers as the quality of the crystal decreases when indium content is increased. For structure A, the buffer is composed of 7% of indium and all the barriers as well. Structure B has a first barrier on the n-side and the buffer with 7% indium content. The indium contents in the following barriers are 13%, 10% and 9%

for the last barrier on the p-side. Fig. 2.9 pictures the simulated structures and Table 2.1 summarizes the indium contents of the barriers for the three structures.

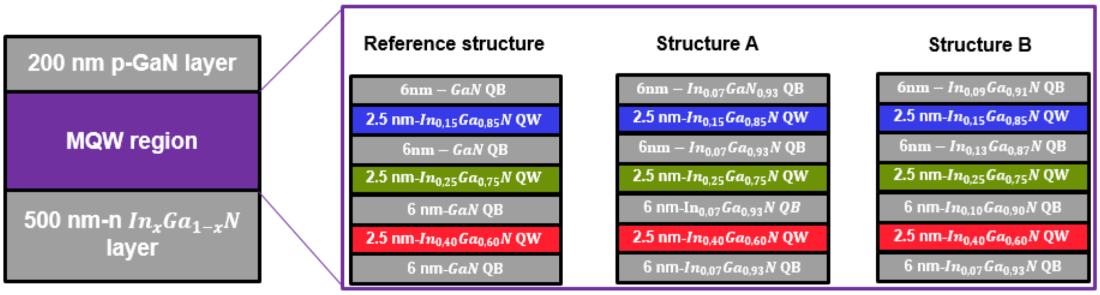

FIGURE 2.9 – From left to right, LED reference structure, structure A and structure B. The indium buffer content is the same as the first barrier indium content (0% for reference structure, 7% for structures A and B).

Structure	In content in buffer and 1st QB	2nd QB In content	3rd QB In content	4th QB In content
ref	0	0	0	0
A	7	7	7	7
B	7	10	13	9

TABLE 2.1 – Nominal indium contents in the barriers for reference structures and structures A and B.

Fig. 2.10 shows the simulated electroluminescence spectra at 30 A/cm^2 for reference structure and structures A and B. The blue, green and red curves are associated with the emission of the quantum wells of the structure with 15%, 25% and 40% In content, respectively. For the reference structure, the emission comes mainly from the blue QW on the p-side (as previously reported) whereas in structure A the emission is better balanced between the wells. Structure B even brings a further improvement.

The better balance of radiative recombination between the QWs can be explained by the way the carriers are distributed in the active region. Fig. 2.11 plots the holes and electron densities for the three structures. One can notice that the holes are trapped in the quantum well on the p-side for the reference structure. For this reason, radiative recombinations occur mainly in this QW. Here the electrons are also lacking, especially in the middle QW. For structures A and B, the potential barriers are lowered by the introduction of indium in the QBs, allowing the holes to escape and flow more easily to the others QWs. In our model, it is particularly important to have a lot of carriers in the

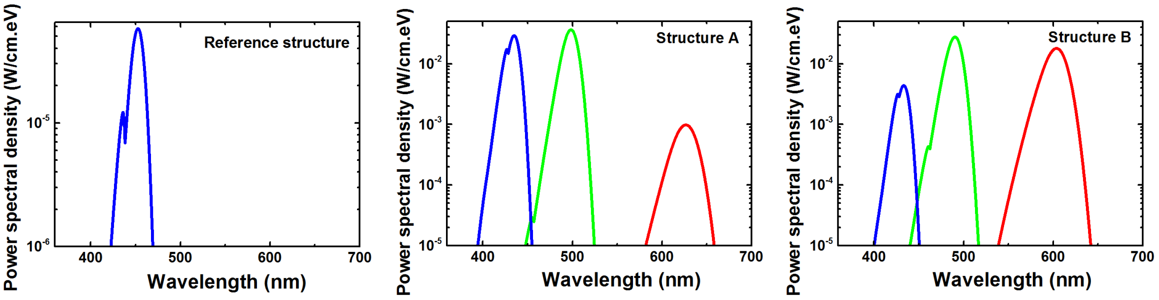

(a) (b) (c)

FIGURE 2.10 – Simulated emission spectra of the reference structure (a), structure A (b) and structure B (c) at 30 A/cm^2.

red quantum well next to the n-side as the nonradiative recombination and the QCSE are stronger due to the high indium content. The more optimal balance is achieved for structure B.

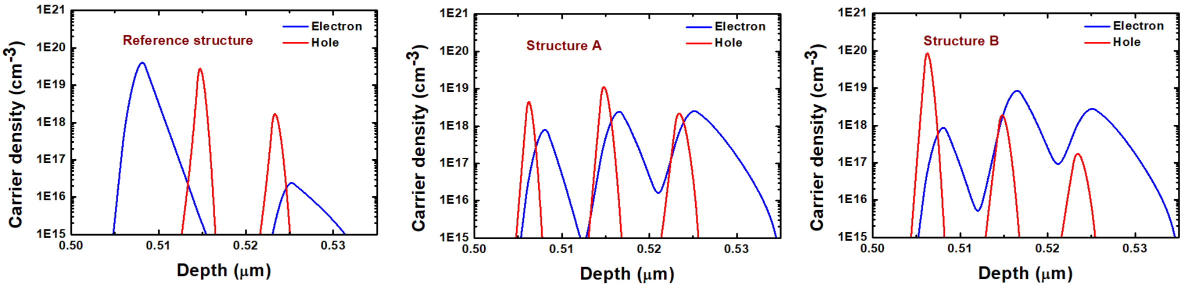

(a) (b) (c)

FIGURE 2.11 – Electron (blue) and Hole (red) densities for the reference structure (a), structure A (b)and structure B (c) at 30 A/cm^2.

We have shown that the introduction of indium in the barriers allows us to tune the emission in the active region by modifying the distribution of carriers in the wells. The theoretical CIE color coordinates of our three structures are represented in Fig.2.12 for currents from 10 A/cm^2 to 50 A/cm^2. Structure B is the optimized structure for which we obtain (0.32 ;0.32) at 30 A/cm^2, very close to (0.33 ;0.33) the exact coordinates of pure white light emission. We can tune these coordinates if we desire colder or warmer types of white emission.

NB : The order of the QWs with the red QW at the bottom imposes a structure which is pratically unfavourable for the growth. Indeed, the strain will be larger in the overall structure if the first well is grown with such a high indium content. Nonetheless, this structure was chosen for the simulation since when we would set the red QW on the p-side, the holes would get trapped in a deep potential well and could not escape, the simulation would not converge as the current would not flow at all. Although this simulation was not ideal and not entirely representative of the real structure, the main goal of showing the tunability of the emission by introducing indium in the barrier was achieved.

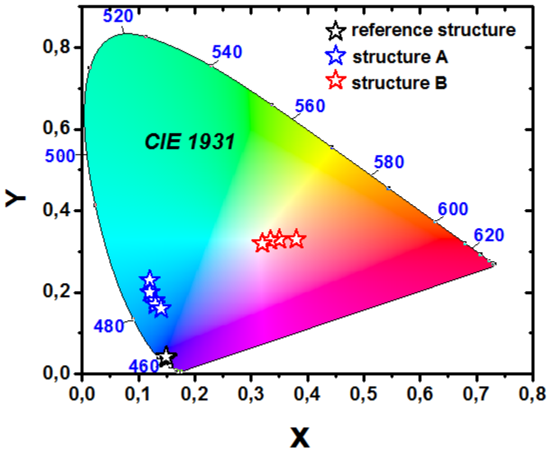

FIGURE 2.12 – Theoretical chromaticity diagram CIE 1931 with the color coordinates of the LED reference structure(black stars), structure A (blue stars) and structures B (red stars) for currents of 10 A/cm^2 to 50 A/cm^2.

2.2 The green gap

For many applications, there is a need for efficient LEDs at wavelength emissions covering the whole visible spectrum. As explained in the first part of the chapter, the quality of white light is greater if the color sources are more numerous and broad. For a modulation of the chromaticity coordinates and of color temperature as illustrated in Fig. 2.13, the systems using different LEDs will be privileged compared to the converted approach. Backlighting also requires LEDs of several different wavelengths to be combined to restitute all visible colors (Fig. 2.14 (a)). Having LEDs emitting at different wavelengths using the same material system is also essential for micro-display applications as it facilitates the post growth processing (Fig.2.14 (b)). Unfortunately, no material system is currently capable to provide efficient LEDs with emission spanning over the whole visible spectrum.

FIGURE 2.13 – Different shades of white corresponding to the light emitted by the sun at different moments of the day (related to the color temperature).

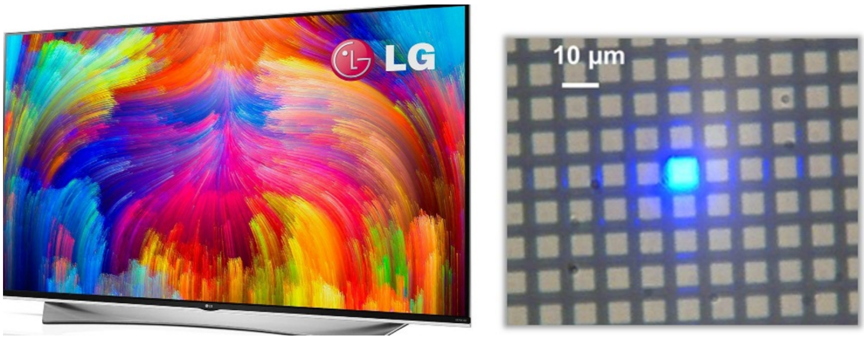

(a) (b)

FIGURE 2.14 – Screen backlighting with saturated colors may be realized using the direct emission from RGB LEDs (a). Blue pixel (technology from CEA-Leti) (b).

Fig. 2.15 shows the maximum EQE reported for LEDs depending on their emission wavelength. Very high efficiencies are disclosed for InGaN-based LEDs in the blue range. An excellent EQE of 84.3 % (WPE of 81.3 %) was reported by Narukawa *et al.* [7] at a wavelength of 444 nm. High EQE was also reached in the red range by OSRAM with AlInGaP based LEDs [41]. A maximum EQE of 72 % was measured at 650 nm. However, the green/yellow range which corresponds to the maximum sensitivity of the human eye lacks efficient emission. EQE of green and yellow LEDs do not exceed 35 % and 10 % respectively. This phenomenon, referred to as the "green gap" is a technological barrier impeding the development of ultra high efficiency white LEDs or low consumption multicolor micro displays.

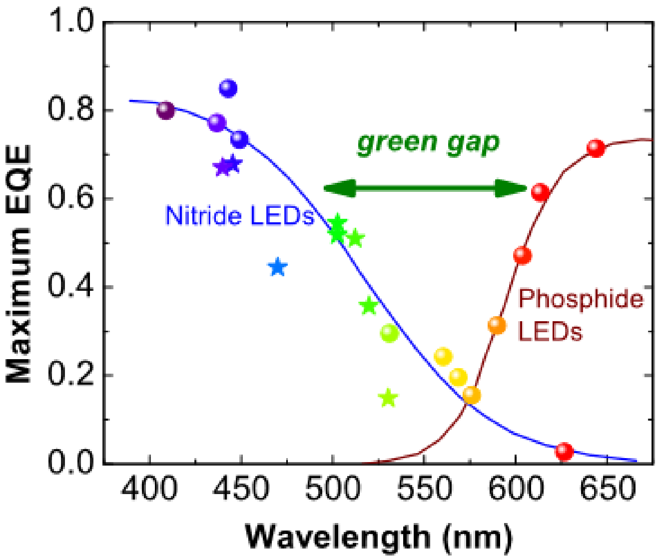

FIGURE 2.15 – Maximum EQE of III-nitride and III-phosphide LEDs [42] adapted from [43].

2.2.1 Reasons for the green gap

Both AlInGaN and AlInGaP material systems meet obstacles to reach green and yellow ranges.

The AlInGaP systems has intrisic limitations. Indeed, in the range of composition needed for the green-yellow emission, the bandgap becomes indirect, facilitating the path for nonradiative recombinations. Furthermore, the band offset between the conduction bands of the active region and the p-doped region becomes smaller, the confinement decreases and the leakage of electrons increases [44]. For this thesis, we will focus on AlInGaN system which has the best potential for realizing emitters through the whole visible range.

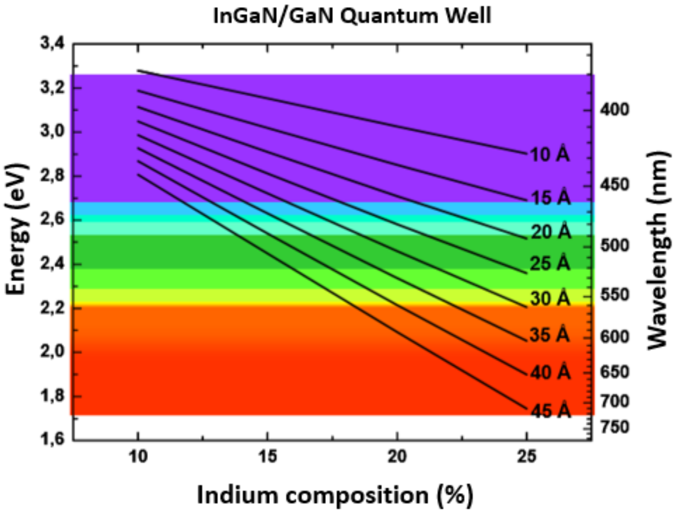

FIGURE 2.16 – Calculated transition energy/wavelength of an $In_xGa_{1-x}N$ as a function of In composition for different well thicknesses (T=10K) from [45].

The AlInGaN system presents a direct bandgap over the whole range of compositions. Fig. 2.16 presents the calculated transition energies of an InGaN/GaN QW as a function of In composition for different well thicknesses. Thus, InGaN theoretically has the potential to emit light spanning from blue to red. To reach long wavelengths one can decide either to increase indium content or to widen the QWs. But several issues limit the efficiency in the long wavelength range.

QCSE One of the most evident reasons is the presence of the QCSE as most LEDs are grown along the c-axis. As described in chapter 1 (see 1.3.3), the piezoelectric field separates electron and holes wavefunctions leading to reduced radiative recombination rate in the QW. The phenomenon is amplified for the high In contents needed to reach long wavelengths and if the well is widenned [46]. Fig. 2.17 illustrates this issue. For a fixed emission wavelength of 570 nm, the well thickness needed is plotted versus the indium content. The corresponding overlap of electron and hole wavefunctions shows a strong

decrease with the increasing well thickness.
The QCSE also has the beneficial effect to red-shift the emission for small injection currents but because of carrier screening, emission blue-shifts back for larger injection currents. This unstability of emission wavelength is very damaging for applications like white light emission. It may be avoided by growing rather thin wells (<3nm). Increasing the In content rather than thickenning the well will be prioritized as a solution to reach long wavelength throughout this thesis as this choice is the best to avoid too much impact of the QCSE (both on the emission wavelength and on the efficiency).

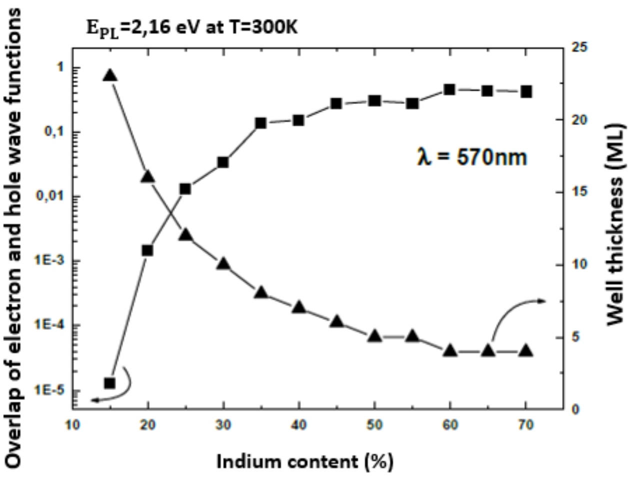

FIGURE 2.17 – Overlap of electron and hole wavefunction and well thicknesses (in monolayers) as a function of In content for a fixed emission wavelength of 570 nm from [45].

Defects The lattice mismatch between the GaN buffer and InGaN QWs increases with indium content. The resulting strain is responsible for the compostionnal pulling effect as detailed in chapter 1 (1.3.4.2). The difficulty in incorporating indium in the alloy compels for a growth at lower temperature to reduce In evaporation rate. Lowering the growth temperature reduces the structural quality of the grown InGaN layer resulting in a lower thermal stability. The lower growth temperature together with the biaxial strain triggers the emergence of more defects. Koleske *et al.* showed that the incorporation of impurities is increased at lower MOVPE growth temperature [47] and the multiplication of defects is known to decrease the IQE [48]. The dissociation of ammonia also becomes more difficult (see section 1.2.2.1). It is possible that this leads to an increase of the vacancies as the stagnating indium atoms at the surface may not find enough nitrogen atoms to be bound to. This would result in a lower In incorporation.
Along with these issues, we can mention the effect of surface segregation of indium in the QWs. Because of its delayed incorporation and the diffusion of atoms in the barriers, the

indium content profile deviates from the ideal rectangle shape (see section 1.3.4.2). As a consequence, the emission is blue shifted and the radiative recombination rate is lowered. This effect is expected to grow stronger as indium concentration is increased (*i.e.* when going towards long wavelengths).

The density of dislocations and V-pits is also increased with the strain leading to a decreased nonradiative liftetime [49]. Indeed, dislocations have been identified as nonradiative recombination centers in GaN [50] and in InGaN [51]. Very high dislocation densities are reported in InGaN-based LEDs (in the $10^8 cm^{-3}$ range) with most of the dislocations already present in the substrate.

However, unlike what happens in other materials (GaAs) InGaN-based LEDs still show very good radiative recombination efficiencies [52]. This peculiarity has been tentatively explained by several groups. The short diffusion lengths (<250 nm according to Rosner *et al*) preventing the carriers to diffuse to dislocations are thought to be induced by the carrier localization in In-rich clusters [53] or by well width fluctuations [54]. Hangleiter *et al.* suggest two other explanations. The binding of electron and holes into free excitons is estimated to be the decisive factor [55]. As the free exciton binding energy increases, the efficiency is improved. The second explanation proposed is that a potential barrier exists around the V-pits, therefore screening the defect and preventing the carriers to recombine nonradiatively [56]. A detailed microscopy study was lead by Massabuau *et al.* [57] who explain the screening of the V-pits by a localization of the carriers in the vicinity of the dislocations through the enhanced formation of In-N chains and atomic condensates. The beneficial aspect of V-pits is reported in the case of blue QWs [58] but refuted in the case of green-based LEDs that exhibit better performance when such defects are concealed [59]. According to the authors, avoiding V-pit generation becomes crucial when trying to reach longer wavelengths. Another study by Wetzel *et al.* [60] reveals the dependance of the EL emission of green LEDs with three different densities of V-pits. The highest performance is obtained for the lowest number of V-pits.

EQE droop In InGaN-based LEDs, the peak in EQE occurs for very low injection currents, followed by an important decrease in EQE as the carrier injection is increased. The phenomenon called the droop is already an important efficiency limitation in blue LEDs [61]. Yet this trend appears to be emphasised in green LEDs [62], [63]. This might be explained by the higher potential disorder (due to thickness or indium concentration variations) that is expected to enhance Auger recombination [64]. Furthermore, the maximum is shifted towards lower currents for the green compared to the blue [65]. The origin of the droop is still under investigation but the main theories incriminate Auger recombinations [66], electron leakage and hole injection [67]. Liu *et al.* [68] proposed to explain the increase of the droop for green LEDs by the higher piezoelectric field, leading to an enhanced carrier leakage but the phenomenon has not been thoroughly studied.

Other In 2016 Auf der Maur *et al.* [42] provide an additional explanation to the green gap based on atomistic simulations. According to them, a consistent part of the EQE drop at long wavelengths may be explained by random alloy fluctuations that are responsible for a decrease of the radiative recombination coefficient B (for more explanations on the ABC model refer to [69] for a recent review).

Many solutions have been proposed to overcome the green gap problem. The following section reviews them.

2.2.2 Solving the green gap

Phosphor-converted green LED An approach in realizing green LEDs while circumventing the green gap problems is to combine a blue LED with green-emitting phosphors. Several types of phosphors may be considered [44]. Using a ceramic platelet of the green phosphor lutetium aluminum garnet (LuAG), OSRAM manufactured a very efficient green LED (191 lm/W at 350 mA to compare to 135 lm/W for the direct approach) [70]. Fig. 2.18 gives the emission spectra for their direct green LED and the phosphor-converted LED. The emission profile is very different with a broader peak in the converted approach. The FWHM goes from 33 nm to 99 nm. Having a broad emission is useful for some applications (including white light emission with three RGB LEDs as detailed in 2.1.2.3), but a poor color purity is also related to a poor efficiency. In addition, the problems associated to this solution are the same as the ones mentionned for phosphor-based white LEDs including the Stokes shift.

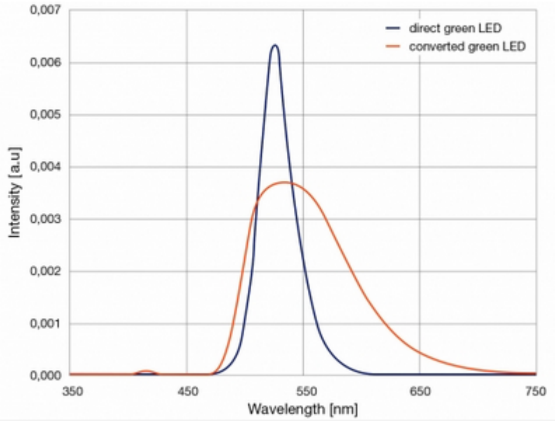

FIGURE 2.18 – Emission spectra of direct InGaN-based LED and a phosphor-converted green LED from OSRAM [70].

Non-polar or Semi-polar orientations The detrimental influence of the piezoelectric field may be supressed or lowered by using non-polar or semi-polar orientations instead of the usual polar orientation along the *c*-axis. Because of the lowering of the

QCSE, this solution will enhance the overlap of wavefunctions thus improving the radiative recombination rate. What's more, the stability of the emission wavelength with current density is improved [71] [72]. Romanov *et al.* [73] studied the impact of the angle to the *c*-axis on the polarization difference between InGaN and GaN for InGaN/GaN QWs (Fig. 2.19). The polarization reaches its maximum along the *c*-axis and is lowered elsewhere and even canceled at an angle of 45 degrees and 90 degrees.

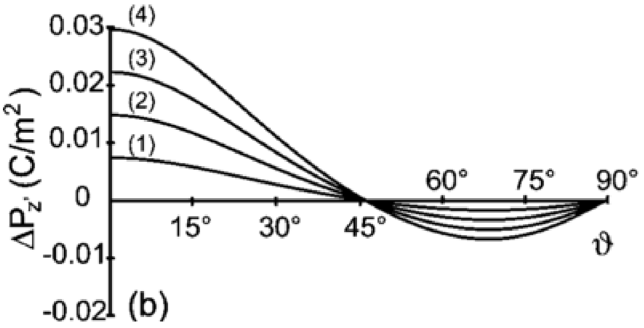

FIGURE 2.19 – Difference ΔP_z of the total polarization at the interface of $In_xGa_{1-x}N/GaN$ QWs as a function of the *c*-axis angle for different indium contents (1) x=0.1, (2) x=0.2, (3) x=0.3, (4) x=0.4 from [73].

However, the orientation has to be chosen carefully because indium incorporates differently on the semi-polar planes. An extensive study conducted by Wernicke *et al.* on several orientations reveal this dependence. $In_{0.15}Ga_{0.85}N/InGaN$ MQWs were grown on various substrates. Fig. 2.20 (a) plots the electric field for the different orientations and Fig. 2.20 (b) gives the indium content of the QWs as a function of growth temperature. Among the ones considered, the $\{10\bar{1}1\}$, $\{11\bar{2}2\}$ orientations are the most favourable for indium incorporation.

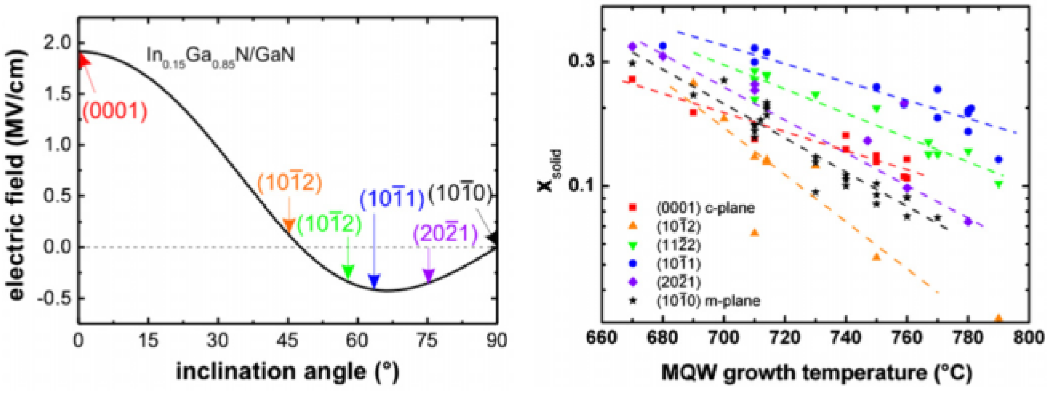

(a) (b)

FIGURE 2.20 – Calculated polarization fields along the different growth directions for $In_{0.15}Ga_{0.85}N$ QWs with a nominal thickness of 3.5 nm (a) Extracted indium mole fraction for the $In_{0.15}Ga_{0.85}N$ QWs from [74].

The University of California, Santa Barbara (UCSB) carried out the growth of LEDs on several orientations with great success over a wide wavelength range. EQEs of 20% at 516 nm and 12% at 552 nm were achieved on $\{20\bar{2}1\}$ plane [75]. On $\{11\bar{2}2\}$ orientation, an EQE of 13.4 % was reached at 563 nm [76]. Studies were also lead on $\{20\bar{2}\bar{1}\}$ orientation with a demonstration of EQE of 50 % in the blue. This orientation demonstrated particularly good characteristics with reduced linewidths (attributed to small potential fluctuations) and reduced efficiency droop [77]. These excellent external quantum efficiencies demonstrated in the green/yellow range compete and sometimes exceed the ones obtained for *c*-axis orientation.

Even with the use of non-polar and semi-polar orientation, a decrease of EQE with wavelength emission is observed [78], [79]. For the implementation of non-polar and semi-polar LEDs, the subject of the substrates is critical. Although the first available substrates showed very high densities of defects propagating into the grown layers [80], recent progress has been made with the commercialization of free standing *m*-plane substrates [72] and $\{20\bar{2}1\}$-plane substrates with very low defect densities [81]. Yet, a larger scaling of the substrates is still necessary for the commercialization of such LEDs. The development of defect free substrates implies complicated processes. Significant improvment of the performance of these devices compared to *c*-axis devices has to be done in order to justify the additional cost of such substrates [80].

AlGaN InterLayers (IL) in the active region In order to reduce the compressive strain in the InGaN QWs, a structure employing AlGaN interlayers (IL) in the barriers (or immediatly adjacent to the QW) has been proposed. Fig. 2.21 displays the TEM image of the active region of such an LED [82].

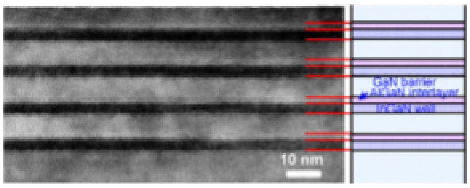

FIGURE 2.21 – Cross-sectional TEM image of InGaN/GaN MQWs employing $Al_{0.3}Ga_{0.7}N$ interlayers (left) and a schematic of the structure (right) from [82].

An increase of IQE has been obtained as compared to a conventional structure [83]. This increase in IQE has been attributed to a compensation of the compressive strain, improving the smoothness of the surface and material quality. AlGaN interlayers are also responsible for a reduction of indium content fluctuations and avoid the generation of new dislocations. Doi *et al.* observed an enhancement in indium incorporation probably due to a reduced pulling effect [84]. The implementation of AlGaN interlayers also improves carrier confinement inside the wells and facilitates the overlap of electron and hole wavefunctions as illustrated in Fig. 2.22. Although this characteristic has a positive impact on radiative recomninations, carrier transportation becomes difficult. Therefore even if quite goods EQEs are reached, Wall-Plug Efficiencies (WPE) may not be very good because of the high operating voltage necessary to power these LEDs.

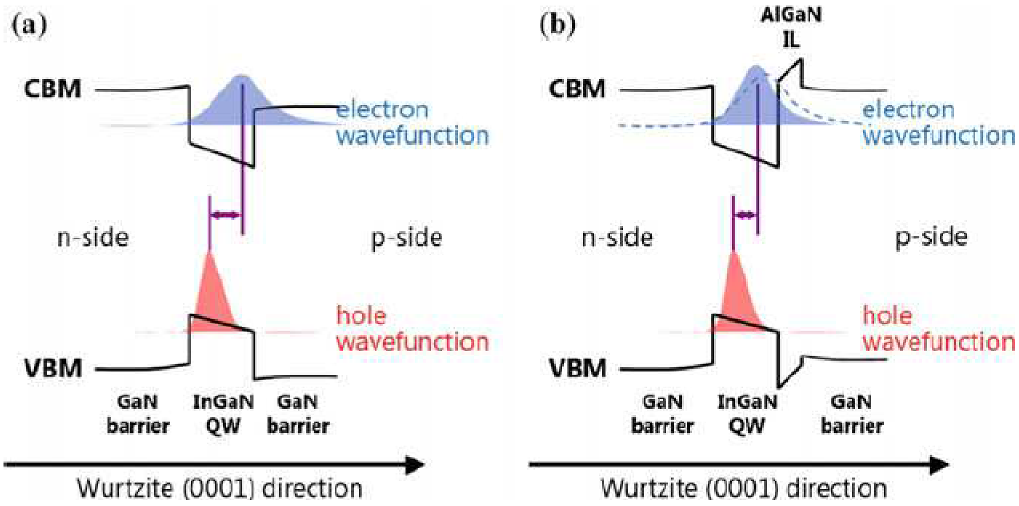

FIGURE 2.22 – Band diagram of an InGaN QW and QB layer (a) grown on a (0001) polar surface, and (b) in the case of an AlGaN IL embedded on the (0001) side of a QW from [85].

Thanks to this technique, Toshiba achieved very high efficiencies in the green, yellow and red range. For the first attempts, an EQE of 25.3 % at 532 nm was obtained [82]. Next the architecture yielded peak EQEs of 24.7 % at 559 nm and 13.3 % at 576 nm [86]. Finally a very encouraging efficiency of 2.9 % was reached in the red range at 629 nm [87].

Prestrained layers Alternatively to the AlGaN interlayers approach, the use of an InGaN underlying (UL) layer or an InGaN/GaN superlattice (SL) under the active region (structure illustrated in Fig. 2.23) may be used to improve efficiency at longer wavelengths. Many groups reported an enhancement of PL, EL or IQE and a decrease of radiative carrier lifetime using InGaN underlayer ([88],[89],[90],[91], [92], [93], [94]) or superlattice ([95], [96], [94], [97]).

In several cases the improvements in the emission were associated with a V-pit reduction (or TD (Threading Dislocation) ([90], [92], [95],) and a decrease in the FWHM of the PL or EL peaks. In the case of InGaN/GaN SL, the reasons for the improvment of PL emission are not clear yet. The alternance of InGaN and GaN layer in the SL is believed to form a good barrier to prevent impurities to enter the active region. The implementation of an InGaN/GaN SL under the QWs helped to achieve EQEs between 8 and 20 % in the deep green between 530 and 560 nm as demonstrated by Lundin *et al.* [97]. In Fig. 2.23 is the TEM image showing the structure of the active region of these LEDs.

The usefulness of InGaN layer is better documented. The partial relaxation is thought to

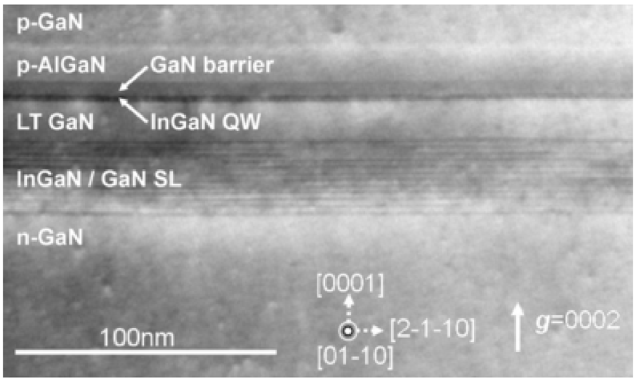

FIGURE 2.23 – TEM image of the active region of the green LED from [97].

be at the origin of the gain in efficiency as evidenced by Li *et al.* [89]. The PL blue shift they observe compared to the conventional structure was explained by a weaker internal electric field as measured by electron holography. However, the InGaN UL does not always induce relaxation so another phenomenon might be at work. In chapter 3, we will detail our different hypotheses.

Other approaches An original approach was developped by Nishikawa *et al.* [98]. A red emission at 620 nm is obtained with an MOVPE grown structure using GaN doped with europium (Eu) as the active layer. Long wavelength emission up to 610 nm was realized by Park *et al.* [99] with self-assembled QDs in an InGaN active layer. The QD In composition is controlled by managing the roughness of the n-GaN layer.
In the last years, approaches relying on 3D growth have been implemented. The benefits of such structures include reduced strain [100], improved light extraction efficiencies, reduced dislocation densities and lowered piezoelectric fields thanks to the growth on semi-polar or non-polar surfaces. Hong *et al.* [101] reported on the growth of color tunable LEDs in the visible range (479 to 632 nm) using InGaN/GaN in nanorod arrays. Using core/multishell nanowires, emission from 365 to 600 nm was achieved [102]. An EQE of 3.9 % was reached at 540 nm. More recently, Ra *et al.* [103] demonstrated emission wavelengths from 450 to 640 nm by varying the diameter of the dot-in-wire nanowires. However, nanowires often deliver relatively broad emission spectra which can be detrimental for some applications [79]. Moreover, reducing the processing cost of LEDs based on nanowires still remains a challenge. Furthermore, the efficiency is still lower than 2D approaches even for blue emission wavelengths. This approach also requires a great homogeneity between the different nanowires.

2.2.3 Our approach to bridge the green gap

Our approach to reach long wavelengths with III-N is to decrease the compressive strain imposed to the active region by the substrate. To reduce the strain in the most effective way in a 2D structure, using a substrate with an a lattice parameter as close as possible to the one of the InGaN QWs appears as the best solution. Indeed, various simulation studies of InGaN/InGaN QWs grown on ternary InGaN substrates showed the positive contribution that such substrates combined with the use of InGaN barriers would have on long-wavelength emitting LEDs [104], [105], [106]. The strain reduction and the consequent lowering of the internal eletric field are shown to lead to an increase in radiative recombination rate. The droop should also be reduced and a better stability of the wavelength emission achieved.

Using such substrate would also reduce the compositional pulling effect, therefore allowing for a higher In incorporation in the InGaN QWs [107], [108] for the same growth temperature. Fig. 2.24 gives the solid indium composition that can be expected for growth on GaN Free Standing (FS) (relaxed GaN) (red), on $In_{0.2}Ga_{0.8}N$ (blue) and on bulk (unstrained) (black) as a function of growth temperature and for different indium partial pressures. In all cases, the growth on $In_{0.2}Ga_{0.8}N$ or on bulk allows a larger indium incorporation as compared to GaN. However, InGaN bulk substrates are not available due to the difficulty in growing thick InGaN layers of good material quality even with small indium contents [109] as presented in chapter 1.

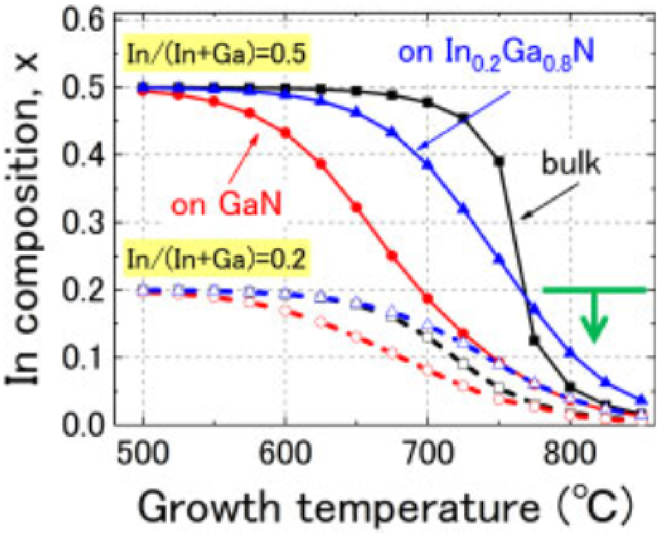

FIGURE 2.24 – Solid composition as a function of growth temperature. The In/(In+Ga) ratio is the ratio of partial pressures. The carrier gas is N_2. From [107].

2.2.3.1 Previous attempts

Recently, several attempts for the realization of such substrates were carried out. Ohata *et al* demonstrated the growth of N-polar InGaN layer by MOVPE at high growth rates (up to 2 µm/h) on previoulsy deposited sputtered InGaN layer on sapphire [110]. Still on the N-polar face, thick InGaN layers (10 μm) with a mole fraction of 0.05 were obtained using tri-halide vapor phase epitaxy on N-polar GaN [111] grown at a very high growth rate (15 μm/h). In 2012, Koslow *et al.* successfully grew green emitting MQWs (525-575 nm) by MOVPE in the $\{11\bar{2}2\}$ direction on a partially relaxed InGaN buffer layer. The stress relaxation was achieved through the formation of misfit dislocations which remained confined at the bottom of the InGaN buffer layer. Thanks to a technique using surface droplet elimination during MBE process, thick InGaN layers over a wide range of composition (between 20 and 70%) were successfully grown [112]. Hestroffer *et al.* achieved the growth of 500 nm-thick $In_{0.1}Ga_{0.9}N$ grown on a graded InGaN layer (with an indium composition gradually varied from 0 to 10%)by PAMBE [113]. Despite the great number of Threading Dislocations (TDs), the relaxed InGaN film showed a rather smooth surface. An interesting approach is the one using strain counterbalanced GaN interlayers in an InGaN buffer layer used by Pantzas *et al.* [114] and Van den Broeck *et al.* [115]. Using this technique combined with a linearly graded buffer layer IQE values were doubled for InGaN/GaN MQWs in the green range as compared to reference samples grown on GaN on sapphire [116]. Xue *et al.* grew an InGaN p-i-n structure by plasma-assisted MBE and reached an indium content of 62 % in the 1200 nm thick n-InGaN region [117]. To achieve such a high indium mole fraction the structure was grown on an 800 nm-thick InGaN template. The propagation of dislocations was prevented thanks to a nanosculpting process at InGaN/GaN interface.

The strategy based on epitaxial lateral overgrowth (ELO) has been successfully applied to GaN to produce thick relaxed layers with low dislocation densities. The technique has also been tested for InGaN layers [118]. A partially relaxed $In_{0.18}Ga_{0.82}N$ layer was successfully grown on *m*-plane GaN with a low dislocation density of $1 \times 10^8 cm^{-2}$. Later on, green emitting InGaN/GaN MQWs with a wavelength emission of 535 nm were grown on such layer [119].

ZnO, which is lattice matched to $In_{0.18}Ga_{0.82}N$ appears as a good alternative candidate. Nonetheless, one issue is the thermal incompatibility of the two materials because Zn0 deteriorates at the temperatures used for InGaN MOVPE growth. By using *m*-plane ZnO with better resistance to temperature and Pulsed Layer Deposition (PLD) for a lower InGaN growth temperature, a good quality $In_{0.25}Ga_{0.75}N$ layer was obtained [120]. However, the process is complicated and does not allow for growth using the same technique for the whole structure. Although some of these attempts gave interesting results, none of them present epi-ready (which do not require additional treatment steps prior to the growth in the MOVPE reactor) reliable solutions.

2.2.3.2 Our solution

Soitec has recently worked on the implementation of such InGaN substrates, originally with the objective to reduce the droop for blue LEDs. They achieved the fabrication of partially relaxed epi-ready InGaN pseudo-substrates called InGaNOS that we will later use in this thesis (presented in chapter 4).
The LED structure that is considered for long wavelength emission is pictured in Fig. 2.25 (b) next to the regular LED structure (Fig. 2.25 (a)). For this full InGaN structure, we propose to combine the InGaN pseudo-substrate with the use of InGaN barriers. The p-layer will be composed of GaN or InGaN with an indium mole fraction smaller than the one used for the barriers. As mentionned above, a release of strain in the active region is expected thanks to the use of the InGaN substrate. Consequently, the compositional pulling effect should be reduced. Compared to a growth on regular GaN template, this will allow for a higher growth temperature while keeping the same indium content, thus reducing the defects related to growth at low temperatures. Secondly, we should be able to go beyond the limitation in indium incorporation observed on GaN template (around 25 %). The strain reduction (in the InGaN QWs and in the InGaN barriers) should also lower the internal electric field and therefore improve the efficiency of the device compared to a regular device (Fig. 2.25 (a)) of same emission wavelength. The use of InGaN barriers is also expected to maximize the efficiency thanks to a better carrier distribution and a further reduction of the piezoelectric effect (for detailed explanation see 2.1.3).

(a) (b)

Figure 2.25 – LED reference structure (a) and LED structure using relaxed InGaN substrate for long wavelength emission (b).

This structure may later be used for the realization of high efficiency white monolithic LEDs. Indeed, thanks to this structure, we should achieve good efficiency for the long-wavelength wells (green, yellow or red) and be able to control the final color of the emission by a fine tuning of the indium content in the barriers.

Conclusion

A rapid overview of the different techniques to produce white light was given with a focus on the solutions using LEDs. The white monolithic case was particularly detailed. We showed the advantages and problems associated with such structures. The simulation study showed that employing InGaN barriers allowed for a fine tuning of the desired color of the emission. Nevertheless, the small efficiency of the QWs in the green and red still impede the implementation of such solution.

We analyzed the reasons for the low efficiency of InGaN-based LEDs in the long wavelength range. The accumulated strain in the structure and the presence of strong internal electric fields are responsible as the wells need to be widened or their indium contents need to be increased to red-shift the emission. Furthermore, this strain hampers the incorporation of indium in the QWs. After reviewing the solutions implemented to circumvent these limitations, we presented the one used during this thesis. We suggested to tackle the question by reducing the strain in the overall structure. For that purpose, we proposed to grow a full InGaN structure on an InGaN pseudo-substrate manufactured by Soitec, called InGaNOS. Before enforcing that solution, we will study the limitations of LEDs grown on GaN template by using different techniques to increase the emission wavelength.

References of chapter 2

[1] E. F. Schubert. *Light-Emitting Diodes.* Cambridge University Press, 2nd edn. (2006).

[2] J. Cho, J. H. Park, J. K. Kim and E. F. Schubert. *Laser Photonics Rev.* **11**, 1600147 (2017).

[3] I. L. Azevedo, M. G. Morgan and F. Morgan. *Proc. of the IEEE* **97**, 481 (2009).

[4] DOE. Energy Savings Forecast of Solid- State Lighting in General Illumination Applications. Tech. rep., US Department of Energy (2014).

[5] S. Nakamura, T. Mukai and M. Senoh. *Appl. Phy. Lett.* **64**, 1687 (1994).

[6] K. Bando, K. Sakano, Y. Noguchi and Y. Shimizu. *J.of Light & Visual Evt* **22**, 2 (1998).

[7] Y. Narukawa, M. Ichikawa, D. Sanga, M. Sano and T. Mukai. *J. Phys. D Appl. Phys.* **43**, 354002 (2010).

[8] E. Taylor, P. R. Edwards and R. W. Martin. *Phys. Status Solidi A* **209**, 461 (2012).

[9] G. Meneghesso, M. Meneghini and E. Zanoni. *J. Phys. D Appl. Phys.* **43**, 354007 (2010).

[10] M. Meneghini, L. Trevisanello, S. Podda, S. Buso, G. Spiazzi, G. Meneghesso and E. Zanoni. *Proc. SPIE* **6337**, R3370 (2006).

[11] E. Radkov, A. Setlur, Z. Brown and J. Reginelli. *Proc. SPIE* **5530**, 260 (2004).

[12] Y. Muramoto, M. Kimura and S. Nouda. *Semicond. Sci. Tech.* **29**, 084004 (2015).

[13] J. Stinson. US Patent 4,992,704 (1991).

[14] S. Chhajed, Y. Xi, Y. L. Li, T. Gessmann and E. F. Schubert. *J. Appl. Phys.* **97**, 054506 (2005).

[15] R. Haitz and J. Y. Tsao. *Phys. Status Solidi A* **208**, 17 (2011).

[16] S. Reineke, F. Lindner, G. Schwartz, N. Seidler, K. Walzer, B. Lüssem and K. Leo. *Nature* **459**, 234 (2009).

[17] Y. Xu, J. Peng, J. Jiang, W. Xu, W. Yang and Y. Cao. *Appl. Phy. Lett.* **87**, 1 (2005).

[18] N. Thejokalyani and S. J. Dhoble. *Renew. Sust. Energ. Rev.* **32**, 448 (2014).

[19] K. T. Kamtekar, A. P. Monkman and M. R. Bryce. *Adv. Mater.* **22**, 572 (2010).

[20] B. Damilano, N. Grandjean, S. Vézian and J. Massies. *J. Cryst. Growth* **228**, 466 (2001).

[21] H. Y. Ryu. *J. Korean Phys. Soc.* **56**, 1256 (2010).

[22] J. H. Zhu, S. M. Zhang, H. Wang, D. G. Zhao, J. J. Zhu, Z. S. Liu, D. S. Jiang, Y. X. Qiu and H. Yang. *J. Appl. Phys.* **109**, 10 (2011).

[23] S. Dalmasso, B. Damilano, C. Pernot, A. Dussaigne, D. Byrne, N. Grandjean, M. Leroux and J. Massies. *Phys. Status Solidi A* **192**, 139 (2002).

[24] A. Dussaigne, J. Brault, B. Damilano and J. Massies. *Phys. Status Solidi C* **4**, 57 (2007).

[25] M. Yamada, Y. Narukawa and T. Mukai. *Jpn. J. Appl. Phy.* **41**, 246 (2002).

[26] I. K. Park, J. Y. Kim, M. K. Kwon, C. Y. Cho, J. H. Lim and S. J. Park. *Appl. Phy. Lett.* **92**, 11 (2008).

[27] S.-H. Lim, Y.-H. Ko, C. Rodriguez, S.-H. Gong and Y.-H. Cho. *Light : Science & Applications* **5**, e16030 (2016).

[28] K. M. Song, D.-h. Kim, J.-m. Kim, C.-y. Cho, J. Choi, K. Kim, J. Park and H. Kim. *Nanotechnology* **28**, 225703 (2017).

[29] S. J. Kowsz, C. D. Pynn, S. H. Oh, R. M. Farrell, S. P. DenBaars and S. Nakamura. *J. Appl. Phys.* **120**, 033102 (2016).

[30] B. Damilano, A. Dussaigne, J. Brault, T. Huault, F. Natali, P. Demolon, P. De Mierry, S. Chenot and J. Massies. *Appl. Phy. Lett.* **93**, 101117 (2008).

[31] C. F. Lu, C. F. Huang, Y. S. Chen, W. Y. Shiao, C. Y. Chen, Y. C. Lu and C. C. Yang. *IEEE J. Sel. Top. Quantum Elect.* **15**, 1210 (2009).

[32] D. Yang, L. Wang, W.-B. Lv, Z.-B. Hao and Y. Luo. *Superlattice Microstruct.* **82**, 26 (2015).

[33] C. B. Soh, W. Liu, S. J. Chua, J. H. Teng, R. J. N. Tan and S. S. Ang. *Phys. Status Solidi C* **6**, 519 (2009).

[34] C. H. Chen, S. J. Chang, Y. K. Su, J. K. Sheu, J. F. Chen, C. H. Kuo and Y. C. Lin. *IEEE Photonic Tech. L.* **14**, 908 (2002).

[35] J. K. Sheu, C. J. Pan, G. C. Chi, C. H. Kuo, L. W. Wu, C. H. Chen, S. J. Chang and Y. K. Su. *IEEE Photonic Tech. L.* **14**, 450 (2002).

[36] Y. Huang, F. Yun, Y. Li, W. Ding, Y. Wang, H. Wang, W. Zhang, Y. Zhang, M. Guo, S. Liu and X. Hou. *Appl. Phy. Express* **7**, 102102 (2014).

[37] N. Ben Sedrine, T. C. Esteves, J. Rodrigues, L. Rino, M. R. Correia, M. C. Sequeira, a. J. Neves, E. Alves, M. Bockowski, P. R. Edwards, K. P. O'Donnell, K. Lorenz and T. Monteiro. *Sci. Rep.* **5**, 13739 (2015).

[38] X. H. Wang, H. Q. Jia, L. W. Guo, Z. G. Xing, Y. Wang, X. J. Pei, J. M. Zhou and H. Chen. *Appl. Phy. Lett.* **91**, 23 (2007).

[39] Y. K. Kuo, J. Y. Chang, M. C. Tsai and S. H. Yen. *Appl. Phy. Lett.* **95**, 2012 (2009).

[40] I. C. Robin. Light emitting diode with multiple quantum well and asymetric p-n junction (2014).

[41] M. Broell, P. Sundgren, A. Rudolph, W. Schmid, A. Vogl and M. Behringer. *Proc. SPIE* **9003**, 90030L (2014).

[42] M. Auf der Maur, A. Pecchia, G. Penazzi, W. Rodrigues and A. Di Carlo. *Phys. Rev. Let.* **116**, 027401 (2016).

[43] K. A. Bulashevich, A. V. Kulik and S. Y. Karpov. *Phy* **212**, 914 (2015).

[44] J. M. Phillips, M. E. Coltrin, M. H. Crawford, A. J. Fischer, M. R. Krames, R. Mueller-Mach, G. O. Mueller, Y. Ohno, L. E. S. Rohwer, J. A. Simmons and J. Y. Tsao. *Laser Photonics Rev.* **1**, 307 (2007).

[45] A. Dussaigne. *Diodes électroluminescentes blanches monolithiques*. Ph.D. thesis, Université de Nice-Sophia Antipolis (2005).

[46] J. Seo Im, H. Kollmer, J. Off, A. Sohmer, F. Scholz and A. Hangleiter. *Phys. Rev. B* **57**, R9435 (1998).

[47] D. D. Koleske, A. E. Wickenden, R. L. Henry and M. E. Twigg. *J. Cryst. Growth* **242**, 55 (2002).

[48] A. M. Armstrong, M. H. Crawford and D. D. Koleske. *Appl. Phy. Express* **7**, 032101 (2014).

[49] T. Langer, H. Jönen, A. Kruse, H. Bremers, U. Rossow and A. Hangleiter. *Appl. Phy. Lett.* **103**, 022108 (2013).

[50] S. J. Rosner, E. C. Carr, M. J. Ludowise, G. Girolami and H. I. Erikson. *Appl. Phy. Lett.* **70**, 420 (1997).

[51] T. Sugahara, M. Hao, T. Wang, D. Nakagawa, Y. Naoi, K. Nishino and S. Sakai. *Jpn. J. Appl. Phy.* **37**, 1195 (1998).

[52] S. D. Lester, F. A. Ponce, M. G. Craford and D. A. Steigerwald. *Appl. Phy. Lett.* **66**, 1249 (1995).

[53] G. B. Stringfellow. *J. Cryst. Growth* **312**, 735 (2010).

[54] C. J. Humphreys. *Philos. Mag.* **87**, 1971 (2007).

[55] A. Hangleiter, D. Fuhrmann, M. Grewe, F. Hitzel, G. Klewer, S. Lahmann, C. Netzel, N. Riedel and U. Rossow. *Phys. Status Solidi A* **201**, 2808 (2004).

[56] A. Hangleiter, F. Hitzel, C. Netzel, D. Fuhrmann, U. Rossow, G. Ade and P. Hinze. *Phys. Rev. Let.* **95**, 1 (2005).

[57] F. C. P. Massabuau, P. Chen, M. K. Horton, S. L. Rhode, C. X. Ren, T. J. O'Hanlon, A. Kovacs, M. J. Kappers, C. J. Humphreys, R. E. Dunin-Borkowski and R. A. Oliver. *J. Appl. Phys.* **121**, 013104 (2017).

[58] H. Takahashi, A. Ito, T. Tanaka, A. Watanabe, H. Ota and K. Chikuma. *Jpn. J. Appl. Phy.* **39**, 569 (2000).

[59] T. Detchprohm, M. Zhu, W. Zhao, Y. Wang, Y. Li, Y. Xia and C. Wetzel. *Phys. Status Solidi C* **6**, S840 (2009).

[60] C. Wetzel, T. Salagaj, T. Detchprohm, P. Li and J. S. Nelson. *Appl. Phy. Lett.* **85**, 866 (2004).

[61] J. Piprek. *Phys. Status Solidi A* **207**, 2217 (2010).

[62] L. Wang, X. Meng, J. Wang, Z. Hao, Y. Luo, C. Sun, Y. Han, B. Xiong, J. Wang and H. Li. *Appl. Phy. Lett.* **97**, 201112 (2010).

[63] M. H. Crawford. *IEEE J. Sel. Top. Quantum Elect.* **15**, 1028 (2009).

[64] M. Shahmohammadi, W. Liu, G. Rossbach, L. Lahourcade, A. Dussaigne, C. Bougerol, R. Butté, N. Grandjean, B. Deveaud and G. Jacopin. *Phys. Rev. B* **95**, 125314 (2017).

[65] M. Peter, A. Laubsch, W. Bergbauer, T. Meyer, M. Sabathil, J. Baur and B. Hahn. *Phys. Status Solidi A* **206**, 1125 (2009).

[66] Y. C. Shen, G. O. Mueller, S. Watanabe, N. F. Gardner, A. Munkholm and M. R. Krames. *Appl. Phy. Lett.* **91** (2007).

[67] M. F. Schubert, S. Chhajed, J. K. Kim, E. F. Schubert, D. D. Koleske, M. H. Crawford, S. R. Lee, A. J. Fischer, G. Thaler and M. A. Banas. *Appl. Phy. Lett.* **91**, 231114 (2007).

[68] J.-L. Liu, J.-L. Zhang, G.-X. Wang, C.-L. Mo, L.-Q. Xu, J. Ding, Z.-J. Quan, X.-L. Wang, S. Pan, C.-D. Zheng, X.-M. Wu, W.-Q. Fang and F.-Y. Jiang. *Chin. Phys. B* **24**, 067804 (2015).

[69] S. Karpov. *Nusod 2014* 17 – 18 (2014).

[70] A. Laffler and M. Binder. *Compound semiconductors* (2013).

[71] J. H. Ryou, P. D. Yoder, J. Liu, Z. Lochner, H. S. Kim, S. Choi, H. J. Kim and R. D. Dupuis. *IEEE J. Sel. Top. Quantum Elect.* **15**, 1080 (2009).

[72] K. C. Kim, M. C. Schmidt, H. Sato, F. Wu, N. Fellows, M. Saito, K. Fujito, J. S. Speck, S. Nakamura and S. P. DenBaars. *Phys. Status Solidi Rapid Res. Lett.* **1**, 125 (2007).

[73] A. E. Romanov, T. J. Baker, S. Nakamura and J. S. Speck. *J. Appl. Phys.* **100**, 023522 (2006).

[74] T. Wernicke, L. Schade, C. Netzel, J. Rass, V. Hoffman, S. Ploch, A. Knauer, M. Weyers, U. Schwarz and M. Kneissl. *Semicond. Sci. Tech.* **27**, 024014 (2012).

[75] S. Yamamoto, Y. Zhao, C. C. Pan, R. B. Chung, K. Fujito, J. Sonoda, S. P. DenBaars and S. Nakamura. *Appl. Phy. Express* **3** (2010).

[76] H. Sato, R. B. Chung, H. Hirasawa, N. Fellows, H. Masui, F. Wu, M. Saito, K. Fujito, J. S. Speck, S. P. DenBaars and S. Nakamura. *Appl. Phy. Lett.* **92**, 221110 (2008).

[77] C. C. Pan, S. Tanaka, F. Wu, Y. Zhao, J. S. Speck, S. Nakamura, S. P. Den Baars and D. Feezel. *Appl. Phy. Express* **5** (2012).

[78] H. Yamada, K. Iso, M. Saito, H. Masui, K. Fujito, S. P. DenBaars and S. Nakamura. *Appl. Phy. Express* **1**, 041101 (2008).

[79] M. H. Crawford, J. J. Wierer, A. J. Fischer, G. T. Wang, D. D. Koleske, G. S. Subramania, M. E. Coltrin, R. F. Karlicek and J. Y. Tsao. *Solid-state lighting : toward smart and ultraefficient material, devices, lamps and systems*, vol. III. John Wiley & Sons (2015).

[80] P. Vennéguès. *Semicond. Sci. Tech.* **27**, 024004 (2012).

[81] R. M. Farrell, E. C. Young, F. Wu, S. P. DenBaars and J. S. Speck. *Semicond. Sci. Tech.* **27**, 024001 (2012).

[82] T. Shioda, H. Yoshida, K. Tachibana, N. Sugiyama and S. Nunoue. *Phys. Status Solidi A* **209**, 473 (2012).

[83] T. H. Ngo, B. Gil, P. Valvin, B. Damilano, K. Lekhal and P. De Mierry. *Appl. Phy. Lett.* **107**, 122103 (2015).

[84] T. Doi, Y. Honda, M. Yamaguchi and H. Amano. *Jpn. J. Appl. Phy.* **52**, 08JB14 (2013).

[85] T. Y. Seong, J. Han, H. Amano and H. Morkoç. *III-Nitride based Light-Emitting Diodes and Applications.* Springer (2017).

[86] S. Saito, R. Hashimoto, J. Hwang and S. Nunoue. *Appl. Phy. Express* **6**, 111004 (2013).

[87] J. I. Hwang, R. Hashimoto, S. Saito and S. Nunoue. *Appl. Phy. Express* **7**, 071003 (2014).

[88] M. J. Davies, F. C. P. Massabuau, P. Dawson, R. a. Oliver, M. J. Kappers and C. J. Humphreys. *Phys. Status Solidi C* **11**, 710 (2014).

[89] T. Li, Q. Y. Wei, A. M. Fischer, J. Y. Huang, Y. U. Huang, F. a. Ponce, J. P. Liu, Z. Lochner, J. H. Ryou and R. D. Dupuis. *Appl. Phy. Lett.* **102**, 10 (2013).

[90] N. Nanhui, W. Huaibing, L. Jianping, L. Naixin, X. Yanhui, H. Jun, D. Jun and S. Guangdi. *J. Cryst. Growth* **286**, 209 (2006).

[91] J. K. Son, S. N. Lee, T. Sakong, H. S. Paek, O. Nam, Y. Park, J. S. Hwang, J. Y. Kim and Y. H. Cho. *J. Cryst. Growth* **287**, 558 (2006).

[92] P. T. Törmä, O. Svensk, M. Ali, S. Suihkonen, M. Sopanen, M. a. Odnoblyudov and V. E. Bougrov. *J. Cryst. Growth* **310**, 5162 (2008).

[93] Y. Xia, W. Hou, L. Zhao, M. Zhu, T. Detchprohm and C. Wetzel. *IEEE T. Electron. Dev.* **57**, 2639 (2010).

[94] S. J. Leem, Y. C. Shin, K. C. Kim, E. H. Kim, Y. M. Sung, Y. Moon, S. M. Hwang and T. G. Kim. *J. Cryst. Growth* **311**, 103 (2008).

[95] K. Sugimoto, Y. Denpo, N. Okada and K. Tadatomo. *Phys. Status Solidi B* **13**, 270 (2016).

[96] T. Jeong, H. J. Park, J. W. Ju, H. S. Oh, J. H. Baek, J. S. Ha, G. H. Ryu and H. Y. Ryu. *IEEE Photonic Tech. L.Technology Letters* **26**, 649 (2014).

[97] W. V. Lundin, a. E. Nikolaev, a. V. Sakharov, E. E. Zavarin, G. a. Valkovskiy, M. a. Yagovkina, S. O. Usov, N. V. Kryzhanovskaya, V. S. Sizov, P. N. Brunkov, a. L. Zakgeim, a. E. Cherniakov, N. a. Cherkashin, M. J. Hytch, E. V. Yakovlev, D. S. Bazarevskiy, M. M. Rozhavskaya and a. F. Tsatsulnikov. *J. Cryst. Growth* **315**, 267 (2011).

[98] A. Nishikawa, T. Kawasaki, N. Furukawa, Y. Terai and Y. Fujiwara. *Appl. Phys. Express* **2**, 071004 (2009).

[99] I. K. Park and S. J. Park. *Appl. Phy. Express* **4** (2011).

[100] E. Ertekin, P. A. Greaney, D. C. Chrzan and T. D. Sands. *J. Appl. Phys.* **97**, 114325 (2005).

[101] Y. J. Hong, C. H. Lee, A. Yoon, M. Kim, H. K. Seong, H. J. Chung, C. Sone, Y. J. Park and G. C. Yi. *Adv. Mater.* **23**, 3284 (2011).

[102] F. Qian, S. Gradečak, Y. Li, C. Y. Wen and C. M. Lieber. *Nano Lett.* **5**, 2287 (2005).

[103] Y. H. Ra, R. Wang, S. Y. Woo, M. Djavid, S. M. Sadaf, J. Lee, G. A. Botton and Z. Mi. *Nano Lett.* **16**, 4608 (2016).

[104] J. Zhang and N. Tansu. *J. Appl. Phys.* **110**, 1 (2011).

[105] S. H. Park, T. H. Chung, J. H. Baek and D. Ahn. *Jpn. J. Appl. Phy.* **54**, 2 (2015).

[106] J. Pal, M. A. Migliorato, C. K. Li, Y. R. Wu, B. G. Crutchley, I. P. Marko and S. J. Sweeney. *J. Appl. Phys.* **114** (2013).

[107] Y. Inatomi, Y. Kangawa, T. Ito, T. Suski, Y. Kumagai, K. Kakimoto and A. Koukitu. *Jpn. J. Appl. Phy.* **56**, 078003 (2017).

[108] M. V. Durnev, A. V. Omelchenko, E. V. Yakovlev, I. Y. Evstratov and S. Y. Karpov. *Phys. Status Solidi A* **208**, 2671 (2011).

[109] K. Hiramatsu, Y. Kawaguchi, M. Shimizu, N. Sawaki, T. Zheleva, R. F. Davis, H. Tsuda, W. Taki, N. Kuwano and K. Oki. *MRS Internet J. Nitride Semicond. Res.* **2**, 1 (1997).

[110] T. Ohata, Y. Honda, M. Yamaguchi and H. Amano. *Jpn. J. Appl. Phy.* **52**, 10 (2013).

[111] T. Hirasaki, M. Eriksson, Q. T. Thieu, F. Karlsson, H. Murakami, Y. Kumagai, B. Monemar, P. O. Holtz and A. Koukitu. *J. Cryst. Growth* **456**, 145 (2016).

[112] T. Yamaguchi, N. Uematsu, T. Araki, T. Honda, E. Yoon and Y. Nanishi. *J. Cryst. Growth* **377**, 123 (2013).

[113] K. Hestroffer, F. Wu, H. Li, C. Lund, S. Keller, J. S. Speck and U. K. Mishra. *Semicond. Sci. Tech.* **30**, 105015 (2015).

[114] K. Pantzas, Y. El Gmili, J. Dickerson, S. Gautier, L. Largeau, O. Mauguin, G. Patriarche, S. Suresh, T. Moudakir, C. Bishop, A. Ahaitouf, T. Rivera, C. Tanguy, P. L. Voss and A. Ougazzaden. *J. Cryst. Growth* **370**, 57 (2013).

[115] D. Van Den Broeck, D. Bharrat, Z. Liu, N. El-Masry and S. Bedair. *J. Elect. Mater.* **44**, 4161 (2015).

[116] J. Daubler, T. Passow, R. Aidam, K. Kohler, L. Kirste, M. Kunzer and J. Wagner. *Appl. Phy. Lett.* **105**, 111111 (2014).

[117] J. J. Xue, D. J. Chen, B. Liu, H. Lu, R. Zhang, Y. D. Zheng, B. Cui, A. M. Wowchak, A. M. Dabiran, K. Xu and J. P. Zhang. *Opt. Express* **20**, 8093 (2012).

[118] M. Iwaya, A. Miura, R. Senda, T. Nagai, T. Kawashima, D. Iida, S. Kamiyama, H. Amano and I. Akasaki. *J. Cryst. Growth* **310**, 4920 (2008).

[119] R. Senda, T. Matsubara, D. Iida, M. Iwaya, S. Kamiyama, H. Amano and I. Akasaki. *Appl. Phy. Express* **2**, 061004 (2009).

[120] A. Kobayashi, J. Ohta and H. Fujioka. *J. Appl. Phys.* **99**, 1 (2006).

3

Towards greater wavelengths on GaN

This chapter presents the attempts to reach long wavelengths by growing LEDs on GaN. For this part, the substrate will be a GaN template which consists of a GaN layer with a thickness of a few microns on sapphire substrate (Al_2O_3). For this whole thesis, we limit the thickness of our quantum wells to approximately 3 nm to avoid having too high detrimental impact from the QCSE. Therefore, our only way to reach green and red wavelengths will consist in achieving high indium contents in the QWs. First, we evaluate the effect of the TMIn flux and the growth pressure for a simple MQW structure. Second, we focus on InGaN layers on GaN. We evaluate the influence of growth conditions on indium incorporation and on the structural quality of the layers. Then, MQW structures are grown and the impact of InGaN/GaN superlattice (SL) and InGaN underlayer (UL) placed beneath the active region is studied. Finally, solutions are implemented to reduce indium surface segregation at interfaces.

3.1 Limitations of the regular structure on GaN

Simple MQW structures were grown on GaN. The typical structure is presented in Fig. 3.1. The QW width is set to 3 nm for all samples.

3.1.1 Influence of TMIn flux

In order to achieve large indium content in the MQWs, the simplest solution is to increase the TMIn flux. The TMIn flux was varied gradually from 200 to 700 sccm (standard cubic centimeter per minute). The room temperature PL spectra of the samples are plotted on Fig. 3.2 (a) and the evolution of the emission wavelength as a function of the TMIn flux is given in Fig. 3.2 (b). The PL wavelength emission increases when the TMIn flux increases from 200 to 700 sccm as more indium atoms are present at the surface and have the possibility to incorporate into the lattice. For this series of samples, we observe an additional emission centered around 450 nm that may be related to a presence of de-

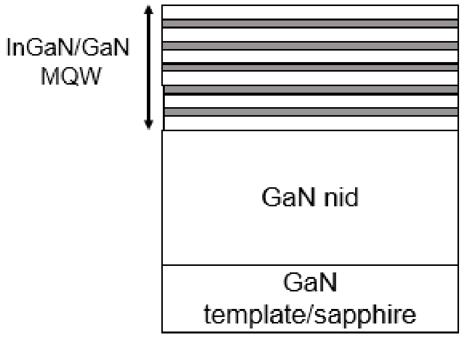

Figure 3.1 – Structure of the MQW samples used for this study.

fects. But, for the sample with the TMIn flux set at 700 sccm, the PL intensity decreases dramatically (by a factor of ten) and the FWHM strongly increases. The emission associated to the defects in the blue range also increases and reaches a PL intensity which is similar the one of the emission peak. If the TMIn flux is too large, In is in excess on the surface and cannot be all incorporated into the layer. When the indium flux is further increased, phase separation may occur as mentionned in 1.2.1 in InGaN layers [1] and in QWs [2]. The signature of phase separation in PL is the appearance of two distinct peaks.

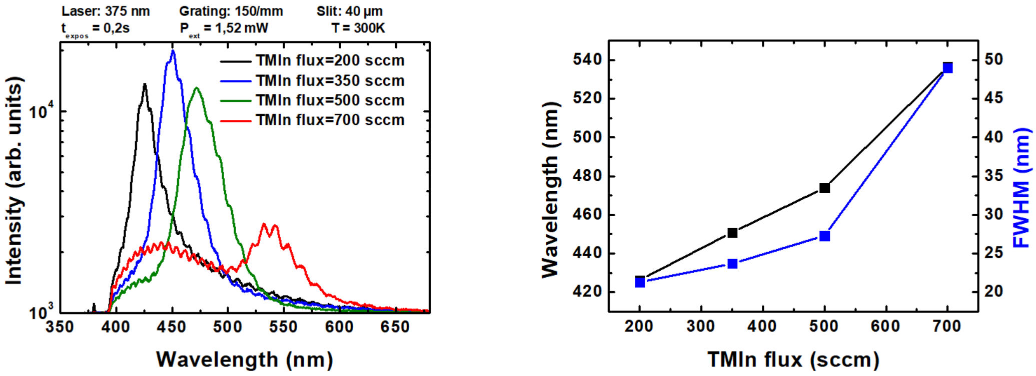

(a) (b)

Figure 3.2 – Room temperature PL spectra of MQW samples grown on GaN template (a). TMIn flux was varied from 200 sccm (black), 350 sccm (blue), 500 sccm (green) and to 700 sccm (red). PL Emission wavelength as a function of TMIn flux (b).

3.1.2 Influence of growth pressure

The growth pressure is a key parameter that can also influence the indium incorporation. Here, during the QW growth, the growth pressure was changed from 400 mbar to 800 mbar. The corresponding PL spectra are given in Fig. 3.3 (a). The evolution of the PL emission wavelength is plotted as a function of the growth pressure (Fig. 3.3 (b)).

As the growth pressure is varied from 400 mbar to 600 mbar, the emission wavelength red-shifts from 444.8 nm to 461.2 nm. Then, as the growth pressure is further increased to 800 mbar, the emission wavelength blue-shifts to 429 nm and the PL intensity strongly decreases. There might be some saturation phenomenon happening as discussed in the following paragraph.

The influence of growth pressure was also analyzed by Park *et al.* [3] with a smaller range of growth pressures studied. TEM measurements revealed that the QWs are thinner as the growth pressure increases (*i.e.* growth rate is decreased). They also observed an increase of the average indium concentration and higher compositional fluctuations. Therefore, the PL red-shift that we observe may be explained by an increased In concentration and increased fluctuations in indium composition (the PL linewidth is increased from 20 to 23 nm) although the QW width is probably decreased. We can suggest that the blue-shift at 800 mbar results from a saturation of the surface with In atoms as the growth rate is enhanced. The nitrogen atoms have difficulties reaching the surface and the In-N bounds are then difficult to form decreasing the In content of the QW. The PL intensity decreases as the structural quality deteriorates.

The surface of samples grown with different pressures in the MQWs were scanned with AFM. Fig. 3.4 displays the surface of the three samples. We can observe an evolution of the quality of the surface, the surface roughness changes from 1.1 nm to 1.4 nm, and to 1.7 nm for growth pressures of 400 mbar, 600 mbar and 800 mbar respectively. The surface of the sample with the MQWs grown at 800 mbar present features that look like some indium inclusions at the surface which may be a consequence of the saturation of indium atoms at the surface.

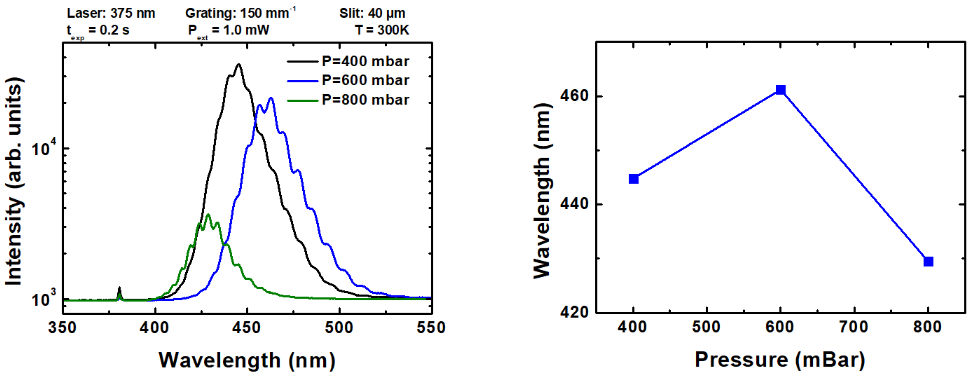

(a) (b)

FIGURE 3.3 – PL spectra of MQW samples grown on GaN template. Pressure during the QW growth was varied from 400 mbar to 600 mbar (a). PL Emission wavelength as a function of growth pressure (b).

In order to incorporate more indium, one solution would be to lower the growth temperature. However, doing so would decrease the structural quality of our layers by triggering the emergence of more defects as detailed in chapter 2. For that reason, a strong decrease

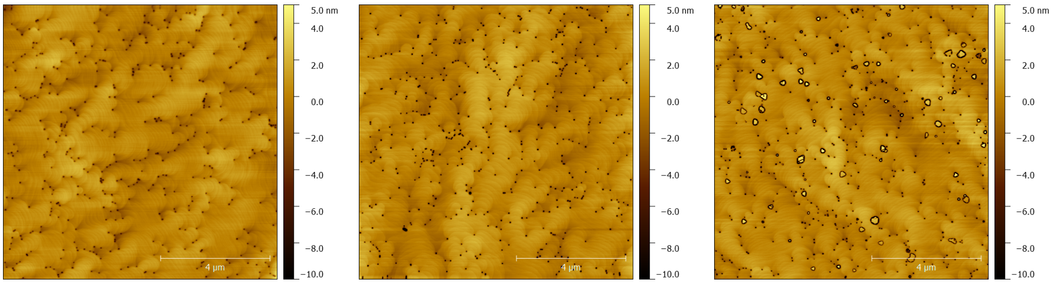

(a) (b) (c)

FIGURE 3.4 – AFM scans of MQW samples grown on GaN template with a pressure during the MQW growth set at 400 mbar (a), 600 mbar (b) and 800 mbar (c).

of the growth temperature is not a solution that we will consider to reach longer wavelengths in the first place.
We have seen that we reach intrisic limitations by simply adjusting the growth parameters of the QWs of the reference structure. Therefore other solutions must be found by modifying either the structure or the growth process.

3.2 InGaN layers on GaN

As presented in section 2.2.2, placing an InGaN layer under the active region is believed to improve the IQE of the MQWs. For this reason, the growth of InGaN layer on GaN was studied as a first step. The influence of growth conditions on indium incorporation and on the optical and structural features are presented below. Fig. 3.5 pictures the structure of the samples.

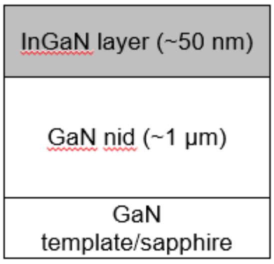

FIGURE 3.5 – Structure of the InGaN on GaN samples used for this study.

3.2.1 Growth conditions

Table 3.1 summarizes the growth conditions tested on the layers. Growth temperature, growth time, growth rate and In/Ga flux ratio were varied. The In content of the layers was estimated using HRXRD measurements.

Thickness (nm)	Growth Temperature	Growth rate (µm/h)	In/Ga	In (%) (from XRD measurement)
50	T	0.05	2.8	6.1
50	T-15	0.05	2.8	9.1
100	T	0.05	2.8	6.8
50	T	0.08	2.8	9.3
50	T	0.11	2.8	10.0
50	T	0.11	2.0	9.6
50	T	0.11	2.4	10.1
200	T+30	0.05	1.9	3.0

TABLE 3.1 – Growth conditions and indium content (measured by XRD) for the InGaN layers grown on GaN template.

Prior to the determination of the In content using XRD, the relaxation state of the InGaN layer was studied. One of the reciprocal space mappings on the asymmetrical (1 0 5) reflection is pictured in Fig. 3.6. On every mapping, the diffraction spots corresponding to GaN (more intense spot at the top) and InGaN are perfectly aligned vertically. Therefore, the growth is demonstrated to be completely pseudomorphic. The InGaN layers are strained on the GaN template for the whole range of growth conditions implemented here.

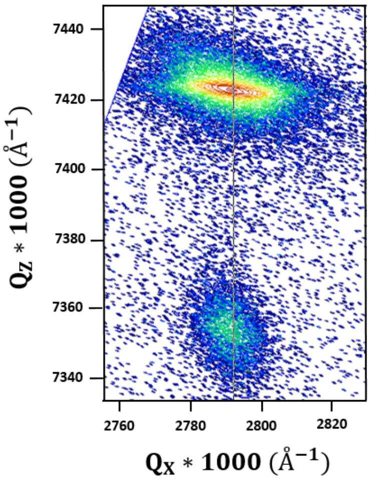

FIGURE 3.6 – Reciprocal Space Mapping (RSM) on the (1 0 5) for an InGaN on GaN sample with 6.8 % In content and 100 nm thickness of InGaN.

The layers were also characterized by PL at 14K with a 325 nm He-Cd laser for excitation. Fig. 3.7 displays the PL wavelength emission of InGaN near band edge as a function of

In content. As expected, PL wavelength increases with indium content (Eq.1.4).

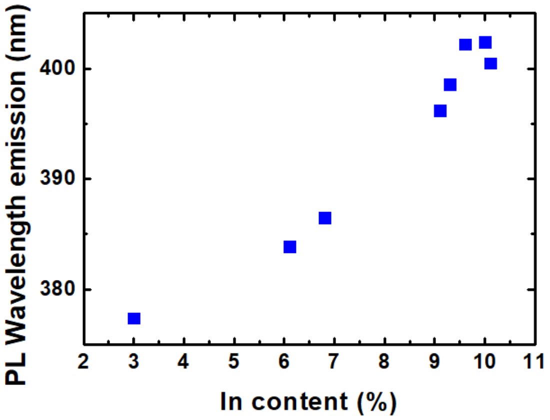

FIGURE 3.7 – PL wavelength vs In content (estimated by XRD) including results for InGaN layers with different thicknesses.

3.2.2 Surface quality assessment

The surface of the InGaN layers was characterized using AFM in tapping mode. An image of the surface is presented on Fig. 3.8 (a). The surface morphology is characteritic of the InGaN on GaN layers as observed by Sumiya et al. [4] (Fig. 3.8 (b)).

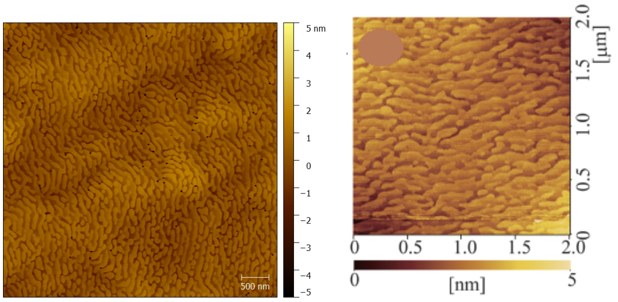

(a) (b)

FIGURE 3.8 – $5 \times 5 \mu m^2$ AFM scan of our InGaN on GaN layer (a) $2 \times 2 \mu m^2$ AFM scan of the InGaN on GaN layer from [4] (b).

For the sample with an indium content of 6.1%, the layer thickness was doubled while keeping the same growth conditions, the surface of the samples observed by AFM is displayed on Fig. 3.9. One can observe the appearance of numerous V-pits at the surface. Compared to the 50-nm thick sample, the density of V-pits is doubled in the 100 nm-thick sample. We also note a significant enlargement of these V-defects. The compressive strain accumulated in the structure is probably responsible for such a behavior. Another kind of relief is also observed, this time positive (therefore pictured in white) : some small peaks of unknown origin are observed on the surface.

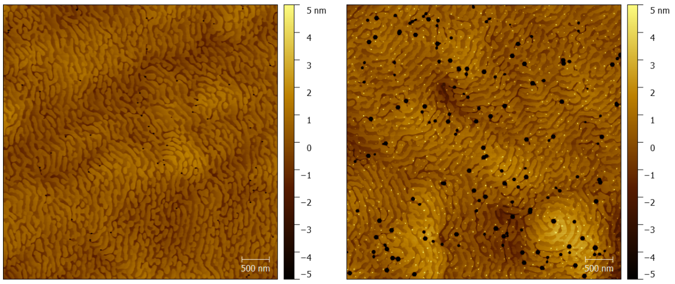

(a) (b)

Figure 3.9 – $5 \times 5 \mu m^2$ AFM scans of InGaN on GaN of small In content (6.1 %) for an InGaN layer thickness of 50 nm (a) and 100 nm (b).

3.2.3 Influence of growth rate

The influence of growth rate on the characteristics of the InGaN layers was studied. The growth temperature was kept constant as well as the In/Ga flux ratio (set to 2.8). The growth rate was varied from 0.05 µm/h to 0.11 µm/h.

3.2.3.1 Optical and surface characterization

The optical and surface characterizations led on the InGaN on GaN layers with different growth rates are summarized in Table. 3.2.

Growth rate (µm/h)	Indium content (%)	PL emission wavelength (nm)	PL FWHM (nm)	RMS (nm)
0.05	6.1	383.9	3.3	0.61
0.08	9.3	398.6	3.5	0.65
0.11	10.0	402.4	5.2	1.0

Table 3.2 – Summary of the optical and surface characteristics for the InGaN on GaN samples grown with different growth rates. The PL characterization was conducted at low temperature (15 K).

Fig. 3.10(a) plots the indium content (estimated by XRD) of the layers as a function of the growth rate. An increase of In content is seen at first but the third point seems to indicate the begining of a saturation of the In content although more data points would allow for a verification of that assumption.

The layers were later characterized by PL with a 325 nm He-Cd laser as excitation source at low temperature (15 K). Fig. 3.10(b) plots the PL wavelength emission and the FWHM of that emission for the different growth rates. Both quantities follow the expected trend considering the increase of indium content noticed before. For the largest growth rate, the

FWHM of the PL spectrum reaches a very high value of 5.2 nm. At this high growth rate, the surface is probably quite saturated in indium which induces a more inhomogeneous alloy.

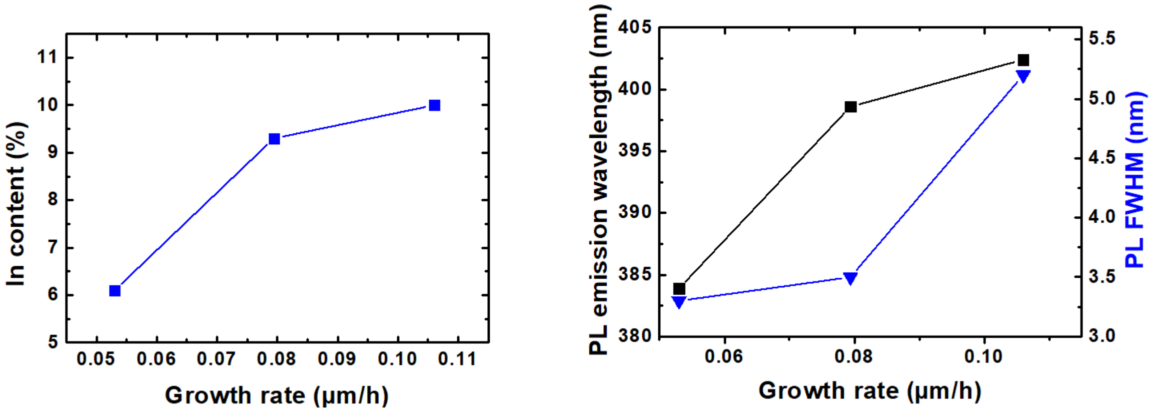

FIGURE 3.10 – In content as a function of InGaN growth rate (a)PL emission wavelength and FWHM as a function of InGaN growth rate (b).

AFM scans for the three different growth rates are displayed in Fig. 3.11. An evolution of the morphology of the surface is observed when increasing the growth rate. From a rather smooth surface, the morphology evolves into a hill-like morphology characteristic of a spiral growth mode around the dislocations. The same tendency is observed by Kimura *et al.* when increasing the indium content [5]. According to them, the spiral growth mode is promoted with the decrease of the interstep distance caused by the larger TMIn flow. Given the change of morphology, the surface roughness and the peak to valley values also increase with the growth rate as shown in Fig. 3.12. The sample with the largest growth rate which showed a large PL FWHM also presents a rather rough surface.

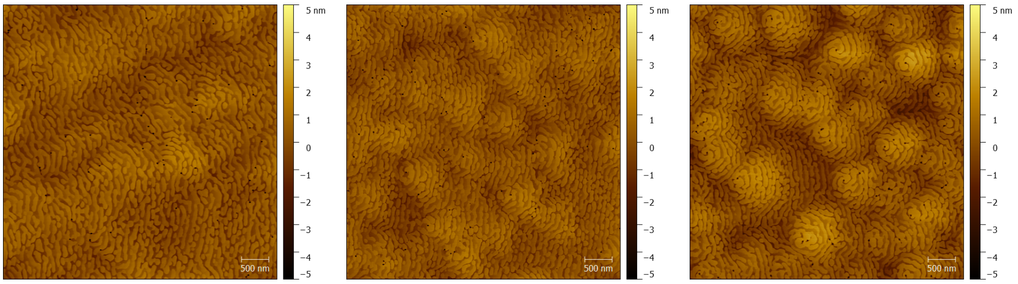

(a) (b) (c)

FIGURE 3.11 – AFM scans of InGaN on GaN (50 nm thick) for different growth rates of 0.05 µm/h (a) 0.08 µm/h (b) and 0.11 µm/h (c).

3.2.3.2 PL vs T

The PL spectra behavior with temperature was studied. An example of the PL emission energy as a function of temperature for the InGaN on GaN layers is presented on Fig.

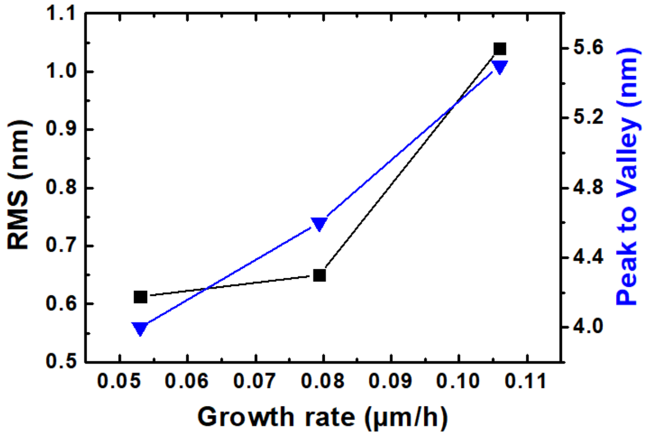

FIGURE 3.12 – RMS roughness as a function of growth rate for constant InGaN layer thickness.

3.13(a). As presented in 1.2.3.2 , the curve follows an S-shape and meets Varshni's equation (eq. 3.1) for high temperatures. In order to determine the localization energy, the difference between the curve and Varshni's fit is measured.

$$E_g(T) = E_g(0) - \frac{\alpha T^2}{\beta + T} \tag{3.1}$$

For the fit, α and β are deduced from the linear interpolation between the end members ($\alpha_{GaN} = 0.593\ meV/K$, $\beta_{GaN} = 600\ K$, $_{InN} = 0.245\ meV/K$, $\beta_{InN} = 624\ K$ [6]) thanks to the knowledge of the In content. The curve is then fitted with $E_g(0K)$ with the assumption that there is no carrier localization at room temperature.

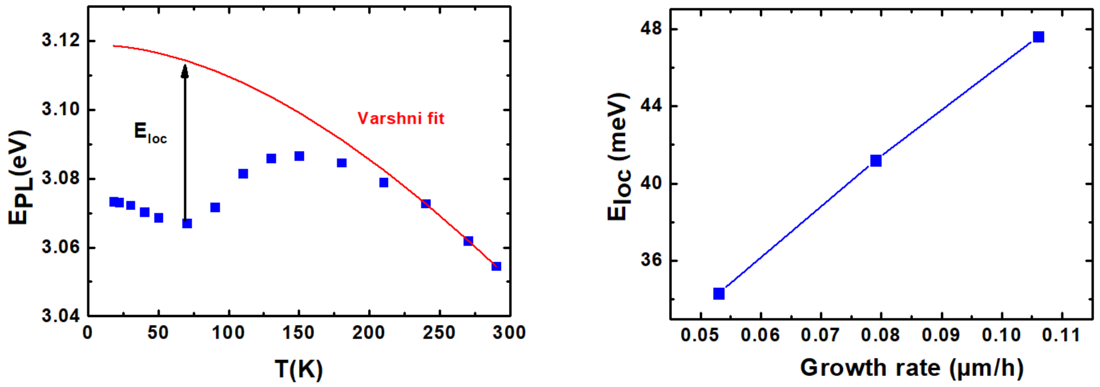

FIGURE 3.13 – PL emission energy as a function of temperature for the InGaN layer with a growth rate of 0.11 $\mu m/h$ (a) Localization energy as a function of growth rate for constant InGaN layer thickness of 50 nm (b).

The localization energy is plotted as a function of growth rate in Fig. 3.13 (b). The carrier localization gets stronger as the indium content increases (since the indium content increases with the growth rate) as also observed in [7] for a wider range of In contents.

The values for the localization energies between 33 and 47 meV obtained for our layers are close to the ones reported by Wu *et al.* but for layers with greater In contents (about 30 %) [7].

A typical plot of the spectrally integrated PL intensity as a function of 1/T for an InGaN buffer layer on GaN is given in Fig. 3.14.

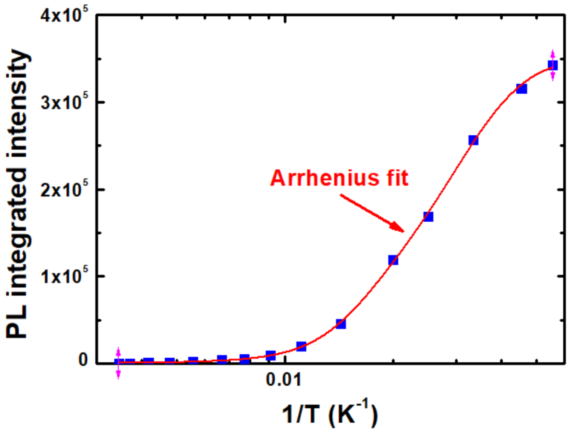

FIGURE 3.14 – PL integrated intensity as a function of 1/T for an InGaN buffer layer on GaN, the curve is fitted with an Arrhenius plot.

Above a certain temperature, the PL integrated intensity decays. This plot follows an Arrhenius plot (eq. below) [8]. The fitting of the curves gives E_A and E_B, the activation energies. As there are two different activation energies, there are two different types of nonradiative recombination paths [9]. These activation energies are related to the height of the potential barrier an electron should pass in order to reach non radiative recombination centers [10].

$$I(T) = \frac{I_0}{1 + Aexp(-E_A/k_BT) + Bexp(-E_B/k_BT)} \tag{3.2}$$

where k_B the boltzmann constant, E_A and E_B the activation energies, I_0 is the PL intensity at 0K and A and B are the pre-exponential factors.

Table 3.3 summarizes the values of localization and activation energies obtained from the analysis of PL vs T for the three samples.

The values of activation energies are ranging between 1.0 meV and 39.3 meV depending on the radiative recombination center type and on the sample considered. These values are similar to what is reported for other InGaN on GaN layers in the litterature [11], [8]. For the nonradiative recombination center of type B, the activation energy decreases as a function of the growth rate (*i.e.* with increasing indium content) while the activation energy increases for the nonradiative recombination center of type A. One hypothesis is that there are more inhomogeneities when the indium content increases, improving the localization of carriers. Because of this localization, the carriers have difficulty to reach the nonradiative recombination center of type A thus increasing the activation energy.

Growth rate (µm/h)	Indium content (%)	Localization energy (meV)	Activation energy E_A(meV)	Activation energy E_B(meV)
0.05	6.1	33	24.6	6.6
0.08	9.3	39	34.5	9.5
0.11	10.0	47	39.3	1.0

TABLE 3.3 – Summary of the localization and activation energies for the InGaN on GaN samples grown at different growth rates.

The values of E_B activation energies are really small and reflect the shape of the curve which quenches really fast at low temperature. Second activation energies in the same range have been reported by Leroux *et al.* for the quenching of neutral donor bound recombination line (I_2) in GaN [12].

We studied the growth conditions of InGaN on GaN layers with a focus on growth rate. For our rather small layer thickness of 50 nm, as soon as the In content reaches values of over 10 % the roughness increases which could have a detrimental influence on the quality of the interfaces (abruptness) between the QWs and the QBs if such layer is placed under the active region. If the thickness of this InGaN layer is increased, the appearance of V-pits in the layer may be damaging for the efficiency of the LED structure because of the creation of nonradiative recombination centers. Therefore, for the implementation of the InGaN underlayer (UL) under the active region of our reference MQW structure, we will maintain a thickness of 50 nm and a rather small In content of 6.1 %.

3.3 MQWs on SL and prestrained layers

As using an InGaN underlayer or InGaN/GaN SL before the active region was shown to improve the efficiency of InGaN/GaN QWs (see 2.2.2), we implemented this principle to our MQW structures. Fig. 3.15 shows the three structures that were grown. For all of them, the growth conditions of the active region calibrated for blue emission are the same. The SL consists in 10 pairs of 3 nm/ 10 nm InGaN/GaN with an aimed In content of 5 %. The InGaN underlayer is 50 nm-thick and grown in the same conditions as the first layer presented in 3.1 (In content of 6.1 %).

3.3.1 PL and IQE measurements

The samples were characterized using PL at room temperature, the results are shown in Fig. 3.16. In order to pump only in the active region, a 405 nm laser diode was used.

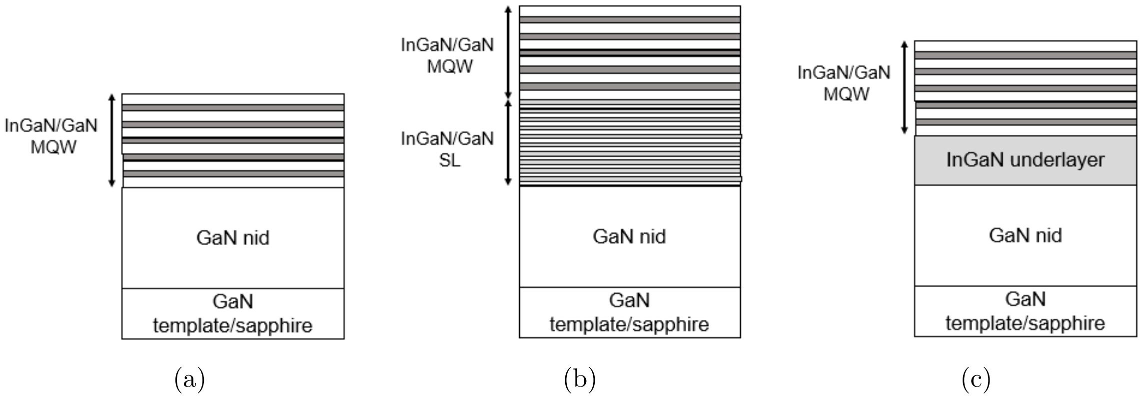

(a) (b) (c)

Figure 3.15 – Structures of the reference sample (a) samples with InGaN/GaN superlattice (b) and InGaN underlayer (c).

With the SL and InGaN UL, an enhancement of PL emission is observed, by a factor of three for the InGaN UL and by a factor of seven in the case of the SL. The emission is very slightly red-shifted with the use of the InGaN/GaN SL (8 nm) and with the InGaN UL (10 nm).

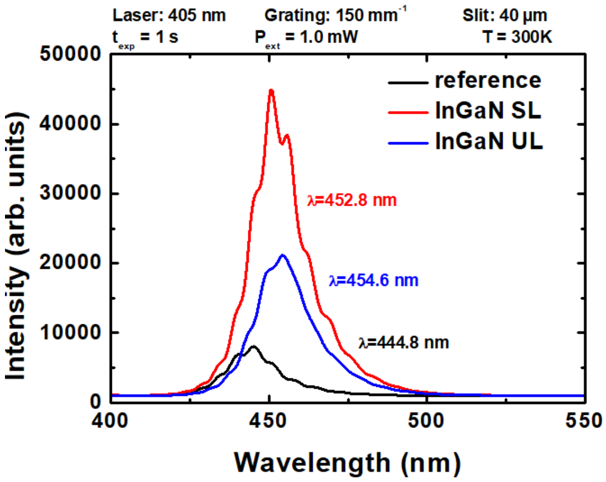

Figure 3.16 – PL spectra at RT for reference sample (black), superlattice under the QWs (red) and InGaN underlayer (blue) measured using a 405 nm laser diode.

Afterwards, some IQE measurements were carried out following the protocol described in annex B. Fig. 3.17(a) plots the integrated PL intensity as a function of 1/T for the three samples. Although an ideal plateau is observed for the points at low temperatures in the case of the InGaN UL, the curve of the reference sample and InGaN/GaN SL sample show a little decrease. Therefore, the IQE might be a bit overestimated for these two last samples. The different tendencies of the integrated PL intensities as a function of 1/T between InGaN UL sample and the reference sample are observed to be the same as the ones described by Hao *et al.* [9] as shown by Fig. 3.17(b).
Fig. 3.18 gives the IQE curves of the three samples at 14K and 290 K. At low tempe-

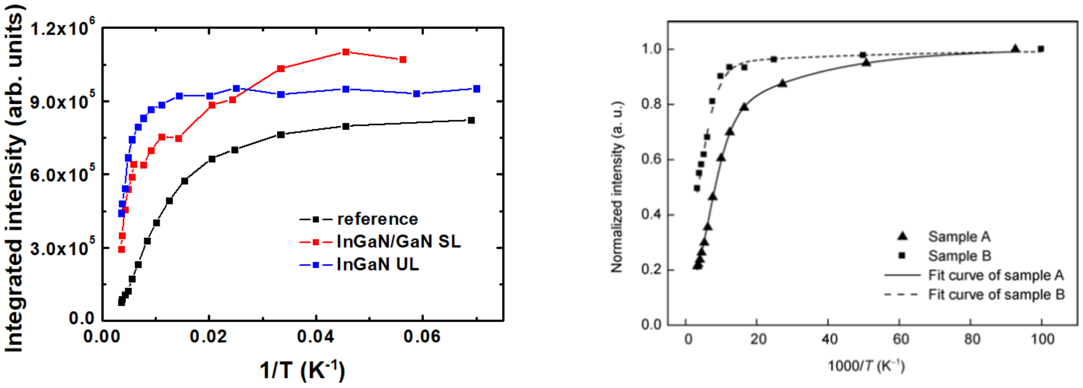

(a) (b)

FIGURE 3.17 – Integrated PL intensity as a function of 1/T for the reference sample (black), InGaN/GaN SL sample (red), InGaN UL sample(blue) (a). Integrated PL intensity as a function of 1/T for a sample without InGaN UL (A) and with an InGaN UL (B) [9] (b).

rature, the InGaN UL sample shows a normalized efficiency plateau for the whole range of excitation powers whereas a slight decrease is observed for the high excitation power for the other two samples. For all the curves at 290 K, we do not see any droop of IQE because high enough carrier densities are probably not reached. Nonetheless, the points at high power suggest an inflexion of the curve with the reduction of the slope. From the IQE value of 12.4 % for the reference sample, the IQE is improved by a factor of two with the use of the SL (26 %) and by more than three with the use of the InGaN UL (41 %). The next paragraph investigates the reasons for the IQE improvement.

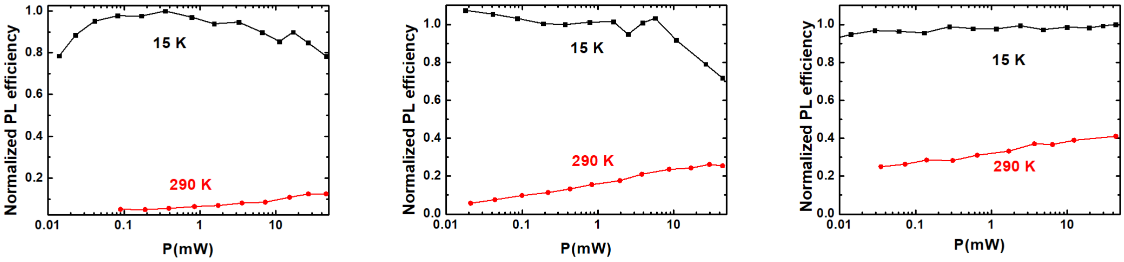

(a) (b) (c)

FIGURE 3.18 – Normalized PL efficiency of MQW samples as a function of laser excitation power for the reference sample (a), InGaN/GaN SL sample (b) and InGaN UL sample (c).

3.3.2 Investigation of the reasons for the IQE improvment

Several hypotheses for the enhancement in IQE thanks to the use of InGaN UL and InGaN/GaN SL are described in section 2.2. We investigate the possible explanations in our case. Table 3.4 summarizes the charcteristics of the three samples.

Sample	PL Wavelength (nm)	IQE (%)	RMS (nm)	V-pit density (cm^{-2})	Localization energy (meV)
reference	444.8	12	1.1	3.9×10^8	45
InGaN/GaN SL	452.8	<26	4.2	4.3×10^8	51
InGaN UL	454.6	41	5.2	4.0×10^8	55

TABLE 3.4 – Summary of the characteristics of the reference sample, sample with InGaN/GaN superlattice and sample with InGaN underlayer.

Surface quality assessment Fig. 3.19 presents the three AFM scans of the surface of reference, InGaN/GAN SL and InGaN UL sample. The surface roughness and the V-pit density are given in table 3.4. Although the density of V-pits remains the same, the surface is rougher with the SL and even more with the InGaN UL. On these rougher surfaces, the V-pits appear darker, as they are deeper. The improvment of IQE is therefore not explained by an improvement of the surface roughness nor by a better screening of the dislocations as the V-pit density is the same. However, we will later see how the roughness might affect the IQE of the QWs.

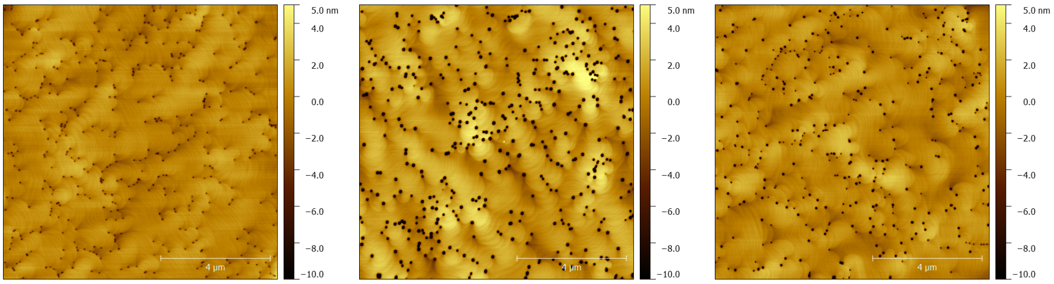

(a) (b) (c)

FIGURE 3.19 – AFM scans of reference sample (a), with the InGaN/GaN superlattice (b), with an InGaN underlayer (c) on a $10 \times 10 \quad \mu m^2$ zone.

Variation of the PL emission wavelength with excitation power Then, we looked into the variation of the PL emission wavelength with the excitation power plot in Fig. 3.20. For the InGaN UL sample, the wavelength is rather stable for the range of carrier densities attained here. On the contrary, the wavelength of the reference sample presents a strong variation which is even bigger for the InGaN/GaN SL sample. We can therefore suspect that the electric field is smaller in the sample with the InGaN UL. Indeed, the screening of the piezoelectric field at high carrier injections provokes a variation of the PL emission wavelength with the laser power. In this case, the electric field was not directly measured to check that assumption. However, Li *et al.* [13] assessed the decrease in electric field by electron holography when using an InGaN UL. They explain the reduction in internal electric field by a decrease of the strain in the QWs because of a partial relaxation. The InGaN UL would therefore act as a strain relief layer which would explain the improvment of IQE. However, a RSM realized on the (1 0 5) reflection showed that here the InGaN UL layer is strained to the GaN template so in our case, there is no strain relief happening. The rather stable PL wavelength emission with excitation power may not be a consequence of a smaller internal electric field in our case.

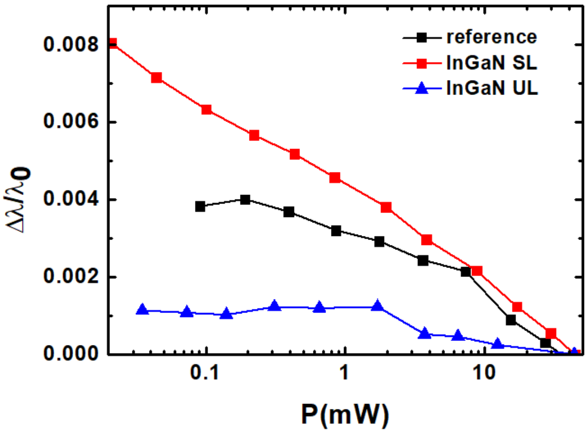

FIGURE 3.20 – $\dfrac{\Delta\lambda}{\lambda_0}$ as a function of excitation power for reference sample (a) samples with InGaN/GaN superlattice (b) and InGaN underlayer (c). The measurement was conducted at 290K with a 405 nm laser diode as excitation source. The reference wavelength λ_0 is the one at maximum power (45 mW).

PL behavior with temperature Finally, an analysis of the PL behavior with temperature was led. Table 3.4 lists the values of localization energies estimated for the three samples. The localization energy is found to be 45 meV for the reference sample. It increases to 51 meV with the addition of the InGaN/GaN SL and to 55 meV with the InGaN UL. According to Wang *et al.* the amplitude of the localization energy plays a role in the efficiency of the active region [14]. Using TRPL, they measured a higher degree of localization at room temperature in a sample with an InGaN underlying layer. The higher efficiency at small injection may in this case be explained by a better insensitivity to the defects thanks to this localization.

In our case, to fit with Varshni's law, carriers are assumed to be fully delocalized at room temperature. It would have been needed to conduct PL measurements above room temperature or acces to a time resolved PL set-up in order to verify this hypothesis. If there is indeed carrier localization at room temperature, the localization energy is underestimated.

Moreover, for the InGaN UL sample the behavior of the curve of the PL integrated intensity as a function of 1/T is characteristic (Fig. 3.17(a))of a sample which shows a strong localization (the curve resembles to the one of a QD based structure as shown in Fig. 5.23 (b). This behavior plus the high localization energy confirms the localized nature of the carriers in the InGaN UL sample. A possible explanation for the carrier localization in InGaN UL sample is the roughenning of InGaN/GaN QW interfaces due to the introduction of the rough InGaN layer (as opposed to GaN) underneath the active region. This roughenning is believed to form QD-like structures and to increase the localization effect. This theory is particularly detailed in 5.2.4.1. However, no TEM measurements were conducted to confirm the presence of roughenning.

Sample	E_A(meV)	E_B(meV)	A/B
reference	46	2.5	19.2
InGaN underlayer	76	13.1	677

Table 3.5 – Summary of the Arrhenius fit characteristics of the reference sample and of the InGaN UL sample.

To determine the activation energies, the curves of Fig. 3.17(a) were fitted with an Arrhenius plot using equation 3.2. In the case of the superlattice, it seems that the plot may be better fitted with three different energies, which would imply that there is an additional nonradiative recombination path as compared to the other two samples. Therefore we will focus on comparing the reference sample and the InGaN UL sample. Table. 3.5 summarizes the different fitting parameters. We observe larger activation energies in the case of the InGaN UL sample. The carriers are more prevented from reaching each type of nonradiative recombination center in the case of the InGaN UL which can probably explain the better IQE. The ratio of A/B is also showed to be stronger with the implementation of the InGaN UL which is characteristic of samples showing stronger RT PL intensity. These observations coincide with the strong localization hypothesis in the case of the InGaN UL sample. As carriers are localized, they will be less likely to reach the nonradiative recombination centers.

To conclude, we have observed an enhancement of the IQE thanks to the use of an InGaN/GaN SL and an InGaN UL under the active region. The InGaN UL sample is believed to show an increased localization and a better insensitivity to defects compared to the reference sample which could explain that IQE improvment. In the case of the InGaN/GaN SL, the reasons are unclear but the SL may act as a barrier for impurities. In that case, the number of point defects would be decreased in the active region [15]. This hypothesis was not verified, but a SIMS analysis could be considered to evaluate the density of the different impurities in the active region of the InGaN/GaN SL sample compared to the reference sample.

3.4 Reduction of indium surface segregation

We saw in the first chapter (section 1.3.4.3) that the indium surface segregation at interfaces between the wells and the barriers had a detrimental effect on the emission by making the well wider. Indium surface segregation also has the effect of blue-shifting the emission. To achieve efficient long wavelength emission, we therefore need to work on how to mitigate it. Foremost, solutions are implemented to improve the first interface (barrier/well), then we focus on the second interface (well/barrier).

3.4.1 First interface

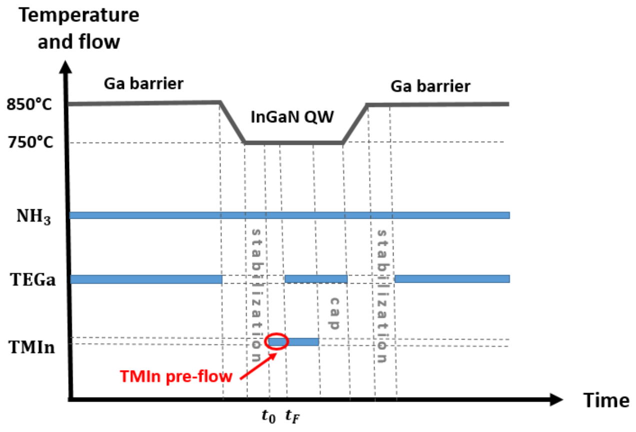

FIGURE 3.21 – Time chart of the temperatures and sources used for QW growth. t_0 and t_F mark the beginning and the end of the TMIn pre-flow phase.

The first interface of the QWs is not abrupt due to a delay of indium incorporation as indium is segregated at the surface, ML after ML. In order to improve the abruptness of this first interface, the idea is to saturate the surface with indium atoms before starting the growth of the QW, with the objective to reach the nominal In content at the first grown ML. The In atoms are provided by the opening of the TMIn flux for a short period before the growth of the QWs while maintaining the TEGa flux cut. This technique was first used to improve with success the InGaAs/GaAs interface [16]. Liu *et al.* [17] first implemented that solution for MOVPE-grown InGaN/GaN LEDs (in that case the ammonia flow was not maintained during the pre-flow TMIn treatment), they reported an amplification of the EL intensity by a factor of 3.5 but no significant red-shift. Park *et al.* [18] demonstrated an improvment in abruptness of the barrier/well interface revealed by an enhancement of the PL intensity, a decrease of the PL FWHM and more distincts satellite peaks in the XRD spectra. With detailed electrical characterizations, Lee *et al.*

[19] showed that the TMIn pre-treatment allows for less defect-assisted leakage of the injected carriers. The droop was also reduced. Deng *et al.* [20] and Senthil Kumar *et al.* [21] reported a red-shift of about 15 nm, and a 30 % improvment in IQE in the latter case.

Fig. 3.21 is a time chart of the temperatures and the fluxes used for the growth of the QWs. Compared to conventional growth, we add a pre-flow TMIn treatment while the TEGa flow is cut during a time $t_{TMIn} = t_F - t_0$. NH_3 flow is maintained during the whole growth and stabilizes the surface. The duration of the TMIn pre-treatment t_{TMIn} is varied to 90, 135 and 180 seconds. We refer to these samples as TMIn90, TMIn135 and TMIn180. Table 3.6 summarizes the characteristics of the reference samples and of the three samples with pre-flow TMIn treatment.

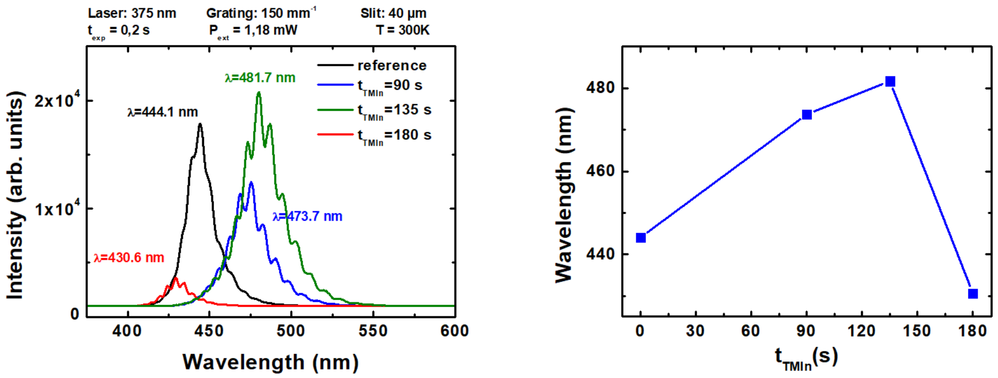

(a) (b)

FIGURE 3.22 – PL spectra at RT for reference sample (black) and for the samples with pre-flow TMIn treatment with t_{TMIn}=90 s (blue), t_{TMIn}=135 s (green), t_{TMIn}=180 s (red) (a) and PL emission wavelength as a function of t_{TMIn} (b) using a 375 nm laser diode.

Fig. 3.22 (a) displays the PL spectra of the reference samples and the three samples with pre-flow TMIn treatment at room temperature excited with a 375 nm laser diode. The PL wavelength emission is increased from 444.1 nm for the reference sample, up to 473.7 for sample TMIn90 and 481.7 nm for sample TMIn135, that is a red-shift of 37.6 nm. Sample TMIn180 provokes a blue-shift compared to the reference sample (430.6 nm) and the PL intensity is significantly reduced. For samples TMIn90 and TMIn135, we may have improved the abruptness of the interface and incorporated more indium compared to the reference sample. For sample TMIn180, the pre-flow TMIn treatment seems too long. The saturation of indium atoms at the surface may hinder the formation of In-N bounds by preventing the N atoms to reach the surface.

IQE measurements were then conducted with a 375 nm laser diode in order to determine the effects of the pre-flow TMIn treatment on the QW efficiency. We plot the integrated PL intensity as a function of 1/T for all the samples (Fig. 3.23). Although the reference presents an acceptable plateau at low temperatures, the longer the TMIn flow is maintained, the bigger is the decreasing slope towards higher temperatures. Compared to reference sample, some additional point defects may have been introduced in the samples with TMIn pre-treatment (due to the saturation of the surface with In atoms that prevent N atoms to reach the surface). Therefore, the normalized (to the maximum at low temperature) PL efficiencies we get from the samples TMIn90, TMIn135 and TMIn135 are only an upper bound of the IQE. These normalized PL efficiencies at 290 K are plotted in Fig. 3.24.

The curves at low temperature show a decrease of the normalized PL efficiency for the samples TMIn90 and TMIn135. As explained in the above paragraph, this may be due to the presence of additional point defects that act as non-radiative recombination centers (NRC) activated at high injections even at low temperature. These values of normalized PL efficiencies are therefore not IQE values. An improvment of normalized PL efficiency at 290 K is observed with the use of the TMIn pre-flow treatment with an increase of 80 % for sample TMIn90 and 67 % for sample TMIn135 even if we are at longer wavelengths but given the curves at low temperature this is difficult to compare. We also remark that for the samples TMIn90 and TMIn135, it seems that at the maximum carrier densities reached, no maximum was reached in the efficiency curve contrary to the reference case which seems to show a PL efficiency curve with a maximum. The difference in behavior might be explained by the presence of more defects in samples TMIn90 and TMIn135. The maximum of the efficiency is thus shift to higher carrier densities as the defects are screened little by little.

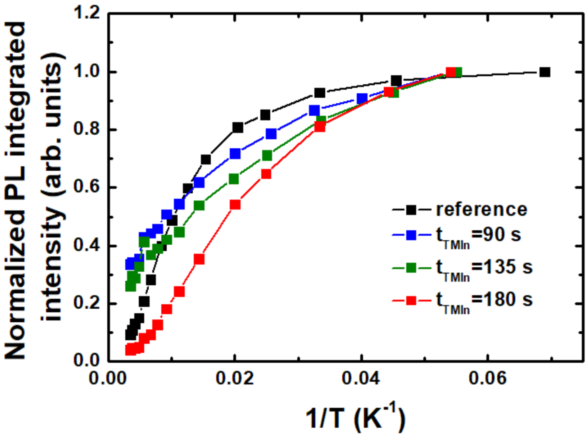

FIGURE 3.23 – Integrated PL intensity as function of 1/T for reference sample (black) and for the samples with pre-flow TMIn treatment with t_{TMIn}=90 s (blue), t_{TMIn}=135 s (green), t_{TMIn}=180 s (red) characterized with a 375 nm laser diode.

Although the PL spectra at room temperature and low power exhibit emissions peaks of similar FWHM, it was noticed that at low temperature, the samples treated with a pre-flow of TMIn unexpectedly present very broad emission peaks. To study that phenomenon, the FWHM of the PL emission peaks is plotted as a function of the laser excitation power in Fig. 3.25. While for the reference sample the FWHM is rather stable and small (15

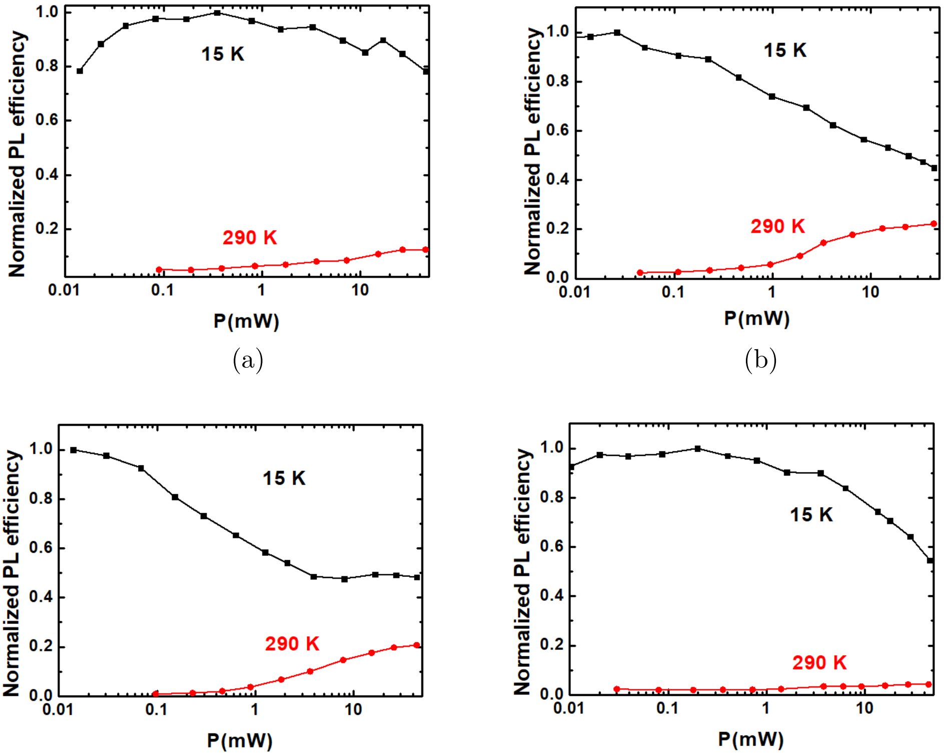

(a) (b)

(c) (d)

Figure 3.24 – Normalized PL effiencies curves at 290 K as a function of excitation power for reference sample (a) and for the samples with pre-flow TMIn treatment with t_{TMIn}=90 s (b), t_{TMIn}=135 s (c), t_{TMIn}=180 s (d) characterized with a 405 nm laser diode as excitation source.

nm), the FWHM of samples TMIn90 and TMIn135 increases dramatically with excitation power to reach values up to 35 nm. It seems that with the pre-flow TMIn treatment, we created more energy levels in which carriers are trapped at low temperature. As the laser power is increased more and more energy levels are populated. This phenomenon is also observed at room temperature to a smaller extent and might be due to the presence of larger indium inhomogeneities compared to reference samples.

Duration of pre-flow TMIn treatment (s)	PL Wavelength (nm)	Normalized PL efficiency (%)
0 (ref)	444.1	12
90	473.7	22
135	481.7	21
180	430.6	4

Table 3.6 – PL characteristics at 290 K of the samples with pre-flow TMIn treatment.

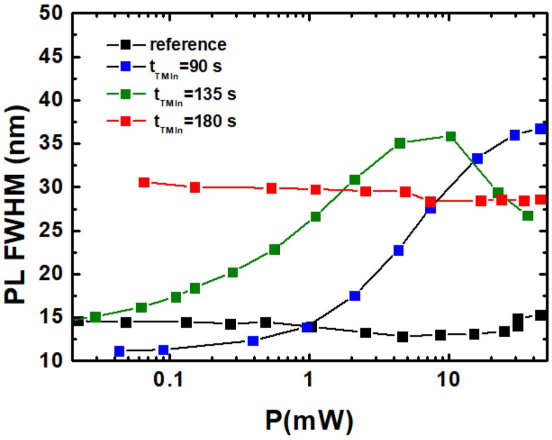

FIGURE 3.25 – FWHM of the PL peaks as a function of the laser excitation power at 14K for reference sample (black) and for the samples with t_{TMIn}=90 s (blue), t_{TMIn}=135 s (green), t_{TMIn}=180 s (red) characterized with a 375 nm laser diode as excitation source.

3.4.2 Second interface

The second interface is also not ideal as indium is present on the surface at the end of the growth of the quantum well (when the TMIn flux is cut). Indeed, in our process the temperature stays the same during a step called the cap layer with approximately the same duration as the growth of the QW. The temperature is then increased by 100 ˚C to grow the barrier. During the cap, the indium present at the surface is therefore incorporated ML by ML to form the "tail" of the indium distribution into the barrier, therefore increasing the thickness of the well (see 1.3.4.3).

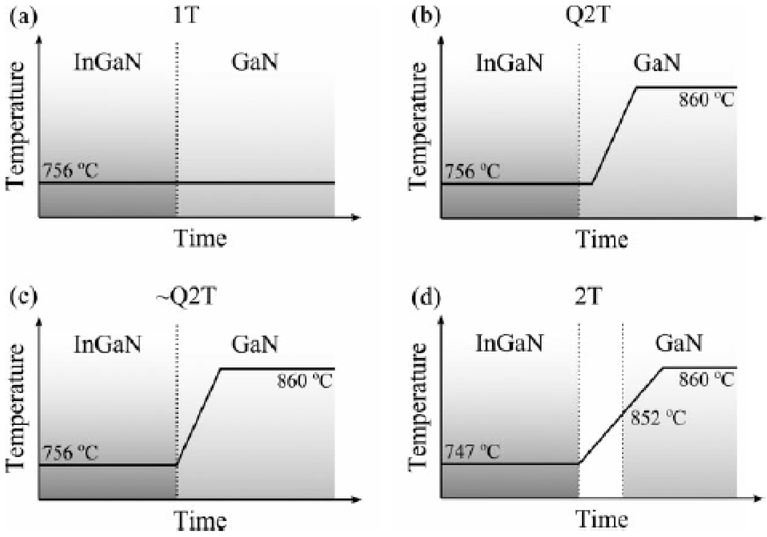

FIGURE 3.26 – Temperature profiles for second interface well/barrier [23].

In order to evaporate the indium atoms from the surface, a rapid temperature increase after the QW growth may be considered. This solution was shown to improve the abruptness of the second interface in the case of InGaAs/GaAs QWs [22]. Massabuau *et al.* [23] later proposed to try several profiles for this well/barrier interface. Fig. 3.26 displays the different profiles that were tested in their work. For the 1T profile, the growth temperature of the barrier is the same as the growth temperature of the QW (similar to our process). For the Q2T sample, a small GaN cap layer is grown (1nm) before increasing the temperature up to the barrier temperature while keeping the TEGa open during the whole process. The ∼Q2T profile is the same but without the GaN cap layer, the ramp begins right after the growth of the InGaN QW. Finally for the 2T profile, the ramp also starts immediatly after the growth of the QW but the TEGa is cut during the ramp. The growth of the barrier starts only soon before the barrier temperature is reached. Massabuau *et al.* demonstrate that a reduced segregation coefficient is obtained with the profiles 2T, ∼Q2T, Q2T (in that order) compared to the 1T profile.

In our standard MQW structures, the growth of the cap layer lasts as long as the growth of the QW (see Fig. 3.21). Therefore we can consider that our growth process is in the 1T case described by Massabuau *et al.*. The profiles ∼Q2T and 2T are tested on our samples. The room temperature PL results from the characterization with a 375 nm laser diode are given in Fig. 3.27. The implementation of the 2T profile provokes a blue-shift from 444.5 nm to 432.7 nm with a strong decrease in PL intensity. The ∼Q2T profile gives a similar PL spectra as the reference 1T.

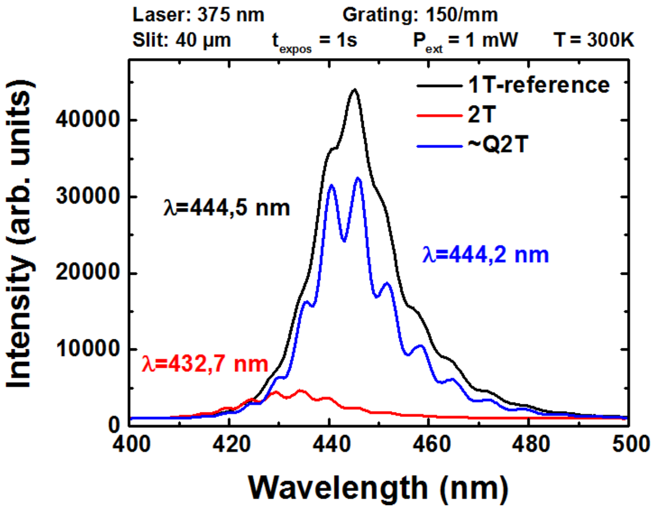

FIGURE 3.27 – PL spectra for reference sample (black), sample with 2T profile (red), with ∼Q2T profile (blue) characterized with a 375 nm laser diode.

According to Massabuau *et al.* the thickness of the well with ∼Q2T profile is smaller (2.2 against 2.6 nm for the 1T profile). Indeed, the rapid temperature increase evaporates the indium on the surface and the last instable ML. Therefore, to compare the influence of the different interfaces for two wells of similar thicknesses we continue the growth for two more monolayers. The new profile is labelled as ∼Q2T+2ML. Fig. 3.28 plots the corresponding PL spectra. We observe a small redshift from 444.5 nm to 451.4 nm and an increase of PL intensity.

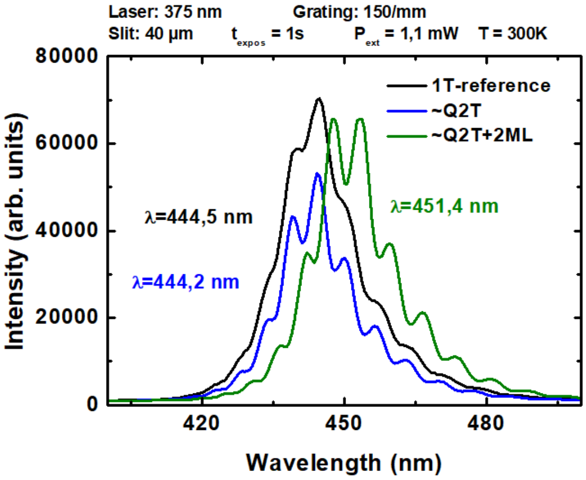

FIGURE 3.28 – PL spectra for reference sample (black), sample with ~Q2T profile (blue), with ~Q2T+2ML profile (green) characterized with a 375 nm laser diode.

Model applied	PL Wavelength (nm)	Normalized PL efficiency(%)
ref (1T)	444.5	12
2T	432.7	-
Q2T	444.2	26
Q2T+2ML	451.4	15

TABLE 3.7 – Summary of the characteristics of the samples with different second interfaces.

IQE measurements were carried on to assess the efficiency of the samples with 1T (reference), Q2T and Q2T+2ML. Fig. 3.29 shows the PL integrated intensity plotted as a function of 1/T. Just like for the trials for the reduction of indium surface segregation at the first interface, the curves are not extremely stable at low temperature, especially for the Q2T and Q2T+2ML samples (although the curve of the reference sample is already not perfect). Therefore, the normalized PL efficiencies can not be considered as IQE values. The normalized PL efficiencies curves at 290 K given in Fig. 3.30 show close values for reference sample and Q2T+2ML (15 against 12 %) although it seems that for the Q2T+2ML sample, the curve has not yet reached its maximum. Like in the case of the first interface, the tendency of the curve may be explained by a larger defect density in the samples where we modified the second interface compared to reference sample. With the Q2T profile, the value of 26 % is reached. The improvment compared to Q2T+2ML may be partly explained by a thinner well therefore lowering the impact of the QCSE although it should not be a decisive factor at such small thicknesses (around 3 nm).

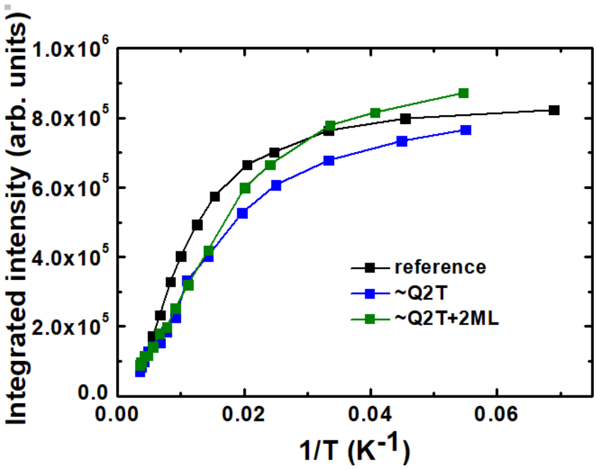

FIGURE 3.29 – Integrated PL intensity as a function of 1/T for reference sample (black), sample with ∼Q2T profile (blue), with ∼Q2T+2ML profile (green) characterized with a 375 nm laser diode.

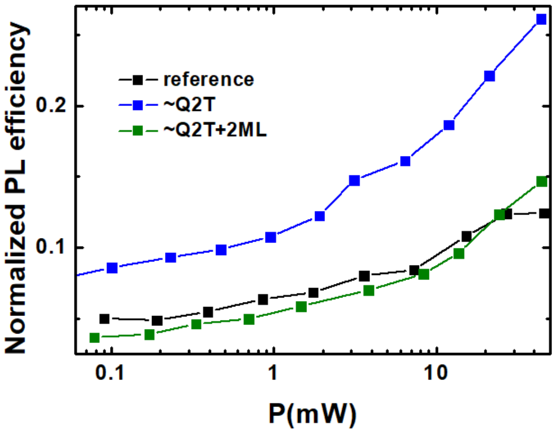

FIGURE 3.30 – Normalized PL efficiencies at 290 K as a function of excitation power for reference sample (black), sample with ∼Q2T profile (blue), with ∼Q2T+2ML profile (green) at 290K characterized with a 375 nm laser diode.

This section showed that longer wavelengths could be reached by changing the growth process at the well/barrier and barrier/well interfaces. Nonetheless, it seemed that doing so also introduced more defects in the active region although the ratio between PL efficiency at room temperature and low temperature was improved.

Conclusion

In this chapter, the goal was to produce a long wavelength emission while maintaining a high efficiency. For this reason, the well thickness was kept at 3 nm to prevent any detrimental effect of the QCSE. Indium content had thus to be increased. We first studied the impact of the growth parameters in a simple MQW structure. We showed that some intrinsic limitations prevent an increase of the indium content. Long wavelengths may be reached by increasing the TMIn flux or lowering the growth temperature but the PL intensity and the structural quality of the MQWs will decrease. By increasing the pressure, we can also see that a limit in terms of wavelength emission is reached before the emission starts to blue-shift again, a sign that the surface is saturated in indium atoms that can not be incorporated anymore. The saturation phenomenon will also be reached by playing on the other growth parameters although we did not go far enough to show it here.

Secondly, the implementation of InGaN layer or InGaN/GaN SL under the active region was studied. Foremost, the growth of the InGaN UL was studied alone as a first step to understand what was the effect of increased indium content and increased thickness on the surface characteristics as this surface will later be used to grow the active region.

Then, we analyzed the effect of such an InGaN layer and InGaN/GaN SL on the properties of the MQWs. The IQE was increased thanks to the use of the InGaN/GaN SL and even further with the InGaN UL. The reason for that IQE improvement is thought to be a strong localization and a better insensitivity to defects in the case of the InGaN UL. In the case of the InGaN/GaN SL, further investigations need to be carried out to understand the IQE improvement.

Finally, we have shown that it was possible to reach longer wavelengths by improving the abruptness of the interfaces in the active region, with a higher redshift observed when improving the first interface (barrier/well). An increase of IQE is also to be expected.

Nonetheless even by combining the approaches (reduction of indium surface segregation, implementation of InGaN UL and reasonable growth parameters that would increase indium incorporation without decreasing the crystal quality), some limitations will be reached because of the strain between the active region and the GaN template. The next chapter will present the characteristics of the InGaNOS substrates and their potential beneficial influence for reducing strain in the overall structure.

References of chapter 3

[1] D. Doppalapudi, S. N. Basu and T. D. Moustakas. *J. Appl. Phys.* **512**, 1389 (1998).

[2] X. H. Wang, H. Q. Jia, L. W. Guo, Z. G. Xing, Y. Wang, X. J. Pei, J. M. Zhou and H. Chen. *Appl. Phy. Lett.* **91**, 23 (2007).

[3] C. G. Park, G. H. Gu, B. H. Lee and D. H. Jang. *Ultramicroscopy* **127**, 114 (2013).

[4] M. Sumiya, N. Toyomitsu, Y. Nakano, J. Wang, Y. Harada, L. Sang, T. Sekiguchi, T. Yamaguchi and T. Honda. *APL Mater.* **5**, 016105 (2017).

[5] A. Kimura, N. Futagawa, A. Usui and M. Mizuta. *J. Cryst. Growth* **229**, 53 (2001).

[6] I. Vurgaftman and J. R. Meyer. *J. Appl. Phys.* **94**, 3675 (2003).

[7] T. Y. Wu, C. C. Chang, K. K. Tiong, Y. C. Lee, S. Y. Hu, L. Y. Lin, T. Y. Lin and Z. C. Feng. *Opt. Mater.* **35**, 1829 (2013).

[8] H. P. D. Schenk, M. Leroux and P. de Mierry. *J. Appl. Phys.* **88**, 1525 (2000).

[9] M. Hao, J. Zhang, X. H. Zhang and S. Chua. *Appl. Phy. Lett.* **81**, 5129 (2002).

[10] J. Yang, D.-G. Zhao, D.-S. Jiang, P. Chen, Z.-S. Liu, J.-J. Zhu, X. Li, W. Liu, F. Liang, L.-Q. Zhang, H. Yang, W.-J. Wang and M. Li. *Chin. Phys. B* **26**, 077101 (2017).

[11] Z. C. Feng, W. Liu, S. J. Chua, J. W. Wu, C. Yang, T. R. Yang and J. Zhao. *Thin Solid Films* **498**, 118 (2006).

[12] M. Leroux, N. Grandjean, B. Beaumont, G. Nataf, F. Semond, J. Massies and P. Gibart. *J. Appl. Phys.* **86**, 3721 (1999).

[13] T. Li, Q. Y. Wei, A. M. Fischer, J. Y. Huang, Y. U. Huang, F. a. Ponce, J. P. Liu, Z. Lochner, J. H. Ryou and R. D. Dupuis. *Appl. Phy. Lett.* **102**, 10 (2013).

[14] J. Wang, L. Wang, W. Zhao, Z. Hao and Y. Luo. *Appl. Phy. Lett.* **97**, 2008 (2010).

[15] C. Haller, J. F. Carlin, G. Jacopin, D. Martin, R. Butté and N. Grandjean. *Appl. Phy. Lett.* **111** (2017).

[16] R. Kaspi and K. R. Evans. *Appl. Phy. Lett.* **67**, 819 (1995).

[17] J. P. Liu, R. Q. Jin, J. J. Zhu, J. C. Zhang, J. F. Wang, M. Wu, J. Chen, Y. T. Wang and H. Yang. *J. Cryst. Growth* **264**, 53 (2004).

[18] J. S. Park, Y.-T. Moon, D.-J. Kim, N.-M. Park, T. Yao and S.-J. Park. *J. Phys. D Appl. Phys.* **41**, 165103 (2008).

[19] Y.-J. Lee, Y.-C. Chen and T.-C. Lu. *J. Phys. D Appl. Phys.* **44**, 224015 (2011).

[20] Z. Deng, Y. Jiang, W. Wang, L. Cheng, W. Li, W. Lu, H. Jia, W. Liu, J. Zhou and H. Chen. *Sci. Rep.* **4**, 6734 (2014).

[21] M. Senthil Kumar, J. Y. Park, Y. S. Lee, S. J. Chung, C. H. Hong and E. K. Suh. *Jpn. J. Appl. Phy.* **47**, 839 (2008).

[22] J. M. Gerard and G. Le Roux. *Appl. Phy. Lett.* **62**, 3452 (1993).

[23] F. C.-P. Massabuau, M. J. Davies, W. E. Blenkhorn, S. Hammersley, M. J. Kappers, C. J. Humphreys, P. Dawson and R. A. Oliver. *Phys. Status Solidi B* 1 (2014).

4

Growth of InGaN layers on InGaNOS substrates

The previous chapter presented the attempts to reach longer wavelengths on regular GaN template. It has been shown that an high indium content is difficult to reach because of the compositional pulling effect induced by the strain state of the InGaN layer on GaN template. As presented in section 2.2.3.2, we propose to overcome that limitation by growing a full InGaN structure on InGaN substrate. The InGaN pseudo-substrate which will be used in this thesis consists in a partially relaxed InGaN layer and is called InGaNOS. Its specificities will first be introduced. In a second part, we will present the results obtained for the regrowth of InGaN layers on InGaNOS substrates as compared to growth on GaN template. Finally, an X-Ray Diffraction (XRD) study conducted at the European Synchrotron will be presented.

4.1 InGaNOS substrates

InGaNOS substrates are manufactured by Soitec using their Smart Cut^{TM} technology [1]. The structure of the substrates is presented on Fig. 4.1 (a). It consists of a partially relaxed InGaN layer on burried oxide on a handle substrate. Handle substrates can be sapphire, silicon or glass. InGaNOS substrates are available in the 4-inch diameter and the technology is compatible with 6-inch diameter and above. The InGaN layer is patterned in square mesas which size can be adjusted from 1000×1000 μm^2 down to a few μm^2. In this study we will use mesas of 500×500 μm^2 or 800×800 μm^2. Fig. 4.2 (a) is a photo of an InGaNOS substrate, and Fig. 4.2 (b) is a zoom at the microscopic scale on one 300×300 μm^2 pattern. The lattice parameter of InGaN patterns can be adjusted from 3.190 Å up to 3.205 Å according to the final application. Higher lattice parameters have not been investigated yet. In this study, 3.190 Å, 3.200 Å and 3.205 Å a lattice parameters will be used. We will later refer to these InGaNOS substrates by naming them InGaNOS 3.190, InGaNOS 3.200 and InGaNOS 3.205, respectively.

The InGaNOS substrate is fabricated from a donor (Fig. 4.1 (a)). It consists of a $\simeq$230 nm-thick InGaN layer grown on GaN template, same type as the samples presented in section 3.1. To fabricate the InGaNOS substrate, a thin top layer of the donor is transferred onto burried oxide on sapphire substrate (Fig. 4.1 (b)). We will first present the properties of such donors and then see how the characteristics are affected by the relaxation process.

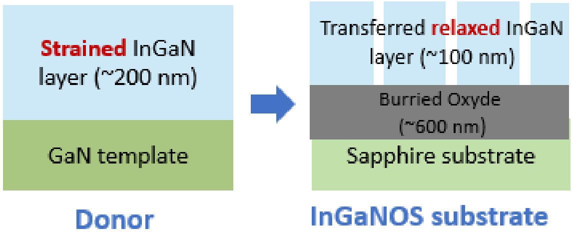

FIGURE 4.1 – Structures of donor and InGaNOS substrate. The InGaNOS substrate is obtained from the donor through the fabrication process described below.

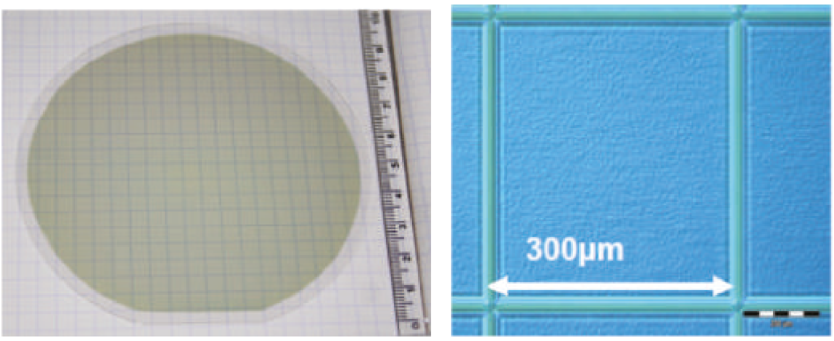

(a) (b)

FIGURE 4.2 – Photo of a 4-inch 3.205 ÅInGaNOS substrate with 300 × 300 μm^2 patterns (a) microscopic view of a 300 × 300 μm^2 pattern of InGaNOS 3.205 Å(b) from [2].

4.1.1 Fabrication process

Fig. 4.3 displays the different steps of the fabrication process of the InGaNOS substrates. First, the InGaN layer of the donor is implanted with hydrogen while a compliant layer is deposited onto a sapphire substrate. The InGaN donor template and the sapphire handle substrate are bonded by molecular bonding. Thanks to the Smart Cut^{TM} technology, the strained InGaN donor layer is then transferred onto the compliant layer of the sapphire substrate.

The second step of the process flow is the patterning of the InGaN layer by photolitography and dry etching. The strained patterns are then relaxed thanks to the compliant layer through a relaxation process using successive thermal annealings. The production of a uniform relaxed InGaN layer is challenging. Indeed, buckling is a competitive relaxation mechanism that leads to a wavy and/or cracked surface.

The relaxation process produces N-type polarity. A second layer transfer is therefore done to recover the top Ga-polarity. The full patterned wafer is bonded to a second sapphire handle substrate by molecular bonding. Finally, the first sapphire substrate is debonded for reuse.

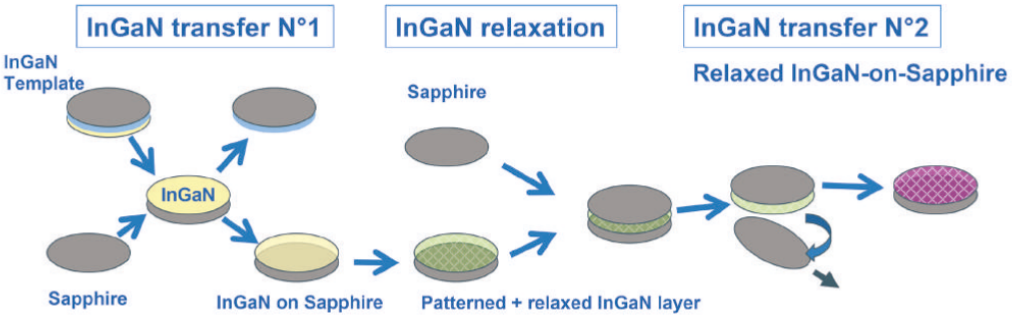

FIGURE 4.3 – Fabrication process of InGaNOS substrates [2].

4.1.2 Donors

To manufacture each nuance of *a* lattice parameter (3.190 Å, 3.200 Åand 3.205 Å), the starting material is a different type of donor with a different In content in the InGaN layer. To simplify the notation we will name "donor 3.190", "donor 3.200" and "donor 3.205" the three different types of donors corresponding, respectively, to the substrates InGaNOS 3.190, InGaNOS 3.200 and InGaNOS 3.205. We do not have access to the growth conditions of the donors but they were exhaustively characterized (see Table 4.1).

Corresponding InGaNOS *a* lattice parameter (Å)	In content (%)	measured *a* lattice parameter (Å)	RMS surface roughness (nm)
3.190	1.8	3.184	0.6
3.200	6.3	3.186	1.5
3.205	8.7	3.188	3.4

TABLE 4.1 – Characteristics of InGaNOS donors.

All the donors were first characterized by XRD to determine the In content in the layers. Fig. 4.4 displays the XRD reciprocal space mapping (RSM) of the donor 3.205 (with the highest indium content) on the (1 0 5) reflection. The spots corresponding to the GaN template (more intense at the top) and to the InGaN layer are aligned which implies that the InGaN layer is strained on the GaN template. The other donors present the same characteristics. The In contents of the donors are deduced from the *a* and *c* lattice parameters from the XRD RSM (see annex 1 for more details). In contents are 1.8 %, 6.3 % and 8.7 % for the donors 3.190, 3.200 and 3.205, respectively. The *a* lattice parameters were also measured thanks to a grazing incidence XRD setup (annex A) and listed in Table. 4.1. We can note the great difference between this measured *a* lattice parameter and the *a* lattice parameter that is expected to be reached after the relaxation process.

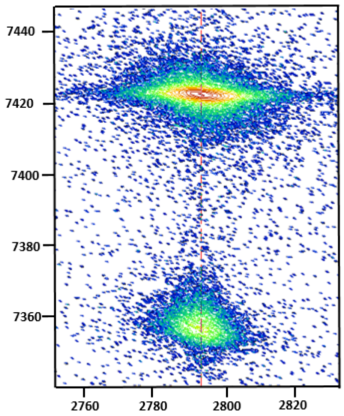

FIGURE 4.4 – Reciprocal space mapping of donor 3.205 on the (1 0 5) reflection.

Three room temperature PL mappings on the different types of donors kindly provided by Soitec are displayed in Fig. 4.5. These mappings show mean PL wavelengths at 370 nm, 390 nm and 399 nm respectively with small amplitude variations of 3 to 5 nm. The emission wavelength distribution does not show any regular pattern. On some donors, the disparity is between the edges and the center, on others it is between bottom and top of the samples. Accordingly, the indium content and/or the strain should also present some inhomogeneities on the resulting InGaNOS substrates.

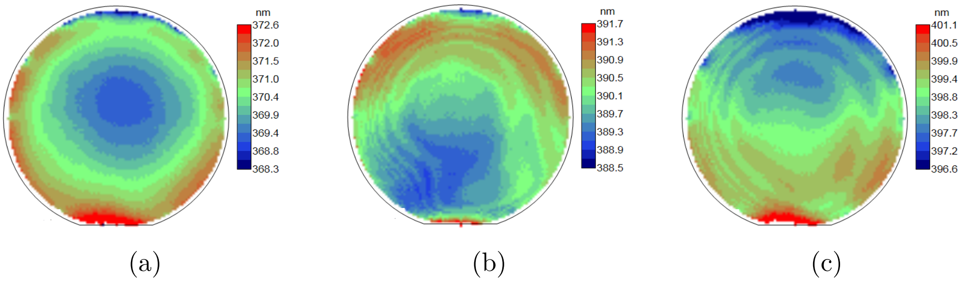

(a) (b) (c)

FIGURE 4.5 – PL mappings at room temperature of InGaNOS donors 3.190 (a), 3.200 (b), 3.205 (c).

The quality of the surface was assessed with AFM. Fig. 4.6 displays the surface of the three donors. An evolution of the surface quality with the indium content is observed. From a rather small roughness of 0.6 nm for donor 3.190, the surface presents some holes and the roughness increases to 1.5 nm for donor 3.200. Finally, the surface of donor 3.205

presents several V-pits, consequently raising the roughness to 3.4 nm. There is also a change in the morphology from the donor 3.190 to the donor 3.205 similar to what is observed when varying the growth rate for the InGaN thick layer on GaN template in chapter 3. The growth rate could have been used to increase the indium content, however we have no information about the donor growth conditions.

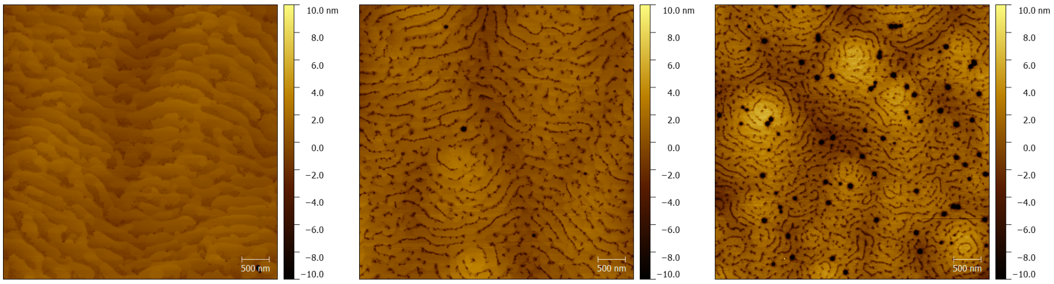

(a) (b) (c)

Figure 4.6 – 5x5 µm^2 AFM scans of donor 3.190 (a), donor 3.200 (b), donor 3.205 (c).

4.1.3 InGaNOS substrates

After the review of the characteristics of the donors, the properties of the InGaNOS substrates are evaluated. Table 4.2 summarizes their characteristics.

InGaNOS substrate nominal lattice parameter (Å)	measured *a* lattice parameter (Å)	measured *c* lattice parameter (Å)	In content (%)	Relaxation (%)
3.190	3.190	5.208	3.2	19.7
3.200	3.199	5.228	6.6	50.1
3.205	3.205	5.242	8.9	54.8

Table 4.2 – Lattice parameters of InGaNOS substrates, resulting indium contents and relaxation percentages.

Fig. 4.7 (a) displays the $2\theta\chi$ spectra on the (3 0 0) reflection (in-plane measurement). The contributions of the K-α1 (lower angle and higher intensity) and K-α2 (higher angle) peaks appear on the graph. The in-plane lattice parameters of InGaNOS substrates deduced from the position of the K-α1 peaks are placed on a scale on Fig. 4.7 (b) together with the ones of free-standing GaN, GaN template on sapphire and relaxed InGaN with 15 % content (average In content needed in MQWs for blue LEDs). Compared to GaN template, InGaNOS substrates present a significant increase in *a* lattice parameter. This is going towards the right direction, getting closer to the lattice parameter of relaxed

$In_{0.15}Ga_{0.85}N$. With further development of the substrates, even higher a lattice parameters may be reached, possibly with smaller mesas.

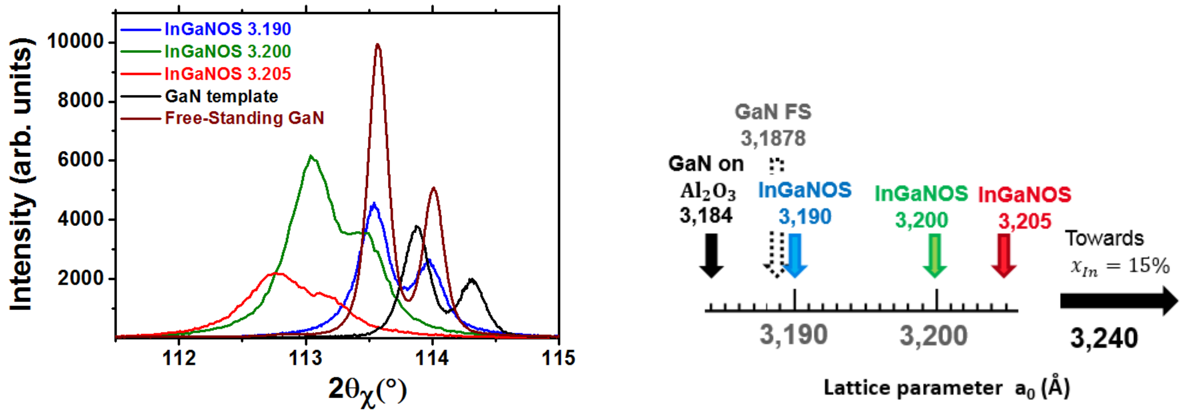

(a) (b)

FIGURE 4.7 – In-plane XRD spectra on the (3 0 0) reflection of the three InGaNOS substrates (3.190 (blue), 3.200 (green) and 3.205 (red) and with the GaN references (GaN free-standing substrates (brown) and GaN template on sapphire (black)) (a) Lattice parameters of the above materials placed on a scale. The lattice parameter of relaxed $In_{0.15}Ga_{0.85}N$ is also displayed (b).

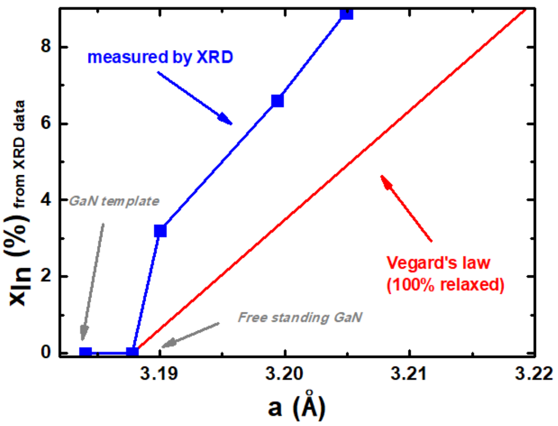

FIGURE 4.8 – In content estimated by XRD as a function of a lattice parameter (estimated by grazing incidence X-ray see 4.7) spectra (black curve) and corresponding Vegard's law (red curve).

The c lattice parameter was also measured using out-of plane XRD. From the knowledge of a and c, the In content of the substrates is determined and presented in Table. 4.2 (see annex A for more details). Larger In contents are found compared to the measurement conducted on the donors. This difference may be explained by the spatial inhomogeneities or by a disparity between two different wafers in the case of InGaNOS 3.200 and InGaNOS 3.205. However, the significant difference in indium content between the donor and the substrate in the case of InGaNOS 3.190 still remains unexplained (3.2 % against 1.8

%). Nonetheless, the measurement was confirmed on several wafers for the substrates. As only one donor was measured, the discrepancy may originate from the fact that this wafer of donor 3.190 was not representative. Based on these findings, the relaxation percentage was calculated with respect to bulk GaN (a=3.1878 Å). The relaxation percentages vary from 19.7 % for InGaNOS 3.190 to 54.8 % for InGaNOS 3.205. The InGaN layers constituting the InGaNOS substrates are thus partially relaxed. The plot of the In content of the substrates as a function of a lattice parameter together with Vegard's law which corresponds to the 100 % relaxed case is given in Fig. 4.8.
To cross-check the measurements of the a and c lattice parameters, we realized reciprocal space mappings of the InGaNOS substrates on the asymmetrical reflection (1 0 5). If we grow layers on the substrates, this will later be the only way to evaluate the a lattice parameter of the substrates as the in-plane measurement with grazing incidence will no longer be possible.

While the InGaN layers from the donors presented a high XRD RSM intensity on the (1 0 5) asymetrical reflection, the measurement on the InGaNOS substrates is much more difficult. The signal detected from InGaNOS 3.200 and 3.205 substrates is not large enough to measure the lattice parameters. This is probably a consequence of the implantation process. The determination of a and c lattice parameters with this method for InGaNOS 3.190 gives the same In content values as previously estimated.
Table 4.3 summarizes the data of the In content, the surface roughness (from AFM) and the Full Width at Half Maximum(FWHM) of the Rocking Curve (RC) on the (0 0 2) reflection. The values of the FWHM of RC vary from 649 to 3026 arcsec for the three InGaNOS substrates (the typical FWHM for GaN template is about 300 arcsec). The evolution as a function of the substrate a lattice parameter is shown in Fig. 4.9. The FWHM increases with the substrate a lattice parameter.

InGaNOS substrate nominal lattice parameter (Å)	In content (%)	FWHM RC (0 0 2)	RMS surface roughness (nm)
3.190	3.2	649	1.0
3.200	6.6	2009	1.3
3.205	8.9	3026	2.4

Table 4.3 – In content, FWHM of RC and RMS of InGaNOS substrates.

Just like for the donors, the surface of the InGaNOS substrates was scanned with AFM. The image of the surface of the samples is displayed in Fig. 4.10. The surfaces look very similar to the donor's surfaces showed above. The roughness evolution is plotted in Fig. 4.11 for the donors and the InGaNOS substrates. As observed, there is indeed no signi-

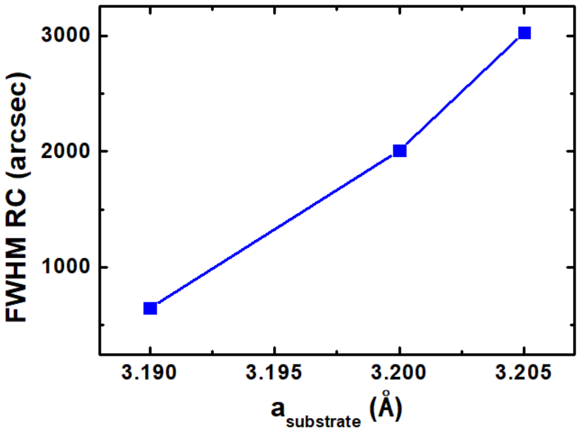

FIGURE 4.9 – FWHM of the RC on the (0 0 2) reflection as a function of the substrate *a* lattice parameter for the InGaNOS substrates.

ficant evolution of the roughness between the donors and the InGaNOS substrates. For both, the roughness increases with the nominal *a* lattice parameter as expected. The density and average diameter of V-defects was determined on donor 3.205 and on InGaNOS 3.205. While the density of V-defects is about 3.3 $\times 10^8$ cm^{-2} for both samples, the average diameter of V-pits increases from 63 nm for donor 3.205 to 81 nm for InGaNOS 3.205 substrate. The broadenning might be a consequence of the relaxation process. Overall, the aspect of the surface is equivalent between the donors and the InGaNOS substrates, the different steps of the fabrication process preserved the material quality.

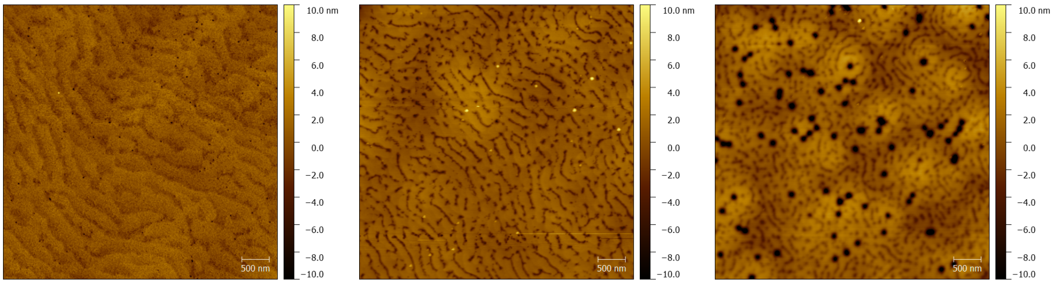

(a) (b) (c)

FIGURE 4.10 – 5x5 µm^2 AFM scans of InGaNOS substrates 3.190 (a), 3.200 (b), 3.205 (c).

InGaNOS substrates are epi-ready with reasonable surface roughness and present larger *a* lattice parameters as compared to GaN template and even compared to free-standing GaN. This feature should allow for an easier incorporation of indium in the quantum wells. Next, we will show that the InGaN buffer regrowth on InGaNOS substrates will already present a decreased compositional pulling effect and an improvment of the structural quality.

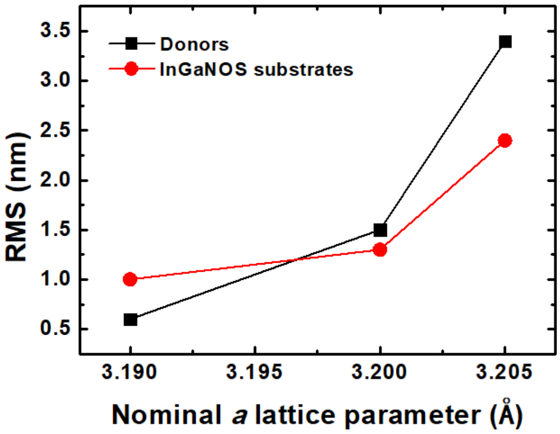

FIGURE 4.11 – RMS as a function of the nominal *a* lattice parameter for the donors (black) and for the InGaNOS substrates (red).

4.2 Regrowth of InGaN layers on InGaNOS

To evaluate the impact of the substrate *a* lattice parameter on indium incorporation, about 200 nm-thick InGaN layers were grown on GaN template and on InGaNOS 3.190, 3.200 and 3.205. The corresponding structures are shown in Fig. 4.12.

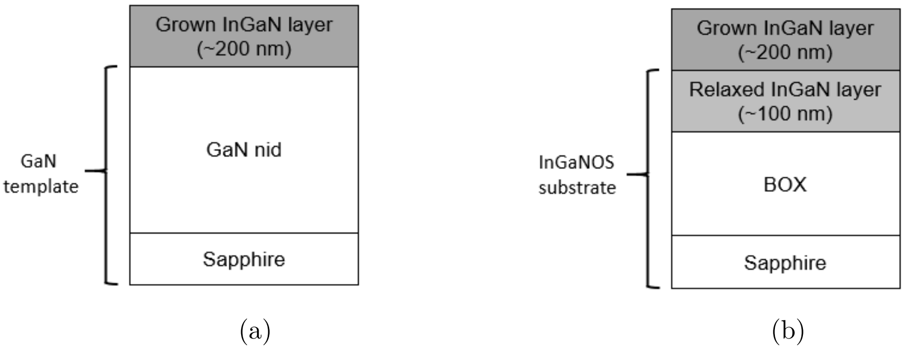

FIGURE 4.12 – Structures of the InGaN on GaN (a) and InGaN on InGaNOS (b) samples.

As the InGaNOS substrates are only partially relaxed, in order to grow a stress-free InGaN layer, one must not aim for the In content of the substrate but should aim for the same *a* lattice parameter. The desired In content for a stress-free layer will therefore be smaller as the In content of the InGaNOS substrate. The corresponding indium contents for a stress-free layer is given in Table. 4.4 are calculated using Vegard's law. These tailored indium content are 0.6 %, 3.5 % and 4.9 % for InGaN layers on InGaNOS 3.190, InGaNOS 3.200 and InGaNOS 3.205 respectively.

First, the same growth conditions are tested on the four different substrates to understand the influence of the substrate's *a* lattice parameter on the InGaN regrown layer. We aimed at an indium content of about 4 % for the first trial as it is in between the

In content required for a stress-free layer on InGaNOS 3.200 and on InGaNOS 3.205. To ensure the growth is occuring under the same exact conditions, all substrates were coloaded together in the same growth run.

Substrate	substrate *a* lattice parameter (Å)	In content of the substrate (%)	Tailored In content (%) for stress-free InGaN layer
GaN template	3.184	-	-
InGaNOS 3.190	3.190	3.2	0.6
InGaNOS 3.200	3.200	6.6	3.5
InGaNOS 3.205	3.205	8.9	4.9

TABLE 4.4 – Lattice parameters of GaN, InGaNOS 3.190, InGaNOS 3.200 and InGaNOS 3.205 substrates, In content of the substrates and tailored In content needed to grow stress-free InGaN buffer layers on the different substrates (calculation from Vegard's law).

4.2.1 Influence of substrate on emission wavelength and In content

The PL spectra of the InGaN layers on GaN and InGaNOS at low temperature are displayed in Fig. 4.13 (a). The layers were characterized using a 325 nm He-Cd laser. From 371.1 nm on GaN, the emission wavelength increases to 380.0 nm on InGaNOS 3.190, 381.1 nm on InGaNOS 3.200 and 384.3 nm on InGaNOS 3.205. The evolution of the PL emission wavelength with the substrate *a* lattice parameter is plotted in 4.13 (b).

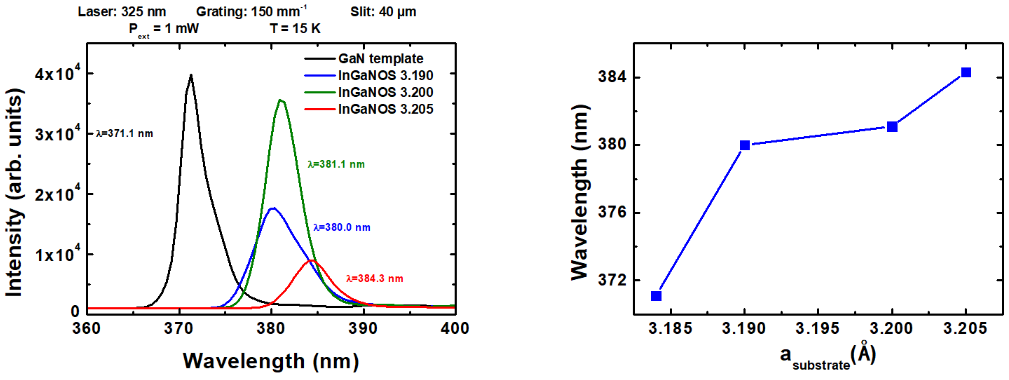

(a) (b)

FIGURE 4.13 – PL spectra at low temperature ($\simeq$ 15 K) of InGaN layer on GaN template (black), InGaNOS 3.190 (blue), InGaNOS 3.200 (green), InGaNOS 3.205(red). The layers were characterized using a 325 nm He-Cd laser as excitation source

For the determination of the In content, some RSM were realized on the (1 0 5) asymmetrical reflection. Fig. 4.14 displays them for the InGaN layers grown on GaN template (a), InGaNOS 3.190 (b) and InGaNOS 3.205 (c).

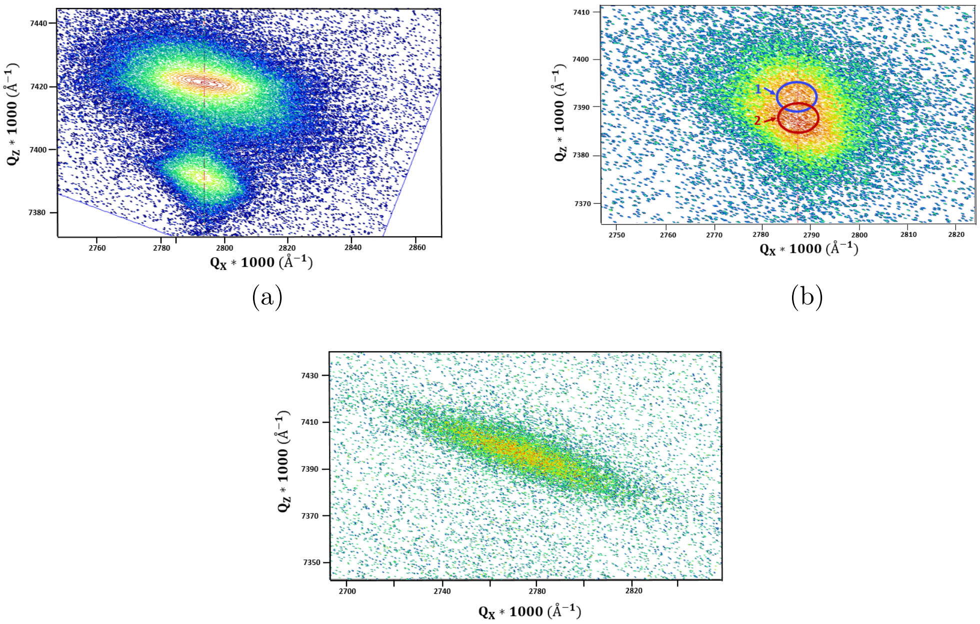

(a) (b)

(c)

FIGURE 4.14 – XRD Reciprocal Space Mapping (RSM) on the (1 0 5) reflection for InGaN layer on GaN template (a), on InGaNOS 3.190 (b), on InGaNOS 3.205 (c). For (b) blue and red circles are signatures of InGaNOS 3.190 substrate and InGaN layer respectively.

For the regrowth on GaN template(Fig. 4.14 (a)), we clearly distinguish the signal of the GaN template which is the most intense and at the top. The two spots are perflectly aligned which reveals that the InGaN layer is strained on GaN and the In content is estimated to be 3.0 % in the layer. On the XRD RSM of the InGaN layer on InGaNOS 3.190 (Fig. 4.14 (b)), the two spots are very close to each other and hard to dissociate. From the previous measurements, the upper spot labelled as 1 is attributed to the substrate (with an indium content of 3.3 %, close to what was previously determined). The lower spot labelled as 2 aligned with the first one correponds to the InGaN layer, and the indium content is determined to be 3.9%. The XRD RSMs of the InGaN layers on InGaNOS 3.200 and 3.205 are very similar. The RSM of the InGaN layer on InGaNOS 3.205 is given on Fig. 4.14 (c). Compared to the two other mappings (Fig. 4.14 (a) and Fig. 4.14 (b)), the two scans have a different aspect as the substrate does not give any signal like previously observed. The shape of the spot corresponding to InGaN is also different. The enlargement in the observed direction compared to the two other InGaN layers can be attributed to an increase of the mosaic tilt or an increase of the screw and mixed dislocation density [3]. In contents of 4.2% and 4.7% were found for the layers on InGaNOS 3.200 and 3.205 respectively. The data on the lattice parameters and the In content is summarized in Table 4.5.

Fig. 4.15 (a) shows the In content of the layer as a function of the substrate's a lattice parameter. The evolution coincides with PL measurements. Although the curve presents a positive slope, the evolution of the In content is not as significant as one could expect especially between the three InGaNOS substrates. Indeed, for larger substrate's *a* lattice parameter, the compositional pulling effect reduction should allow for a larger incorporation of indium. That phenomenon is responsible for the difference in indium content from 3.0 to 3.9 % between the InGaN layers on GaN template and InGaNOS 3.190. However, one should note that in the case of the InGaN layers on InGaNOS 3.200 and 3.205 we are actually above or very close to the tailored indium content (for stress-free InGaN buffer layers) previously determined. In that case, the compositional pulling effect is not clearly evidenced as the indium atoms present on the surface can already be easily incorporated without deforming the lattice. Since the substrates are themselves partially strained, this could also have an effect on indium incorporation. Considering the *a* lattice parameters of the layers (all the layers are grown pseudomorphically) and their In content (equation 1.9), the strain is likely to be very different in the four InGaN layers.

substrate	measured *a* lattice parameter (Å)	measured *c* lattice parameter (Å)	In content (%)	Strain (%)
GaN template	3.185	5.210	3.0	-0.41
InGaNOS 3.190	3.191	5.214	3.9	-0.34
InGaNOS 3.200	3.200	5.209	4.2	-0.084
InGaNOS 3.205	3.205	5.209	4.7	0.027

Table 4.5 – Lattice parameters, In contents and strain of the InGaN layers on GaN, InGaNOS 3.190, InGaNOS 3.200 and InGaNOS 3.205.

Fig.4.15 (b) shows the strain in the InGaN layers as a function of the substrate *a* lattice parameter. The InGaN layer strained on GaN template shows a compressive strain of -0.41 %. For the other layers, the strain can be considerated as low (especially in the case of the InGaN layer on InGaNOS 3.200). For the InGaN layer on InGaNOS 3.205, the strain is above zero, the InGaN layer is therefore under slight tensile strain (contrary to all other layers that are under compressive strain). There is a strong decrease of the strain amplitude of the layer thanks to the use of the InGaNOS substrates. When aiming at high indium content in the quantum wells grown on the different InGaN layers, this should allow for a larger indium incorporation and the compositional pulling effect reduction should be demonstrated more significantly.

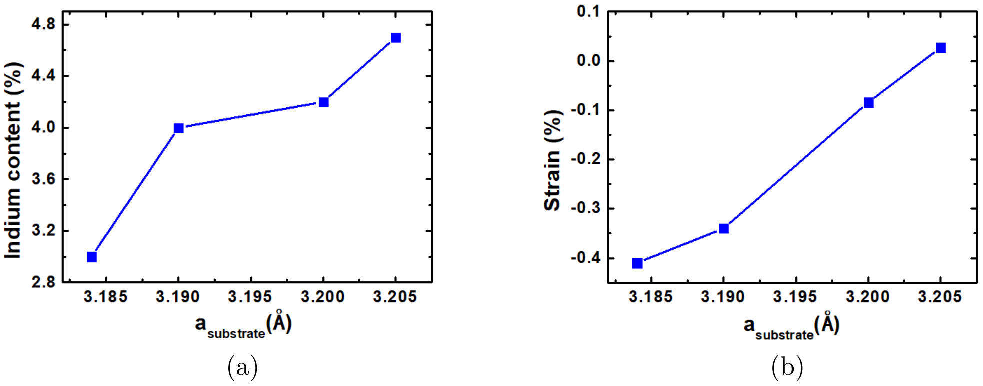

FIGURE 4.15 – Evolution of the In content (a) and strain (b) of the InGaN regrown layers as a function of substrate *a* lattice parameter.

4.2.2 Assessment of the quality of the layers

substrate	In content (%)	RMS (nm)	FWHM RC (0 0 2) (arcsec)	FWHM PL (nm)	V-pit density (cm^{-2})
GaN template	3.0	1.8	414	4.1	5.8×10^{8}
InGaNOS 3.190	3.9	4.5	395	6.4	1.2×10^{9}
InGaNOS 3.200	4.2	4.2	933	4.6	2.0×10^{9}
InGaNOS 3.205	4.7	9.1	1707	5.2	1.8×10^{9}

TABLE 4.6 – RMS, FWHM RC, FWHM PL and V-pit density of InGaN layers grown on InGaNOS. The PL spectra were measured at 15K.

The surface quality of the layers was assessed using AFM. By comparing the FWHM of the RC on the (0 0 2) reflection, the structural quality was looked at. Table 4.6 gathers the corresponding data as well as the FWHM of the PL spectra at LT. The PL linewidth does not follow a trend, all the FWHMs are about 5 nm. This may be due to the fact that the homogeneity in In composition does not change significantly. On the contrary, the surface roughness and the V-pit density change significantly from one sample to another. The AFM scans are displayed in Fig. 4.16 and the evolution of the surface roughness and the V-pit density is plotted as a function of the substrate's *a* lattice parameter in Fig. 4.17 (a). Although the layers have similar indium contents, the surface roughness increases with the substrate's *a* lattice parameter.

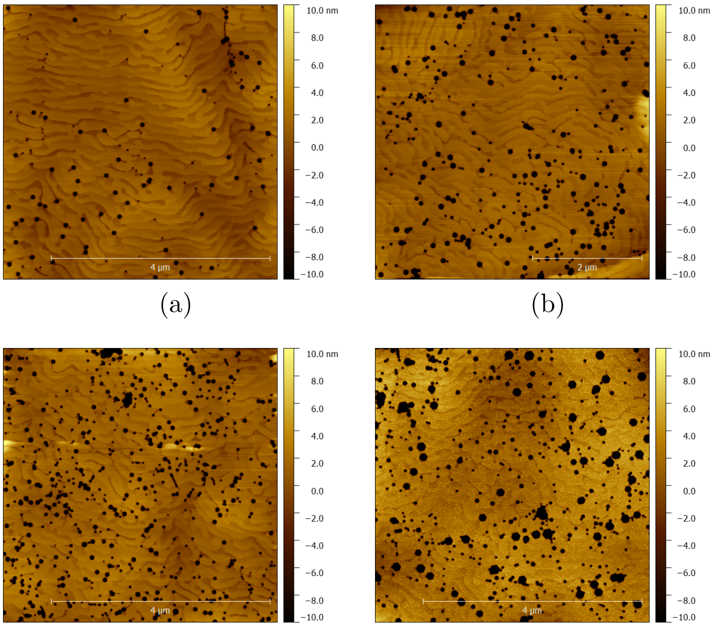

(a) (b)

(c) (d)

FIGURE 4.16 – 5x5 µm^2 AFM scans of InGaN layer on GaN template (a), on InGaNOS 3.190 (b), on InGaNOS 3.200 (c), on InGaNOS 3.205 (d).

The V-pit density follows the same trend. Yet, it is a bit smaller for the InGaN layer on InGaNOS 3.205 compared to the InGaN layer on InGaNOS 3.200 but we can also see that V-pits have a larger diameter on InGaN layer on InGaNOS 3.205. Except for the layer on GaN template, the V-pit densities that are reached already at this regrowth stage are larger than $1 \times 10^9 cm^{-2}$. The V-pit density is related to the dislocation density present already in the substrate and to the strain in the layer. Indeed, as some numerous V-pits are already present on the surface of InGaNOS 3.205 substrate and InGaNOS 3.200 substrate (to a smaller extent), after the growth of the InGaN layer, large V-pit densities are found. Furthermore, the V-pits that were already present on the substrate are enlarged. The additional V-pits come from dislocations. For the layer on InGaNOS 3.205, the V-pit density increased by a factor of six compared to the substrate alone (from 3.3 $\times 10^8$ to 1.8 $\times 10^9$). The observation of numerous additional V-pits in these layers under low compressive strain mitigates the hypothesis identifying V-pits as the principal relaxation mechanism [4], [5], [6], [7]. We will later see how it is possible to significantly decrease the density of V-pits in the regrown layer.

The FWHM of the RC on the (0 0 2) reflection is plotted as a function of the substrate's a lattice parameter in Fig. 4.17 (b). We observe that samples on GaN template and InGaNOS 3.190 show close values of 414 arcsec and 395 arcsec, respectively. It shows that we were able to grow an InGaN layer of good structural quality on InGaNOS 3.190 although the original substrate showed a FWHM of 650 arcsec. Then, for the layers on InGaNOS 3.200 and InGaNOS 3.205, the FWHM strongly increases and reaches very high values of 933 and 1707 arcsec, respectively. Nevertheless, compared to the substrates, there is a significant improvment since the FWHM of the RC has been divided by two. We show that we are able to grow layers of a "reasonnable" structural quality on InGaNOS substrates even if the implanted InGaN layer constituing the substrate has some additional defects.

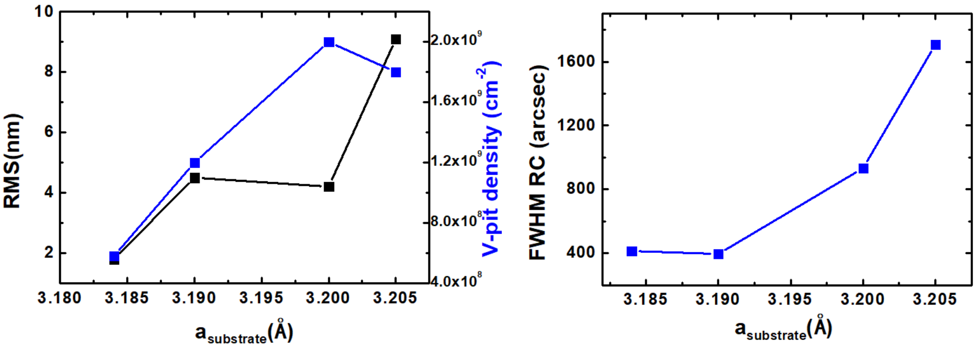

(a) (b)

FIGURE 4.17 – RMS surface roughness, V-pit density (a) and FWHM of the XRD RC on the (0 0 2) reflection (b) as a function of substrate *a* lattice parameter.

4.2.3 PL behavior with temperature

The InGaN layers grown on GaN template and on the three InGaNOS substrates were characterized by PL as a function of temperature (15-290 K) using a 325 nm He-Cd laser as excitation source. The localization and activation energies are given in Table. 4.7. The values of localization energies range between 34 and 43 meV and are close to the ones reported for the InGaN layers on GaN template of chapter 3. However it is difficult to compare the samples as here the InGaN layers are four times thicker but with an average indium content two times smaller. The activation energies of the PL thermal decay are calculated to be between 60 meV and 107 meV. We note an increase of this activation energy as a function of the indium content for the first three samples. It is possible that as the indium content increases, there are more potential fluctuations that would trap the carriers further, preventing them to get to the nonradiative recombination centers but this hypothesis could not be verified.

With this series of InGaN layers grown on GaN template and InGaNOS substrates, the indium content increase with the *a* substrate's lattice parameter is demonstrated. The compositional pulling effect is thus demonstrated even if it is for a small range of indium content. The strain in these InGaN layers also decreases as a function of the substrate's *a* lattice parameter. Even if these layers show high V-pit densities for this first trial, we will demonstrate in the next paragraph that it is possible to significantly reduce it.

substrate	In content (%)	E_{loc} (meV)	$E_{activation}$ (meV)
GaN template	3.0	34	60
InGaNOS 3.190	3.9	42	105
InGaNOS 3.200	4.2	43	107
InGaNOS 3.205	4.7	39	74

TABLE 4.7 – Localization energies and activation energies of the PL thermal decay for InGaN layers grown on GaN template and on the three InGaNOS substrates.

4.2.4 Insertion of GaN interlayers

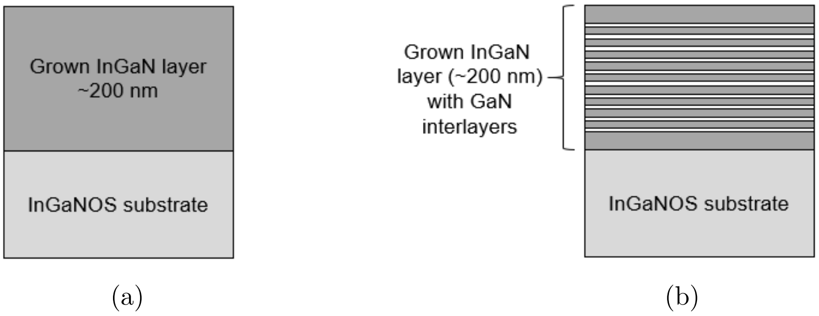

(a) (b)

FIGURE 4.18 – Structures of InGaN layers on InGaNOS. The reference is on the left (a). For the second structure, 10 GaN interlayers of 2 nm were regularly placed in the InGaN layer (b).

As mentionned in Chapter 2, in the attempts to grow thick InGaN layers, a recent approach is based on the use of GaN interlayers placed periodically in the InGaN buffer. The improvement of the quality of the surface was first demonstrated by Pantzas *et al.* [8] by inserting 2 nm-thick GaN interlayers in a 126 nm thick InGaN layer with an indium content of 9%. They showed that they were able to increase the critical thickness thanks to this method but the mean average composition of the InGaN is decreased from 9% to 8%. By using the same GaN interlayers in a 144-nm thick InGaN layer with 11 % indium content, Van den Broeck *et al.* report a suppression of the V-pits at the surface and lower linewidths for the PL and XRD spectra [9] as well as a very slight decrease of the In content down to 10.5 %. In both of these papers, the interlayers were placed into layers that were elastically relaxed and for which the 3D growth had started. With the GaN interlayers, the critical thickness is increased.

That solution was also implemented in our structure to improve the surface and structural quality of the InGaN layers on InGaNOS 3.205. The two different structures are displayed on Fig. 4.18. Ten GaN interlayers of 2 nm are periodically inserted in the InGaN buffer (approximately one every 20 nm). For both samples, the InGaN buffer is Si-doped.

The two samples were thoroughly characterized using PL, XRD and AFM. The corresponding data are given in Table 4.8 and Table 4.9.

Interlayers	*a* lattice parameter (Å)	PL emission wavelength (nm)	In content (%)	Strain (%)
No	3.2057	373.4	2.2	0.32
Yes	3.2054	374.7	2.7	0.26

Table 4.8 – Characteristics of the InGaN layers grown on InGaNOS 3.205 without and with GaN interlayers.

The PL emission spectra of the two samples are given in Fig. 4.19. The PL emission wavelength increases from 373.4 to 374.7 nm which suggest a very slight increase in indium content. The PL linewidth is increased from 5.2 nm to 6.5 nm. The higher number of transitions reavealed by the larger PL linewidth may originate from the indium inhomogeneity resulting from the interfaces with the GaN interlayers.

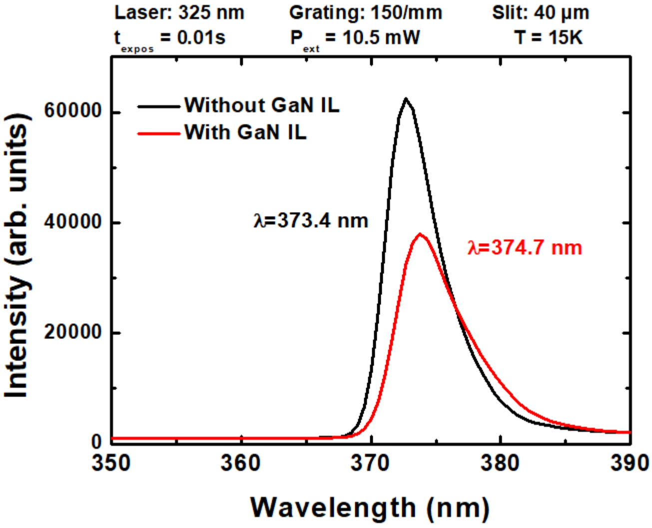

(a)

Figure 4.19 – PL spectra of samples without (black) and with (red) GaN interlayers. Samples were characterized at 15 K with a 325 nm He-Cd laser as an excitation source.

The indium content and the strain were calculated using the *a* and *c* lattice parameters from XRD measurements. With the implementation of the GaN interlayers, the indium content was increased from 2.2 to 2.7 %. This is unexpected as the contrary was observed elsewhere (see above) and might be due to a different growth process. Because the indium content is smaller than the tailored In content for a stress-free InGaN layer which is of 4.9 % for InGaNOS 3.205 (see Table 4.4), the layers are in tensile strain. As the indium content was increased, the tensile strain was reduced from 0.32 % to 0.26 %. The *a* lattice parameter was measured to be 3.2057 Å and 3.2054 Å without and with interlayers respectively. In both cases we were able to maintain the *a* lattice parameter of the substrate which is very important for the following step of the MQWs.

Interlayers	RMS (nm)	FWHM RC (0 0 2) (arcsec)	V-pit density (cm^{-2})	PL linewidth (nm)
No	2.5	1708	3.5 $\times 10^8$	5.2
Yes	1.0	795	0.3 $\times 10^8$	6.5

TABLE 4.9 – Data for the quality assessment of InGaN layers grown on InGaNOS 3.205 with or without interlayers.

Fig. 4.20 displays the rocking curves on the (0 0 2) reflection for the two structures. With the implementation of the GaN interlayers, the FWHM decreases from 1708 to 795 arcsec. This decrease emphasizes the significant improvement of the structural quality thanks to the use of the GaN interlayers.

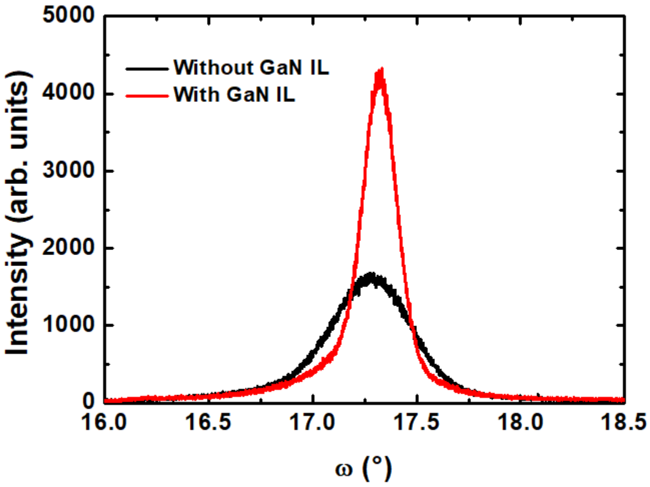

(a)

FIGURE 4.20 – Rocking curves on the (0 0 2) reflection for samples without (black) and with (red) GaN interlayers.

Fig. 4.21 displays the AFM scans of the surface of the two samples. A clear improvement of the surface quality is shown after the implementation of the GaN interlayers while surface morphology does not change significatively. The surface roughness is decreased from 2.5 nm to 1 nm. The V-pit density is divided by a factor of ten from 3.5 $\times 10^8$ cm^{-2} to 0.3 $\times 10^8$ cm^{-2}. The GaN interlayers are believed to smoothen the surface and as they are regularly placed, they could fill the V-pits before they get too big. A similar behavior was observed by Liu *et al.* [10] when growing p-doped InGaN alternatively with p-doped

GaN. Additional TEM characterizations would have been interesting to conclude on the microscopic explanation of the phenomenon.

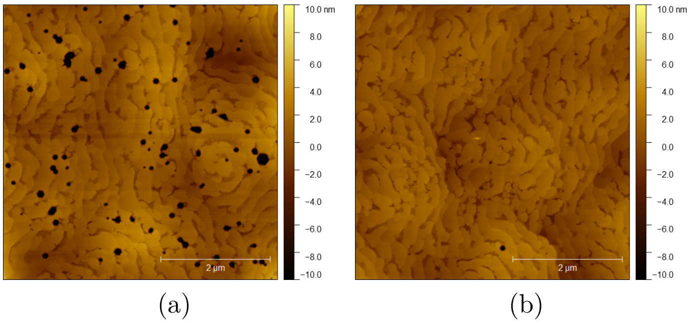

(a) (b)

FIGURE 4.21 – 5x5 µm^2 AFM scans of InGaN layers grown on InGaNOS 3.205 without (a) and with (b) GaN interlayers.

We showed that thanks to the implementation of the GaN layers, the quality of the surface of the InGaN layer grown on InGaNOS substrates can be improved. The surface roughness and the density of V-pits are significantly decreased. Therefore we should be able to increase the thickness of the n-doped InGaN regrown layer which is crucial to realize an efficient LED (see 5.3.3.1).

4.2.5 Variation of the growth temperature

Using the structure of the InGaN buffer on InGaNOS 3.205 with GaN interlayers (Fig. 4.18 (a)), we studied the impact of the growth temperature on the indium content and on the structural quality of the InGaN layer. The growth temperature was changed from 850 ˚C to 875 ˚C and then 900 ˚C. The samples were characterized using PL, XRD and AFM. The corresponding data can be found in Tables 4.10 and 4.11.
Fig. 4.22(a) displays the PL spectra of the three samples and the evolution of the PL emission wavelength as a function of growth temperature is given by Fig. 4.22 (b). As expected, PL wavelength decreases as growth temperature increases, the emission wavelength shifts from 404.2 nm to 382.5 nm.
As shown above, the indium content and the strain in the InGaN layers were calculated from the lattice parameters measured by XRD. Fig. 4.23 shows the evolution of the two quantities as a function of the growth temperature. The indium contents range from 3.9 % for the higher growth temperature to 7.5 % for the lower growth temperature. The strain varies from 0.17 % to -0.26 %, the sign of the strain changes as we shift from a compressive strain to a tensile strain. The InGaN layer grown at 875 ˚C is a stress-free layer with an indium content of 5.5 %. This In content for a stress-free InGaN layer is slightly larger than the 4.9 % In content found previously because here the a lattice parameter is 3.207 Å(instead of 3.205 Å).
The growth temperature also affects the quality of the InGaN layers. As stated in Chapter

Growth temperature (˚C)	*a* lattice parameter (Å)	PL emission wavelength (nm)	In content (%)	Strain (%)
900	3.207	382.5	3.9	0.17
875	3.207	392.1	5.5	0.00
850	3.205	404.2	7.5	-0.26

TABLE 4.10 – Characteristics of the InGaN layers grown on InGaNOS 3.205 grown at different temperatures.

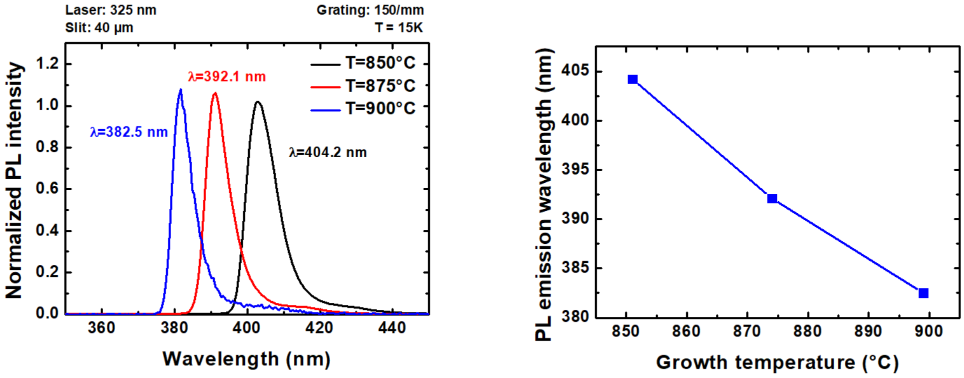

(a) (b)

FIGURE 4.22 – PL spectra of InGaN layers grown on InGaNOS 3.205 grown at 850 ˚C (black), 875 ˚C (red) and 900 ˚C (blue) (a). Evolution of the PL emission wavelength as a function of the growth temperature (b). The samples were characterized at 15 K using a 325 nm He-Cd laser as the excitation source.

1 and Chapter 2, a lower growth temperature usually goes with a decrease of the structural quality. Fig. 4.24 displays the AFM scans of the surface for the three different growth temperatures. As the temperature is increased, the surface shows less defects and appears smoother. Indeed, the surface roughness decreases as a function of the growth temperature as shown in Fig. 4.25 (a) changing from 9.6 nm for the smallest growth temperature to 1.5 nm for the largest growth temperature. The V-pit density is divided by a factor ten from 1.4 $\times 10^9$ at 850 ˚C to 1.5 $\times 10^8$ at 900 ˚C. The V-pit density does not follow the tendency of the strain amplitude since the sample which has zero strain is not the one with the smallest V-pit density. In our layers, the V-pit formation is therefore not influenced by the strain but proportional to the indium content.

The FWHM of the rocking curve on the (0 0 2) reflection is plotted in Fig. 4.25 (a) as a function of the growth temperature. It decreases from 1580 to 964 arcsec between the lower and higher growth temperature. The PL linewidth whose evolution is shown in Fig. 4.25 (b) decreases from 9.9 nm to 7.1 nm with the increasing growth temperature. The larger energy spanning of the different radiative recombination paths may be related to

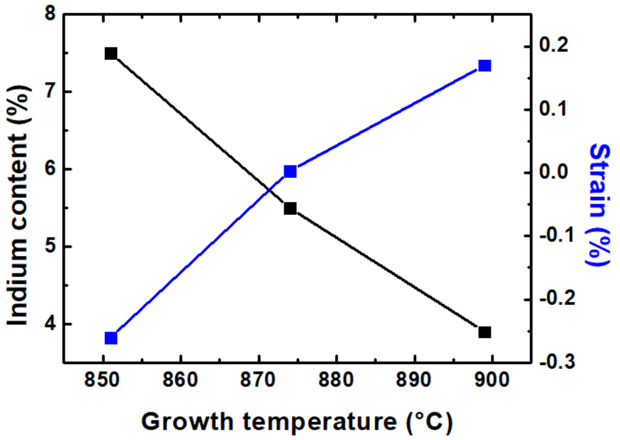

(a)

Figure 4.23 – Indium content and strain calculated from XRD measurements as a function of growth temperature for the InGaN layers grown on InGaNOS 3.205.

Growth temperature (˚C)	RMS (nm)	FWHM RC (0 0 2) (arcsec)	V-pit density (cm^{-2})	PL linewidth (nm)
900	1.1	964	1.5 $\times 10^8$	7.1
875	6.5	1244	9.6 $\times 10^8$	8.3
850	9.6	1580	1.4 $\times 10^9$	9.9

Table 4.11 – V-pit density, RMS roughness, PL linewidth and FWHM of the RC on the (0 0 2) reflection for InGaN layers grown on InGaNOS 3.205 at different growth temperatures.

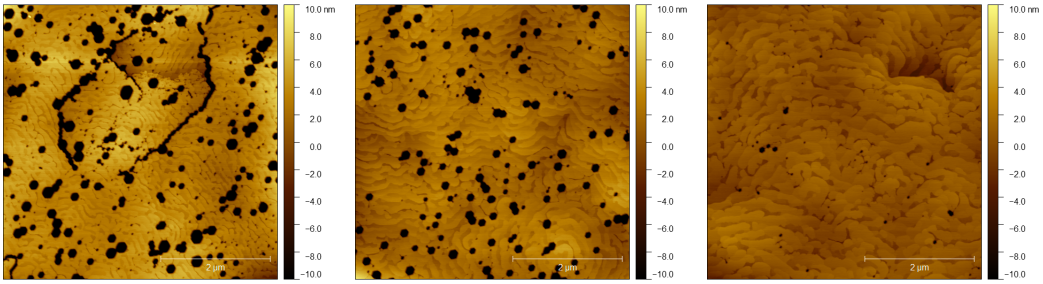

(a) (b) (c)

Figure 4.24 – 5x5 µm^2 AFM scans of InGaN layers grown on InGaNOS 3.205 grown at 851 ˚C (a), 874 ˚C (b) and 899 ˚C (c).

a higher degree of inhomogeneity of the indium content in the InGaN alloy which may be solely related to the higher indium content. It could also be related to the increasing V-pit density. Indeed, it has been shown in section 1.4.6 that the V-pit sidewalls exhibit a luminescence which have a different emission energy compared to the luminescence from the surface around the V-pits. The overall decrease of the structural quality might be explained by an enhanced incorporation of the impurities with the lowering of the growth temperature [11].

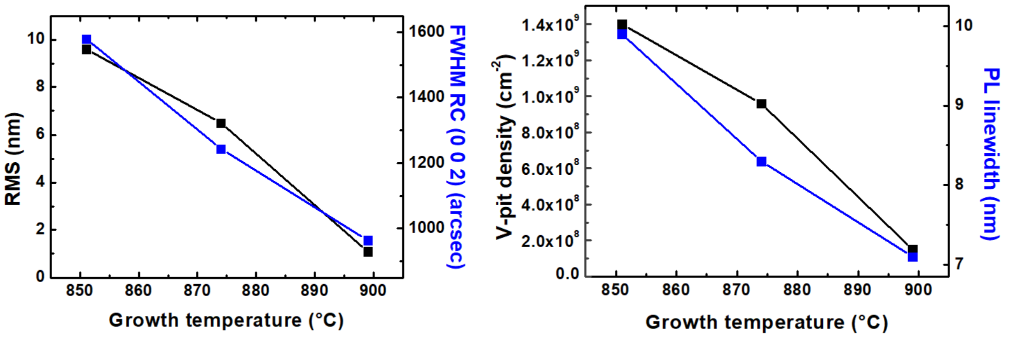

(a) (b)

FIGURE 4.25 – RMS (black) and FWHM of the rocking curve (blue) on the (0 0 2) reflection (a), V-pit density (black) and PL linewidth (blue) (b) for the three InGaN layer grown on InGaNOS 3.205 at different growth temperatures.

Variations on the growth temperature showed that the structural quality increased as a function of growth temperature while the V-pit density decreased. We were able to grow a stress-free InGaN layer with a 5.5 % In content on InGaNOS 3.205. In our following experiments, we will prefer InGaN layers with GaN interlayers grown at higher temperatures (not too high to keep the tensile strain to a reasonnable value).

4.3 ESRF experiment

4.3.1 Description of the experiment

We were given the opportunity to scan one of our samples at the European Synchrotron Radiation Facility (ESRF). Compared to a standard XRD set-up, ESRF beneficiates from a very intense and focused X-Ray source. The energy of the beam may also be varied. Our measurements were conducted at the beamline ID01 under the supervision of Dr. Tobias Schulli. The technique of the K-MAP described in [12] that allows a quick mapping of an area of the sample was developped at ID01. A 3D RSM (Q_x, Q_y, Q_z) is aquired for every point of the scanned area (see annex A for more information on RSMs). The latter is recorded by using a 2D X-Ray detector and repeating the 2D scan at every point of the rocking curve (for each ω). The data are later analyzed and the peaks of the reflections are fitted (using the center of mass) with the XSOCS software developped at ID01. The resulting data is an 5D array with the columns x, y, Q_x, Q_y, Q_z. At ID01, a resolution of a few hundred nanometers may be obtained for the real space mapping.

The idea was to study the strain at a small scale for a sample grown on an InGaNOS substrate. An InGaN layer on InGaNOS 3.190 was chosen for the scan (structure in Fig. 4.12 (b)) as among the three different InGaNOS substrates, this is the only one that produces an XRD spot of sufficient intensity in XRD RSM. To facilitate the interpretation and data treatment, a sample in which the spots corresponding to InGaNOS 3.190 substrate and to InGaN layer can be clearly distinguished was selected. For this reason, a sample was grown at a low temperature (816 ˚C). Since there are patterns (of size 800*800 μm^2 in that case) and there might be some peculiarities at the edges and the corners, it has been decided to scan a corner of the sample. The size of the scanned area is 40*40 μm^2 and 150*150 points were acquired, the step was about 267 nm. Fig. 4.26 displays the SEM image of the mapped area. It can be seen that there are defects (mostly V-pits although some unknown types of defects may also exist) at the surface of the layers and that they are more numerous on the edges. A more detailed study using AFM could be conducted to assess the nature and density of the defects.

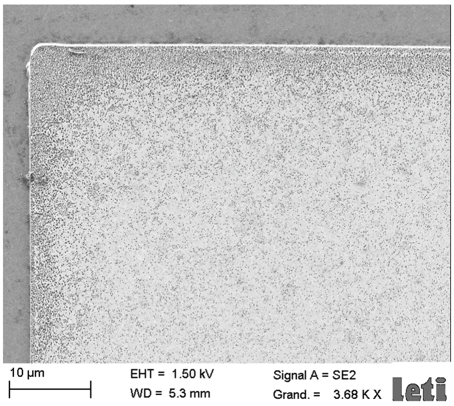

FIGURE 4.26 – SEM image of the mapped area from the InGaN buffer on InGaNOS 3.190 (corner of a pattern).

Since there is an instability inherent to the set-up, a scan on a symmetrical reflection (0 0 4) and on an asymmetrical reflection are necessary to determine the a and c lattice parameters. In order to maximize the signal, the incident angle needs to be as close to 90 ˚as possible. Therefore the (1 0 3) reflection was chosen and an energy of 7.0 keV was used to reach it (8.5 keV for the (0 0 2) reflection). In order to get the b lattice parameter, a second scan at a 60 ˚offset in phi is conducted (we generally assume that $a = b$ in III-N). The analysis of this second (1 0 3) scan will not be shown here.

The developement of the raw data with XSOCS was led by people from the ID01 beamline at ESRF. They first transformed the data to get the Qx, Qy and Qz 3D RSM images for each point in the 2D-real space of the mapping. Fig. 4.27 gives an example of the RSM on the (0 0 4) and the (1 0 3) for one position in the mapped area. Then, the data were fitted using the center of mass. They therefore provided us the values of Qx, Qy and Qz for every position of the scanned area on the three reflections.

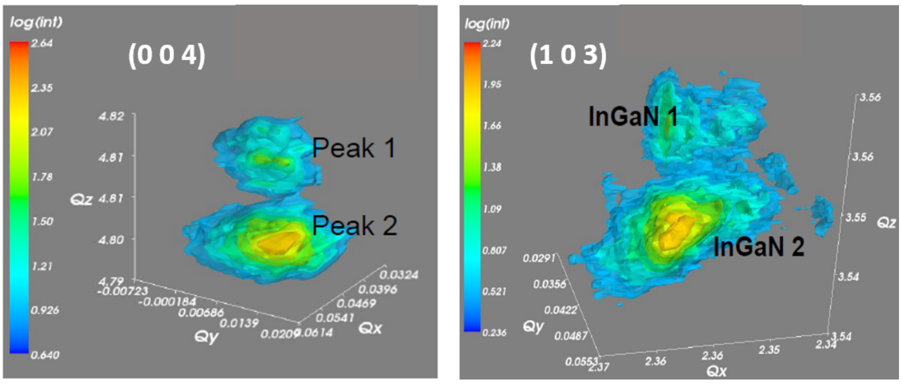

(a) (b)

FIGURE 4.27 – 3D RSM of the (0 0 4) and the (1 0 3) reflections on one position in the mapped area.

4.3.2 Results

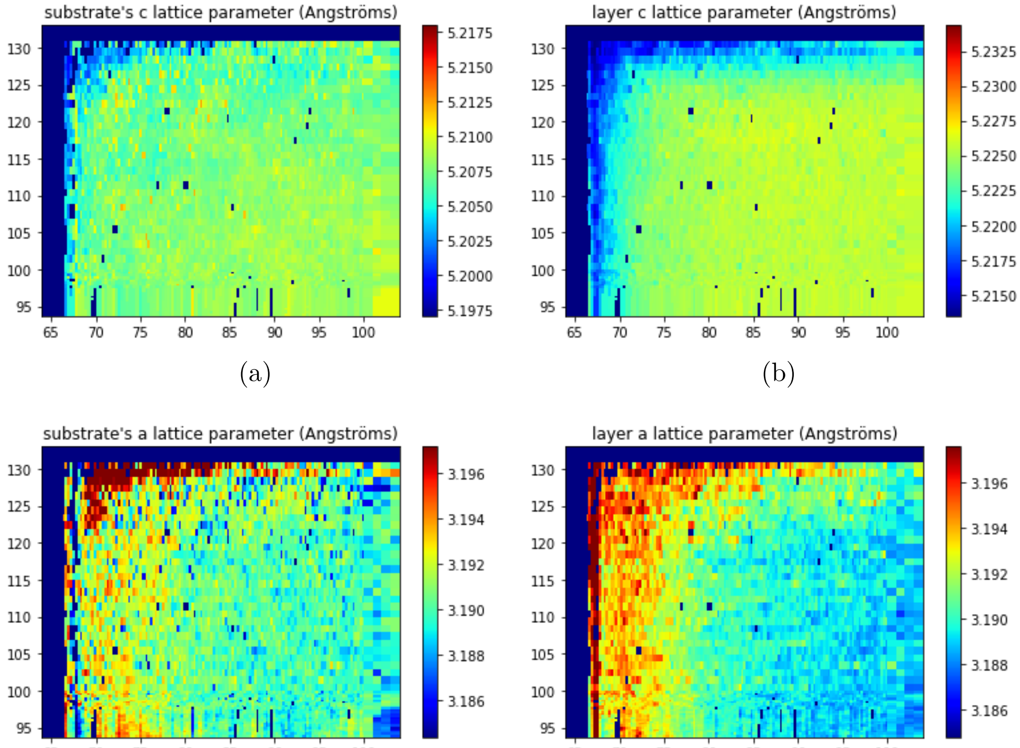

(a) (b)

(c) (d)

FIGURE 4.28 – Mappings of c lattice parameter of the substrate (a) and of the InGaN buffer layer (b) and a lattice parameter of the substrate (c) and of the InGaN buffer layer (d) for a 40*40 μm^2 size area.

From these scans, the c parameters of the substrate and of the buffer layer deduced from the RSMs on the (0 0 4) symmetrical reflection are first mapped. The a lattice parameters for the first (1 0 3) asymetrical reflection are then calculated from the c

parameter and the Qx, Qy and Qz coordinates from the (1 0 3) reflection. The four different scans are displayed in Fig. 4.28. The *c* lattice parameter decreases at the edges and the corner of the pattern while the *a* lattice parameter increases. This tendency is further evidenced for the *a* and *c* lattice parameters of the buffer layer as compared to the mappings of the substrate. We can also notice an asymmetry in the distribution which is particularly visible on the mapping of the *a* lattice parameter for the buffer layer (Fig. 4.28 (d)). The vertical direction presents a larger gradient of lattice parameter and on a larger area as compared to the horizontal dimension. The origin of this asymmetry has not been investigated yet.

From the knowledge of *a* and *c* lattice parameters, similarly to what has been done in this chapter, the indium content of the substrate and the InGaN grown layer was calculated for all the points in the area and is displayed in Fig. 4.29 (a) and in Fig. 4.29 (b). Then the relaxation percentage of the substrate and the strain in the InGaN grown layer were computed and are shown in Fig. 4.29 (c) and in Fig. 4.29 (d).

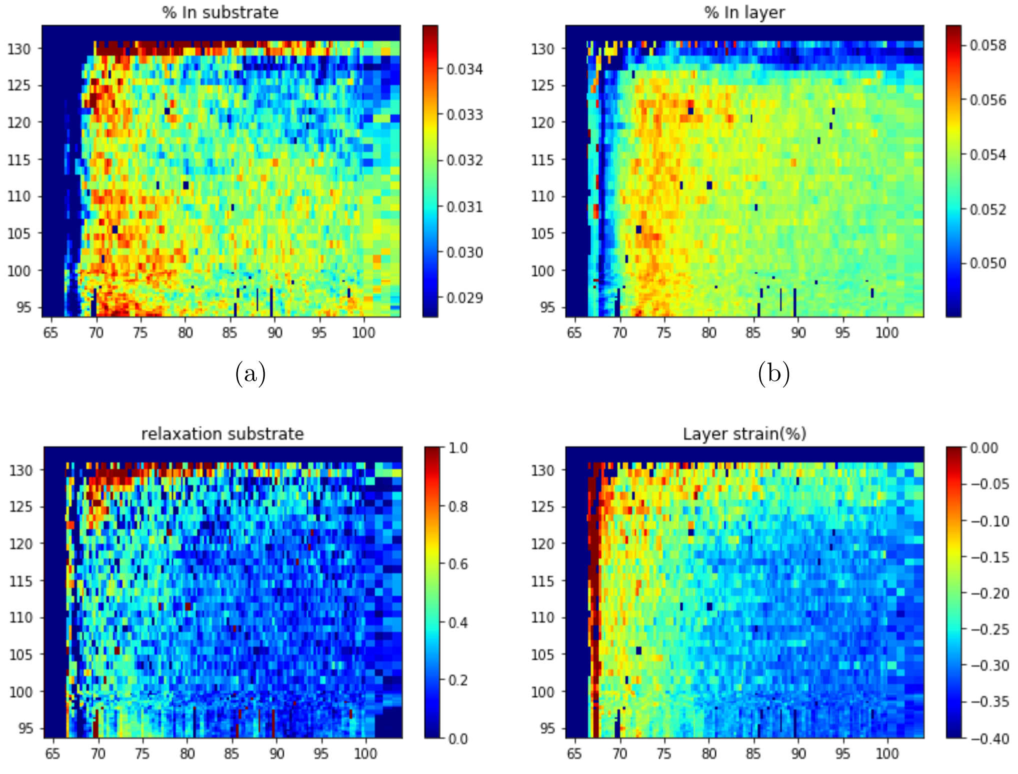

(a) (b)

(c) (d)

FIGURE 4.29 – Mappings of indium content of the substrate (a) and the InGaN buffer layer (b), relaxation percentage for the substrate (with respect to bulk GaN) (c) and strain in the buffer layer (d) for a 40*40 μm^2 size area.

The indium contents are ranging from 2.9 % to 3.5 % and from 4.9 % to 5.8 %. The indium content is smaller on the very edges but larger next to the edges compared to the center of the pad. The relaxation of the substrate has an average value of about 20 % with a larger

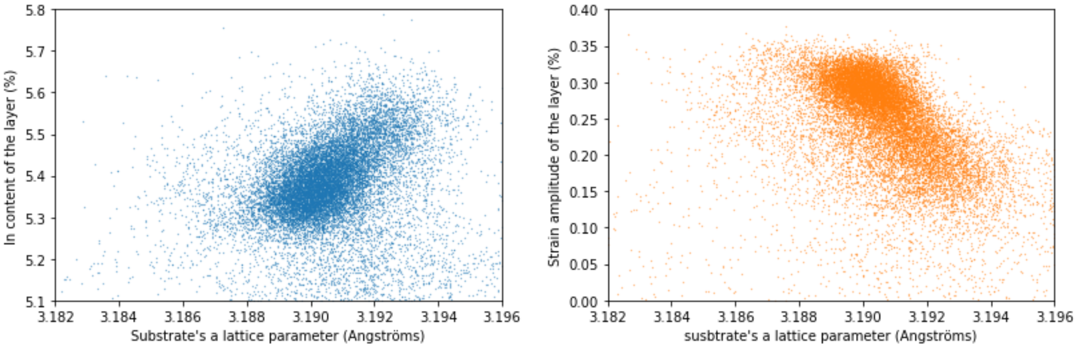

(a) (b)

FIGURE 4.30 – Indium content (a) and strain (b) as a function of the substrate *a* lattice parameter for all the points in the mapped area.

value on the edges. The average strain in the layer is about 0.3 % and decreases towards 0 on the edges. As the mapped area is only of 40*40 μm^2 as compared to the total size of the pattern of 800*800 μm^2, it is hard to conclude on the homogneity inside the patterns. However, the indium contents, the relaxation and the strain are homogeneous inside the patterns for the mapped area and changes only on the edges with a caracteristic distance of less than 15 µm.

When looking at the scans with the naked eye, one can think that there might be a correlation between the *a* lattice parameter of the substrate and the incorporation of indium in the layer and the strain like what was seen at the macro scale. In order to know if this correlation is accurate, the indium content of the grown layer and the strain in the layer are plotted as a function of the substrate's *a* lattice parameter for all the points in the mapped area in Fig. 4.30.

The indium contents and the strain indeed seem to follow the same trend as a function of the *a* lattice parameter that the one observed at the macro scale. Yet, the range of indium contents is quite small, from 5.3 to 5.7 %. A larger range would have been needed to conclude. For the strain, the range of amplitudes is large enough to conclude. Strain amplitude decreases with increasing *a* lattice parameter.

NB : As the original settings of the set-up were not done (using a well known material like silicon for instance) , there was an offset on the Qx, Qy and Qz values obtained and therefore an offset on the *a* and *c* lattice parameters. In order to display the right lattice parameters, the average lattice parameters were first calculated using a regular macro XRD measurement on the lab set-up and the offset was applied.

Conclusion

To conclude, we characterized thouroughly the InGaNOS substrates and the donors. The InGaNOS substrates present larger *a* substrate's lattice parameters as compared to GaN template. The InGaNOS substrates are epi-ready with a reasonnable surface roughness.

The compositional pulling effect was then demonstrated with the growth of InGaN layers on InGaNOS substrates as well as a decrease of strain in this layer as a function of the a lattice parameter.

Then, we showed that thanks to the insertion of GaN interlayers placed regularly, we were able to signficantly improve the structural quality of an InGaN grown layer on InGaNOS 3.205 while decreasing the V-pit density. Thanks to these GaN interlayers we should be able to increase the InGaN layer thickness from about 200 nm in this chapter to 1µm ideally. The study on the growth temperature showed the importance of maintaining a high growth temperature to preserve a good crystal quality even if it comes with a decrease of the In content.

Next, the uniformity of the lattice parameters, the strain and the indium content was studied for the InGaN regrown layer and the InGaNOS substrate (InGaNOS 3.190 in that case) thanks to XRD measurements at ESRF. We found that these quantities are stable inside the patterns (although we did not scan the whole pattern but this is the tendency observed) despite the fact that there are edge effects.

The growth of the InGaN buffer is the first step for the realization of a full InGaN LED on InGaNOS substrate. As we demonstrated the growth thick InGaN layer while maintaining the a lattice parameter of the substrate and while preserving a good structural quality, we are ready for the growth of the active region. Next chapter will elaborate on this MQW growth and on the realization of a complete LED structure on InGaNOS substrate.

References of chapter 4

[1] A. Tauzin, T. Akatsu, M. Rabarot, J. Dechamp, M. Zussy, H. Moriceau, J. F. Michaud, A. M. Charvet, L. D. Cioccio, F. Fournel, J. Garrione, B. Faure, F. Letertre and N. Kernevez. *Elect. Lett.* **41**, 11 (2005).

[2] A. Dussaigne and D. Sotta. *Compound semiconductors* **23**, 28 (2017).

[3] M. a. Moram and M. E. Vickers. *Rep. Prog. Phys.* **72**, 036502 (2009).

[4] A. V. Lobanova, A. L. Kolesnikova, A. E. Romanov, S. Y. Karpov, M. E. Rudinsky and E. V. Yakovlev. *Appl. Phy. Lett.* **103**, 152106 (2013).

[5] T. L. Song. *J. Appl. Phys.* **98**, 84901 (2005).

[6] S. Srinivasan, L. Geng, R. Liu, F. A. Ponce, Y. Narukawa and S. Tanaka. *Appl. Phy. Lett.* **83**, 5187 (2003).

[7] C. Bazioti, E. Papadomanolaki, T. Kehagias, T. Walther, J. Smalc-Koziorowska, E. Pavlidou, P. Komninou, T. Karakostas, E. Iliopoulos and G. P. Dimitrakopulos. *J. Appl. Phys.* **118**, 155301 (2015).

[8] K. Pantzas, Y. El Gmili, J. Dickerson, S. Gautier, L. Largeau, O. Mauguin, G. Patriarche, S. Suresh, T. Moudakir, C. Bishop, A. Ahaitouf, T. Rivera, C. Tanguy, P. L. Voss and A. Ougazzaden. *J. Cryst. Growth* **370**, 57 (2013).

[9] D. Van Den Broeck, D. Bharrat, Z. Liu, N. El-Masry and S. Bedair. *J. Elect. Mater.* **44**, 4161 (2015).

[10] J. Liu, J.-h. Ryou, Z. Lochner, J. Limb, D. Yoo, R. D. Dupuis, Z. Wu, A. M. Fischer and F. A. Ponce. *J. Cryst. Growth* **310**, 5166 (2008).

[11] D. D. Koleske, A. E. Wickenden, R. L. Henry and M. E. Twigg. *J. Cryst. Growth* **242**, 55 (2002).

[12] G. A. Chahine, M.-i. Richard, R. A. Homs-Regojo, T. N. Tran-Caliste, D. Carbone, L. Robert, P. Boesecke, J. Katzer, I. Costina and H. Djazouli. *J. Appl. Crystallogr.* **47**, 762 (2014).

5

InGaNmultiple quantum wells on InGaNOS substrates

The previous chapter showed a decrease of the compositional pulling effect when growing InGaN layers on InGaNOS substrates as compared to the growth on GaN template. In this chapter, multiple quantum wells (MQW) structures are grown on GaN template and on InGaN buffer layer on InGaNOS substrates. The samples are then compared using optical and structural characterization techniques. The best IQE values obtained for the MQW structures are then benchmarked to the literature and the In surface segregation problem studied for GaN templates in Chapter 3 is also reviewed here. Finally, the last part evaluates the characteristics of the first LED structure grown on InGaNOS substrate and analyzes the remaining challenges in order to succeed in growing an efficient LED on InGaNOS substrate in the green and red ranges.

5.1 Growth of full InGaN structures on InGaNOS substrates

Fig. 5.1 presents the two different structures that are studied in this chapter. Fig. 5.1 (a) is the reference MQW structure consisting in an InGaN/GaN MQW active region of five wells grown on a GaN layer regrown on GaN template. Target thicknesses of the QWs and the QBs (Quantum Barriers) are 3 nm and 10 nm, respectively. The second structure (Fig. 5.1 (b)) is the full InGaN structure as described in Chapter 2 without the p-type region and with a 200 nm-thick undoped InGaN regrowth. The 5 x InGaN/InGaN MQWs have nominal thicknesses of 3 nm and 8 nm, respectively. The growth conditions of the InGaN regrowth and the InGaN QBs are set to be the same so that In content is expected to be the same in these two types of layers.

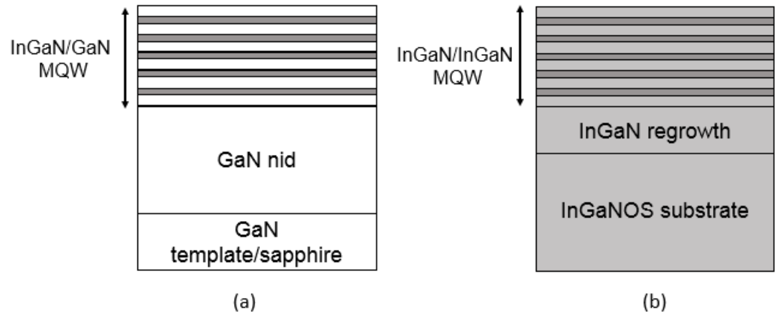

FIGURE 5.1 – (a) Reference structure on GaN template and (b) full InGaN structure on InGaNOS substrates

5.1.1 Influence of substrate on emission wavelength

In order to apply strictly the same growth conditions, the three types of InGaNOS substrates were coloaded in the same MOVPE run. A full InGaN structure is then grown. The three samples were compared to the reference structure grown on GaN template with the same growth conditions being applied to the InGaN QWs. We conducted the experiment for three different QW growth conditions labelled as blue, green and amber conditions with their corresponding set of samples labelled A, B and C for the full InGaN structures on InGaNOS substrates and D and E for the reference structures on GaN template.

	Full InGaN structure InGaN well conditions	Reference structure InGaN well conditions	InGaN buffer (200 nm)	Substrates
Samples A	Standard blue	/	Yes	The 3 InGaNOS
Samples B	-20 ˚C	/	Yes	The 3 InGaNOS
Samples C	-20 ˚C + $V_{InGaN} \times 3$	/	Yes	The 3 InGaNOS
Sample D	/	Standard blue	No	GaN template
Sample E	/	-20 ˚C	No	GaN template

TABLE 5.1 – Structure, substrates and growth conditions of the different samples. "The 3 InGaNOS" refers to the three types of InGaNOS substrates, namely, InGaNOS 3.190, InGaNOS 3.200 and InGaNOS 3.205 as presented in chapter 4.

For the set of samples A, same growth conditions as our standard blue QWs were applied. They are referred to as the "blue conditions". A growth temperature of 730 ˚C and a growth rate of $0.1\mu m/h$ have been used in this case. In order to reach "green conditions", the growth temperature was then lowered by 20 ˚C for the set of samples B. Finally, in the case of set of samples C, *i.e.* the "amber conditions", the growth temperature was kept the same as in the case of green conditions with an additionnal variation on the growth rate, which was multiplied by a factor of three for the whole active region. The reference structures on GaN template for which QWs were grown with the blue and green conditions are labeled D and E, respectively. Table 5.1 lists the different samples together with their growth conditions.

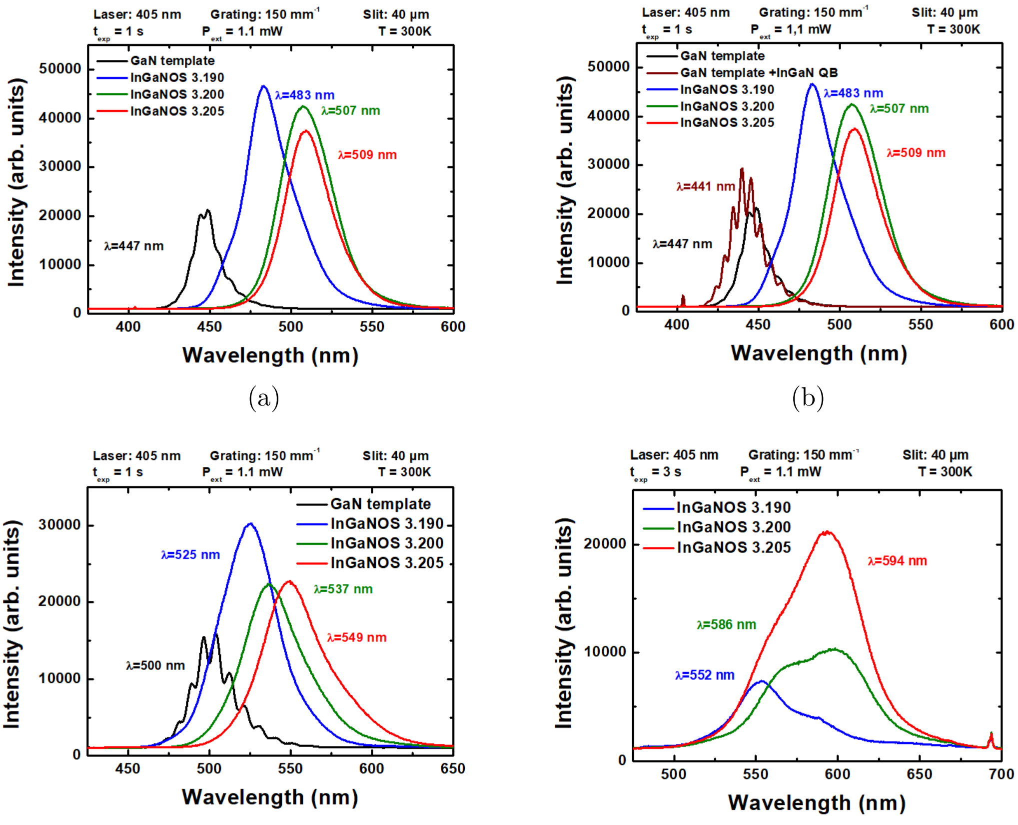

(a) (b)

(c) (d)

FIGURE 5.2 – PL spectra at room temperature of set of samples A and sample D (a), set of samples A, sample D and sample F (b), set of samples B and sample E (c) and set of samples C (d).

The samples were characterized at room temperature by PL using a 405 nm laser diode. The resulting spectra are shown in Fig. 5.2. For the blue conditions in Fig. 5.2 (a), sample D on GaN template emits at 447 nm while MQWs on InGaNOS 3.190 show an emission wavelength of 483 nm. Wavelengths of 507 and 509 nm are reached on InGaNOS 3.200 and 3.205, respectively. The wavelength red-shift observed is up to 62 nm thanks to the use of the full InGaN structure on InGaNOS substrates compared to the conventional structure on GaN template with the same QW growth conditions. This red-shift is of 26 nm among the three samples on InGaNOS substrates. For comparison, a sample on GaN template with the same active region as set of samples A has also been grown, *i.e.* with InGaN barriers in the same growth conditions (sample F). In that case, the observed wavelength red-shift was increased to 68 nm, as this sample emits at 441 nm (see Fig.

5.2) (b). The slight blue-shift observed compared to reference structure (sample D) can be explained by a smaller confinement in the MQWs induced by the InGaN barriers.
For the green growth conditions (Fig. 5.2 (c)), as expected, emission also shift towards greater wavelengths as an emission wavelength of 500 nm is observed for sample E on GaN template. Full InGaN structures on InGaNOS emit at 525, 537 and 549 nm for InGaNOS 3.190, InGaNOS 3.200 and InGaNOS 3.205, respectively. The resulting red-shift is of 49 nm between GaN template reference structure and full InGaN structure on InGaNOS. Between the three InGaNOS substrates, the red-shift is of 24 nm with an increased difference between InGaNOS 3.200 and 3.205 (12 nm) compared to what was observed in the blue conditions.

For the amber conditions, we did not grow a reference sample on GaN template as the PL intensity is usually very low for these wavelengths. From the MQWs on InGaNOS 3.190 to the MQWs on InGaNOS 3.205, the emission wavelength increases from 552 to 594 nm, *i.e.* a red-shift of 42 nm. This redshift is the largest observed among the three different series of samples. For these growth conditions, the PL spectra on InGaNOS 3.190 and 3.200 exhibit two contributions with a stronger peak on the green side on InGaNOS 3.190 and a stronger peak on the amber side on InGaNOS 3.200. These features may be attributed to a phenomenon of phase separation taking place because of a too high indium content. On the InGaNOS 3.205, a stronger main peak is observed at 594 nm with a small shoulder.
On InGaNOS 3.205, an additional sample was grown starting from the amber conditions with an additional lowering of the growth temperature that will later be referred as the red conditions. A long wavelength of 617 nm was reached at room temperature. Fig. 5.3 shows the PL spectrum corresponding to that sample.

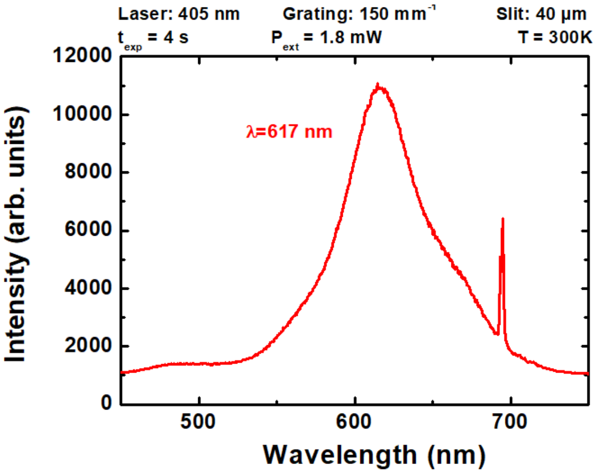

FIGURE 5.3 – PL spectrum of the MQW sample grown in the red conditions on InGaNOS 3.205.

For the four growth conditions, the evolution of emission wavelength is plotted as a function of the substrate's a lattice parameter on Fig. 5.4 for the full InGaN structures on the three different types of InGaNOS substrates. As previously mentionned, the PL emission wavelength increases with the substrate's *a* lattice parameter whatever the growth conditions that were tested. To our knowledge, this is the first time that such a red-shift is demonstrated to this extent and it is only due to the InGaNOS substrates and their large *a* lattice parameter. This red-shift in PL emission may either be explained by a larger QW width or by a greater indium content in the QWs. Considering that the QW growth time remains unchanged and that the strain in the InGaN QWs is reduced, an increase in indium content is expected. This will later be verified thanks to additional characterizations presented below.

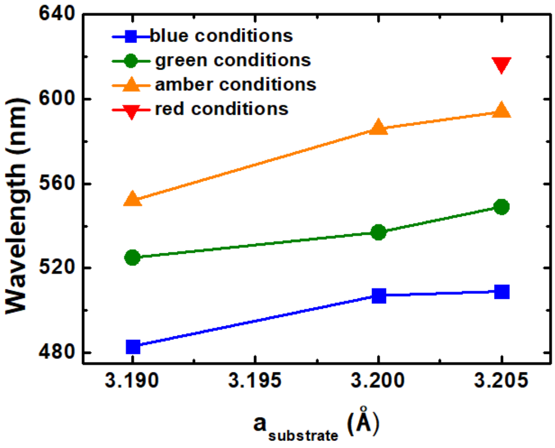

FIGURE 5.4 – Evolution of the PL emission wavelength as a function of the substrate's *a* lattice parameter (set of samples A, B and C).

Later on, some trials were conducted in order to reach even further wavelengths than 617 nm. Starting from the green growth conditions, the growth temperature was lowered. Here, the full InGaN structure was grown on all substrates including GaN template. Because of the weakness of the signal, the PL spectra are recorded at low temperature ($\simeq$ 15K) and displayed Fig. 5.5. The full InGaN structure on GaN template emits at a wavelength of 552 nm while the emission red-shifts to 578, 623 and 653 nm on InGaNOS 3.190, 3.200 and 3.205 respectively. Compared to what was observed for the previous sets of samples (A and B), the red-shift is increased to 101 nm here. The emission at RT is very weak and for this reason it was not shown here. There are probably too many nonradiative recombinations occuring because of the low structural quality of the InGaN in the QWs. This trial demonstrates the ability to get to very long wavelengths in the red range when working with InGaNOS substrates. Wavelengths longer than 650 nm can be reached although a great work should be put into improving the structural quality of these layers (which first step would probably be to work on the structural quality of the substrates and of the InGaN buffer) in order to reduce the number of nonradiative recombination centers, the V-pit density and to allow for an increase of the radiative efficiency.

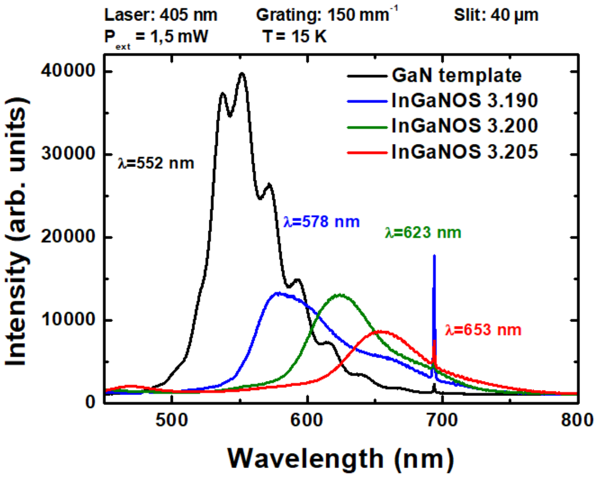

FIGURE 5.5 – PL spectra of full InGaN structures grown on GaN template (black), on InGaNOS 3.190 (blue), on InGaNOS 3.200 (green) and on InGaNOS 3.205 (red). The samples were characterized at 15K with a 405 nm laser diode as excitation source.

5.1.2 Study of In surface segregation on InGaNOS

In Chapter 3, we were able to reach longer wavelengths on GaN by applying a TMIn pre-treatment before the growth of the QW. By providing In atoms on the surface prior to the arrival of Ga atoms, it is likely that the nominal In content can be reached faster, therefore improving the abruptness of the barrier/well interface. In the full InGaN structure, the barriers are made of InGaN. Therefore, as some indium atoms are already present on the surface when starting the QW growth, the segregation phenomenon should be reduced but it probably still exists. Furthermore, the reduced strain in these structures compared to the conventionnal structure may also limit the surface segregation.

The TMIn pre-treatment was applied to full InGaN MQW structures grown on GaN template, on InGaNOS 3.200 and on InGaNOS 3.205. The duration of the TMIn pre-treatment is varied between 0, 60 and 120 seconds and (refer to 3.21 for a detailed time chart). Fig. 5.6 shows the PL spectra that were obtained at room temperature using a 405 nm laser diode. With the 60 seconds TMIn pre-treatment, the emission wavelength red-shifts from 451.6 nm to 462.1 nm on GaN template and from 483.1 nm to 502.6 nm on InGaNOS 3.205. Then, when the duration of the TMIn pre-treatment is extended to 120 seconds, the wavelength blue-shifts back, as a saturation phenomenon is occuring. The behavior is similar as what was observed on GaN in chapter 3. Here too, an hypothesis for the blue shift is the saturation of the surface with In atoms therefore preventing the N adatoms to reach the dangling bonds. All the corresponding data may be found in Table 5.2.

NB : the PL emission wavelengths observed for these three series of samples are not long as the ones observed previously. These results were obtained at a time when we were having some problems with the MOCVD machine and were not able to incorporate as much indium as we used to (this problem was observed on all substrates). Later, we were able to retrieve the long wavelengths observed for the set of samples A, B and C.

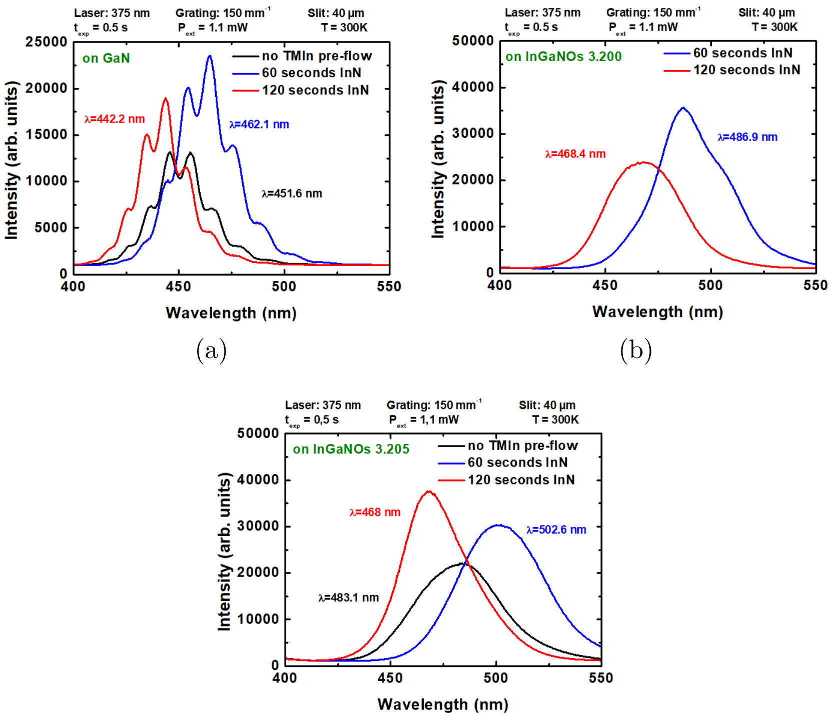

(a)

(b)

(c)

Figure 5.6 – PL spectra for reference sample (black) and for the samples with pre-flow TMIn treatment with t_{TMIn}=60 s (blue) and t_{TMIn}=120 s (red) for full InGaN structure on GaN template (a), on InGaNOS 3.200 (b), on InGaNOS 3.205 (c).

Substrate	TMIn pre-treatment duration (s)	PL emission wavelength (nm)
GaN template	0	451.6
	60	462.1
	120	442.2
InGaNOS 3.200	60	486.9
	120	468.4
InGaNOS 3.205	0	483.1
	60	502.6
	120	468.0

Table 5.2 – Characteristics of QWs on InGaNOS after TMIn pre-treatment.

5.1.3 MQW sample characterizations

The structural and the surface quality of the green emitting samples (set of samples B and sample E) were assessed using AFM and XRD characterizations. The homogeneity in In composition in the MQW layers has been studied by comparing the PL linewdiths.

5.1.3.1 Crystal quality

Table. 5.3 summarizes the PL linewidths and the FWHM of the rocking curves on the (0 0 2) reflection for the four samples grown on the green conditions (set of samples B and sample E). Fig. 5.7 (a) and Fig. 5.7 (b) plot the two quantities as a function of the substrate's a lattice parameter.

Sample	Substrate	PL emission wavelength (nm)	PL FWHM (nm)	FWHM RC (002) (arcsec)
Sample E	GaN template	500	31	379
Samples B	InGaNOS 3.190	525	43	484
	InGaNOS 3.200	537	47	827
	InGaNOS 3.205	549	50	884

Table 5.3 – PL linewidths and FWHM on the (0 0 2) reflection for sample E and set of samples B.

The FWHM of the PL emission increases substantially between sample E on GaN template and set of samples B on InGaNOS substrates. Between the three samples B on InGaNOS 3.190, InGaNOS 3.200 and InGaNOS 3.205, there is also an increase of the PL linewidth from 43 to 50 nm. The increase of the FWHM of the PL linewith in an MQW sample is related to an increase of the potential fluctuations (related to inhomogeneities in In composition or variations of QW width).This phenomenon is called the inhomogeneous broadenning. TEM and APT characterization should later provide more information on the origin of the potential fluctuations. For the MQWs of grown on InGaNOS substrates, some inhomogeneities in In content and in QW thicknesses can be expected.

The FWHM of the RC on the (0 0 2) reflection also increases with the substrate's a lattice parameter. It remains reasonable for sample E and sample B on InGaNOS 3.190 with values of 379 and 484 arcsec. The FWHM then increases up to 827 and 884 arcsec for samples B on InGaNOS 3.200 and InGaNOS 3.205, respectively. The structural quality of

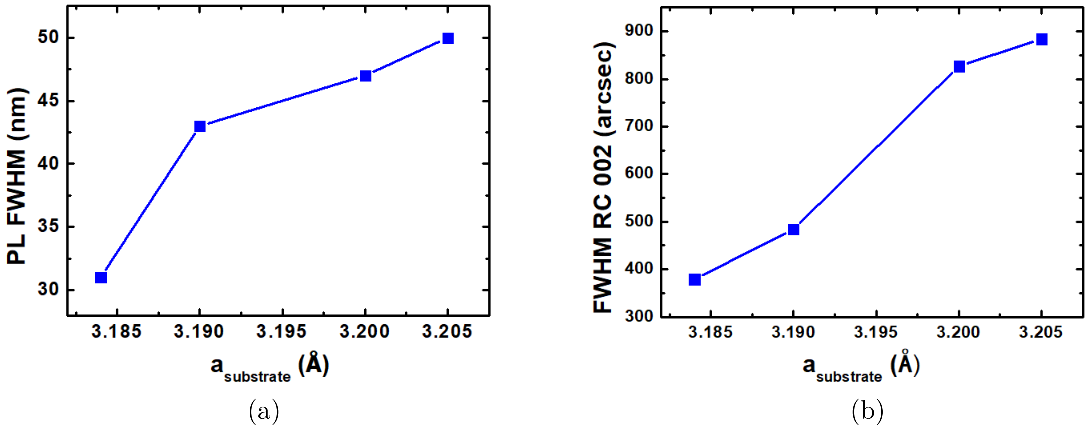

(a) (b)

FIGURE 5.7 – Evolution of the FWHM of the PL emission (a) and of the RC on the (0 0 2) reflection as a function of the substrate lattice parameter for the MQWs structures grown on the green conditions (series of samples B and sample E).

these two samples is substantially decreased as compared to sample E and on sample B on InGaNOS 3.190 which are of good structural quality. This high value for the FWHM of the RC for samples B on InGaNOS 3.200 and InGaNOS 3.205 originate from the substrates themselves (see section 4.1.3). This demonstrates that the full InGaN structure does not deteriorate the structural quality on InGaNOS substrates.

5.1.3.2 Visualization of the V-defects

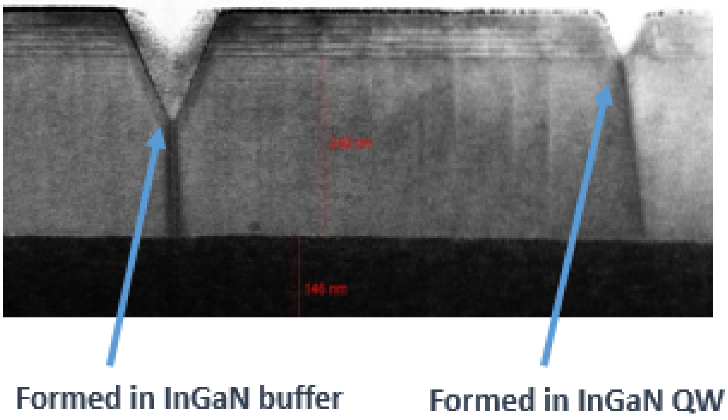

FIGURE 5.8 – TEM image of the green MQWs on InGaNOS 3.205. The V-pits are arising from dislocations and form either in the InGaN buffer or in the InGaN/InGaN MQWs.

The set of samples B and sample E were imaged by TEM. Fig. 5.8 displays a cross-sectional view of sample B grown on InGaNOS 3.205. Two V-pits can clearly be seen with their apex emerging from threading dislocations as pointed by the blue arrows on the figure. One is formed in the InGaN buffer while the other is formed in the active region.

The formation mechanism of the V-pits is enhanced by an increasing indium content and a large strain. More details are given in 1.3.2.3.

5.1.3.3 Surface quality assesment

The qualities of the surface of sample E and the set of samples B have been assessed by AFM. The surface roughness as well as the density and average diameter of the V-pits are summarized in Table. 5.4. Fig. 5.9 displays the AFM scans of the samples with MQWs grown with the green conditions (set of samples B and sample E). It is observed that the surface of set of samples B on InGaNOS substrates presents a large number of V-pits with a rather large diameter. Indeed, the InGaN buffer is not customized for each type of InGaNOS as the same growth conditions were applied, which results in the emergence of more V-pits which are later propagating across the whole structure. On the contrary, the surface of sample E on GaN template is smoother although some V-pits can be identified. They are less numerous and rather small. Nevertheless we note the presence of small regions of higher height surrounded by small holes. They might be indium-rich inclusions as observed in [1]. The difference in V-pit average diameter between sample E (48 nm) and sample B on InGaNOS 3.190 (70 nm) may seem small considering the visual aspect. However, the average V-pit diameter for the samples on the InGaNOS substrates is lowered by the presence of very small V-pits, the standard deviation is therefore much higher for these samples that present some very big V-pits with a diameter up to 150 nm.

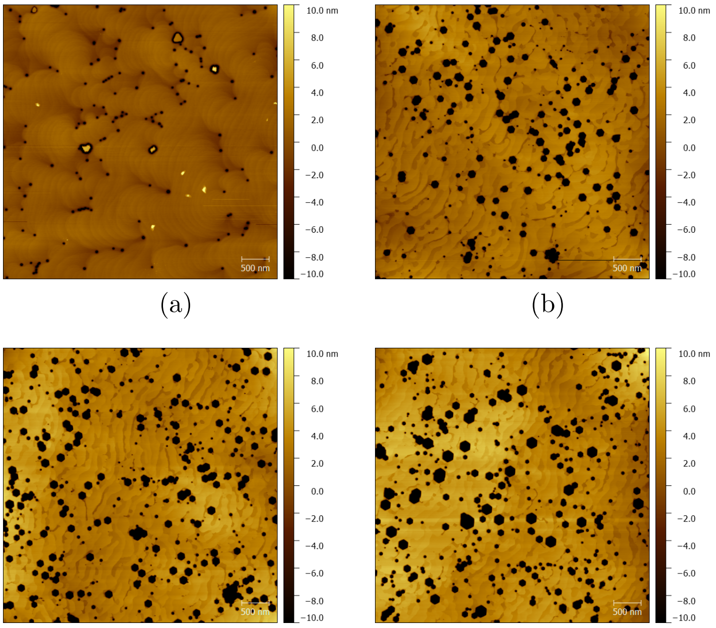

(a) (b) (c) (d)

FIGURE 5.9 – $5 \times 5\mu m^2$ AFM scans of sample E (a), sample B on InGaNOS 3.190 (b), sample B on InGaNOS 3.200 (c) and sample C on InGaNOS 3.205 (d).

Fig. 5.10 displays the V-pit density and the V-pit average diameter as a function of the substrate's a lattice parameter. Both quantities increase with the a lattice parameter of the substrate. Nonetheless, as observed with the naked eye, we note a significant increase between sample E on GaN template and set of samples B on InGaNOS substrates. Between the three samples on InGaNOS substrates the evolution is weaker. This may be due to the fact that the indium content is lower in the MQWs of sample E compared to MQWs of set of samples B. In addition, the InGaN buffer in the full InGaN structure of the set of samples B is also a region of formation of the V-pits that is not present in sample E. MQWs grown on InGaNOS substrates also suffer from the presence of larger dislocation densities (and even V-pits in the case of InGaNOS 3.205) in the InGaNOS substrates as opposed to GaN template. Furthermore the barriers are made of GaN in case of sample E instead of InGaN for set of samples B. Between the MQWs where the V-pits form, the surface is thus smoothened. The V-pits that have just been formed and are still rather small can be filled before getting larger.

Substrate	PL emission wavelength (nm)	RMS (nm)	V-pit density (cm^{-2})	V-pit average diameter (nm)	Standard deviation (nm)
GaN template	500	1.5	5.3×10^8	48	11
InGaNOS 3.190	525	8.6	1.3×10^9	70	39
InGaNOS 3.200	537	9.5	1.4×10^9	74	40
InGaNOS 3.205	549	12.8	1.5×10^9	82	42

TABLE 5.4 – Characteristics of sample E and set of samples B.

Even if the V-pits have an important diameter and are numerous, one should note that the growth of these MQW structures are not optimized. Indeed, as all three InGaNOS substrates are all coloaded in the same growth run, the InGaN regrowth is not tailored for each substrate. Consequently, a great number of V-pits propagate into the active region and since they originate from a deep region, they are very big. In Chapter 4, we already saw that we were able to significantly decrease the number and the diameter of these V-pits thanks to the insertion of GaN interlayers. The surface of MQW grown on such a tailored substrate will be of much better quality compared to what is observed here.

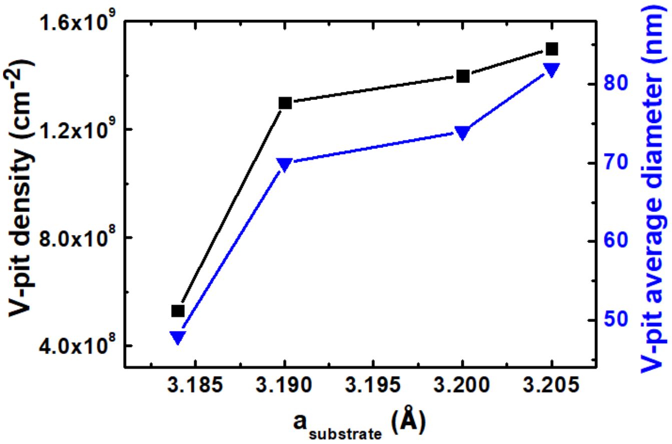

(a)

FIGURE 5.10 – Evolution of the V-pit density and V-pit average diameter as a function of the substrate lattice parameter for the MQWs structures grown on the green conditions (set of samples B and sample E).

5.1.3.4 Cathodoluminescence characterization

Sample B grown on InGaNOS 3.190 was characterized by CL at room temperature with an energy of 3 keV. An area of 2.5 × 2.5 μm^2 was mapped. A sampling of the spectra at different points in the area are plotted in Fig. 5.11 (a). Three peaks are observed. The first one is centered around 530 nm corresponding to the MQW emission that emit at 525 nm with PL. The two other peaks are centered around 430 nm and 378 nm. The SEM image of the mapped area is displayed in Fig. 5.11 (b). Fig. 5.11 (c) maps the intensity of the different peaks with a color code that we will correlate with the SEM image.

The blue signal is the intensity of the MQW peak centered at about 530 nm. The correlation with the SEM image shows that CL intensity decreases around the V-pit. In the regions where there are no or very few V-pits, the CL intensity is stronger. This observation confirms that the V-pits can be identified as nonradiative recombination centers. The hypothesis proposed by Massabuau *et al.* [2] proposing that the V-pits do not act as nonradiative recombination centers thanks to a localization in their vicinity is not verified here. The emission centered around 378 nm mapped in red get its maximum intensity inside the V-pits. This wavelength approximately corresponds to the one of the buffer layer below the active region. The signal that we see inside the V-pits may therefore be a signature of the InGaN buffer. We can notice that this signal is only present in the large V-pits. The hypothesis might be that the large V-pits are actually formed in the InGaN buffer (as observed in the TEM image in Fig. 5.8) and the pear-shape interaction will only go deep enough inside the large V-pits. A variation on the energy of the electron beam would have been necessary to conclude. In green, the intensity of the peak centered around 430 nm is mapped. This emission is particularly intense at the V-defects and in the surrounding regions when several V-pits are very close to each other. This emission might originate from the V-pit sidewalls. Indeed, on the $\{10\bar{1}1\}$ planes the indium incorporation is different as compared to the incorporation on $\{0001\}$ planes (see 2.2.2).

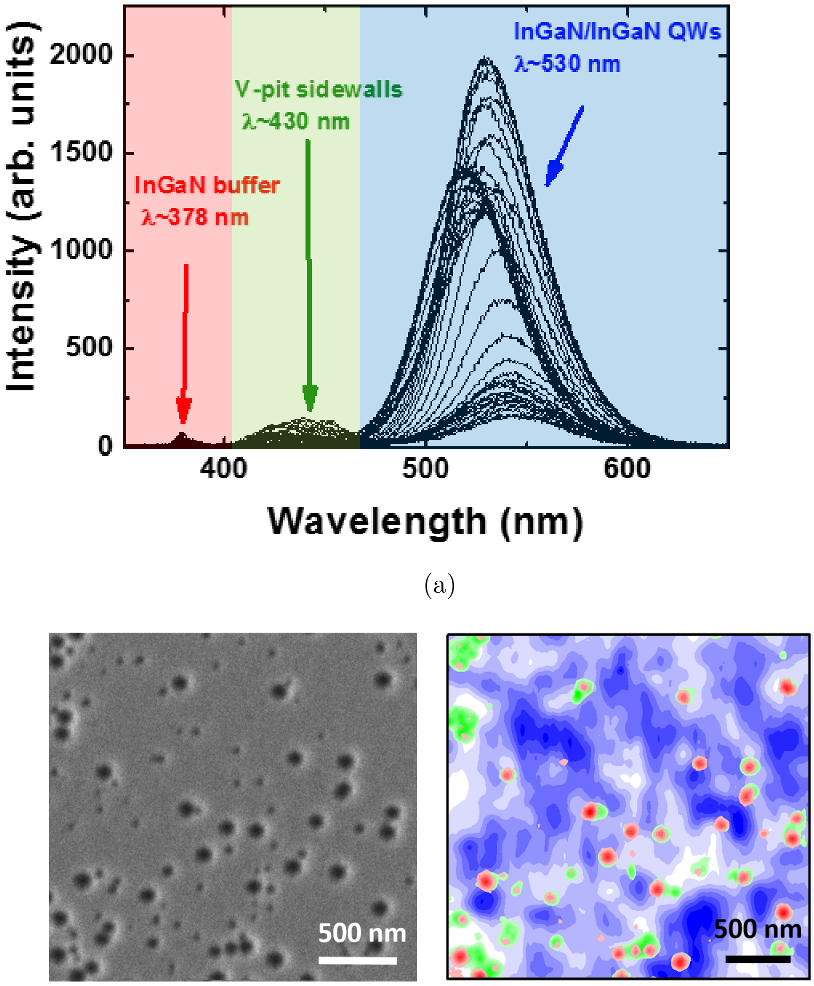

(a)

(b) (c)

FIGURE 5.11 – Cathodoluminescence spectra (a) and SEM image (b) of 2.5 × 2.5 μm^2 area of sample B on InGaNOS 3.190. Relative intensity mapping (c) of that same area from the fitting of the three main peaks from (a)

The V-pits have shown a beneficial impact (see Chapter 2) in some cases. But here, the cathodoluminescence studies show the importance of reducing the V-pit density and the V-pit average diameter in order to decrease the nonradiative recombination rate and for increasing the light-emitting surface.

5.2 Fine characterizations of the green MQWs on InGaNOS

5.2.1 Quantum well width

In order to determine the thicknesses of the QWs in the green-emitting structures, images were acquired using STEM. In STEM, samples are scanned with a focused electron beam. A transmitted signal is generated that allows to obtain an image of the sample with high spatial resolution. When using the HAADF (High Angle Annular Dark Field), the image intensity is related to the atomic mass [3]. Heavy atoms like indium will therefore appear bright while lighter atoms (gallium atoms here) will be dark.

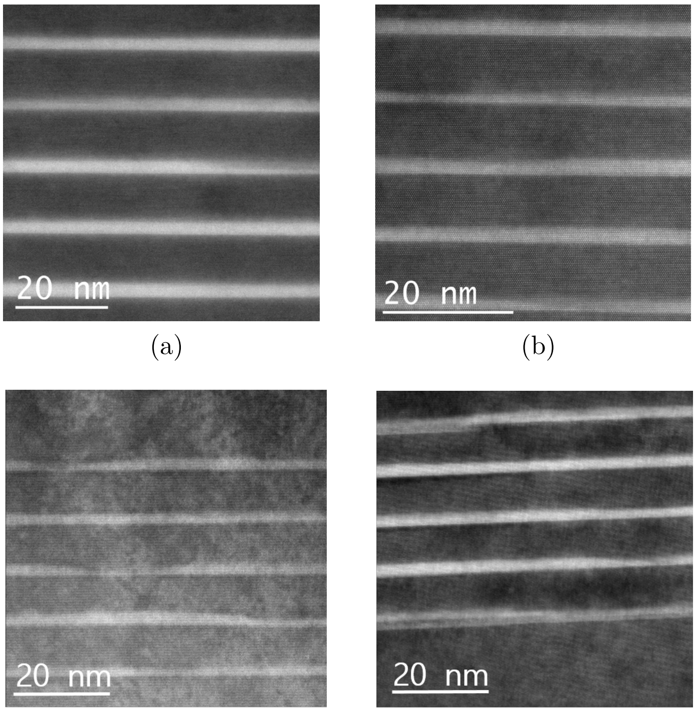

(a) (b)

(c) (d)

FIGURE 5.12 – HAADF STEM images of MQW samples grown on the green conditions, sample E (a), samples B on InGaNOS 3.190 (b), on InGaNOS 3.200 (c), on InGaNOS 3.205 (d).

Fig. 5.12 displays the STEM images of the active regions of sample E and of the set of samples B. The scanned areas were carefully chosen without V-pits. By comparing the active regions of sample E on GaN template and of set of sample B on InGaNOS substrates, it is observed that the well/barrier interfaces seem more abrupt for sample E. This can probably be explained by the fact that the barriers are made of GaN in sample E and of InGaN for the set of samples B. Contrary to sample E, the set of samples B also shows inhomogeneities in the width of the QWs. This discrepancy exists between the five QWs of the active region but also inside one QW. In some regions, the QW width variations are so large that some Quantum Dot (QD)-like structures appear (this can particularly be seen in Fig. 5.12 (c)). There also seems to be inhomogeneities in indium content as some regions in the MQWs appear brighter or darker. However, it should be kept in mind that as this analysis are very local, it may not be representative of the whole sample. The intensity of the electron beam was kept low to make sure we did not damage the sample. No evolution was seen during extended exposure (see 1.2.3). These inhomogeneities explain the large PL linewidths [4] previously observed for the set of samples B. We will later see that the observed QW width variations and highly inhomogeneous In content might actually be beneficial.

The average QW width was determined for all four samples and is given in Table. 5.5. The average QW widths range from 2.3 to 3.1 nm for all samples although one should keep in mind that the measurement is very local (70*70 nm^2). The average QB width are of 9.6 nm for sample E and of 7.7, 7.9 and 7.9 nm for samples B on InGaNOS 3.190, InGaNOS 3.200 and InGaNOS 3.205, respectively. Since the QW thickness remains rather small, the piezoelectric field should only have a rather small impact on the emission properties and should not be, in any case, strong enough to explain the PL red-shift. There is no clear tendency of thickening of the QWs as a function of susbstrate's *a* lattice parameter (2.8 ±0.5 nm). Therefore, the observed increase in PL emission wavelength is attributed to an increase in indium content in the QWs, thanks to a reduced compositional pulling effect.

Substrate	PL emission wavelength (nm)	QW average thickness (nm)
GaN template	500	2.8
InGaNOS 3.190	525	2.3
InGaNOS 3.200	537	2.3
InGaNOS 3.205	549	3.1

Table 5.5 – PL emission wavelengths and QW average thickness for sample E and set of samples B.

5.2.2 Quantification of indium content in the MQWs

Now that the increase in PL emission wavelength has been credited to an increase in indium content, this indium content needs to be quantified. As explained in 1.4, the quantification in the MQWs is rather complicated. Table 5.6 summarizes the indium contents as obtained with the different characterization techniques. XRD, APT and EDX were implemented here. PL could not be used because of the great uncertainty on the internal electric field and strain state in the active region of the samples.

5.2.2.1 XRD measurements

The easiest and most inexpensive method to implement is based on XRD. This method was carried out for sample E. We conducted an $\omega - 2\theta$ scan and simulated the spectra of the structure with the X-pert epitaxy software. It is assumed that the whole MQW structure is strained on the GaN template. Fig. 5.13 displays the experimental and simulated $\omega - 2\theta$ scans. The simulated spectrum matches the experimental data for a QW width of 2.8 nm and an indium content of 18 %. Unfortunately, this method could not be used on the set of samples B. Indeed, because of the non abrupt interface between well and barrier (as revealed by TEM), the satellite peaks of the MQWs can not be observed distinctly. Furthermore, in the full InGaN structure as the indium content of the buffer layer and the InGaN barriers is unknown, the fitting of the simulated $\omega - 2\theta$ scan to the experimental data requires too many parameters.

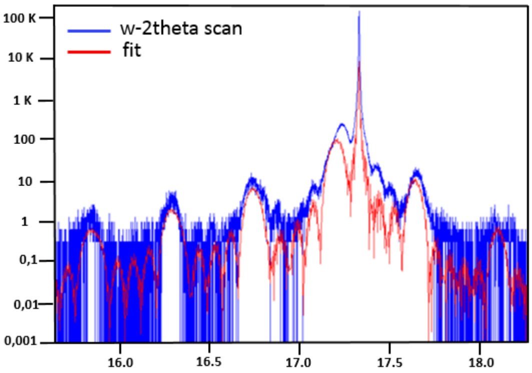

FIGURE 5.13 – w-2theta scan on the (0 0 2) reflection for green MQWs on GaN template (sample E).

5.2.2.2 EDX

Sample E and samples B on InGaNOS 3.190 and 3.200 were characterized by EDX (see 1.4.3 and annex C.6 for more details on the technique). Fig. 5.14 displays the active regions of the three samples. The indium atoms can be seen in red. As observed above with STEM, the QWs of samples B on InGaNOS 3.190 and 3.200 look inhomogeneous between one another and the inhomogeneities also exist while looking inside one QW. Sample E also shows here a disparity between the QWs in that region with the first QW that seems to have a much lower In content as compared to the others. Just like in STEM, the size of the analyzed regions is very small and several areas need to be looked at in order to describe the samples as well as possible.

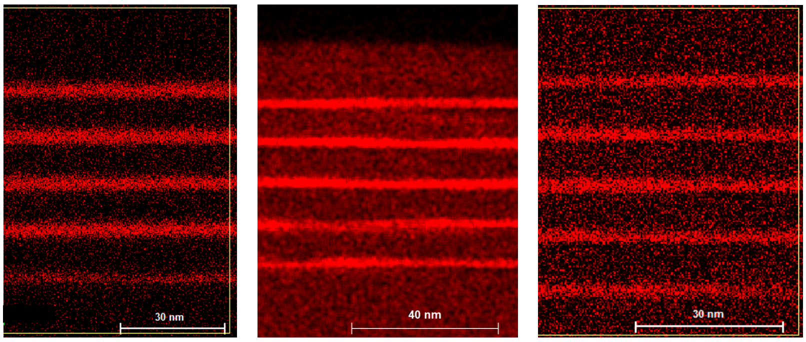

(a) (b) (c)

FIGURE 5.14 – Distribution of the indium atoms (one red dot is one indium atom) in the active regions of sample E (a), sample B on InGaNOS 3.190 (b) and sample B on InGaNOS 3.205 (c), as measured by EDX.

The indium composition profiles obtained with the zeta-factor method for sample E and samples B on InGaNOS 3.190 and InGaNOS 3.200 are given in Fig. 5.15. For sample E and sample B on InGaNOS 3.200 the In content was obtained from two different regions in the sample. The average indium content over the active region is given in Table 5.6 for the three samples. The indium content was found to be 12.5 % for sample E, 15.3 % for sample B on InGaNOS 3.190 and 18.5 % on InGaNOS 3.205. The indium content values that are obtained by EDX seem very small compared to what is expected considering the PL emission wavelength. However, the In concentration increases with the substrate's *a* lattice parameter as was previously predicted with the PL results.

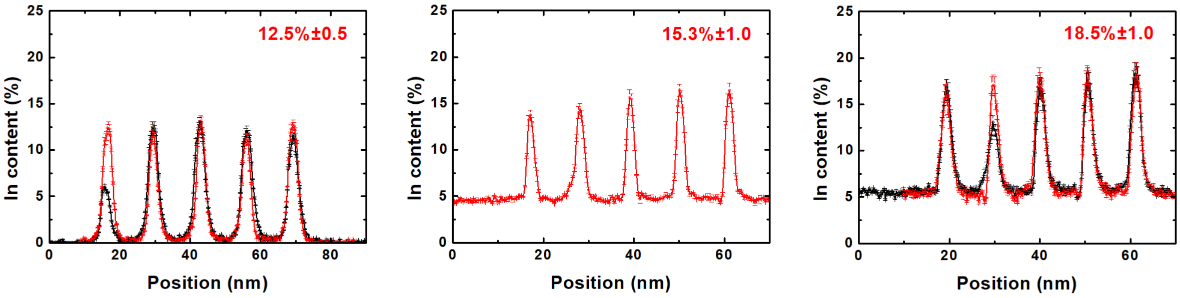

(a) (b) (c)

FIGURE 5.15 – Indium composition profiles measured by EDX for sample E (a), sample B on InGaNOS 3.190 (b) and sample B on InGaNOS 3.205 (c).

5.2.2.3 APT

The APT analysis was carried out on sample E (see 1.4.2 and annex C.4 for more details on the technique). Because of difficulties encountered during sample preparation, only the first two QWs (starting from substrate's side) were analyzed. Fig. 5.16 gives the indium composition profiles obtained for these two QWs. The measured average indium content is 17.5 % for sample E, very close to the value of 18 % given by XRD. However, EDX gave a significantly smaller value of 12.5 %. The reason for the appearing underestimation with EDX remains unclear. Yet, we can still compare the three samples between one another with this technique which was the only one applied for the three samples. Table 5.6 summarizes the indium contents obtained in sample E and set of samples B with the three different characterization techniques. Fig. 5.17 displays the iso-curves in indium composition for a volume of 20 × 30 × 3 nm^3 for the two MQWs of sample E analyzed with APT. The indium distribution is very inhomogeneous inside the QWs with concentrations up to 25 %. A statistical study was led to assess the presence of clusters. Fig. 5.18 plots the distribution of indium atoms with the distance to the nearest neighbour which is fitted by the green curve. The distribution can not be solely fitted with the binomial distribution plotted in red. To fit the distribution, another contribution is needed. This contribution is attributed to the clusters and is plot in blue (β phase) (see 1.2.3 for

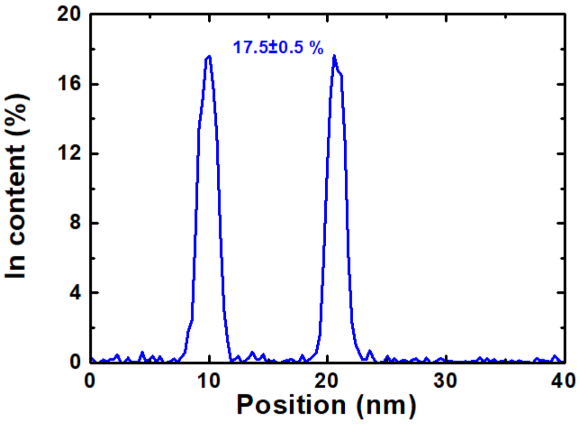

Figure 5.16 – Indium composition profile from APT quantification for the two first QWs of sample E.

Substrate	PL emission wavelength (nm)	XRD In content (%)	APT In content (%)	EDX In content (%)
GaN template	500	18.0	17.5	12.5
InGaNOS 3.190	525	-	-	15.3
InGaNOS 3.200	537	-	-	-
InGaNOS 3.205	549	-	-	18.5

Table 5.6 – Indium content measured by the different characterization techniques for sample E and set of samples B.

more explanation). From the statistical investigation on In distribution, the fraction of In atoms in the form of clusters into the MQWs has been estimated around 25 %.

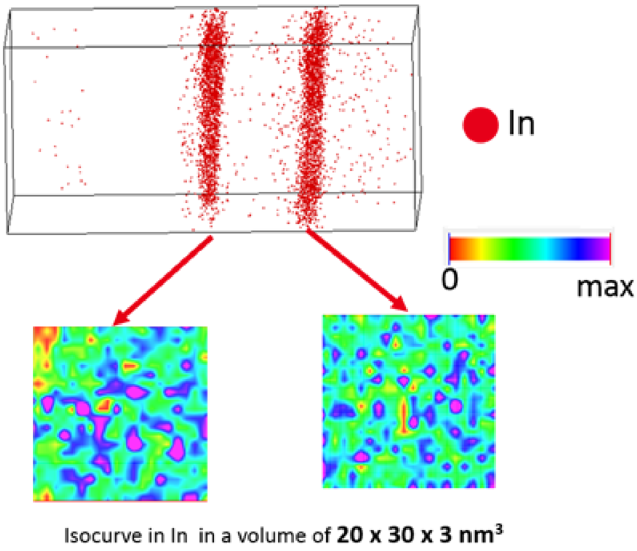

FIGURE 5.17 – 3D reconstruction of a volume of 20 × 30 × 3 nm^3 from sample E active region and In isocurves for the two first QWs.

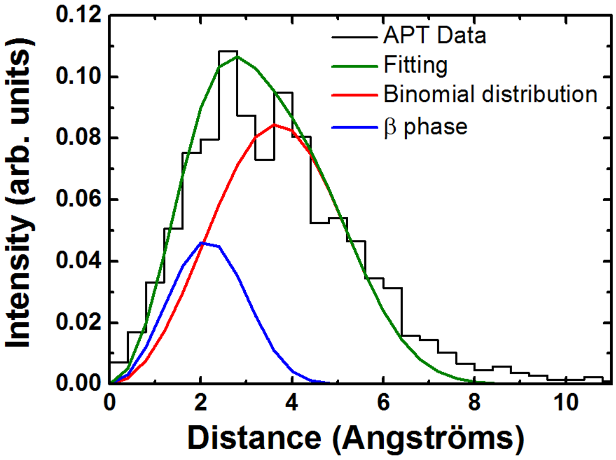

FIGURE 5.18 – Distribution of indium with the distance to the nearest neighbour (black) fitted with the green curve. The fitting curve has two contributions, the binomial distribution (red) and another phase (blue) attributed to the indium clustering.

Sample B on InGaNOS 3.205 is currently being analyzed with APT. Because of delays in the preparation and in the analysis, we will not be able to show the results here. There might be some clustering occuring but we will not be able to confirm it. More measurements detailed below (behavior of PL with temperature) provide useful indications.

5.2.3 Determination of electric field by electron holography

As shown in section 2.2.3, because of the reduced strain in the MQWs grown on InGaNOS, the internal electric field should be reduced compared to MQWs grown on GaN template (for InGaN QWs of same In content).

5.2.3.1 Principle

In order to assess the internal electric field inside the layers, they were examined by off-axis electron holography. Off-axis electron holography is a TEM based technique where an electron biprism is used to interfere an object wave that has passed through a specimen of interest with a reference wave that has passed through only vacuum [5]. Fig. 5.19 shows a schematic for off-axis electron holography. A field emission gun is required to provide a coherent source of electrons. By applying a voltage to the biprism, two virtual electron sources are formed in the back focal plane to form the electron hologram. By increasing the voltage on the biprism, the virtual sources are pushed further apart which will increase the width of the hologram and decrease the fringe spacing. For medium resolution electron holography, a Lorentz lens is used instead of a conventional objective lens in order to provide a useful field of view in the range 200 nm to 2 μm.

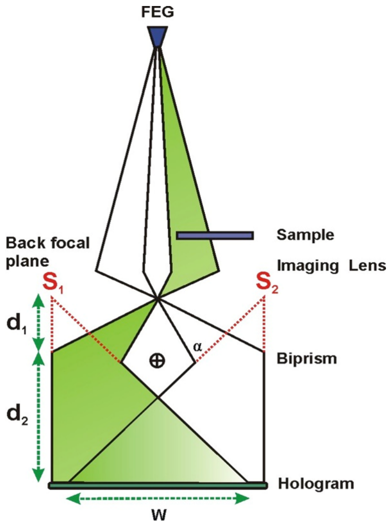

FIGURE 5.19 – Schematic for off-axis electron holography setup.

The holograms are then reconstructed by taking a Fourier transform of the hologram, and selecting a sideband containing the phase information that is carried by the interference fringes. An inverse Fourier transform of this sideband will then provide a complex image from which phase and amplitude images of the specimen can be calculated.

If the specimen of interest is thin and diffraction effects can be minimised, then the phase change of an electron that has passed through the specimen in the direction of the beam z, is given by :

$$\Phi = C_E \int V(x,z)dz - (\frac{e}{\hbar}) \int A_z(x,y)dz \tag{5.1}$$

where C_E is a constant dependent on the operating voltage of the TEM, V the electrostatic potential and A_z the component of the magnetic vector potential in the direction of the electron beam. In a weakly diffracting and non magnetic system, the measured phase can be directly linked to the electrostatic potentials in and around the specimen.
Holography was first used by Cherns *et al.* to measure the internal electric field in InGaN/GaN QWs [6] and a few attempts have been carried out ever since [7].

5.2.3.2 Results

In these experiments, specimens were prepared by Focused Ion Beam (FIB) milling using an operating voltage of 16kV and then cleaned using 2 kV ions to a final thickness of 100 nm. In order to provide the required spatial resolution the microscope was operated in free lens mode such that holographic fringe spacing of 0.7 nm could be obtained to provide a resolution of 1.4 nm. To improve the sensitivity, stacks of 64 holograms of 8 seconds each were acquired then aligned and averaged. To test that the technique was suitable for the field measurement, a calibration specimen containing well known structure was used. Fig. 5.20 shows the maps of the electrostatic potential for sample E, sample B on InGaNOS 3.190 and sample B on InGaNOS 3.205. From the HAADF STEM image of sample E shown in Fig. 5.12 (a), it appears that the layers are rather homogeneous and as such the corresponding map of the electrostatic potential shows homogenous values in each QW. For the samples B on InGaNOS 3.190 and 3.205, the HAADF STEM images of Fig. 5.12 (b) and (c) showed that the layers are of variable homogeneity and as such the measured potentials in Fig. 5.20 (b) and (c) are also varying and are thus difficult to interpret.

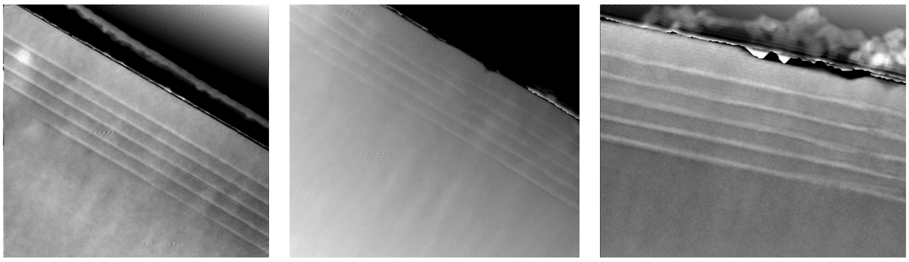
(a) (b) (c)

FIGURE 5.20 – Potential maps of sample E (a), sample B on InGaNOS 3.190 (b) and sample B on InGaNOS 3.205 (c) as measured by off-axis electron holography.

Fig. 5.21 plots the electric potentials and the electric fields measured accross the different specimens. As the layers are of variable homogeneity for the samples B, the values of the electric fields should be treated with caution. Furthermore, as the spatial resolution used for this measurement is relatively high (1.4 nm), the error on the electric field which is the derivative of the potential will be high as well. Table 5.7 summarizes the average potential average amplitudes and the average electric fields.

The electric fields are measured to be 3.2±0.1, 2.5±0.4 and 3.3±0.3 MV/cm for sample E, sample B on InGaNOS 3.190 and sample B on InGaNOS 3.205. These values are close to the theoretical values calculated by Bernardini *et al.* of 3.3 MV/cm for an InGaN/GaN QW with an indium content of 20 %. Because of the uncertainty in the indium contents measured by EDX, we could not run a satisfactory simulation to know if these results were expected. However, we can note that the electric field is similar between sample E and sample B on InGaNOS 3.205 although the indium content in the MQWs is higher in the second sample (see EDX measurement). The electric field is also smaller for sample B on InGaNOS 3.190 compared to sample E although the indium content is higher here too. It would have been interesting to compare samples with the same indium content in the MQWs grown on the different substrates. But, from these preliminary measurements it seems that the electric field is decreased in the samples B thanks to the use of the full InGaN structure on InGaNOS substrates.

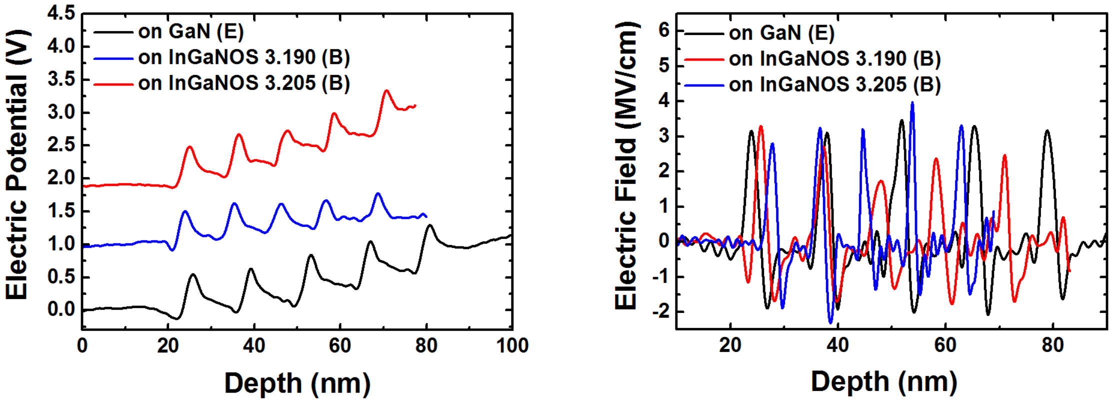

(a) (b)

FIGURE 5.21 – Potential profiles measured across the different specimens (a) and resulting electric fields (b).

Substrate	*a* lattice parameter (Å)	Potential average amplitude (V)	Electric Field (MV/cm)
GaN template	3.184	0.92	3.2±0.1
InGaNOS 3.190	3.190	0.72	2.5±0.4
InGaNOS 3.205	3.205	0.94	3.3±0.3

TABLE 5.7 – Potential average amplitude (rebalanced in the case of all the barriers having similar width) and electric field in the active region of sample E and samples B on InGaNOS 3.190 and InGaNOS 3.205.

5.2.4 IQE measurements and PL behavior with temperature

For sample E and the set of samples B, the PL spectra behavior was studied as a function of temperature and the optical IQE was determined.

5.2.4.1 PL spectra behavior with temperature

Carrier Localization The PL emission energy as a function of temperature is displayed in Fig. 5.22 (a) for sample E and in Fig. 5.22 (b) for sample B on InGaNOS 3.205. Samples B on the two other InGaNOS substrates show similar behavior as sample B on InGaNOS 3.205. Sample E follows the usual S-shape and the amplitude of the PL emission energy between low and room temperature is rather small. On the contrary, for the set of samples B, the curve does not follow a S-shape and the energy amplitude between low and room temperature is larger , about 80 meV (both curves are represented with a scale of same amplitude). The nature of the localization seems to be different between the structure grown on GaN and the samples grown on InGaNOS substrates. It is possible that the carriers are 100 % localized (or partially localized) throughout the whole range of temperatures for the set of samples B which would then follow a Varshni law with an offset corresponding to the localization energy.

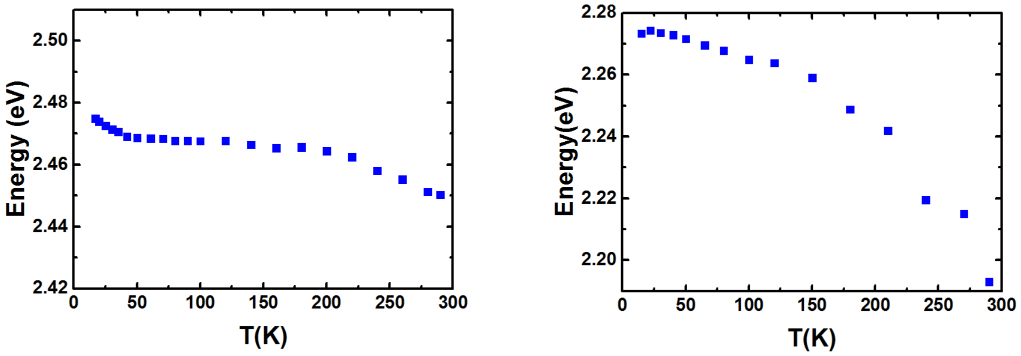

(a) (b)

FIGURE 5.22 – PL Emission energy as a function of temperature for sample E (a) and for sample B on InGaNOS 3.205 (b). The samples were excited using a 405 nm laser diode.

Fig. 5.23 (a) plots the normalized PL integrated intensity as a function of 1/T for sample E (black curve) and for set of samples B (blue, green and red). All the curves are fitted with an Arrhenius plot using two exponential terms in case of sample E and a single exponential term in the case of samples B. The corresponding activation energies are given in Table. 5.8. We note a very different behavior for sample E on GaN template as opposed to set of samples B on InGaNOS substrates. For the set of samples B, the PL intensity remains stable up to high temperatures (about 120 K) as opposed to sample E for which intensity starts to decrease around 50 K. While curve of sample E is characteristic of InGaN QWs, for the set of samples B the behavior resembles the one of QDs. Indeed, Fig. 5.23 (b) from

[8] plots the PL intensity as a function of 1/kT for InGaN MQWs and InGaN QDs, the difference between the two curves seems comparable to our observations. The MQWs on InGaNOS (set of samples B) therefore present a strong carrier localization which seems similar to the one obtained in QDs.

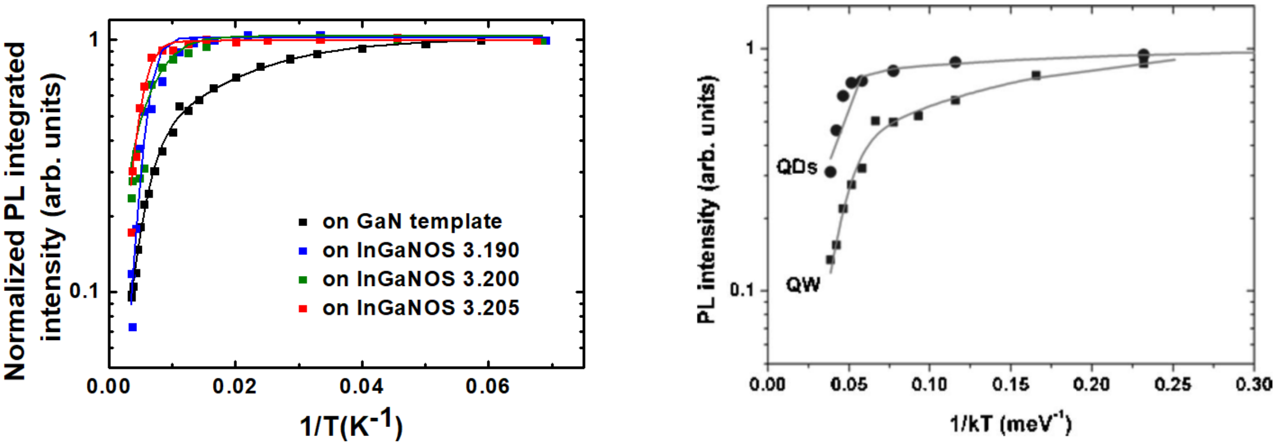

(a) (b)

Figure 5.23 – Normalized PL integrated intensity as a function of 1/T for sample E (black) and samples B on InGaNOS 3.190 (blue), on InGaNOS 3.200 (green) and on InGaNOS 3.205 (red) (a) Normalized PL integrated intensity as a function of 1/T in the case of a InGaN/GaN QW and in the case of InGaN QDs (b) [8].

Origin of the localization This QD-like behavior may originate from QW width fluctuations, In inhomogeneities, and/or indium clustering (see 1.2.3). Indeed such phenomena further confine the carriers compared to an active region with smooth interfaces and QW indium content that follows the random alloy distribution (the localization however already exists in such a structure as commented in 1.2.3). Unfortunately, the presence of clusters cannot be confirmed in the set of samples B as the APT analysis was not yet carried out. However, the QW width fluctuations are confirmed.

The great QW width fluctuations in the set of samples B can be seen on the TEM images in Fig. 5.12. The growth of InGaN with high indium content that generates defects might be responsible for the non-abruptness of the well/barrier interface (second interface). Furthermore, as the barriers are made of InGaN and not of GaN the surface is not smoothened between the different QWs. Such well width fluctuations were also previously observed in commercial LEDs probably to a smaller extent [9].

Discussion on the clustering (see section 1.2.3.3) The strong localization may also originate from the presence of clusters. If clustering is confirmed for sample E, it is possible that an enhanced clustering occurs in the set of samples B (to be confirmed with APT). The origin of this enhanced clustering (if it exists) is unclear. However, it may be related to the different strain state between sample E and the set of samples B. Wang *et al.* [10] demonstrated the presence of In-rich QDs in InGaN QWs induced by phase separation of indium thanks to the use of an InGaN underlayer, relaxed with respect to the GaN buffer. This may be explained by the phase diagram from [11] (Fig. 1.18). Indeed, as the InGaN alloy is more relaxed the phase diagram shifts to the right and more instability is induced. For the same In content (around 20 % in our case), the probability of phase separation increases as the InGaN layer is more and more relaxed (*i.e.* this probability is increased for the set of samples B compared to sample E which is totally strained on GaN). However, there is only one PL emission peak here whereas phase separation is usually evidenced by the presence of at least two PL emission peaks [10].

For Griffiths *et al.* [12], the presence of clusters red-shifts the emission wavelength. Indeed for an *a*-plane sample and a *c*-plane sample with the same mean indium composition in the QWs, they observe that the *a*-plane sample with clustering emits at a longer wavelength although the electric field is smaller. Although the wavelength red-shift observed in PL as a function of the substrate's *a* lattice parameter is mainly due to a different indium content (as shown with the EDX measurements), it is possible that it is also influenced by a different degree of clustering between sample E and the set of samples B.

According to Gerthsen *et al.* [13], the presence of clustering depends on the growth conditions. The InGaN alloy should present more clustering when grown at lower growth rate. However, that paper was written before the reconsideration of the clustering question, so these observations are questionable. Samples C are grown with the same growth temperature as the set of samples B but the growth rate of the active region is multiplied by a factor of three. The normalized integrated intensity of sample C on InGaNOS 3.205 is plotted in Fig. 5.24. The curve is an intermediate between sample E and the set of samples B. The fitting requires two exponentials and the PL intensity plateau is smaller compared to set of samples B as the PL intensity starts to decrease at about 90K. The localization seems to be less strong although the mean In content is probably larger (PL emission peak at 594 nm). There might be less clustering here compared to the set of samples B. The smaller intensity plateau could also be a consequence of an increased defect density that can be more easily reachable as the temperature is raised.

In light of these comments, coming back to the InGaN UL sample presented in 3.3, the behavior of the PL integrated intensity as a function of 1/T from Fig.3.17 looks like the one of QDs as well. In this case, the QD-like behavior probably originates from the increased surface roughness resulting from the 50 nm-thick InGaN layer under the active region as compared to the reference structure. The resulting increased localization due to the QW thickness fluctuations is likely to be the reason for the IQE improvement compared to the reference structure as will be detailed in the next section.

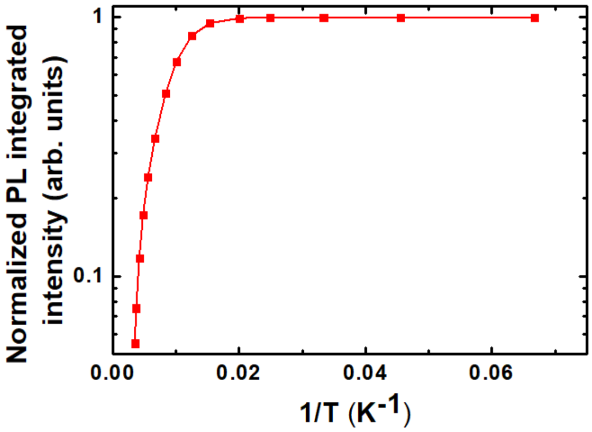

FIGURE 5.24 – Normalized PL integrated intensity as a function of 1/T for sample C on InGaNOS 3.205.

5.2.4.2 Internal Quantum Efficiency

The normalized PL efficiencies at 15 K and 290 K for sample E and the set of samples B are given in Fig. 5.25. Table. 5.8 gives the maximum IQE that were measured for the four samples. IQE of 13 %, 9 %, 16.5 % and 10 % were obtained for sample E and samples B on InGaNOS 3.190, InGaNOS 3.200 and InGaNOS 3.205 respectively.

Substrate	PL emission wavelength (nm)	Max IQE	1st activation energy(meV)	2nd activation energy (meV)
GaN template	500	13.0	50.1	7.4
InGaNOS 3.190	525	9.0	78.3	-
InGaNOS 3.200	537	16.5	29.2	-
InGaNOS 3.205	549	10.0	65.6	-

TABLE 5.8 – Characteristics of full InGaN structures on InGaNOS.

The behavior is different between sample E on GaN template and set of samples B on InGaNOS substrates. At low temperature, the normalized PL efficiency presents a plateau for small carrier injections except for sample B on InGaNOS 3.205 for which the curve is less stable. At 290 K, the IQE reaches its maximum at rather high power for sample E while it remains rather stable throughout the whole range of excitation powers and reaches a maximum at lower powers for the set of samples B. Therefore, the droop should be larger for set of samples B even if the range of excitation power reached with the 405 nm laser diode does not correspond to very high injection densities like the ones reached in electroluminescence. If we refer to the ABC model (see for instance [14] for a recent review), the maximum is reached later in the case of sample E which will therefore have a larger A coefficient. As the A coefficient is related to the nonradiative recombination, this would imply a better insensitivity to the nonradiative recombination centers in the case of set of samples B probably thanks to the stronger localization.

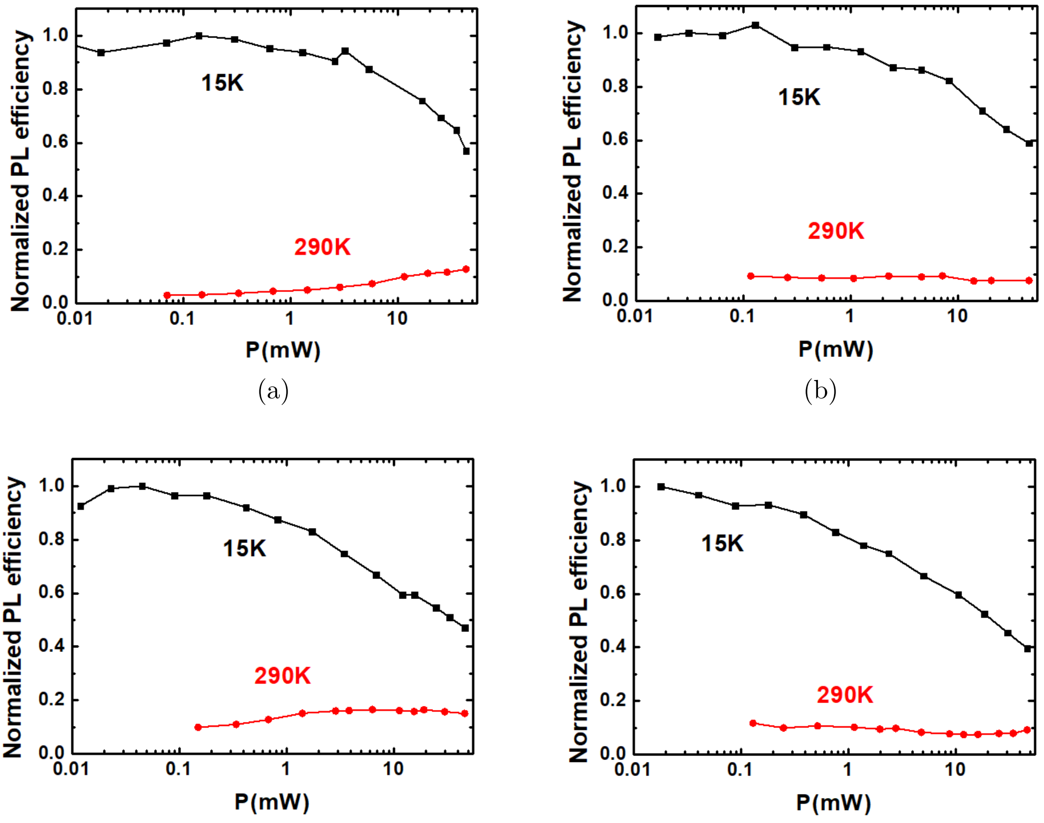

(a) (b)

(c) (d)

FIGURE 5.25 – Normalized PL efficiency of MQW samples grown under the "green conditions", sample E (a), samples B on InGaNOS 3.190 (b), on InGaNOS 3.200 (c), on InGaNOS 3.205 (d).

Despite a quite high density of defects (numerous V-pits observed in TEM and AFM, large FWHM of the RC), the IQE values that are found are quite high for such long-wavelength emitting structures that are not optimized. The QD-like behavior is probably responsible for this characteristic. Carriers are prevented from reaching the nonradiative recombination centers if they are localized in deep potential wells. Indeed, higher room temperature QW efficiencies have been reported for QWs with large fluctuations in width before [15]. Lundin *et al.* [16] demonstrated an increase in EL efficiency as their QWs transformed into QDs (thanks to a variation in growth pressure). Other examples of high quantum efficiencies thanks to the use of QDs or QD-like structure may be found. A good electrical IQE value of 10.2 % at 585 nm [17] has been obtained in an MQW structure showing strong localization. A white LED based on QDs has also been previously demonstrated in the literature[18].

5.2.4.3 Best IQE achieved and comparison with literature

IQE values of our best MQW samples on InGaNOS substrates have been measured. Most of them come from the non-optimized A, B or C series of samples mentionned in this chapter. Nonetheless, some more recent samples yielded high IQE values in the yellow range using improved InGaN buffer layers.
In order to compare our results to the litterature, a bibliographic review was led. First, the values of EQE were transcribed. As some references give EQE peak values and some give it for a given current (usually about 20 mA), we always used the maximum value that was mentioned. Then, the EQE values were converted into electrical IQE values using the values of light extraction efficiencies (LEE). When the LEE is not specified, we used values of 60% for sapphire substrates. If patterned sapphire substrates (PSS) are used or if the removal of the sapphire is mentionned, an LEE of 80% is assumed. In the case of semi-polar orientations, the LEE was set at 60 % when not specified. The values of electrical IQE are displayed in Fig. 5.26 using full black squares for *c*-plane samples and open black squares for samples grown on semi-polar or non-polar planes. Secondly, peak optical IQE values were extracted from other references. They are displayed in Fig. 5.26 using blue triangles. Finally, our optical IQE measurements (peak values) are pictured with red stars. The IQE from the preliminary results (set of samples A, B and C) are displayed with the full red stars. Moreover, the open red stars are IQE values obtained with MQW structure grown on improved InGaN buffer layers, specifically tailored to the substrate or using GaN interlayers.

Whereas our IQE values can be directly compared to the optical IQE values from the litterature, it is delicate to compare them to the electrical IQE values as the injection efficiency is not taken into account in the first case. Moreover, quite often, the EQE values are given at an operating current which does not correspond to the maximum EQE because of the droop phenomenon. As the green and yellow-emitting InGaN-based LEDs present more droop compared to their blue counterparts, it is known that the green gap is even more important when we look at the efficiencies at high current densities. Our samples also seem to present an important droop. In addition, it is difficult to compare our results to the latest results as sometimes only performances in lm/W or WPE are given without further details.
Nonetheless, some high values of IQE were obtained considering that the active region is still not optimized. We can cite the values of 45 % at 516 nm, 31 % at 536 nm, 17 % at 563 nm, 10 % at 598 nm and 2.7 % at 617 nm.

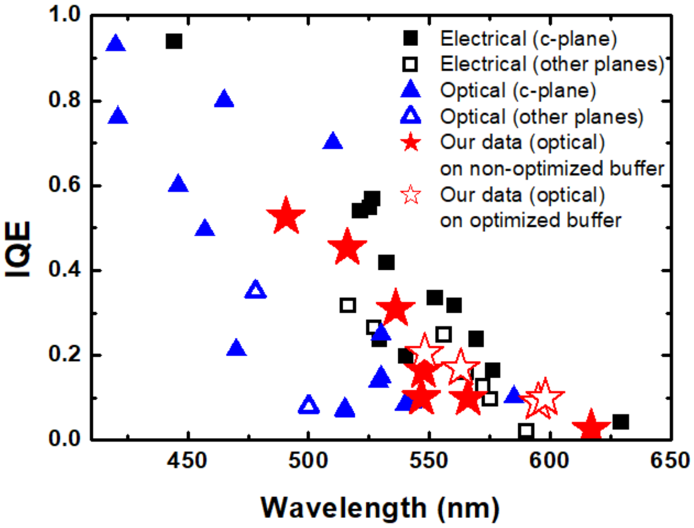

FIGURE 5.26 – Electrical IQE for c-plane (full black squares) [19], [20], [21], [22], [16], [23], [24], [25], [26] and semi-polar planes (open black squares) [27] [28],[29] optical IQE for c-plane (full blue triangles) [30], [31], [17], [32], [33], [34], [35], [36], [37], [38], [39] and for semi-polar planes (open blue triangles)[40] measurements from the litterature and our optical IQE measurements (red stars).

5.3 LED structures

As high values of IQE (when comparing to the litterature) were obtained for MQW structures, a green LED structure was fabricated. The doped parts of the LED structure were first tested before growing the complete LED structure.

5.3.1 n-InGaN and p-GaN layers

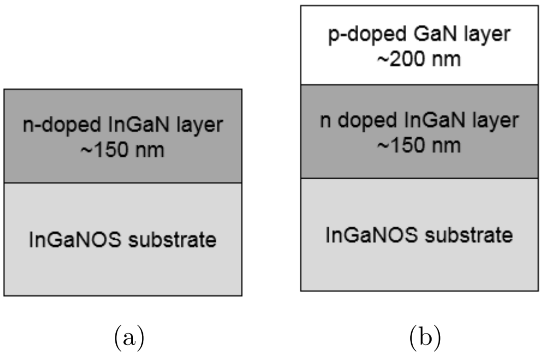

(a) (b)

FIGURE 5.27 – Structures of n-InGaN on InGaNOS substrate (a) and p-n junction on InGaNOS substrate (b).

Two structures were grown in order to test, first, how the InGaN alloy reacts to n-doping and secondly how p-GaN reacts on a layer with a different strain state compared to GaN on sapphire. The structures are displayed in Fig. 5.27. The first structure that is grown is a 150 nm-thick n-InGaN layer doped with silicon. The second structure is a p-n junction with the same n-InGaN layer with a 200 nm-thick p-doped GaN layer (doped with magnesium) grown on top. These structures were grown on the three InGaNOS substrates and on GaN template.

Because of the patterning of the InGaNOS substrates, Electrochemical Capacitance Voltage (ECV) measurements are not possible on the structures grown on such substrates. Fig. 5.28 displays the values of donor and acceptor concentrations measured by ECV for the p-n junction grown on GaN template. The values are 1.4 $\times 10^{19}/cm^{-3}$ for the acceptor concentration in the p-doped part and 2.8 $\times 10^{19}/cm^{-3}$ for the donor concentration in the n-doped part. Whereas p-GaN value is almost the same value as for our standard blue LED, n doping level is higher than the 7 $\times 10^{18}/cm^{-3}$ usually observed in our standard GaN based LED structure. To account for the lower growth rate of InGaN as opposed to GaN (20 times lower), SiH_4 flux has been decreased accordingly.

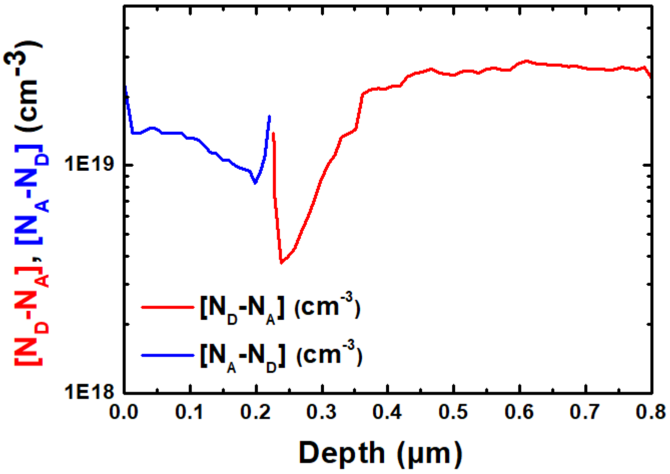

FIGURE 5.28 – Donor and acceptor concentrations measured by ECV in case of p-n junction grown on GaN template.

However, magnesium and silicon will incorporate differently on InGaNOS substrates as the a lattice parameter will be different. We should expect a higher incorporation of silicon and magnesium as the a lattice parameter increases. Fig. 5.29 shows the silicon and magnesium concentrations that were obtained by SIMS for the n-InGaN layer and the p-n junction grown on InGaNOS 3.190. The numerical values are given in Table 5.9. Unfortunately, this analysis was not led on the other three samples so the comparison to the doped layers on GaN is not possible. The Si concentration is in the right range. An efficient n-doping can be expected due to low Si ionization energy. The Mg concentration seems high (5 $\times 10^{19}$ cm^{-3}) as the optimum is about 2 $\times 10^{19}$ cm^{-3}. Indeed, if the Mg concentration is too high, some defects such as Mg clusters could appear, which will be detrimental for p-type conductivity.

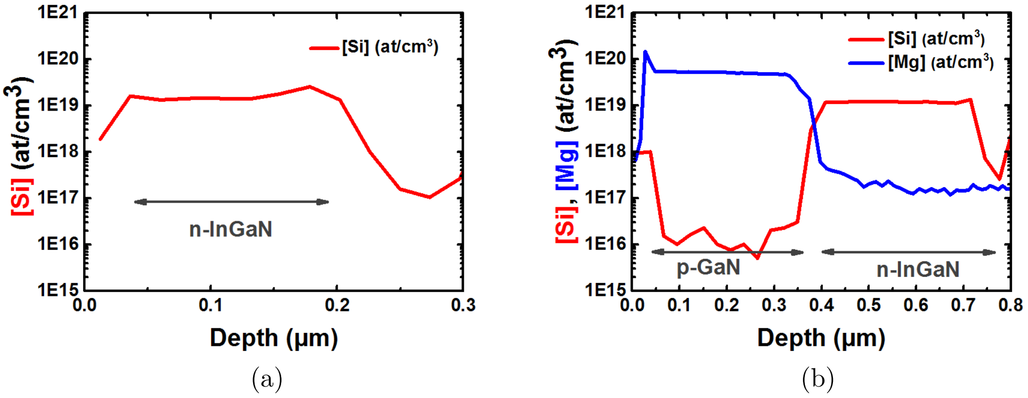

(a) (b)

FIGURE 5.29 – Silicon and magnesium concentrations measured by SIMS for the n-InGaN layer (a) and the p-n junction (b) grown on InGaNOS 3.190.

Bulk resistivity and contact resistance of the n-doped InGaN layer and the p-GaN from the p-n junction were also measured by Transmission Line Measurement (TLM) which is described in annex C.9 For the n-InGaN layer, the low contact resistance indicates an ohmic contact and the bulk resistivity is in the same range as commercial LEDs. However, the p-type contact is not entirely ohmic. The value of the bulk resistivity is particularly high in the p-GaN (values around 0.5 *ohm.cm* are usually reported for commercial LEDs) maybe because of the Mg concentration which is too large.

	n-InGaN	p-GaN
$[Si]\ (at/cm^3)$	$1.5\ \times 10^{19}$	-
$[Mg]\ (at/cm^3)$	-	$5\ \times 10^{19}$
Bulk resistivity $(ohm.cm)$	$2.6\ \times 10^{-3}$	2.5
Contact resistance $(ohm.cm^{-2})$	$1.4\ \times 10^{-4}$	$2.9\ \times 10^{-2}$

TABLE 5.9 – Summary of the SIMS and TLM measurements for the n-InGaN and p-GaN (from the p-n junction) grown on InGaNOS 3.190.

Despite strong improvements that can be made on the p-GaN layer, these first doping trials on InGaNOS 3.190 yield enough conductivity values for a first test of a complete LED structure on InGaNOS substrate.

5.3.2 LED structure emitting at 510 nm

For this first LED, the full-InGaN structure with p-GaN on top was grown on InGaNOS 3.190 as presented in Fig. 5.30.

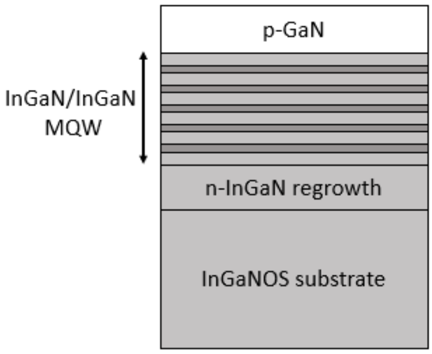

Figure 5.30 – Structure of the LED grown on InGaNOS 3.190.

5.3.2.1 Optical characteristics

Before LED processing, PL measurement were performed using a 405 nm laser diode to excite the samples. Fig. 5.31 (a) displays the PL spectrum at 1.2 mW and Fig. 5.31 (b) the IQE curves at 15 K and 290 K. The peak emission wavelength is 524.7 nm and the emission is rather broad ($\sim$ 60 nm). The maximum IQE is measured to be 58.5 %. However, this high IQE value is obtained for a very small excitation power of 0.16 mW and the droop observed is already large in the range of excitation powers used here.

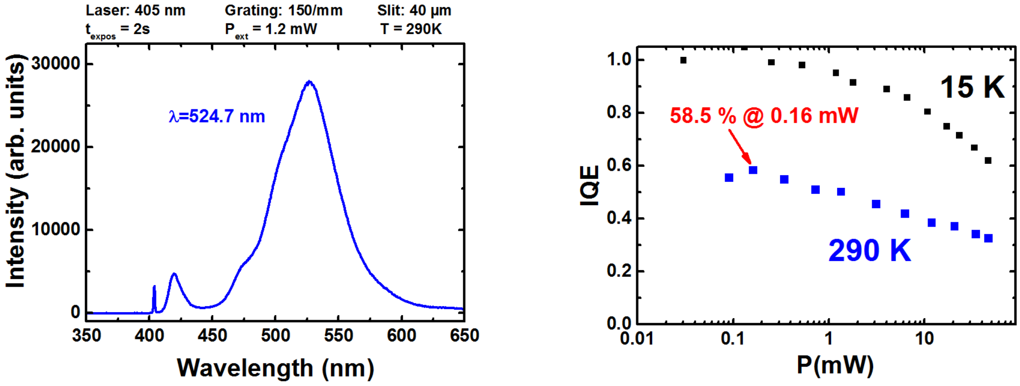

(a) (b)

Figure 5.31 – PL spectrum (a) and optical IQE at 290 K (b) of the LED structure grown on InGaNOS 3.190.

5.3.2.2 Processing details

After the thermal annealing of the sample to activate the p-GaN layer, the LED was processed using conventional chip technology (CC). A thick p-type reflective contact is first deposited on top of the LED. Then, the structure is etched in order to reach the n-type layer, before n-type contact deposition. Due to reflective p-type contact, the LED will emit only on the back side. Note that, as the n-type layer is thin, a careful etching has to be applied to be sure to stop the etching process in the n-InGaN layer.

5.3.2.3 Caracterization after processing

Table 5.10 sums up the TLM measurements that were made on the processed LED. Alike for the previous results, the n-InGaN presents good characteristics (low contact resistance implying an ohmic contact and bulk resistivity in the same range as commercial LEDs). In case of p-type layer, the bulk resistivity and the contact resistance are high. This implies that the p-doping level is not high enough. The operating voltage of the LED is thus expected to be high. Note that circular TLM measurements would be required for a finer analysis.

	n-InGaN	p-GaN
$[Si]$ (at/cm^3)	$1.8\ \times 10^{19}$	-
$[Mg]$ (at/cm^3)	-	$1.1\ \times 10^{20}$
Bulk resistivity $(ohm.cm)$	$1.0\ \times 10^{-3}$	12.8
Contact resistance $(ohm.cm^{-2})$	$1.0\ \times 10^{-4}$	$4.5\ \times 10^{-2}$

Table 5.10 – Summary of the SIMS and TLM measurements for the n-InGaN and p-GaN (from the LED) grown on InGaNOS 3.190.

Fig. 5.32 displays the Mg and Si concentration profiles in the LED structure as measured by SIMS. The values in the n-InGaN and p-GaN regions are given in Table 5.10. The magnesium concentration is really high and deviates even further from the optimum concentration ($2\ \times 10^{19}\ \ cm^{-3}$) compared to what was observed for the p-n junction. This is in accordance with values deduced from the TLM measurements. A high number of defects related to Mg are likely to be present due to this high Mg concentration. Furthermore, if the Si concentration is appropriate in the n-InGaN, Si atoms are also present in the p-GaN region. This is detrimental as it could partially compensate the Mg doping. The Mg concentration in the n-InGaN region is also non-negligeable. The presence of Si on the last 150 nm of the p-GaN layer is unexplained.

The electrical characterizations are not shown here. I-V characteristics present an important leakage current as could be expected from the low conductivity of the p-GaN layer. Because of the low intensity of the EL emission, we will not be able to give any EQE value.

Fig. 5.33 displays the photos of the front side of the LED for different injection currents. Here, we can only see light coming from the contour of the LED as most of the emission is coming from the back side. The emission wavelength changes from low injection to high injection current. Fig. 5.34 (a) displays the electroluminescence (EL) spectra at different injection currents for one of the wafer chips. The dependance of the EL emission wavelength is plotted as a function of injection current for several LEDs on different parts

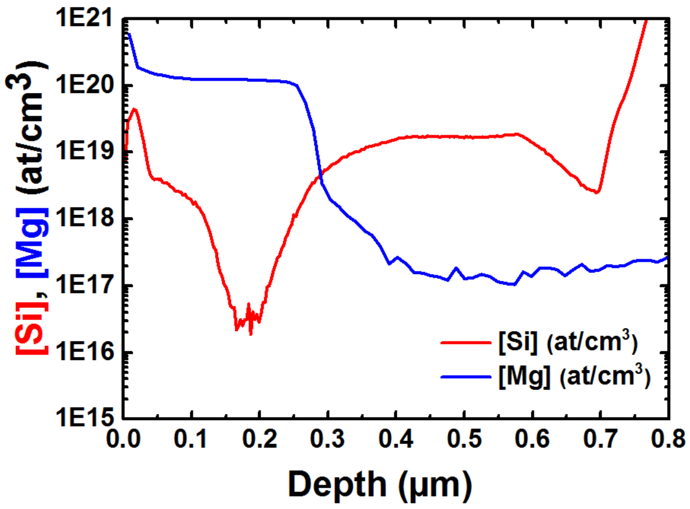

Figure 5.32 – Silicon and magnesium concentration measured by SIMS for the LED on InGaNOS 3.190.

of the wafer. For all the LEDs, a blue shift of 1 to 4 nm is observed as the injection current is increased, because of the screening of the electric field. Above 20 mA, the emission wavelength is rather stable. The EL emission wavelength is scattered between 506 and 520 nm at 0.5 mA and between 504 and 514 nm above 10 mA depending on the LED chip.

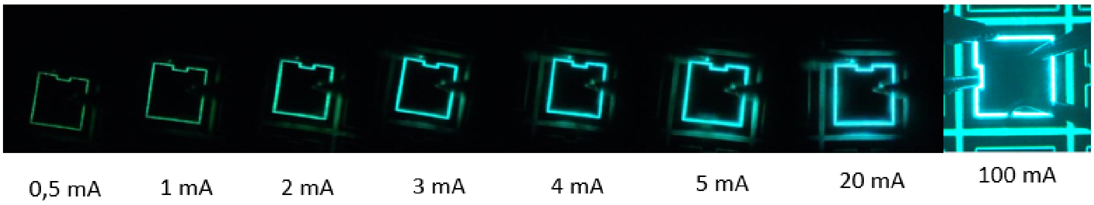

Figure 5.33 – Photos of one LED on InGaNOS 3.190 taken from above under current injection from 0.5 mA to 100 mA. The emission mostly comes from the back of the LEDs and therefore cannot be seen here.

Despite the non optimized LED building blocks, we fabricated the first green LED using a full InGaN structure on InGaNOS substrate. This first test teaches us about the challenges that are to be met when growing such a structure and the leads to follow in order to succeed in manufacturing an efficient LED. The next section will detail some of the remaining challenges.

5.3.3 Remaining challenges

With the fabrication of the full InGaN LED on InGaNOS substrates, we faced several challenges. The issues related to current spreading and the p-doped layer are detailed below.

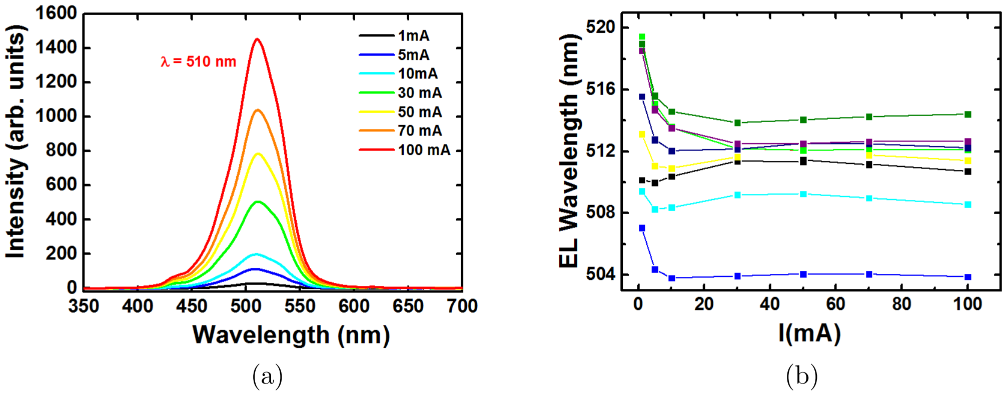

(a) (b)

FIGURE 5.34 – Electroluminescence spectra under different current injections for one of the wafer chips for the LED structure grown on InGaNOS 3.190 (a). EL wavelength emissions as a function of injection current for several LEDs on InGaNS 3.190 taken in different regions of the wafer (b).

5.3.3.1 Current spreading

In our full InGaN LED structure (5.3), the n-InGaN layer thickness is only about 200-nm whereas in the conventional structure the n-GaN layer is at least 1 µm-thick. The thinness of n-doped layer is troublesome. First, during the processing of the LED, one needs to control the etching depth in order to ensure that the n-contact is on the n-doped region. As the n-doped region is thinner, this control gets more difficult and there is a chance that the n-contact might be misplaced.

Secondly, the thinness of the n-doped layer may worsen the current spreading problem [41]. Indeed, the current has a tendency to "crowd" near the contact edges in structures where lateral injection is used. As a result, the light intensity decreases as a function of the distance to the contact edge. This non-uniform current spreading significantly degrades the performance of the device because current crowding results in Joule heating [42].

One of the challenges is therefore to be able to grow a thick n-InGaN layer while maintaining a good structural quality. As discussed in Chapter 4, the use of GaN interlayers might allow us to get to a thickness of about 1 µm which would substantially reduce the current crowding.

5.3.3.2 p-doping

The second challenge that we are facing is related to the p-doped layer. When growing the p-n junctions on the different InGaNOS substrates (5.3.1), we noticed that the surface of 200 nm-thick p-GaN grown on InGaNOS 3.205 was cracked as can be observed on the Scanning Electron Microscope (SEM) image of the surface in Fig. 5.35. Indeed, the p-GaN is under tensile strain on InGaNOS substrates. Here, the critical thickness was probably reached and the p-GaN layer relaxed while forming cracks. As a certain p-doped layer thickness is necessary to have enough carriers, in order to maintain the p-doped layer strained, the implementation of a p-InGaN layer seems unavoidable.

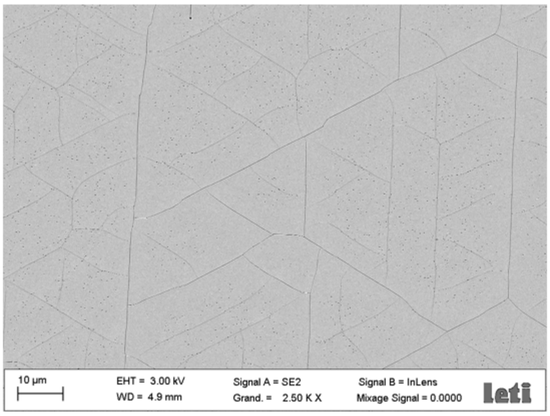

FIGURE 5.35 – Surface of the p-n junction sample grown on InGaNOS 3.205. Some cracks can be observed.

The p-doping of the InGaN alloy with Mg will require a thorough optimization study as the behavior will differ from what has previously been studied for GaN. Limb *et al.* [43] observed an enhancement in EL intensity in green LEDs with the use of p-InGaN instead of low temperature p-GaN. In addition, one of the advantages of using InGaN as the p-doped layer is that the activation energy of Mg dopant decreases with the In mole fraction [44], [45]. Hence, once the right number of Mg atoms have been introduced, the activation should then be easier as compared to p-GaN.
To decrease the V-pit formation which is likely to happen in this p-InGaN layer, Liu *et al.* [46] suggested to use a graded pInGaN :Mg or a p :InGaN :Mg/p-GaN :Mg SL instead of regular p-InGaN in an LED structure. The pit density at the surface was successfully reduced to 3 $\times 10^8$ using the SL p-doped layer for a LED grown on sapphire.

Conclusion

In this chapter, we grew MQW structures on InGaNOS substrates and compared them to MQW structures grown on GaN template. We observed that a PL redshift occurred as the *a* lattice parameter of the substrate was increased. Thanks to the use of InGaNOS substrates, we showed that we were able to reach PL wavelengths up to 617 nm at RT with interesting preliminary results above 650 nm at low temperature. Several fine characterizations of these reference structures on GaN template and full InGaN structures on InGaNOS substrates revealed the increase of the indium content with the *a* lattice parameter of the substrate.
The localization of the carriers was found to be very strong in MQWs grown on InGaNOS substrates. In addition to the QW width variation, a significant indium clustering is possibly responsible for this QD-like behavior. The IQE and the internal electric field were

also measured in the samples. High values of IQE (as compared to the existing litterature) were obtained in the green and amber range, probably thanks to this intense localization. Finally, the first LED structure was grown on an InGaNOS substrate. It was characterized and we reviewed the remaining challenges in order to manufacture an efficient LED on such substrates.

References of chapter 5

[1] Y. El Gmili, G. Orsal, K. Pantzas, T. Moudakir, S. Sundaram, G. Patriarche, J. Hester, A. Ahaitouf, J. P. Salvestrini and A. Ougazzaden. *Acta Mater.* **61**, 6587 (2013).

[2] F. C. P. Massabuau, P. Chen, M. K. Horton, S. L. Rhode, C. X. Ren, T. J. O'Hanlon, A. Kovacs, M. J. Kappers, C. J. Humphreys, R. E. Dunin-Borkowski and R. A. Oliver. *J. Appl. Phys.* **121**, 013104 (2017).

[3] S. J. Pennycook. *Ultramicroscopy* **30**, 58 (1989).

[4] N. Chery, T. H. Ngo, M. Chauvat, B. Damilano, A. Courville, P. De Mierry, T. Grieb, T. Mehrtens, F. Krause, K. Müller-Caspary, M. Schowalter, B. Gil, A. Rosenauer and P. Ruterana. *J. Microsc.* **00**, 1 (2017).

[5] F. A. Ponce. *Ann. Phys.* **523**, 75 (2011).

[6] D. Cherns, J. Barnard and F. A. Ponce. *Solid State Commun.* **111**, 281 (1999).

[7] T. Li, Q. Y. Wei, A. M. Fischer, J. Y. Huang, Y. U. Huang, F. a. Ponce, J. P. Liu, Z. Lochner, J. H. Ryou and R. D. Dupuis. *Appl. Phy. Lett.* **102**, 10 (2013).

[8] M. Sénès, K. L. Smith, T. M. Smeeton, S. E. Hooper and J. Heffernan. *Phys. Rev. B* **75**, 045314 (2007).

[9] G. H. Gu, D. H. Jang, K. B. Nam and C. G. Park. *Microsc. mincroanal.* **19**, 99 (2013).

[10] X. H. Wang, H. Q. Jia, L. W. Guo, Z. G. Xing, Y. Wang, X. J. Pei, J. M. Zhou and H. Chen. *Appl. Phy. Lett.* **91**, 23 (2007).

[11] S. Y. Karpov. *MRS Internet J. Nitride Semicond. Res.* **3**, 16 (1999).

[12] J. T. Griffiths, F. Oehler, F. Tang, S. Zhang, W. Y. Fu, T. Zhu, S. D. Findlay, C. Zheng, J. Etheridge, T. L. Martin, P. A. J. Bagot, M. P. Moody, D. Sutherland, P. Dawson, M. J. Kappers, C. J. Humphreys and R. A. Oliver. *J. Appl. Phys.* **119**, 0 (2016).

[13] D. Gerthsen, E. Hahn, B. Neubauer, V. Potin, A. Rosenauer and M. Schowalter. *Phys. Status Solidi C* **0**, 1668 (2003).

[14] S. Karpov. *Nusod 2014* 17 – 18 (2014).

[15] R. A. Oliver, F. C. P. Massabuau, M. J. Kappers, W. A. Phillips, E. J. Thrush, C. C. Tartan, W. E. Blenkhorn, T. J. Badcock, P. Dawson, M. A. Hopkins, D. W. E. Allsopp and C. J. Humphreys. *Appl. Phy. Lett.* **103**, 141114 (2013).

[16] W. V. Lundin, a. E. Nikolaev, a. V. Sakharov, E. E. Zavarin, G. a. Valkovskiy, M. a. Yagovkina, S. O. Usov, N. V. Kryzhanovskaya, V. S. Sizov, P. N. Brunkov, a. L. Zakgeim, a. E. Cherniakov, N. a. Cherkashin, M. J. Hytch, E. V. Yakovlev, D. S. Bazarevskiy, M. M. Rozhavskaya and a. F. Tsatsulnikov. *J. Cryst. Growth* **315**, 267 (2011).

[17] P. Li, H. Li, Z. Li, J. Kang, X. Yi, J. Li and G. Wang. *J. Appl. Phys.* **117**, 1 (2015).

[18] H. Li, P. Li, J. Kang, J. Ding, J. Ma, Y. Zhang, X. Yi and G. Wang. *Sci. Rep.* **6**, 35217 (2016).

[19] M. Peter, A. Laubsch, W. Bergbauer, T. Meyer, M. Sabathil, J. Baur and B. Hahn. *Phys. Status Solidi A* **206**, 1125 (2009).

[20] D. Schiavon, M. Binder, A. Loeffler and M. Peter. *Appl. Phy. Lett.* **102** (2013).

[21] T. Shioda, H. Yoshida, K. Tachibana, N. Sugiyama and S. Nunoue. *Phys. Status Solidi A* **209**, 473 (2012).

[22] Y. Narukawa, M. Ichikawa, D. Sanga, M. Sano and T. Mukai. *J. Phys. D Appl. Phys.* **43**, 354002 (2010).

[23] R. Hashimoto, J. Hwang, S. Saito and S. Nunoue. *Phys. Status Solidi C* **10**, 1529 (2013).

[24] J.-I. Hwang, R. Hashimoto, S. Saito and S. Nunoue. *Jpn. J. Appl. Phy.* **52**, 08JL13 (2013).

[25] S. Saito, R. Hashimoto, J. Hwang and S. Nunoue. *Appl. Phy. Express* **6**, 111004 (2013).

[26] J. I. Hwang, R. Hashimoto, S. Saito and S. Nunoue. *Appl. Phy. Express* **7**, 071003 (2014).

[27] S. Yamamoto, Y. Zhao, C. C. Pan, R. B. Chung, K. Fujito, J. Sonoda, S. P. DenBaars and S. Nakamura. *Appl. Phy. Express* **3** (2010).

[28] I. L. Koslow, M. T. Hardy, P. Shan Hsu, P.-Y. Dang, F. Wu, A. Romanov, Y.-R. Wu, E. C. Young, S. Nakamura, J. S. Speck and S. P. DenBaars. *Appl. Phy. Express* **101**, 121106 (2012).

[29] M. Funato, M. Ueda, Y. Kawakami, Y. Narukawa, T. Kosugi, M. Takahashi and T. Mukai. *Jpn. J. Appl. Phy.* **45**, L659 (2006).

[30] J. Danhof, U. T. Schwarz, T. Meyer, C. Vierheilig and M. Peter. *Phys. Status Solidi B* **249**, 600 (2012).

[31] J. Daubler, T. Passow, R. Aidam, K. Kohler, L. Kirste, M. Kunzer and J. Wagner. *Appl. Phy. Lett.* **105**, 111111 (2014).

[32] A. M. Armstrong, M. H. Crawford and D. D. Koleske. *Appl. Phy. Express* **7**, 032101 (2014).

[33] K. Cheng, S. Degroote, M. Leys, L. Y. Zhang, J. Derluyn, M. Germain and G. Borghs. *Phys. Status Solidi C* **7**, 2082 (2010).

[34] C. G. M., S. Hammersley, M. J. Davies, P. Dawson, M. J. Kappers, F. C.-P. Massabuau, R. A. Oliver and C. J. Humphreys. *Phys. Status Solidi C* **13**, 248 (2016).

[35] C. H. Liao, C. Y. Chen, H. S. Chen, K. Y. Chen, W. L. Chung, W. M. Chang, J. J. Huang, Y. F. Yao, Y. W. Kiang and C. C. Yang. *IEEE Photonic Tech. L.* **23**, 1757 (2011).

[36] X. Li, F. Zhang, S. Okur, V. Avrutin, S. J. Liu, U. Özgür, H. Morkoç, S. M. Hong, S. H. Yen, T. S. Hsu and A. Matulionis. *Phys. Status Solidi A* **208**, 2907 (2011).

[37] J. Wang, L. Wang, W. Zhao, X. Zou and Y. Luo. *Sci. Chi. Technol. Sci.* **53**, 306 (2010).

[38] D. Fuhrman, H. Jönen, L. Hoffmann, H. Bremers, U. Rossow and A. Hangleiter. *Phys. Status Solidi C* **5**, 1662 (2008).

[39] H. Yamada, K. Iso, M. Saito, H. Masui, K. Fujito, S. P. DenBaars and S. Nakamura. *Appl. Phy. Express* **1**, 041101 (2008).

[40] T. Detchprohm, M. Zhu, Y. Li, L. Zhao, S. You, C. Wetzel, E. a. Preble, T. Paskova and D. Hanser. *Appl. Phy. Lett.* **96** (2010).

[41] X. Guo and E. F. Schubert. *J. Appl. Phys.* **90**, 4191 (2001).

[42] H. Kim, S. J. Park and H. Hwang. *IEEE T. Electron. Dev.* **48**, 1065 (2001).

[43] J. B. Limb, W. Lee, J. H. Ryou, D. Yoo and R. D. Dupuis. *J. Elect. Mater.* **36**, 426 (2007).

[44] M. E. Zvanut, W. R. Willoughby, U. R. Sunay, D. D. Koleske, A. A. Allerman, K. Wang, T. Araki and Y. Nanishi. *Phys. Status Solidi C* **11**, 594 (2014).

[45] S.-N. Lee, J. Son, T. Sakong, W. Lee, H. Paek, E. Yoon, J. Kim, Y.-H. Cho, O. Nam and Y. Park. *J. Cryst. Growth* **272**, 455 (2004).

[46] J. Liu, J.-h. Ryou, Z. Lochner, J. Limb, D. Yoo, R. D. Dupuis, Z. Wu, A. M. Fischer and F. A. Ponce. *J. Cryst. Growth* **310**, 5166 (2008).

General conclusion and perspectives

In this thesis, the issues related to the long wavelength emission with III-N compounds have been investigated in view of applications as the white monolithic LEDs and LED display (monochromatic green and red LEDs). A solution based on the use of InGaN pseudo-substrates, such as InGaNOS, has been explored to relieve the strain in the active region, detrimental to the quantum efficiency. The different steps for the MOCVD growth of a full InGaN structure on this InGaNOS substrate were implemented from the InGaN regrowth stage to the complete processed LED. The grown samples have been characterized using optical and structural characterizations to analyze the crystal quality and emission properties of the structures.

First, the properties of the InGaN alloy were reviewed. The growth of InGaN on GaN on sapphire was found to be difficult as the strain could become very large when increasing the indium content as needed for long wavelength emission. Indeed, the strain induces a strong internal electric field, responsible for the quantum confined Stark effect (QCSE) in the InGaN/GaN quantum wells (QWs). The QCSE separates the electron and hole wavefunctions and becomes more and more detrimental as the indium content is increased or the QW is widened. Increasing the indium mole fraction was preferred as a solution to reach long wavelengths. But, getting to contents higher than 20 to 25 % is difficult because of the low miscibility of indium in GaN and the compositional pulling effect. The In distribution in the InGaN alloy was also shown to be very inhomogeneous and can even present some clustering depending on the growth conditions.
As a first step, the growth of a regular MQW structure on GaN on sapphire was carried out. By simple variations of the growth parameters of the MQWs (growth pressure and TMIn flux), the emission wavelength did not reach wavelength larger than 500 nm as a saturation phenomenon appeared. The lowering of temperature was not tested as a solution as it is known to decrease the structural quality. Then, after a study of the influence of growth parameters (growth rate, growth temperature, thickness) on InGaN buffer layers on GaN, such a buffer layer was placed under the active region (InGaN underlayer (UL) sample). A structure with an InGaN/GaN superlattice (SL)under the active region was also studied. Both of these structures showed an improvement of IQE compared to the

regular MQW structure. A particulary good value was obtained for the InGaN UL sample probably thanks to the strong carrier localization. Next, the indium surface segregation phenomenon at the top and bottom interfaces of the QWs with the QBs was examined. A red-shift was achieved when applying treatments to improve the abruptness of both interfaces. However, even if all these approaches were combined, it would be impossible to increase significantly the emission wavelength while keeping a good effciency because of the strain between the active region and the substrate.

Following these observations, the characteristics of the InGaN pseudo-substrate called InGaNOS have been introduced together with their fabrication process. The *a* lattice parameter which was measured to be larger than the one of GaN on sapphire and even than the one free standing GaN is a great asset. Indeed, regrowth of InGaN buffer layer on InGaNOS substrates and GaN templates showed a decrease of strain with the *a* lattice parameter. The decrease of the compositional pulling effect was also evidenced as when grown with the same growth conditions, the indium content of the InGaN buffer layer increased with the *a* lattice parameter of the substrate. It was shown that the surface quality of such InGaN buffer layers could be greatly improved thanks to the implementation of GaN interlayers placed regularly. By counterbalancing the strain, these interlayers allow to grow InGaN layers of sufficient thickness for an efficient n-doping considering an LED structure. The critical thickness will be pushed further while conserving the large *a* lattice parameter of the InGaNOS substrate. Then, variations of the growth temperature confirmed the importance of maintaining a rather high growth temperature to prevent the degradation of the surface and overall structural quality. An additional study led at the European Synchrotron Radiation Facility (ESRF) showed the homogeneity of the emission at the submicrometer scale for an InGaN buffer layer grown on InGaNOS substrate. The MQW that were grown on InGaN buffers on InGaNOS substrates showed the potential of InGaNOS for long wavelength emission. For MQWs grown under the same growth conditions, a red-shift resulted from increasing *a* lattice parameter of the substrate . Wavelengths up to 617 nm and 653 nm were demonstrated at room temperature and low temperature, respectively. A series of green MQWs grown on GaN template and the different InGaNOS substrates was characterized using PL, TEM, AFM, APT, XRD and EDX. The red-shift observed in PL was attributed to an increase of indium content with increasing *a* lattice parameter of the substrate. The samples grown on InGaNOS showed inhomogeneous indium distribution and QW widths. The PL analysis with temperature revealed a strong carrier localization in these full InGaN MQW structure grown on InGaNOS, as opposed to reference MQW structures grown on GaN for the same QW growth conditions. This localization which seems to be as strong as what can be observed in QDs may originate from the QW width fluctuations observed or possibly from indium clustering (determination on-going). This clustering (if it exists) might be a consequence of the reduced strain in the structure. The optical internal quantum efficiencies (IQE) of the MQW samples grown on InGaNOS were measured and compared to the ones reported in literature. Good values were obtained in the green, yellow and amber ranges thanks to the strong carrier localization which might still exist at room temperature. Then, the first full InGaN LED on InGaNOS substrate was grown and electrically characterized. The remaining challenges related to the control of current spreading and p-doping were reviewed.

The following steps should be applied to achieve efficient long wavelength emission. It was shown that the InGaN regrown buffer can be tailored for each InGaNOS substrate. The idea is therefore to grow an InGaN buffer at high temperature while staying close to the ideal indium content to avoid building up too much strain. GaN interlayers should then be placed regularly to be able to grow buffers up to 1 µm thick while preventing the emergence of numerous V-pits. Then, the MQWs can be grown on top of this buffer. This thesis presented preliminary results for the MQW growth that still require optimization. Applying the TMIn treatment and testing variations on the growth parameters should yield an active region with an improved structural quality. Then, depending on the InGaNOS substrate that is used and on the indium content of the QWs, p-InGaN might be needed. This step will also require a complete study.
Once the growth process of monochromatic green, yellow and red LEDs will be mastered, a white monolithic LED could be grown on InGaNOS subsrate. The distribution of the carriers in the QWs with the different emission wavelengths can then be controlled by adjusting the indium content in the QBs and in the InGaN buffer. This adjustement will also require some additional optimizations to maintain the structural quality.

Despite the remaining optimization steps, the first building blocks for an efficient InGaN based LED in the green and red range have been successfully created. These developments could also later be used for the implementation of an efficient white monolithic LED with high color rendering index or for native micro-displays.

A XRD

A.1 XRD Principle

This method uses an X-Ray beam which is diffracted by the crystal revealing structural information about the material.

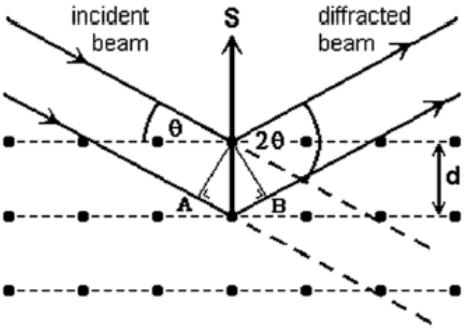

FIGURE A.1 – Schematic of XRD illustrating the conditions required for Bragg difraction to occur [1].

A crystal may be considered as a periodic 3D repetition of atoms called nodes and pictured by the black dots in Fig. A.1. Fig. A.1 represents a sectional view of reticular planes (dotted lines) spaced appart by a distance *d*. The Bragg angle θ is the incident angle of the X-ray beam on these reticular planes. When interacting with the atoms of the crystal, the X-rays will produce a constructive interference only when the following condition is satisfied :

$$2dsin\theta = n \times \lambda \tag{A.1}$$

with n an integer and λ the X-ray wavelength. This relation is called the Bragg's law. Fig. A.2 displays a section through reciprocal space for a c-oriented GaN film. The family of planes are represented with dots. The planes of the family ((0002), (0004)...) parallel to the wafer surface are known as symmetrical reflections while the other types of planes ($(10\bar{1}5)$ for example) inclined to wafer surface are called asymmetrical reflections.

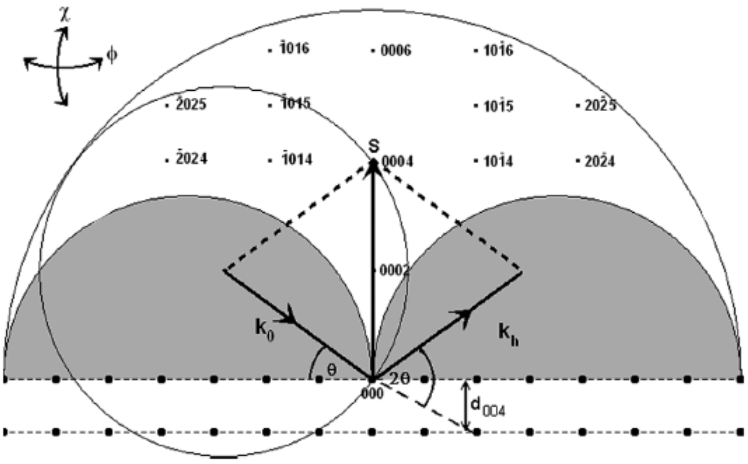

FIGURE A.2 – A section through reciprocal space for a c-oriented GaN film. The regions shown in grey are the inaccessible regions (where the sample blocks the beam). k_0 and k_h, and S are the incident, diffracted and scattering vectors with respect to the crystal [1].

Fig. A.3 displays a schematic of the sample reference frame to show the different possible axes of rotation.

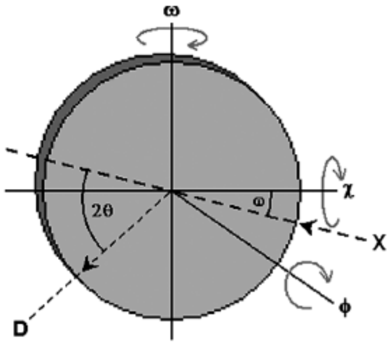

FIGURE A.3 – Sample reference frame showing the axes of rotation. The ϕ axis projects out of the plane of the page; the ω and χ axes lie within the plane of the page. X refers to the x-ray source and D to the detector. [1].

A.2 Different types of measurements

The different types of scans that were conducted during this thesis and shown in this manuscript are the following :

- ω scan (1D scan) : The detector does not move and the sample is rotated around the ω axis. The scattering vector S changes its direction while its length remains constant.
- $2\theta - \omega$ (1D scan) : For this scan, the X-ray source (or the sample) is rotated by an angle ω while the detector is rotated by an angle of 2θ. The scattering vector S keeps the same direction (which depends on the offset) but its length changes. In

the case of a scan on a symmetrical reflection, the offset is set to zero and $\omega = \theta$. If the results are represented with 2θ on the x-axis, the scan is called a 2θ-ω while if the x-axis is in units of ω, the scan is called ω-2 θ.

- Reciprocal Space Mapping (RSM) (2D scan) : RSMs are obtained by taking a series of ω-2θ scans at different ω values.

Several other types of scans were also conducted for the settings like ϕ scans, for more information, refer to Moram *et al.* [1].

A.3 What can be obtained from the different scans

The standard XRD measurements (sometimes referred to as "out-of plane XRD" as the out-of plane lattice parameter c is measured in this configuration) were realized on a Panalatycal setup. In our case the X-ray source is a copper rotating anode tube. The wavelength of the $K\alpha_1$ transition is of 1.540597Å. The resolution of the X-Ray diffraction is of several millimiter square depending on the beam incidence angle.

A.3.1 ω scan-Rocking Curve (RC)

The curve obtained by conducting an ω-scan can be referred to as Rocking Curve (RC). An example of a rocking curve is given in Fig. A.4. The Full Width at Half Maximum (FWHM) is the width of the spectrum measured at an intensity that equals the maximum intensity reached by the spectrum divided by a factor of 2. Arcseconds units are used (3600 arcsec=1 °).

A broad FWHM of the RC may be attributed to several phenomena :

- High dislocation density
- Large mosaic spread
- Large curvature

Since, all the studies from this thesis were conducted on small substrates (a few centimeters square), the curvature should not have a significant impact. The FWHM of the RC will be attributed to the structural quality of the sample, this notion including the mosaicity and the dislocation density.

A.3.2 Reciprocal Space Mapping (RSM)

For a graphical representation of an RSM, Reciprocal Lattice Units (RLU) are used. They are defined by :

$$Q_x = \frac{2\pi}{\omega} \times (cos(\omega) - cos(2\theta - \omega)) \tag{A.2}$$

$$Q_z = \frac{2\pi}{\omega} \times (sin(\omega) + sin(2\theta - \omega)) \tag{A.3}$$

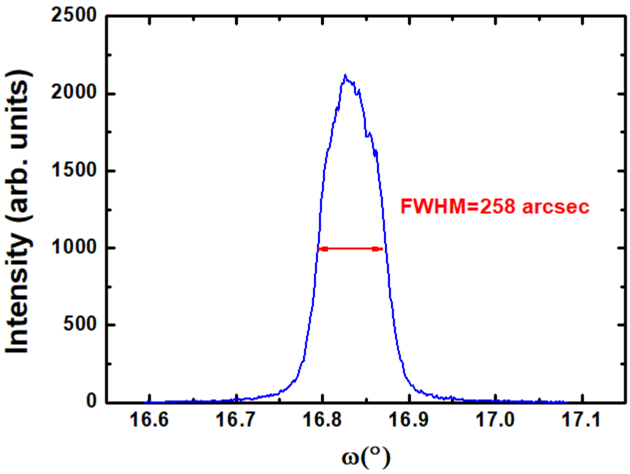

Figure A.4 – Rocking curve for a Free Standing (FS) GaN sample on the (0 0 2) reflection

RSMs on asymmetrical reflections are useful to determine the strain state of a layer on the substrate (usually on the $(10\bar{1}5)$ reflection in our case). Fig. A.5 displays the RSMs on the $(10\bar{1}5)$ reflection for an InGaN layer of different thicknesses on GaN. Two different cases may be found. On the right, the InGaN layer is strained on the GaN layer. The contributions of the InGaN layer (top) and the contribution of the GaN layer (bottom) are vertically aligned (the critical thickness has not yet been reached). On the left, the InGaN layer has two contributions, with the most intense one which is not vertically aligned with the GaN contribution. In this case, the InGaN layer is relaxed (or partially relaxed in certain cases).

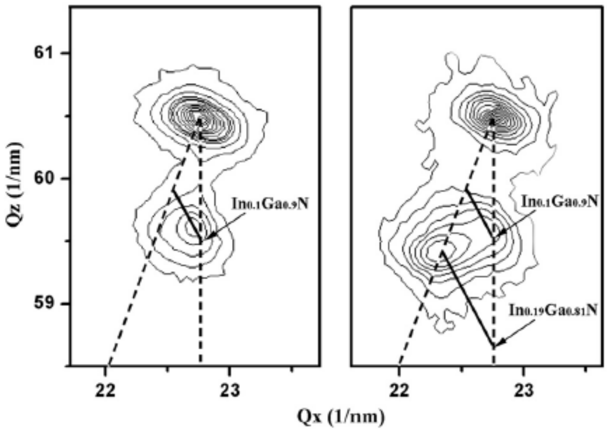

Figure A.5 – Reciprocal Space Mappings of X-ray diffraction density from the $(10\bar{1}5)$ reflection for two InGaN on GaN samples with InGaN thicknesses of 100 nm (a) and 450 (nm) from [2]. In the first case, the InGaN layer is fully strained on GaN (a) whereas in the second case the layer is fully relaxed (b)

A.3.3 $2\theta - \omega$

An example of $2\theta - \omega$ scans for InGaN layers on GaN grown at different temperatures are given in Fig. A.6. For an InGaN layer grown pseudomorphically on GaN, the interplanar spacing d_{hkl} is deduced from the position of the $2\theta - \omega$ corresponding to InGaN (smaller angle, smaller intensity than the peak corresponding to GaN) thanks to the Bragg law. In Fig. A.6 one can observe that as the indium content is increased, the peak associated to the InGaN layer shifts towards the smaller angles.

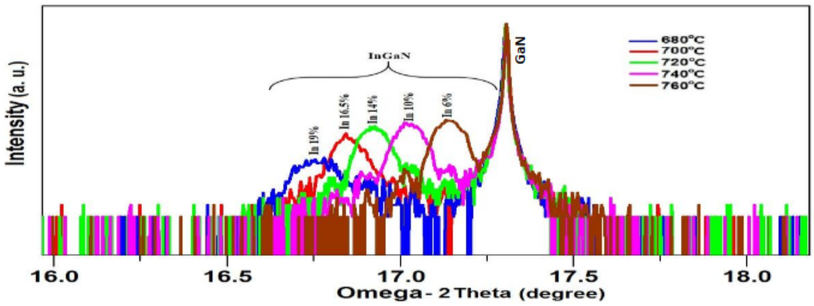

FIGURE A.6 – ω-2θ scan on the (0 0 2) reflection for InGaN on GaN layers grown at different growth temperatures [3].

In a hexagonal system, the interplanar spacing d_{hkl} is related to the a and c lattice with the following equation

$$d_{hkl} = \frac{a}{\sqrt{\frac{4}{3}(h^2 + k^2 + l^2) + l^2 \frac{a^2}{c^2}}} \tag{A.4}$$

From the $2\theta - \omega$ on a symmetrical reflection, one can therefore access the c lattice parameter.

A.4 Grazing incidence XRD

In this configuration, both the incident and the diffracted beams are nearly parallel (grazing) to the sample surface. With this geometry, the family of planes parallel to the surface may be attained in order to have acccess to the in-plane lattice paramater a. In the manuscript, this configuration is sometimes referred to as "in-plane XRD". The grazing incidence XRD measurements were conducted on a SmartLab setup (Rigaku). The configuration of our set-up is similar to the one shown in Fig. A.7 (a). In the sketch of Fig. A.7 (b), the different instrumental angles are shown (description of the angles from [4] :

- θ_s is the angle between the line connecting the sample and the X-ray source and the plane of the sample holder.

- θ_d is the angle between the axis of the in-plane arm rotation and the plane of the sample holder ; in the case of no in-plane arm rotation θ_d is the angle between the line connecting the sample and the detector and the plane of the sample holder.
- $2\theta_\chi$ is the angle of the in-plane arm rotation.
- χ is the angle of the sample tilt against the plane of the sample holder.
- ϕ is the angle of the sample rotation around the sample normal.

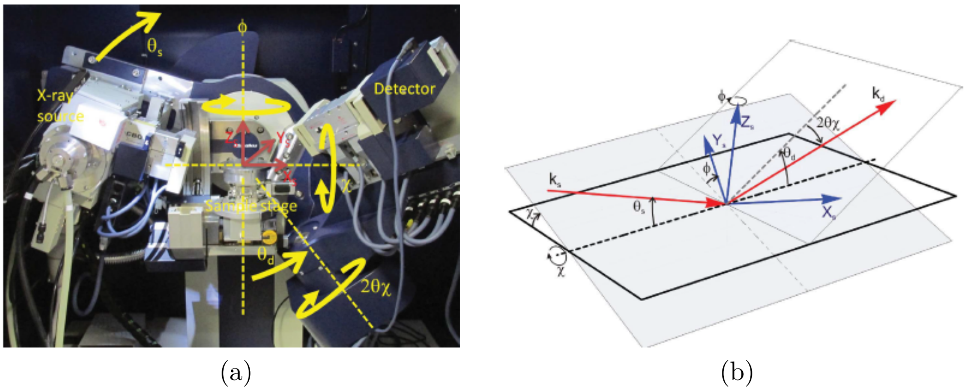

(a) (b)

FIGURE A.7 – In-plane diffractometer similar to our set-up (a). Sketch of the geometry for in-plane diffraction (b) from [4].

In our case, the family of planes (3 0 0) was chosen for the measurements as for GaN, the value of the $2\theta_\chi$ angle is high (113.57 °), therefore decreasing the error on the interplanar spacing [5]. To measure the in-plane lattice parameter, a $2\theta - \chi$ scan is conducted. The X-ray spectrum presents two contributions as the source emits both $K-\alpha 1$ and $K-\alpha 2$ spectral lines from copper (Cu). The spectrum is then fitted to obtain the maximum $2\theta_\chi$angle corresponding to the $K-\alpha\ \ 1$ contribution. Afterwards, from the value of $2\theta_\chi$, θ_s, θ_d, the value of the Bragg angle θ_B is obtained with the following equation :

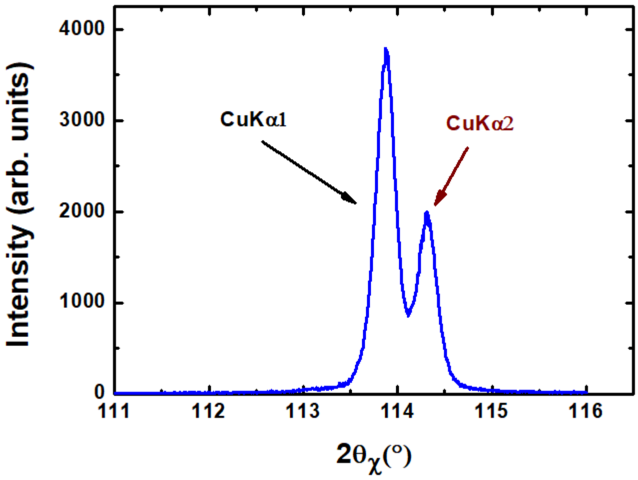

FIGURE A.8 – $2\theta-\chi$ scan on the (3 0 0) reflection for a GaN template (GaN on sapphire).

$$cos2\theta_B(\theta_s, \theta_d, 2\theta_\chi) = cos2\theta_\chi cos(\theta_s + \theta_d) \tag{A.5}$$

Then, thanks to the Bragg's law and equation A.4, the a lattice parameter can be calculated.
When increasing the angle of incidence of the θ_S, deeper layers may be reached. Accessing the depth profile of the a lattice parameter is also possible. However, the relation between θ_S and the depth is non trivial and depth profiling may require additional measurements as one must take into account the attenuation of the incident and diffracted X-ray into the layer. A method of depth profiling of stress with an in-plane geometry has for instance been implemented by Benedikyoitch *et al.* [4].
NB : Because of the very small incident angle θ_S the scanned area is as big as a few cm^2 and the a lattice parameter which is obtained is an average over this area.

A.5 Determination of the strain and the indium content for an InGaN on GaN layer from the a and c lattice parameters

A.5.1 First case : pseudomorphic growth

In the case of a pseudomorphic growth, the indium content may be calculated from the following formula [1] (see section 1.3.1.2 for more details on the different terms of the equation) :

$$x = \frac{1 - \nu_{InGaN}}{1 + \nu_{InGaN}} \times \frac{c_{meas}^{InGaN} - c_0^{GaN}}{c_0^{InN} - c_0^{GaN}} \tag{A.6}$$

The strain s is defined by the following equation :

$$s = \frac{a_{InGaN}^{meas} - a_{InGaN}^{relax}}{a_{InGaN}^{relax}} \tag{A.7}$$

a_{InGaN}^{relax} is calculated thanks to the knowledge of the In content x previously determined and by using Vegard's law.

A.5.2 Second case : non pseudomorphic growth

When the growth is not pseudomorphic, the determination of the In content is more complex and cannot be solely determined using only the c lattice parameter, the value of the measured a lattice parameter is also used. To calculate the indium content, the following equation must be solved (see section 1.3.1.2 for an explanation).

$$2c_{13}\,\varepsilon_{xx} + c_{33}\,\varepsilon_{zz} = 0 \tag{A.8}$$

The equation is expressed using Poisson coefficient ν, a_{InGaN}^{relax} and c_{InGaN}^{relax} dependent on the In content x, and using the measured a and c lattice parameters. For more details see section 1.3.1.2.

$$c_{InGaN}^{relax}(x) + (1 - \frac{2\nu_{InGaN}(x)}{1-\nu_{InGaN}(x)}) \times \frac{a_{InGaN}^{meas} - a_{InGaN}^{relax}}{a_{InGaN}^{relax}(x)} - c_{InGaN}^{meas} = 0 \tag{A.9}$$

This equation is solved using a small Python program and the indium content x is calculated. Then, the strain is calculated similarly as the pseudomorphic case.

References of annex A

[1] M. a. Moram and M. E. Vickers. *Rep. Prog. Phys.* **72**, 036502 (2009).

[2] H. Wang, D. S. Jiang, U. Jahn, J. J. Zhu, D. G. Zhao, Z. S. Liu, S. M. Zhang, Y. X. Qiu and H. Yang. *Phys. B* **405**, 4668 (2010).

[3] S. Surender, K. Prabakaran, R. Loganathan, S. Pradeep, S. Singh and K. Baskar. *J. Cryst. Growth* **468**, 249 (2017).

[4] A. Benediktovitch, T. Ulyanenkova and J. Keckes. *J. Appl. Crystallogr.* **47**, 1931 (2014).

[5] P. F. Fewster and N. L. Andrew. *J. Appl. Crystallogr.* **28**, 451 (1995).

B

Photoluminescence (PL)

Photoluminescence is a characterization technique which principle is to excite with a laser the electrons from the valence band to the conduction band. After a short lapse of time, each electron recombines with a hole, releasing a photon in the process. The photons are then analyzed by a spectrometer coupled to a charge coupled device camera (CCD).

B.1 What information can be obtained with PL measurements

The output is called the PL spectrum and shows the PL intensity as a function of the wavelength. An example of the PL spectrum for a MQW structure emitting in the blue range is given in Fig. B.1.

The Full Width at Half Maximum (FWHM) otherwise reffered to as PL linewidth is the width of the spectrum measured at an intensity that equals the maximum intensity reached by the spectrum divided by a factor of 2. The FWHM of a PL spectrum is usually expressed in meV because only energy can be directly related to the physical mechanisms involved. However, throughout this thesis, only wide spectra will be studied as only InGaN layers (on various substrates) and MQW samples have been grown therefore the FWHMs will be given in nm units. The FWHM of a spectrum for an InGaN layer informs about the homogeneity of a layer (homogeneity in quantum well thickness and/or in composition and/or strain). Indeed, more inhomogeneity leads to more potential fluctuations which results in a wider variety of transitions of the electron from the conduction band to the valence band therefore emitting photons of a variety of different energies.

In this thesis, PL measurements will be used to compare the peak emission wavelengths of different structures to one another. Thanks to the knowledge of the PL emission wavelengths, a tendency on the indium content or the strain in InGaN layers (or InGaN/GaN MQWs) can be seen (see 1.4.5 for more details on the determination of the In content with PL). The value of FWHM of the PL spectra will also be measured in order to evaluate

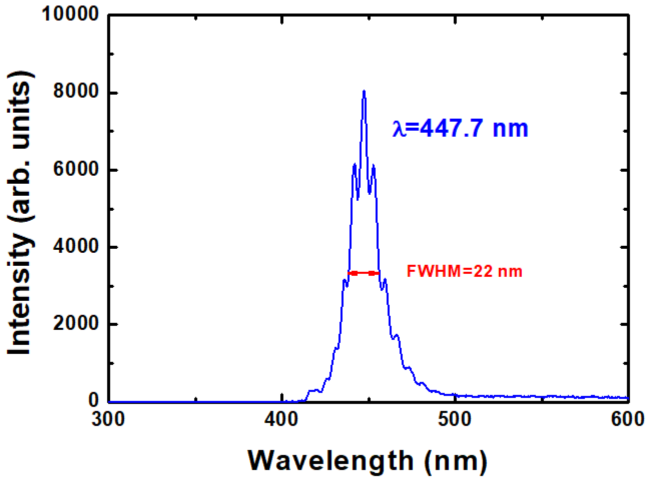

FIGURE B.1 – PL spectrum for a MQW structure emitting in the blue range. The sample is excited with a 405 nm laser diode. The measurement is performed at room temperature (290K).

the inhomogeneity of the alloy.

B.2 Experimental set-up

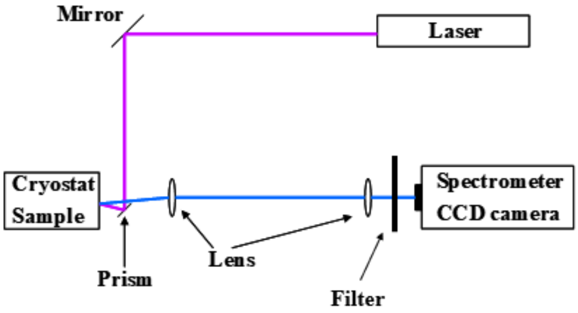

FIGURE B.2 – Schematic of the PL experimental set-up.

Fig. B.2 displays the schematic of the experimental set-up that was used to characterize all the samples presented in this thesis. With the laser, one can excite the sample placed in the cryostat. The temperature of the sample may be varied from 15 K to 300 K (unfortunately the temperature cannot be increased above 300K). The emission is then collected by the spectrometer coupled with the CCD camera. Thanks to the mirrors, the laser beam is sent to the sample with an angle close to the normal of the sample. The laser angle is chosen so that the specular beam from the sample does not reach the PL collecting optics. The PL is collected at the perpendicular of the sample. Two lenses are used to focus the luminescence on the spectrometer's entrance. A filter is also used after the lenses to filter the wavelengths corresponding to the laser emission in order not to saturate the detector.

B.3 Choice of experimental conditions

B.3.1 Choice of the laser

The set-up can be used with three different lasers. The first laser is an He-Cd laser with an emission wavelength of 325 nm. The two others are GaN laser diodes emitting at 375 and 405 nm, respectively.
There are two main types of structures studied in this thesis. The samples belonging to the first category can be referred to as the "MQW samples". It includes all the samples containing MQW layers. The second category includes all the other types of samples, mainly InGaN layers grown either on GaN templates following a GaN regrowth (section 3.2) or on InGaNOS substrates directly (chapter 4). In all cases, the same laser is used to compare samples of a series between one another.
For the second category, the PL caracterization is conducted with the 325 nm He-Cd laser. Indeed, the photon energy of this laser is the only one which is above the transition energy of the low In content InGaN constituing the layers. In the case of layers presenting an In content close to 10 % the 375 nm laser diode could have been preferred. But, for consistency and to avoid any screening of the spectra with the filter, the 325 nm He-Cd laser has been used in all cases.

For the first category, samples including MQWs are considered. The transitions in these QWs with an indium content exceeding 15 % or more can be excited using all three available lasers. However, in order to avoid exciting the underlying GaN layers, the 325 nm He-Cd laser will not be used to characterize such structures. The 4-MQW structure used in the In quantification study section 1.4 (sample 2) is an exception as it includes QWs with low indium contents.
The structures grown on GaN presented in chapter 3 have been characterized with the 375 nm laser diode with the exception of the samples of section 3.3 that were characterized with a 405 nm laser diode. Indeed, one of these samples contains an InGaN underlayer (UL) and another one contains an InGaN/GaN superlattice (SL). In both cases, the In content of the InGaN layers is around 5 %. Therefore, for the IQE measurements, it is important not to excite transitions in the InGaN layers under the active region. Since no variations of the growth parameters of the UL nor of the SL were conducted, the PL characteristics of the UL and SL have not been studied here (using the 325 nm He-Cd laser).
The MQW structures grown on InGaNOS introduced in chapter 5 were characterized using the 405 nm laser diode. Similarly to the case of samples of section 3.3 mentioned above, with this choice, we avoid to excite transitions in the InGaN regrowth regions or in the InGaN barriers of the active region. Since a complete study on InGaN buffers was conducted in chapter 4, we did not focus on the InGaN buffer emission in these MQW

samples grown on InGaNOS in chapter 5 and therefore did not use the 325 nm He-Cd laser to characterize them.

NB : Unfortunately, for several months, the 405 nm laser diode was not available, therefore the samples of section 5.1.2 were only characterized with the 375 nm laser diode. For this reason, no IQE measurements were conducted for these samples.

The laser power density is proportional to the laser power. One should divide the laser power by the surface of the laser spot to obtain the laser power density.

- for the 325 nm He-Cd laser the surface of the laser spot is of 0.045 mm^2
- for the 375 and 405 laser diodes the surface of the laser spot is of 0.020 mm^2

B.3.2 Choice of the measurement temperature

For this thesis, PL measurements have been conducted at Room Temperature (RT) and at Low Temperature (LT) (15 K in our case). For all MQW samples, measurements are shown at RT as the final goal is to fabricate devices emitting at RT. Additional PL measurements are sometimes conducted at LT for a better understanding of physical mechanisms, to quantify the In content (see 1.4.5) or because the PL intensity at RT is too low. For all the other samples (first category), the PL spectra are shown at LT and for some of them the behavior of the PL with the temperature is also studied.

B.4 IQE measurements

IQE is defined as the proportion of electron-hole recombinations that are radiative in the active region (as opposed to the nonradiative ones).

B.4.1 Procedure

For the IQE measurements, we followed a procedure as described for instance by Hangleiter *et al.* [1]. The IQE at a given temperature may be defined as the ratio between the PL efficiency (PL integrated intensity/excitation power) at that temperature and the PL efficiency at low temperature (15K in our case). For this definition, it is assumed that the efficiency is 100% at low temperature, that is to say there are no nonradiative recombinations active at that temperature. Next, the conditions to verify this hypothesis are detailed. The measurement is conducted as follows :

- in the first phase, the sample is cooled to 15 K. A reference sample of high quality GaN is also placed in the cryostat to verify that the samples are indeed at 15K. The PL signal is then maximized by adjusting the lenses. Then, several spectra are recorded as a function of the laser excitation power. Usually, the PL efficiency as a function of the excitation power should follow a plateau before decreasing.

- in the second phase, the PL spectra are recorded for different temperatures at a given laser power. This is to verify that the integrated PL intensity remains constant through a range of low temperatures (between 15 and 50K typically). With this verification, one is sure that the recombination regime is not already in a decay phase with the presence of nonradiative recombination.
- finally, in the third phase several spectra are recorded as a function of the laser excitation power at room temperature

Then, computing treatment is done to plot the PL efficiency at rooom temperature and normalize this value by the maximum value obtained at 15 K. The maximum of this normalized PL efficiency corresponds to the IQE of the sample at room temperature. An example of the curves of the normalized PL efficiencies at 15 K and room temperature are given in Fig. B.3.

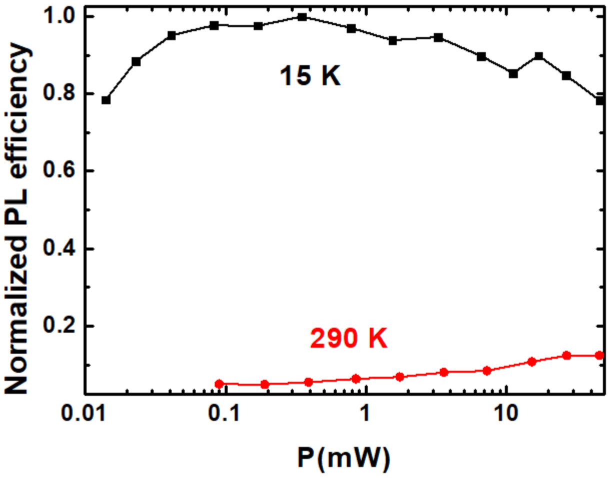

FIGURE B.3 – Typical plot of PL efficiencies at 15 K and room temperature (290 K here) for a MQW structure emitting in the blue range

B.4.2 Hypothesis

In order to verify that efficiency is 100% at low temperature, that is to say there are no nonradiative recombinations active at that temperature, one should plot the integrated efficiency as a function of the inverse of temperature.

A typical plot of the integrated intensity as a function of 1/T is given Fig. B.4 for a MQW sample with an InGaN layer under the active region (sample presented in section 3.3) emitting in the blue range. The integrated intensity increases with the decreasing temperature. For low temperatures (<50 K), a plateau of intensity is expected as can be seen here. If it is the case, one can consider that there are no nonradiative recombinations at LT. When the plateau at low temperature is not observed, the curves of PL efficiencies are not referred to as IQE but simply as normalized PL efficiencies.

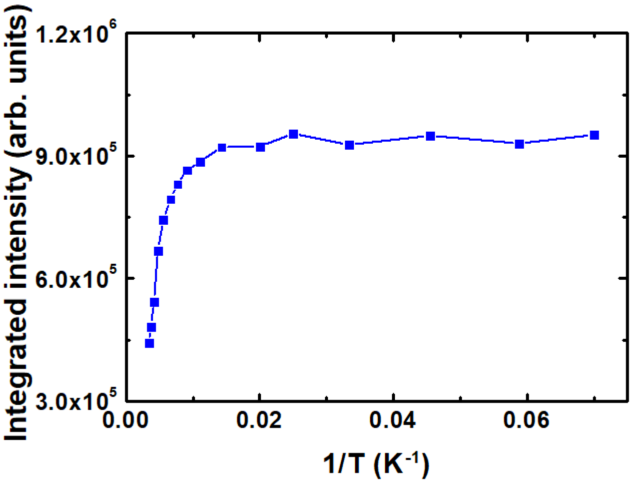

Figure B.4 – Typical plot of the variation of the integrated PL intensity as a function of 1/T (here for a MQW structure with an InGaN underlayer emitting in the blue range).

References of annex B

[1] A. Hangleiter, D. Fuhrmann, M. Grewe, F. Hitzel, G. Klewer, S. Lahmann, C. Netzel, N. Riedel and U. Rossow. *Phys. Status Solidi A* **201**, 2808 (2004).

C Other characterization techniques

In this annex, several characterization techniques used throughout this thesis are rapidly introduced.

C.1 Notion of standard

A standard is a sample which has a well known given composition and which is used as a reference to calibrate a measurement. For instance, in the Energy Dispersive X-ray spectroscopy (described below) set-up used to characterize the samples of this thesis, the standard used is InAs to calibrate In as the In composition is known very accurately. Some techniques require a standard to quantify an element while some others do not.

C.2 Atomic Force Microscopy (AFM)

The Atomic Force Microscopy (AFM) is a type of scanning probe microscopy with a very high resolution enabling to visualize the topography of a sample. AFM exploits the interaction between the atoms of the nanometric sized apex of a probe and the surface atoms of a sample. Fig. C.1 displays Lennard-Jones potential curve. This mathematically simple model approximates the interaction between two atoms (here the atoms of the sample and the atoms of the probe) consists of two term. The first term describes Pauli repulsion at short ranges while the second term dominant at long ranges describe the attraction (for instance of Van der Waals type). Three operation modes may be distinguished :

— the contact mode uses the repulsive forces : the probe presses on the surface and is pushed away because of the Pauli exclusion principle therefore provoking a deviation of the cantilever.

— the non contact mode uses the attractive forces : the forces are very weak and therefore very difficult to measure. Practically, this mode is seldom used.

— the tapping mode uses both repulsive and attractive forces. In this mode, the cantilever is put under vibration at its resonance frequence (typically around a few hundred kHz) with a given amplitude. When the probe interacts with the surface, the amplitude decreases as the resonance frequency decreases. This phenomenon pushes the probe away from the surface of the sample which is then submitted to the attractive forces (the amplitude increases). With the measure of the amplitude, the topography of the surface of the sample may be reconstructed.

In this thesis, the AFM is used exclusively in tapping mode.
The atom force microscope allows to scan an area of a few nanometer square up to a few micron square area.

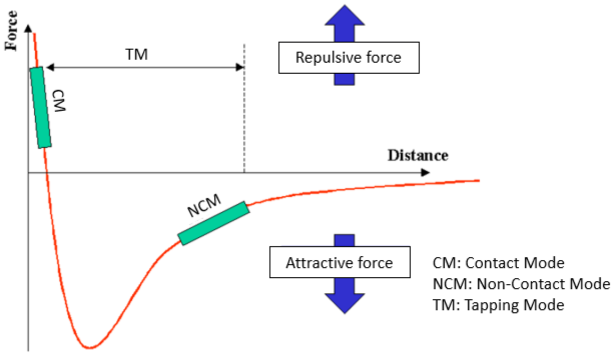

FIGURE C.1 – Lennard-Jones potential curve. The three principal modes are associated to two different domains of the probe-sample interaction

C.3 Cathodoluminescence (CL)

For this technique, the sample is excited with an electron beam from a Scanning Electron Microscope (SEM). The incident electron is slowed down by a multiplicity of shocks, each one creating an electron-hole pair that can later recombine. The random trajectory of the electron is represented by a pear shape region (as the electron energy is larger, the pear shape region grows bigger and deeper). Fig. C.2 displays a schematics of a CL set-up. The green pear shape region corresponds to the generation volume where CL photons are produced.

The advantage of a CL spectrometer coupled to a SEM is the high spatial resolution allowing to scan objects up to the nanometer scale. By changing the energy of the electron beam, one can also access to different depths in the sample (the size pear shape region of Fig.C.2 changes). Indeed, when one increases the energy of the electron beam, the interaction radius increases and additional electron-hole pairs are created in the sample. For our two characterizations using CL, the energy was set to 3 keV (further investigations have not been conducted by varying the energy).

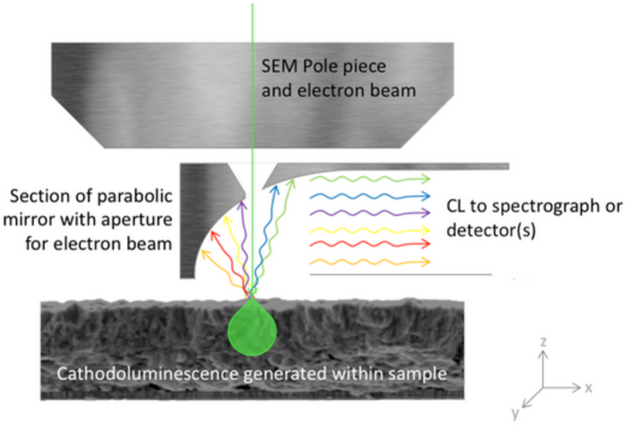

Figure C.2 – Schematics of CL principle

C.4 Atom Probe Tomography (APT)

* APT is an analytical microscopy method which allows mapping the chemical distribution of atoms in three dimensions at a nanometric scale. The principle is illustrated in Fig. C.3. This technique is based on the field effect evaporation of atoms. The sample is prepared with a tip-shape and is submitted to an electric voltage. The evaporation of atoms with their ionic form is controlled and assisted by ultrashort laser pulses. The ions are collected by a time and spatial resolved detector. The chemical nature of ions is determined using time of mass spectrometry (measure of flight time between tip and detector). The initial position (x,y) of atoms is given by the impact of coordinates on the detector. The total number of ions gives the depth of analyzed volume. The volume size depends on materials and analysis conditions ; and can reach (100*100*900) nm^3 for III-N materials. The spatial resolution is anistropic and around 1 nm for III-N. The preparation of the samples is difficult as one needs to extract a tip-shape sample with a radius of curvature of 100 nm or less from a TEM specimen previously prepared. The tip-shape sample is fragile and can break during the experiment if not properly prepared or if the

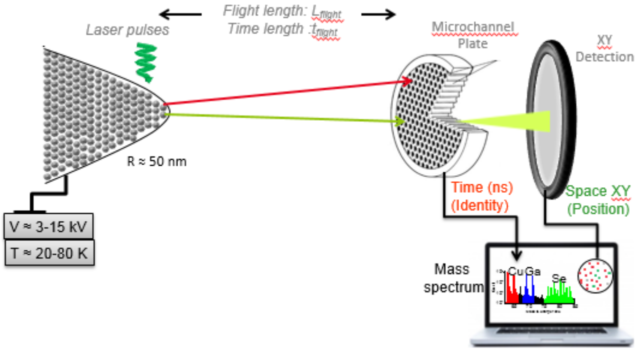

Figure C.3 – Principle of APT

experimental conditions are not appropriate. Although this characterization technique is recent, it has lately been extensively applied to the structural investigation of III-nitrides [1] [2] [3].

C.5 Transmission Electron Microscope (TEM)

Transmission Electron Microscope (TEM) is a microscopy technique based on the transmission of an electron beam through a specimen to form an image as the electrons interact with the sample. The specimen is usually very thin (in our case about 80 μm) and prepared by Focused Ion Beam (FIB) in our case. TEM allows to scan at a very small scale as the atoms can be distinguished.

C.6 Energy Dispersive X-ray (EDX)

EDX is anatycal technique used to chemically identify and quantify the atoms of a sample. In EDX the sample is excited using an X-ray source. It relies on the principle which is that during the beam scanning of the surface of the sample, the incident electrons excite the core energy levels of the different atoms. The de-excitation of the ionized atoms releases X photons of a given energy which are then collected by a detector. EDX requires the use of very thin specimens like the ones used in TEM.

The chemical identification can be conducted using different methods. For all EDX quantifications conducted in this thesis, the method of the zêta factors [4] was implemented. This method takes into account the thickness of the TEM specimen and the absorption of the X-photons by the material. The use of a standard is compulsory to ensure the quantification is accurate.

C.7 Rutherford Backscattering Spectrometry (RBS)

RBS is a characterization technique based on radioanalytical chemistry. An ion flux at high energy interacts with the atoms of the sample. The back-scattered particles are then analyzed to determine the composition of the sample thanks to the good knowledge of the energy loss process of the ions in the material. This technique does not require a standard.

C.8 Secondary Ion Mass Spectroscopy (SIMS)

SIMS is a characterization method which consists of bombarding the surface of the sample with an ion beam. The sample is then sputtered and a part of the sputtered matter is ionized (this technique is destructive). These secondary ions are then accelerated towards a mass spectrometer which supplies information about the elemental, isotopic and molecular composition of the sample. Fig. C.4 presents the main elements of a magnetic sector SIMS analysis instrument All the SIMS analyses in this thesis were conducted by Probion.

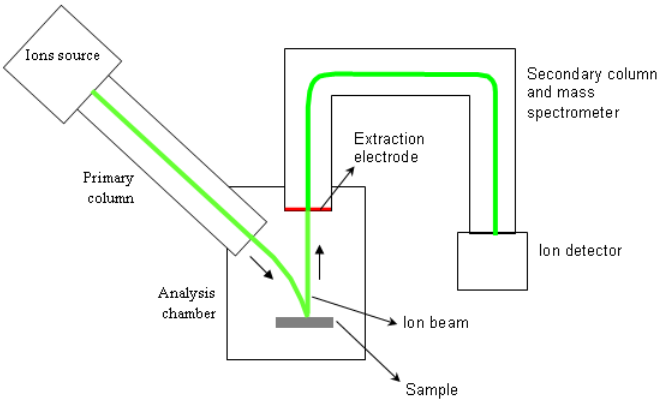

Figure C.4 – Main elements of a magnetic sector SIMS analysis instrument (from Probion's website)

The depth resolution of this technique is about 5 to 10 nm.

C.9 Transmission Line Measurements (TLM)

TLM is a technique used to determine the contact and bulk resistance of a layer. In order to implement this technique, several contacts are deposited separated by various distances on the layer as illustrated in Fig. C.5 (a). A voltage is then applied between the different pairs of contacts to measure the resistance. The plot of the resistance as a function of the distance between the contacts then yields the sheet resistance R_S (from the slope) and the contact resistance R_C (from the intercept with y-axis). A typical plot is given in Fig. C.5 (b)

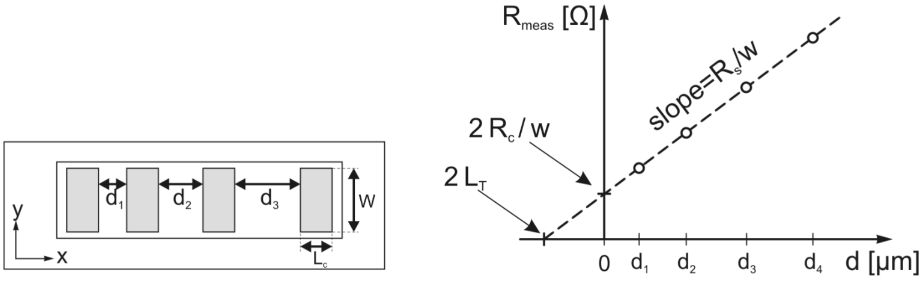

(a) (b)

Figure C.5 – Resistance test pattern for the TLM configuration (a) Evaluation of the contact and sheet resistance for TLM measurements (b).

When the layer evenly conducts the current, the bulk resistivity may be obtained by multiplying the sheet resistance by the layer thickness.

References of annex C

[1] Y.-R. Wu, R. Shivaraman, K.-C. Wang and J. S. Speck. *Appl. Phy. Lett.* **101**, 083505 (2012).

[2] F. Tang, T. Zhu, F. Oehler, W. Y. Fu, J. T. Griffiths, F. C. P. Massabuau, M. J. Kappers, T. L. Martin, P. A. J. Bagot, M. P. Moody and R. A. Oliver. *Appl. Phy. Lett.* **106**, 072104 (2015).

[3] L. Rigutti, L. Mancini, D. Hernández-Maldonado, W. Lefebvre, E. Giraud, R. Butté, J. F. Carlin, N. Grandjean, D. Blavette and F. Vurpillot. *J. Appl. Phys.* **119**, 0 (2016).

[4] M. Watanabe and D. B. Williams. *J. Microsc.* **221**, 89 (2006).

D French Summary

D.1 Introduction

En 2014, le prix Nobel de Physique a été attribué à Isamu Akasaki, Hiroshi Amano and Shuji Nakamura pour l'invention des Diodes Electroluminescentes(DELs) bleues ayant permis l'emergence de sources de lumières blanches basées sur la famille de matériaux AlInGaN. Depuis les années 70, cette famille de matériaux avait été étudiée mais la mauvaise qualité des matériaux et la forte résistivité des couches dopées p ont freiné les recherches qui ont été abandonnées. Pourtant, en 1989 Amano *et al.* ont réussi à activer le magnésium dans le GaN, permettant d'obtenir une jonction p-n. Nakamura *et al.* ont ensuite réalisé la première DEL bleue en insérant des puits quantiques InGaN/GaN dans la zone active en 1994.
Ensuite, avec l'ajout de phosphores YAG, la lumière blanche a été obtenue. En comparaison avec d'autres sources de lumière blanche (lampe à incandescence, tube fluorescent...) les DELs blanches présentent plusieurs avantages comme leur longue durée de vie et leur bon rendement d'efficacité. Par conséquent, la part des DELs est croissante sur le marché de l'éclairage et le taux de pénétration sur le marché était de 22 % en 2017 et devrait atteindre 63 % en 2022. Pourtant les DELs à base de phosphores ont plusieurs problèmes liés à la durée de vie des phosphores et à la stabilité de la longueur d'onde d'émission avec la température de fonctionnement (incompatible avec un éclairage de haute qualité) ainsi que des pertes liées au processus de conversion. Alternativement à cette approche, la DEL blanche monolithique a été introduite en 2001 avec une zone active composée de puits quantiques émettant dans le bleu et dans le jaune. Néanmoins, l'efficacité de ces DELs est limitée par le faible rendement d'émission des puits jaunes et des puits rouges.
Les DELs sont également utilisées pour l'application display, le retro-éclairage et les cristaux liquides. Pourtant si les pixels bleus sont fabriqués à partir des matériaux AlInGaN, les pixels rouges sont fabriqués à partir de la famille de matériaux AlInGaP. Pour les pixels verts ou jaunes, il n'existe pas actuellement de famille de matériaux permettant

une émission DEL efficace, ils sont actuellement fabriqués à partir des nitrures d'éléments III (III-N. Ce problème est connu sous le nom de "green gap". L'intégration des pixels RGB fabriqués à partir de matériaux différents est difficile pour les micro-displays et l'idéal serait de les faire croitre à partir des III-N.

Cependant, si l'on peut théoriquement couvrir tout le spectre de la lumière visible grâce aux III-N, le rendement d'émission diminue lorsque la longueur d'onde augmente. La faible miscibilité de l'indium dans le GaN et la forte contrainte entre la zone active à base d'InGaN et le substrat de GaN sur sapphir sont à l'origine de ce phénomène. De plus, le champ électrique interne qui augmente lorsque les puits quantiques sont élargis ou lorsque la concentration en indium est accrue a un effet néfaste sur le rendement d'émission. De surcroît, la contrainte est à l'origine du "pulling effect" qui rend plus difficile l'incorporation d'indium déjà compliquée à l'origine.

Pour résoudre le problème du "green gap" avec la famille de matériaux AlInGaN, dans cette thèse nous proposons de faire croître la structure DEL sur un substrat InGaN. Grâce à cette méthode, une amélioration de l'incorporation d'indium ainsi qu'une diminution du champ électrique devrait être observée. Puisque l'InGaN massif n'existe pas, des pseudo-substrats d'InGaN appelés InGaNOS sont utilisés pour cette étude. Ils sont fabriqués par Soitec grâce à leur technologie SmartCut. Sur ce substrat, une structure tout-InGaN peut être réalisée. Ces structures pourront ensuite être utilisées pour l'obtention de DELs monochromatiques dans le vert ou dans le rouge pour l'intégration des pixels RGB ou pour l'éclairage de haute qualité. Une DEL blanche monolithique efficace peut également être envisagée grâce à ce process.

D.2 L'alliage InGaN

Ce chapitre a permis d'introduire les propriétés des nitrures d'élements III dont l'énergie de gap (à 0 K) peut potentiellement s'étendre de 0.78 eV pour l'InN jusqu'à 6.35 eV pour l'AlN. Pour les alliages ternaires, cette energie est calculée grâce à la loi de Vegard. La structure crystallographique la plus stable du GaN, la structure wurtzite sera celle étudiée dans cette thèse. Toutes les structures épitaxiées dans ce travail seront de polarité gallium (selon l'axe c).

L'alliage InGaN a plusieurs particularités. L'indium est peu miscible dans le GaN comme le révèle le diagramme de phase. Ainsi, pour la croissance par EPVOM utilisée pendant cette thèse, des conditions de croissance spécifiques sont nécessaires (basse température, faible vitesse de croissance) pour la croissance de l'InGaN. Le distribution de l'indium dans l'alliage est très inhomogène, dans certains cas cette distribution peut dévier de la distribution binomiale et présenter des clusters. La localisation des porteurs est généralement forte dans l'InGaN, celle-ci peut être accentuée par la présence de clusters ou d'inhomogénéités en épaisseur des puits quantiques InGaN/GaN. La croissance d'InGaN sur GaN, nécessaire pour la structure Diode ElectroLuminescente(DEL) est difficile. En effet le désaccord de paramètre de maille (11 % entre l'InN et le GaN) provoque une forte contrainte compressive. Pour cette raison l'épaisseur critique est limitée à seulement quelques nanomètres pour les forts pourcentages d'indium (>20 %). A cause de cette contrainte considérable, de nombreux défauts structurels peuvent être présents dans ce matériau. Ils peuvent être ponctuels (impuretés, etc.) ou sous la forme de dislocations. Ces dislocation peuvent ensuite évoluer en V-pits. La contrainte compressive est également à l'origine de la présence d'un champ électrique interne dans les puits quantiques InGaN/GaN. Celui-ci a pour effet de séparer les fonctions d'onde des électrons et des trous lorsque le puits est élargi ou lorsque le pourcentage d'indium est augmenté. Le phénomène appelé "pulling effect" caractérise la difficulté croissante à incorporer l'indium lorsque la contrainte compressive augmente, celui-ci est très présent lors de la croissance d'InGaN sur GaN. Un phénomène de segrégation de surface de l'indium est également mis en évidence dans la littérature. Les interfaces puit/barrière ne sont par conséquent pas abruptes ce qui décale la longueur d'onde d'émission vers le bleu et élargit le puits (ce qui diminue le taux de recombinaisons radiatives à cause du champ électrique).

Dans la dernière partie du chapitre, une étude a été menée pour quantifier l'indium dans deux échantillons référence. Un échantillon d'InGaN épais (300 nm, $x_In \simeq 5\%$) et un échantillon avec 4 puits quantiques avec différents pourcentages d'indium. Les techniques de caractérisation qui ont été testées sont les suivantes : spéctroscopie de rétrodiffusion de Rutherford (RBS), sonde atomique tomographique (APT), photolumiescence (PL), cathodoluminescence (CL), diffraction par rayons X (XRD), analyse dispersive en energie de rayons X (EDX) et spectrométrie de masse à ionisation secondaire (SIMS). La quantification de l'indium dans l'InGaN est difficile. Compte tenu des inhomogénéités existantes, la valeur de concentration donnée sera toujours une valeur moyenne. Pour la quantification de l'indium dans l'InGaN en couche épaisse, les méthodes XRD, EDX, APT et PL sont les plus adaptées. Pour la quantification dans les puits quantiques, les méthodes utilisées seront l'EDX et l'APT ainsi que XRD dans certains cas. Il faut également noter que APT est la seule méthode permettant d'étudier la distribution d'indium à l'échelle du nm ce qui sera utile par la suite.

D.3 LEDs blanches et LEDs de couleur

Une couleur est définie par ses coordonnées de chromaticité (x, y) qui peuvent êtres représentées sur un diagramme de chromaticité. Les coordonnées (0,33 ; 0,33) correspondent au blanc. La qualité d'une source de lumière blanche peut être évalué grâce à l'indice de rendu de couleur (IRC) qui varie entre 0 et 100. Par rapport aux autres sources de lumière blanche (lampe à incandescence, tube fluorescent), la DEL présente plusieurs avantages tels que la longue durée de vie ($\simeq$ 25 000 heures), le bon rendement et la couleur de température ajustable. Il existe plusieurs types de DELs blanches mais la plupart des LED commercialisées reposent aujourd'hui sur l'approche qui consiste à utiliser une DEL bleue avec des phosphores jaunes. Cette approche a plusieurs inconvénients tels que l'instabilité des coordonnées de chromaticité avec la température de fonctionnement et avec le temps ainsi que les pertes liées à la conversion. Dans ce contexte, la LED blanche monolithique pour laquelle chaque puits quantique émet à une longueur d'onde différentes a été proposée en 2001. Deux problèmes principaux sont identifiés : le faible rendement d'émission des puits verts, jaunes et rouges et dans une moindre mesure la répartition des porteurs dans les puits. Une simulation menée grâce au logiciel de TCAD Silvaco a montré l'avantage d'introduire de l'indium dans les barrières de la zone active afin d'ajuster cette répartition pour contrôler les coordonnées de chromaticité.

Améliorer le rendements d'émission de puits verts, jaunes et rouges est aussi une problématique importante dans le cadre de l'application display. En effet, si les DELs bleues sont fabriquées à partir des matériaux AlInGaN, les matériaux AlInGaP sont utilisés pour les DELs rouges. Pour la région spectrale de 520 à 570 nm, il n'existe pas de matériaux permettant une émission efficace, néanmoins pour l'émission de couleur verte les nitrures d'éléments III sont utilisés. Ce phénomène est appelé comme le problème du "green gap". La difficulté pour atteindre les grandes longueurs d'onde tout en conservant un bon rendement d'émission peut s'expliquer par plusieurs raisons. Pour parvenir à de grandes longueurs d'ondes, la solution est soit d'augmenter la concentration en indium dans les puits, soit de les élargir. Or pour chacun de ces procédés, le champ électrique interne est amplifié ce qui diminue le rendement d'émission en séparant les fonctions d'onde de l'électron et du trou. Augmenter la concentration en indium est difficile en raison du "pulling effect" conséquence de la contrainte compressive. De plus, la baisse de la température de croissance nécessaire pour atteindre une forte concentration d'indium provoque l'apparition de défauts lié notamment à une incorporation d'impuretés plus importante. De plus, le phénomène de DROOP (diminution du rendement d'émission pour les grandes injections) déjà présent pour les DELs bleues est accentué lorsque de plus grandes longueurs d'ondes sont atteintes.

Dans la littérature, plusieurs solutions sont envisagées pour contourner ces problèmes comme la croissance sur plans semi-polaires ou non-polaires, l'insertion de couches d'AlGaN dans la zone active, ou l'introduction d'une couche d'InGaN épais ou de super réseau InGaN/GaN sous la zone active. La solution que nous proposons est basée sur l'emploi de substrats InGaN dans le but de diminuer la contrainte compressive. Cela devrait permettre de faciliter l'incorporation d'indium et diminuer le champ électrique. Les substrats InGaN utilisés sont en fait des pseudo-substrats appelés InGaNOS et fabriqués par l'entreprise Soitec. Une structure de DEL "tout-InGaN" est envisagée.

D.4 Vers de plus grandes longueurs d'ondes sur GaN

Dans ce chapitre, plusieurs tentatives pour atteindre de grandes longueurs d'ondes sur GaN sur saphir sont présentées. Pendant toute cette thèse, la largeur des puits quantiques est maintenue autour de 3 nm. La seule solution pour atteindre ces longueurs d'ondes est donc d'augmenter la concentration en indium dans les puits.
En premier lieu, des variations sur les conditions de croissance des puits quantiques d'une structure référence ont été effectuées. En augmentant la pression du réacteur pendant la croissance des puits quantiques et le flux de TMIn, un décalage des longueurs d'onde vers le rouge est observé. Néanmoins on ne dépasse pas 500 nm et lorsque ces paramètres dépassent une certaine valeur, la longueur d'onde se décale de nouveau vers le bleu, un phénomène de saturation apparait.
Ensuite, des couches d'InGaN ($\simeq$ 50 nm) on été crues pour étudier l'influence des paramètres de croissances sur la qualité de la surface et l'incorporation d'indium. Puis, une de ces couches épaisses d'InGaN a été placée sous la zone active d'une structure classique de puits quantiques InGaN/GaN. L'introduction d'un super réseau InGaN/GaN a également été testé. Ces deux échantillons ont démontré des rendements d'efficacité quantique interne (IQE) supérieurs par rapport à l'échantillon référence, tout particulièrement dans le cas du super réseau. Dans ce cas, le bon rendement d'efficacité est la conséquence d'une forte localisation des porteurs.
Le phénomène de ségrégation de surface de l'indium a été étudié à la fois à la première interface barrière/puits et à la deuxième interface puits/barrière. Pour améliorer la qualité de la première interface, la vanne de TMIn est ouverte en amont afin de saturer la surface en indium avant l'arrivée du gallium. Ce traitement a permis d'observer un décalage vers le rouge jusqu'à 30 nm. Pour la deuxième interface une remontée en température avant la croissance de la barrière à également permis d'observer un faible décalage vers le rouge.
Néanmoins même si toutes ces approches étaient combinées, il serait difficile d'atteindre de grandes longueurs d'ondes tout en conservant un bon rendement d'émission.

D.5 Croissance de couches InGaN sur substrats InGaNOS

Le substrat InGaNOS consiste en une couche d'InGaN reportée sur oxyde et saphir. Les substrats sont fabriqués à partir d'un donneur, constitué d'une couche d'InGaN sur GaN. Les caractéristiques des donneurs et des substrats InGaNOS ont été étudiées et le processus de fabrication est décrit. Le paramètre de maille a des substrats InGaNOS sont supérieurs à ceux du GaN sur saphir et également à celui du GaN relaxé (autrement appelé Free-Standing). Les substrats InGaNOS sont disponibles en 3 nuances, 3,190 Å, 3,200

Ået 3.205 Å. La comparaison de la dépendance du paramètre de maille à la concentration d'indium par rapport à la loi de Végard révèle que les couches d'InGaN des substrats sont partiellement relaxées.

La reprise de croissance InGaN ($\simeq$ 200 nm) est ensuite testée sur les différents substrats (Trois substrats InGaNOS et template GaN) en les plaçant dans le même run MOCVD pour être sur que les mêmes conditions de croissance sont appliquées. Un décalage vers le rouge de la longueur d'onde d'émission mesurée en PL est observée en fonction du paramètre de maille a du substrat. Ce décalage en longueur d'onde est associé à une augmentation de la concentration en indium de 3,0 % à 3,9 %, 4,2 % puis 4,7 % pour l'échantillon sur GaN, InGaNOS 3.190, InGaNOS 3.200 et InGaNOS 3.205, respectivement. La réduction du "pulling effect" est ainsi démontrée. La contrainte diminue également en fonction du paramètre de maille a.

Ensuite, des intercouches de GaN ont été introduites à intervalle régulier dans cette reprise de croissance InGaN. Grâce à cet ajout, la qualité de la surface et la qualité crystalline sont améliorées tout en conservant le paramètre de maille a. Ceci devrait permettre de croitre des couches InGaN plus épaisses sans former trop de défauts (V-pits). Des variations de la température de croissances ont également été testées. Augmenter la température de croissance entraine une baisse de la concentration en indium ainsi qu'une amélioration de la qualité crystalline et de la qualité de la surface. Cette étude rappelle l'importance de conserver une température relativement haute tout en conservant une concentration d'indium assez élevée pour ne pas augmenter trop la contrainte en tension.

Enfin, une étude menée à l'ESRF sur un échantillon d'InGaN sur InGaNOS 3.190 est présentée. Cette mesure a permis de réaliser une cartographie en paramètres de maille a et c sur une zone de 40 µm x 40 µm à un pas de $\simeq$ 260 nm. Après traitement, une cartographie en concentration d'indium et contrainte est obtenue pour le substrat et la couche de reprise de croissance. La dépendance de la contrainte de la couche InGaN avec le paramètre de maille a du substrat est observée à cette échelle sub-micrométrique comme à l'échelle macro-métrique. L'homogénéité en concentration d'indium et contrainte est également établie à l'intérieur des patterns (la surface des substrats est patternée).

D.6 Puits quantiques sur substrats InGaNOS

Dans ce chapitre, des structures de puits quantiques InGaN/InGaN sont crues sur les couches InGaN sur substrat InGaNOS du chapitre précédent (structure "tout-InGaN". Les 3 nuances de substrats sont placées dans le même run de croissance MOCVD pour être soumises au mêmes conditions de croissance. Pour comparaison, une structure classique de puits quantiques est crue sur GaN template avec les mêmes conditions de croissance pour les puits. Pour différentes conditions de croissance de base, un décalage de la longueur d'onde vers le rouge est observé en fonction du paramètre de maille a du substrat.

Par exemple, pour des conditions de croissance donnant la couleur verte, des longueurs d'onde de 500, 525, 537 et 549 nm sur GaN, sur InGaNOS 3,190, sur InGaNOS 3,200 et InGaNOS 3,205, respectivement. Avec les conditions de croissance ambre, une longueur d'onde de 594 nm a été atteinte.
La série d'échantillons émettant dans le vert a été caractérisée grâce à plusieurs techniques sophistiquées. Grâce aux mesures TEM, les largeurs des puits quantiques ont été mesurées à 2,8, 2,3, 2,3 et 3,1 pour les échantillons sur GaN, sur InGaNOS 3,190, sur InGaNOS 3,200 et InGaNOS 3,205, respectivement. Ainsi, la raison du décalage de la longueur d'onde vers le rouge avec le paramètre de maille a du substrat ne peut pas être un élargissement des puits et a donc été attribuée à une augmentation de la concentration en indium. Ceci a ensuite été vérifié grâce à des mesures EDX. Les mesures EDX et TEM révèlent également des inhomogénéités de largeur des puits quantiques pour les échantillons sur InGaNOS alors que l'échantillon sur GaN présente des interfaces plus homogènes (attention les analyses sont très locales et pourraient ne pas être totalement représentatives). Des inhomogénéités de composition sont également observées, particulièrement sur les échantillons sur InGaNOS. L'analyse de l'émission de photoluminescence en fonction de la température indique un comportement très différent pour les échantillons sur InGaNOS par rapport à l'échantillon sur GaN. Les échantillons sur InGaNOS présentent une très forte localisation des porteurs, un comportement qui se rapproche de celui des boites quantiques. Cette localisation accrue par rapport à l'échantillon sur GaN peut être attribuée à une plus forte inhomogénéité des largeurs des puits quantiques et/ou à une plus grande présence d'agrégats d'indium (la définition précise des agrégats a été abordée dans le chapitre 1). Les IQE des meilleurs échantillons sur InGaNOS ont été mesurés et de bonnes valeurs ont été obtenues pour des longueurs d'onde correspondant à la couleur verte, jaune et ambre. Ces bonnes valeurs sont probablement la conséquence de la localisation importante des porteurs.
Pour réaliser la structure DEL entière, des essais de dopage ont ensuite été réalisés. Des couches d'InGaN dopées n et GaN dopé p formant une jonction p-n ont été épitaxiées sur les trois substrats InGaNOS ainsi que sur un template GaN. Les mesures SIMS et TLM effectuées sur l'échantillon sur InGaNOS 3.190 ont révélé de bonnes caractéristiques pour le n-InGaN (concentration de Si et résistances de contact et de couches satisfaisantes) mais le p-GaN est moins satisfaisant (concentration de magnésium trop élevée et forte résistances de contact et de couche). Néanmoins pour un premier essai, ces caractéristiques seront suffisantes pour la première structure DEL. La première structure DEL a été réalisée sur InGaNOS 3.190 avec une structure "tout-InGaN" en ajoutant le p-GaN. La longueur d'onde d'émission a été mesurée en électroluminescence à 510 nm. Malheureusement, les mesures électriques ne sont pas assez satisfaisantes pour mesurer une valeur de rendement quantique externe (EQE). En effet, la mauvaise qualité du p-GaN est responsable de courants de fuite importants. Il existe deux défis importants a

relever pour obtenir une DEL "tout-InGaN" sur InGaNOS. Le premier est lié au "current spreading" ; la couche InGaN dopée n doit être suffisamment épaisse pour permettre une bonne circulation du courant. Ceci devrait être possible grâce à l'insertion d'intercouches de GaN permettant d'augmenter l'épaisseur d'InGaN jusqu'à 1 µm. Le second est lié à la couche dopé p. La contrainte en tension pouvant devenir trop importante, la couche dopée p doit être constituée d'InGaN dans certains cas. Cette étape va donc nécessiter une optimisation supplémentaire car le comportement du magnésium dans l'InGaN est différent de celui du GaN.

D.7 Conclusion

Lors de cette thèse, les problématiques liées à l'émission à grande longueur d'onde avec les nitrures d'éléments III pour les applications de la DEL blanche monolithique et les displays DELs (DELs vertes et rouges monochromatiques) ont été étudiées. Une solution basée sur l'utilisation de pseudo-substrats InGaN appelés InGaNOS a été explorée pour diminuer la contrainte dans la zone active préjudiciable à l'efficacité quantique. Les différentes étapes de croissance MOVPE ont été implémentées depuis l'étape de la recroissance sur le substrat jusqu'à la DEL complète. Les échantillons épitaxiés ont été caractérisés grâce à des techniques optiques et et structurales pour analyser la qualité cristalline et les propriétés d'émission.

En premier lieu, les propriétés de l'alliage InGaN ont été examinées. La croissance d'InGaN sur GaN se révèle difficile en raison de la forte contrainte compressive entre l'InGaN et le GaN. En effet, la contrainte provoque l'apparition d'un champ électrique interne responsable de l'effet Stark confiné quantique dans les puits quantiques InGaN/GaN. L'effet Stark sépare les fonctions d'onde des électrons et des trous et devient de plus en plus mauvais à mesure que les puits quantiques sont élargis ou la concentration en indium est augmentée. Augmenter la concentration en indium a été la solution choisie pour atteindre les grandes longueurs d'ondes. Néanmoins, atteindre des concentrations plus grandes que 20-25 % est difficile à cause de la faible miscibilité de l'indium dans le GaN et du "pulling effect". Il a été montré que la distribution de l'indium dans l'InGaN était très inhomogène et pouvait même présenter des clusters dans certains cas.

Pour la première étape, la croissance d'une structure classique de puits quantiques sur GaN sur saphir a été menée. Avec de simples variations sur les paramètres de croissance des puits quantiques (pression dans le réacteur et flux TMIn), la longueur d'onde d'émission n'a pas dépassé 500 nm car un phénomène de saturation est apparu. La diminution de la température de croissance n'a pas été testée car il résulterait en une diminution de qualité cristalline. Ensuite, après une étude sur l'influence des paramètres de croissance (vitesse de croissance, température de croissance, épaisseur de la couche) pour des couches d'InGaN sur GaN, une de ces couches a été introduite sous la zone active d'un échantillon de puits quantiques (échantillon InGaN UL). Une structure avec un super réseau (échantillons InGaN SL) sous la zone active a également été étudié. Ces deux structures ont montré une amélioration du rendement quantique interne (IQE) par rapport à une structure classique. Pour l'échantillon InGaN UL, la valeur d'IQE était particulièrement satisfaisante grâce à une bonne localisation des porteurs. Puis, le phénomène de ségrégation de surface de l'indium a été étudié à l'interface barrière/puits et à l'interface puits/barrière. Un décalage de la longueur d'onde vers le rouge (red-shift) a été obtenu en améliorant les interfaces des puits. Néanmoins, même en combinant toutes ces approches, il est impossible d'atteindre de grandes longueurs d'onde tout en préservant une bonne efficacité à cause de la forte contrainte compressive.

Les caractéristiques des substrats InGaNOS ont été introduites ainsi que leur processus de fabrication. Le paramètre de maille a de ces substrats est supérieur à celui du GaN sur saphir et du GaN bulk (Free-Standing), ce qui est un grand atout. En effet, la croissance d'une couche d'InGaN sur les substrats InGaNOS et sur GaN a montré une réduction de la contrainte avec le paramètre de maille a. La réduction du "pulling effect" a également été démontrée car pour les mêmes conditions de croissances, la concentration en indium de la couche d'InGaN a augmenté avec le paramètre de maille a du substrat. Grâce à l'implémentation d'intercouches de GaN placées régulièrement, il a été établi que la qualité de surface de ces couches InGaN pouvait être améliorée. En compensant la contrainte, ces intercouches vont permettre de croître des couches InGaN avec un bon dopage n pour la structure DEL. Ensuite des variations sur la température de croissance ont confirmé l'importance de maintenir une température de croissance élevée pour éviter une dégradation de la surface et la qualité du matériau. Une étude complémtaire menée à l'ESRF à démontré l'homogénéité de l'émission à l'échelle sub micrométrique pour une couche InGaN sur susbtrat InGaNOS.

Les structures de puits quantiques crues sur la couche InGaN sur susbtrat InGaNOS ont montré le potentiel de l'InGaNOS pour l'émission à grande longueur d'onde. Pour des structures de puits quantiques crues avec les mêmes conditions de croissance, un décalage de la longueur d'onde vers le rouge a été observé avec l'augmentation du paramètre de maille a du substrat. Des longueurs d'onde de 617 nm et 653 nm ont été atteintes à température ambiante et à basse température, respectivement. Une série d'échantillons de puits quantiques émettant dans le vert sur GaN et sur les substrats InGaNOS a été particulièrement caractérisée par PL, TEM, AFM, APT, XRD et EDX. Le décalage en longueur d'onde vers le rouge observé en PL a été attribué à une augmentation de la concentration en indium avec le paramètre de maille a du substrat. Les échantillons sur InGaNOS présentent une inhomogénéité dans la largeur des puits ainsi qu'une forte localisation des porteurs. Le rendement quantique interne optique (IQE) des échantillons de puits quantiques a été mesurées et comparées à la littérature. De bonnes valeurs ont été obtenues dans ls régions spectrales correspondant au vert, au jaune et à l'ambre grâce à la forte localisation des porteurs qui existe peut-être encore à la température ambiante. Ensuite la première DEL tout-InGaN a été crue sur substrat InGaNOS et caractérisée électriquement. Les challenges liées au "current spreading" et à la couche dopée p ont été révélés.

Malgré les étapes d'optimisation restantes, les premières pierres angulaires ont été posées pour l'obtention du DEL à base d'InGaN efficace dans le vert et le rouge. Ces développements pourront par la suite être utilisés pour réaliser une DEL blanche monolithique efficace avec un grand indice de rendu de couleur ou pour les micro-displays.

Amélioration de l'incorporation d'indium dans la zone active grâce à la croissance sur pseudo-substrat InGaN pour l'application à la DEL blanche monolithique

Les Diodes Electroluminescentes (DEL) à base de composés III-nitrures sont très efficaces pour les longueurs d'ondes correspondant à la couleur bleue. Ces DELs bleues sont très utilisées sur le marché car leur combinaison avec des phosphores produit une lumière blanche. Néanmoins, cette approche a plusieurs inconvénients tels que l'instabilité de la température de couleur ou les pertes liées à la conversion. Dans ce contexte la DEL blanche monolithique dont la lumière blanche est obtenue directement dans la zone active grâce à l'émission des puits quantiques à différentes longueurs d'ondes est envisagée. Pourtant, lorsque la longueur d'onde d'émission augmente, le rendement d'émission des puits quantiques InGaN/GaN diminue. Ceci est problématique pour l'application de la DEL blanche monolithique mais également pour l'application micro-display qui nécessite idéalement des DELs monochromatiques bleues, vertes et rouges fabriquées à partir de la même famille de matériaux. Ce problème est principalement du à la différence importante de paramètre de maille entre les puits quantiques InGaN et la couche GaN sur saphir utilisée comme substrat qui provoque une forte contrainte compressive. Cette contrainte est à l'origine d'un champ électrique interne dans les puits quantiques, préjudiciable au rendement d'émission, et d'un taux d'incorporation d'indium faible bien qu'originellement thermodynamiquement difficile. Cette thèse de doctorat propose de résoudre ce problème en réalisant la croissance de la DEL sur un pseudo-substrat InGaN appelé InGaNOS fabriqué par Soitec.
Après avoir identifié les limitations des structures InGaN/GaN sur substrat GaN sur sapphire classique pour l'émission efficace à grande longueur d'onde, des structures « tout-InGaN » ont été crues par EPVOM sur substrats InGaNOS. Il a été démontré que la contrainte était partiellement relaxée et que l'incorporation d'indium était plus facile. Grâce à des caractérisations optiques et structurelles fines, les différentes étapes depuis la reprise de croissance InGaN jusqu'à la DEL complète ont été étudiées. En photoluminescence (PL), la longueur d'onde de 617 nm a été atteinte à température ambiante. Les performances optiques de ces structures de puits quantiques dans les régions spectrales correspondant au vert, jaune et ambre ont été mesurées et sont comparables aux meilleures valeurs de la littérature. Enfin, la croissance de la première DEL « tout InGaN » sur substrat InGaN a révélé les challenges restants qui nécessiteront des développements complémentaires.
Mots-clés : DEL, GaN, InGaN, émission de lumière blanche monolithique, semi-conducteurs

---

In incorporation improvement in InGaN based active region using InGaN pseudo substrate for monolithic white LED application

Light emitting diodes (LEDs) based on nitride materials are very efficient in the blue range. These blue LEDs combined with phosphors are used to manufacture white LEDs widely used in the lighting market. Nonetheless, this converted approach presents some disadvantages , like an instability of the color temperature or conversion losses. In this context, the white monolithic LED which produces the white color thanks to different emission wavelengths produced from quantum wells (QWs) placed in the active region is one of the considered solution.
However, as emission wavelength increases the quantum efficiency of the InGaN based QWs decreases. This is problematic for the white monolithic application but also for micro-display application which both ideally requires red, green and blue monochromatic LEDs grown in the same material system. This issue is mainly due to the great lattice mismatch between the InGaN QW and the GaN layer on sapphire substrate which induces an important compressive strain. This strain is responsible for a strong internal electric field in the QWs, which is detrimental for the quantum efficiency, and for low indium incorporation rate in GaN, originally thermodynamically difficult. This PhD thesis proposes to tackle this issue by growing the LED on an InGaN pseudo-substrate called InGaNOS manufactured by Soitec.
After identifying the limitations of InGaN based structures grown on regular GaN on sapphire substrate for efficient long wavelength emission, full InGaN structures were grown by MOCVD on InGaNOS substrates. It was shown that the strain was partially released and the indium incorporation was made easier. Through fine structural, optical and electrical characterizations, the different steps leading from the InGaN buffer regrowth stage to the complete processed LED were studied. PL emission wavelengths up to 617 nm were reached at room temperature. The optical performances of these MQW structures in the green, yellow and amber range were measured to be comparable to the best ones achieved in the literature. Finally, the growth of the first full InGaN LED structure on InGaN substrate revealed the remaining challenges that will require some additional developments.
Keywords : LED, GaN, InGaN, monolithic emission of white light, semi-conductors